Title
Development of Catalytically Active Au(I) Metal-Mediated Base Pairs and Applications in vitro and in vivo

Author
Green, Sydnee Alexis

Publication Date
2021

Peer reviewed|Thesis/dissertation

UNIVERSITY OF CALIFORNIA

Los Angeles

Development of Catalytically Active Au(I) Metal-Mediated Base Pairs and Applications *in vitro* and *in vivo*

A dissertation submitted in partial satisfaction of the requirements

for the degree of Doctor of Philosophy in Chemistry

by

Sydnee Alexis Green

2021

ABSTRACT OF THE DISSERTATION

Development of Catalytically Active Au(I) Metal-Mediated Base Pairs and Applications *in vitro* and *in vivo*

By

Sydnee Alexis Green

Doctor of Philosophy in Chemistry

University of California, Los Angeles, 2021

Professor Hosea Nelson, Chair

The union of transition metal catalysis with native biochemistry presents a powerful opportunity to perform abiotic reactions within complex biological systems. However, several chemical compatibility challenges associated with incorporating reactive metal centers into complex biological environments have hindered efforts in this area, despite the many opportunities it may present. More challenging than chemical compatibility is biocommunicative transition metal catalysis, where the reactivity of the metal species is regulated by native biological stimuli, akin to natural biocatalytic processes. This dissertation describes the discovery of Au(I)-bound metal-mediated base pairs (MMBPs) in pyrimidine mismatches. Additionally, the application of

these Au(I)-DNA complexes as catalysts that are dependent on genetic information was shown. These Au(I)-DNA catalysts form fluorescent product in response to nucleic acid fragments and can be used to detect nucleic acids in complex biological matrices.

Chapter One is a perspective on transition metal bound to RNA and DNA sequences. These complexes often possess nuclease-type activity in natural biological systems. However, there are some examples of researchers creating abiotic metalallo-nucleic acid complexes that are asymmetric catalysts, that exhibit sequence rate enhancing ligands, or in a few rare examples, are activated through addition of a specific sequence.

Chapter Two details experimental and computational studies of Au(I) metal-mediated base pairs with all three pyrimidine mismatches. Au(I) is incorporated into DNA duplex and hairpin structures containing a C–C, C–T, and T–T mismatch leading increases in thermal stability, changes in circular dichroism, and mass adducts through mass spectrometry. The stable complexes formed through the addition of $(Me_2S)AuCl$ to these mismatches can be used in further applications in nanotechnology and biocatalysis.

Chapter Three describes the activity of a Au(I)-DNA catalyst formed through a C–Au(I)–T metal-mediated base pair. This catalyst is composed of a DNA hairpin structure with a toehold sequence, to aid in hybridization, and a C–T mismatch in the stem. Once the Au(I) precursor is added, an inactive catalyst is formed. Only through hybridization does this catalyst become active, catalyzing the formation of a fluorescent BODIPY molecule through a Au(I)-catalyzed hydroamination reaction. This catalyst become active when hybridized to DNA or RNA complement and exhibits sequence selectivity for the nucleic acid analyte.

Chapter Four outline the development of a Au(I)-DNA catalyst that exhibits turnover, unlike the previous catalyst system (Chapter Three). This catalyst, formed through a C–Au(I)–C metal-mediated base pair, catalyzes the formation of a fluorescent coumarin derivative through a Au(I)-catalyzed hydroarylation. The Au(I)-DNA catalyst or Au(I)-CAP (chemocatalytic amplification probe) with substrate, leads to significant increases in fluorescence, even at low nM concentrations of catalyst. This Au(I)-CAP system outperforms standard molecular beacon technology and works in complex biological systems, such as cell lysates and *E. coli* whole cells, leading to a fluorescent response.

Chapter Five describes the use of a Au(I)-CAP that hybridizes to SARS-CoV-2 related nucleic acid fragments. Hairpins were designed such that they hybridize to either the viral RNA or viral cDNA of the N gene of the SARS-CoV-2 genome. These catalysts form a fluorescent coumarin product in response to the viral genetic information leading to detection levels in the low fM range. In addition, this can be paired with a nucleic acid amplification technique to detect less than 1 copy/μl of viral RNA or DNA. Finally, direct detection of viral RNA from heat-inactived virus in human saliva was achievable in this system.

The dissertation of Sydnee Alexis Green is approved.

Neil K. Garg

Alexander M. Spokoyny

Patrick G. Harran

Hosea M. Nelson, Committee Chair

University of California, Los Angeles

2021

This dissertation is dedicated to my mom, Tiffini

TABLE OF CONTENTS

LIST OF FIGURES

CHAPTER ONE

CHAPTER TWO

CHAPTER FOUR

CHAPTER FIVE

LIST OF TABLES

CHAPTER TWO

CHAPTER THREE

CHAPTER FOUR

CHAPTER FIVE

LIST OF ABBREVIATIONS

α	alpha
A	adenine
B3LYP	Becke, 3-parameter, Lee-Yang-Parr (functional)
BE	base pairing energy
BODIPY	4,4-difluoro-4-bora-3a,4a-diaza-*s*-indacene
°C	degrees Celsius
C	cytosine
CAP	chemocatalytic amplification probe
CD	circular dichroism
comp	complement
DFT	density functional theorem
DNA	deoxyribonucleic acid
ds	double stranded
Et	ethyl
f	femto
FRET	Fluorescence resonance energy transfer
ee	enantiomeric excess
equiv	equivalents
G	guanine
HPLC	high performance liquid chromatography
hr	hour
Hz	hertz
kcal/mol	kilocalories to mole ratio
K_M	binding constant

μ	micro
M	molar
m	milli
m	meta
Me	methyl
min	minutes
MMBP	metal-mediated base pair
MS	mass spectrometry
n	nano
NMP	nuclear magnetic resonance
nt	nucleotide
o	ortho
π	pi
p	para
Ph	phenyl
pM	picomolar
RNA	ribonucleic acid
ss	single stranded
Std. Dev.	standard deviation
T_m	melting temperature
T	thymine
TON	turnover number
UV	ultraviolet
V_{max}	maximum rate

ACKNOWLEDGEMENTS

As I get closer to finishing graduate school, I am thankful for all of the support that I have received throughout the last five years. I will admit, I knew entering graduate school that I would be challenged and was prepared for the long hours and hard work; however, I did fully not understand how much I would learn and grow as a scientist by joining a young lab.

I would like to begin my acknowledgments by thanking my advisor, Professor Hosea M. Nelson. Throughout the years, Hosea has always saw my potential and pushed me to do the research that I wanted to do. He challenged me to learn new skills, outside of my scientific comfort zone, and through it all I became a better scientist. Hosea was always around to discuss science and help with my experiments, even to the point of coming into lab and setting things up if I was having trouble. I think what I appreciate most of all was Hosea's encouragement of our own ideas and creativity. Not only did he allow us to explore our own ideas, but he often pushed us to come up with our own research plans. Through this process, I was able to grow as a scientist and our lab was able to make some very interesting discoveries along the way! Hosea, I will forever be grateful to you for all that you have taught me, thank you.

I would also like to acknowledge the remaining members of my doctoral committee: Professors Neil K. Garg, Alexander M. Spokoyny, and Patrick G. Harran. Their guidance during my advancement to candidacy exam and 4th year meetings was greatly appreciated. They were always quick to answer any questions or offer any support when necessary and I appreciate all that they have done.

I knew that joining a young lab would mean that everyone would get very close and need to rely on each other a lot but I did not expect to get so close to all of my lab mates. I will forever

consider the students in my lab friends. For nearly five years, I have spent over 10,000 hours with most of these students and, over that time, I feel like we became a family. I would first like to thank the two students that started the lab, Alex Bagdasarian and Brian Shao, my UC Davis boys. Although I never worked on a project with either of them, they taught me so many important things in lab. Bags was always willing to drop whatever he was doing to show other students in lab how to set something up or how to do something specific in lab. He was one of the most dedicated scientists I have ever met, spending more time in lab than any other student I have seen in my time at UCLA. I know he is doing great things in his industry and I am so proud of him. Shao was the best person to share a lab room with. He has a good taste in music and an amazing sense of humor. His knowledge from working in a chemical biology lab at UC Davis also made him one of the best students for me to talk chemistry with, and he gave me a lot of valuable advice for my project. He never made me feel like I was in the way when I would ask for his help, which was way too often. I hope he is as excited as I am about working with me for the foreseeable future at Terray Therapuetics!

Next, I would like to give a special thanks to Stasik Popov. Stasik and I started on the same day in the Nelson lab and I feel like he has always been very supportive of me. He is always excited to talk chemistry and is very knowledgeable. I got the opportunity to work on a related project at the end of my graduate career and he was probably the most helpful person I have ever worked with. He would take time away from his own work to show me where things are or talk to me about experiments that I was planning. I will forever consider Stasik a good friend and I am sure we will stay in touch! Thank you for all of your help and support over the last five years. I would also like to thank Roy Pan and Luke Boralsky. Those two made my day so much more entertaining and I have so many amazing memories from my first year because of them.

When the next class joined the lab, our size basically doubled. Ben Wigman, Jessica Burch, Lee Joon Kim, Sepand Nistanaki, and Chris Jones were all amazing coworkers and I am so thankful that you all joined the lab. I had the pleasure of collaborating with most of these students on projects throughout the last five years. Ben, Sepand, and Chris were invaluable coworkers to me during my project as they were able to come on during the lab shutdown and help me with the COVID-19 project development. Ben is hilarious and always says something to make me laugh and brighten the mood. Lee Joon and I have also worked on many projects together and put in many hours trying to get a crystal structure of the DNA-Au(I) complex, I still have hope that she will get it, as she is an amazing scientist! Jessica is so much fun and I am so happy that she came to our lab as we have had many good times together as 3221 friends.

Chloe Williams and Woojin Lee always come to lab with a smile on their face. They both always seem to be in a good mood and make the lab a more cheerful place to be. Throughout my time I have seen Chloe grow so much as a scientist and I know she will do amazing things in her future career. I am excited to see what these two students do in coming years.

Lily Sloan and Steven Zhao were the most recent additions to the lab. I had the pleasure of working with Steven as an undergraduate, where he helped me make some fluorophores for my project. He is an extremely smart and talented synthetic chemist. Lily is such a hard worker and she is such a brave scientist, willing to push herself to learn new skills to make research progress. I know these students are going to do great things in the next few years.

Last but not least of the Nelson lab alumni is Hayden (Blossy) Montgomery. I took Hayden in as a first-year graduate student and immediately realized she would be such an important person to my graduate experience, personally and scientifically. She is the person who taught me how to be a mentor and how to push someone to see all of their potential. She has helped me so much in

lab and was always so excited about working on the DNA project. I am so thankful for all of the help she has given me, from all of our late nights in lab to her help with edits proposals and papers, even after she left the lab. I was able to see her grow from an undergraduate who wanted to go to pharmacy school to the amazing scientist she is today (Hopefully you aren't too made that I convinced you to go to graduate school)! I will forever cherish our friendship and I am so excited to see you grow over the next two years.

The friends that I have made outside of the Nelson lab in graduate school were also invaluable to my graduate experience. From day 1, Rachael Day and I predicted that we would be best friends. We even said that Edris Rivera, Dan Estabrook, her and I would all move in together and be best friends, which at first the boys did believe at first…but look where we are now! We have all lived together since our second year and I honestly can't think of any other people I would have rather spent 1/5 of my life thus far with. They were there for me at a point in my life when I really needed it and felt like I was going through a lot, and I will be forever thankful for that. They have truly been my family away from home and I know that we will remain friends and keep in touch for the rest of my life. I would also like to include Jessica Logan in this group of close friends, although she never lived with us, she was heavily involved in most of our shenanigans and she is definitely one of the gang.

In addition to the everyone that helped me at UCLA, there are a few people before I came to graduate school that were very important to my academic success. The first being all of my professors in high school, at butte college, and UC Davis. Most importantly, my coworkers and mentors in Sheila David's lab. Professor David took me in as a transfer student, something a lot of professors do not do, and was very supportive to me as an undergraduate. I would not have gone to graduate school if it wasn't for her giving me the research opportunities that she did. Phil Yuen

was an amazing mentor and taught me everything I knew about doing research from the start. He always made me feel like I could do anything and I appreciate all of his mentorship and friendship over the past 7 years.

Last, but certainly not least, I need to acknowledge my family; Tiffini, Lane, Brian, and Shelby. My parents always supported every decision I made. Even at a young age, I feel like my parents believed in me and trusted me to know what I want and I am so grateful to them for that. They always wanted what was best for me and made me feel like they were so proud of me. I owe everything to them and I would not have been able to accomplish anything that I did without their support.

Chapter One is an unpublished perspective on transition metal-DNA complexes and their catalytic activity written by Green.

Chapter Two is unpublished studies by Green. Green is responsible for writing. Montgomery and Green are responsible for experiments and Benton is responsible for computation.

Chapter Three is a version of Sydnee A. Green, Hayden R. Montgomery, Tyler Benton, Neil J. Chan, Hosea M. Nelson, *Regulating Transition Metal Catalysis Through Interference by Short RNAs. *Angew., Chem. Int. Ed,* **2019**, *58*, 16400–16404. Green, Montgomery, and Chan contributed to experiments. Green and Nelson contributed to writing.

Chapter Four is a version of Sydnee A. Green, Benjamin Wigman, Sepand K. Nistanaki, Hayden R. Montgomery, Christopher G. Jones, Hosea M. Nelson *Chemocatalytic Amplification Probes Composed of a C–C Mismatch Enables Transcriptionally-Regulated Au(I) Catalysis *in*

vitro and *in vivo*. **2020**, *ChemRxiv. Preprint.* https://doi.org/10.26434/chemrxiv.12915761.v2. Green and Montgomery contributed to experiments. Nelson and Green contributed to writing.

Chapter Five is Sydnee A. Green, Benjamin Wigman, Sepand K. Nistanaki, Hayden R. Montgomery, Christopher G. Jones, Hosea M. Nelson *Chemocatalytic Amplification Probes for the Femtomolar Detection of SARS-CoV-2 Fragments. **2020**, *ChemRxiv. Preprint.* https://doi.org/10.26434/chemrxiv.12915761.v2. Green, Wigman, and Nistanaki contributed to experiments. Jones contributed to data analysis. Nelson and Green contributed to writing.

Throughout these studies, I was supported by the Dissertation Year Fellowship, UCLA Department Fellowship Winter 2020, and Majeti Alapati Excellence in Research Award. Additional funding sources for the work described herein include UCLA, Sloan Foundation, Packard Foundation, NIH NIGMS, UCLA AIDS Institute: Coronavirus Pilot Funding Seed Grant, and instrumentation grants from the NSF and the NIH.

BIOGRAPHICAL SKETCH

Education:
University of California, Los Angeles, Los Angeles, CA
Ph.D. in Chemistry, anticipated June 2021
Specialization: Organic Chemistry
Advanced to Candidacy, September 12, 2018
GPA: 3.78

University of California, Davis, Davis, CA
BS in ACS Chemistry, June 2016
GPA: 3.87/3.92

Butte Community College, Oroville, CA
Transfer, June 2014
GPA: 3.79/3.95

Professional and Academic Experience:
Graduate Research Assistant
University of California, Los Angeles, Department of Chemistry and Biochemistry
Advisor: Prof. Hosea M. Nelson

- Discovered Au(I) metal-mediated base pair and studied stability and properties through UV-vis spectroscopy, Mass spectrometry, and CD measurements.
- Developed metalloDNAzymes composed of C–Au(I)–C and C–Au(I)–T metal-mediated base pairs.
- Studied activity of metalloDNAzymes as chemocatalytic amplification probes for nucleic acid detection in complex biological media (e.g. cell lysates and *E. coli* cells).
- Developed chemocatalytic amplification probes for detection of SARS-CoV-2 viral RNA and cDNA fragments.

Undergraduate Research Assistant
University of California, Davis, Department of Chemistry and Biochemistry
Advisor: Prof. Sheila Davis

- Synthesized library of DNA glycosylase transition-state mimics *via* Click Chemistry.
- Determined binding constants of azasugar transition-state mimics with various DNA glycosylase repair enzymes.
- Developed fluorescence-based inhibition assay for DNA glycosylase transition-state mimics.

Honors and Awards:
Graduate
Dissertation Year Fellowship Fall 2020 - Spring 2021
Majeti Alapati Excellence in Research Award Spring 2020
UCLA Department Fellowship Winter 2020

Undergraduate
3rd Place, Presentation at Larock Undergraduate Research Symposium May 2016
Award for Outstanding Graduating Senior June 2016
Graduated with Highest Honors, UC Davis June 2016
ACS Inorganic Undergraduate Award June 2015
Maureen Belletini Undergraduate Research Award June 2015
Deans' Honors List, UC Davis Fall 2014 - Spring 2016

Publications:

Green, S. A.; Wigman, B.; Nistanaki, S. K.; Montgomery, H. M.; Jones, C. G.; Nelson, H. M. Chemocatalytic Amplification Probes Enable Transcriptionally-Regulated Au(I)-Catalysis in *E. coli* and Sensitive Detection of SARS-CoV-2 RNA Fragments. *Submitted for publication,* 2020

Green, S. A.; Montgomery, H. R.; Benton, T. R.; Chan, N. J.; Nelson, H. M. Regulating transition metal catalysis through interference by short RNAs. *Angew. Chem. Int. Ed.*, 2019, *58,* 16400–16404.

Yuen, P.K.; Green, S. A.; Ashby, J.; Lay, K. T.; Santra, A.; Chen, X.; Horvath, M. P.; David, S. S. Targeting Base Excision Repair Glycosylases with DNA containing Transition State Mimics prepared *via* Click Chemistry. *ACS Chem. Biol.*, 2019, *14*, 27–36.

Patents:

Chemocatalytic Viral Detection Methods and Compositions Hosea M. Nelson, Sydnee A. Green. US Provisional Patent Application No. 63/068,525.

Compositions and Methods Related to Gold-Mediated Nucleic Acid Hybridization Hosea M. Nelson, Sydnee A. Green. US Provisional Patent Application No. 62/816,103.

CHAPTER ONE

Metal-Nucleic Acid Complexes and Their Role in Catalysis

1.1 Abstract

The unique structural and metal binding properties of DNA makes it an ideal candidate for forming metal-dependent nucleic acid catalysts. This chapter discusses the various metal-DNA complexes and the strategies utilized to form them. This includes the formation of metal-DNAzymes through *in vitro* selection, as well as the covalent and noncovalent anchoring of synthetic ligands to a DNA structure to form an active metal-DNA complex. Catalysts formed through *in vitro* selection often have reactivity limited to canonical nucleotide chemistry, similar to that of natural ribozymes. Catalysts formed through anchoring, covalent or noncovalent anchoring, have a wider reaction scope that includes abiotic transformation, such as aryl iodide reduction and asymmetric Diels-Alder reactions. Despite these advances in forming metal-nucleic acid complexes for catalysis, developing complexes from simple and cheap nucleic acid sequences, composed of natural bases, that have activity divergent from natural ribozymes, remains unexplored.

1.2 Introduction

Since the discovery of nucleic acid catalysts by Westheimer and Cech in the 1980's, interest in the utility of nucleic acids has rapidly expanded.[1,2] While DNA and RNA were initially thought of just as a molecule for information storage, their well programed hybridization and

inherent metal binding properties make them an optimal candidate for the use as catalysts, whose structure and reactivity are readily optimized through standard *in vitro* selection protocols.

Early developed DNA catalysts (DNAzymes) resemble, in structure and reactivity, natural ribozymes. However, a few strategies have been utilized to expand the chemical scope of DNAzymes. Along with in vitro selection to incorporate unnatural metals, the use of noncovalent and covalent anchoring of ligands has been used to create novel metal-DNAzymes (*Figure 1.1*), whose reactivity is divergent from that of natural RNAzymes. In the examples discussed, single and double stranded DNA is used to enhance the reactivity of the metal center and induce asymmetry onto the products formed.[3]

Figure 1.1 Catalytically active transition-metal-bound nucleic acid complexes.

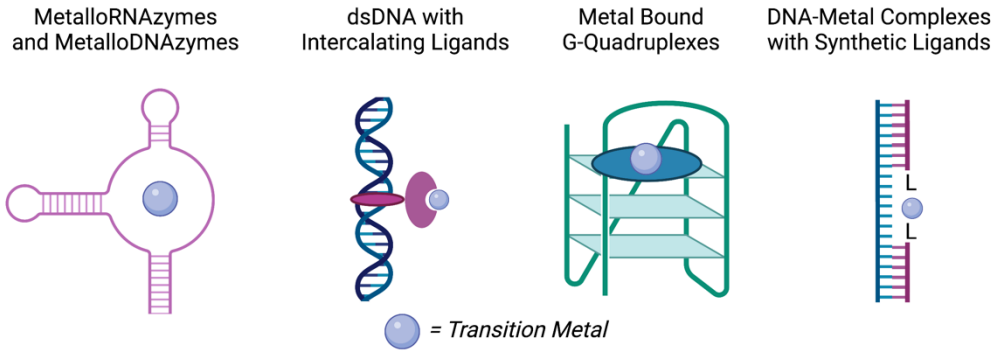

1.3 Metal-DNAzymes formed through *in vitro* selection

RNAzymes, also known as ribozymes, were first discovered by Cech in 1986 as self-cleaving RNA molecules that rely on a Lewis Acidic metal interaction, specifically Mg^{2+}.[4] Since these initial reports, the repertoire of metal bound RNA- and DNAzymes has expanded to include even abiotic (in the context of RNAzymes) transition metals, such as Cu^{2+}, Mn^{2+}, Hg^{2+}, Pb^{2+}, Ni^{2+}, and Ag^{+}, among others.[3] While natural ribozymes are responsible for the cleavage of

the phosphodiester bond of RNA, many DNAzymes have been produced through *in vitro* selection methods to catalyze a variety reactions, such as DNA cleavage,[5] DNA and RNA ligation,[6] phosphorylation,[7] nucleopeptide linkage,[8] and, in a few rare examples, amide hydrolysis.[9]

The most thoroughly developed catalytic chemistry involving metal-DNAzymes, natural an unnatural, is the cleavage of DNA and RNA. Although many of these nucleic acid catalysts have metal cofactors, only a few contain d-block transition metals which are traditionally associated with more complex chemical transformations. Most of these examples contain a transition metal that acts as a Lewis acid, inducing cleavage through activation of the phosphate backbone, allowing for nucleophilic attack by the 2' hydroxyl of the adjacent ribose sugar or another endogenous or exogenous nucleophile, such as water (*Figure 1.2a*).[10] Alternatively, it has been shown that the cleavage of DNA can be induced through a Cu-catalyzed oxidative cleavage mechanism, in which oxidation of the bases or sugars can lead to depurination and finally β-elimination (*Figure 1.2b*). In addition, DNAzyme activity including phosphorylation and dephosphorylation of peptides and nucleic acids has been shown to involve DNA-metal complexes with Mn^{2+}, Cu^{2+}, and Zn^{2+} through a similar phosphate activation mechanism.

Figure 1.2 DNA and RNA cleavage mechanisms with metal-dependent DNAzyme.

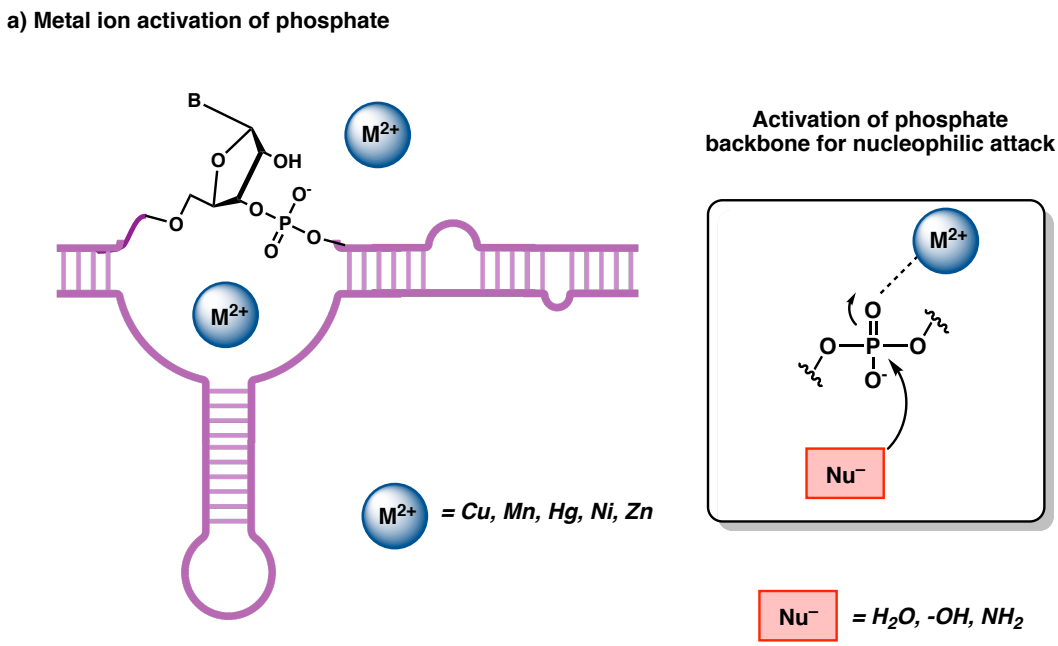

Researchers have more recently developed complexes with catalytic activity that is more divergent from that of natural RNAzymes. In 2016, Silverman and co-workers showed that in vitro selection can be used to discover metal-DNAzymes with catalytic activity other than DNA ligation

and cleavage.[9] They were able to successfully develop a Zn^{2+} dependent DNAzyme with amide hydrolysis activity that cleaves an amide bond linking two distinct nucleic acid segments together (*Figure 1.3a*). In this way, they were able to use *in vitro* selection methods to optimize the 40-nucleotide metal binding sequence that consisted of modified nucleobases (**1.1**), an early example of using *in vitro* selection methods to design a catalyst with activity other than phosphate cleavage and ligation.

Figure 1.3 Zn(II)-DNAzyme catalyzed amide hydrolysis.

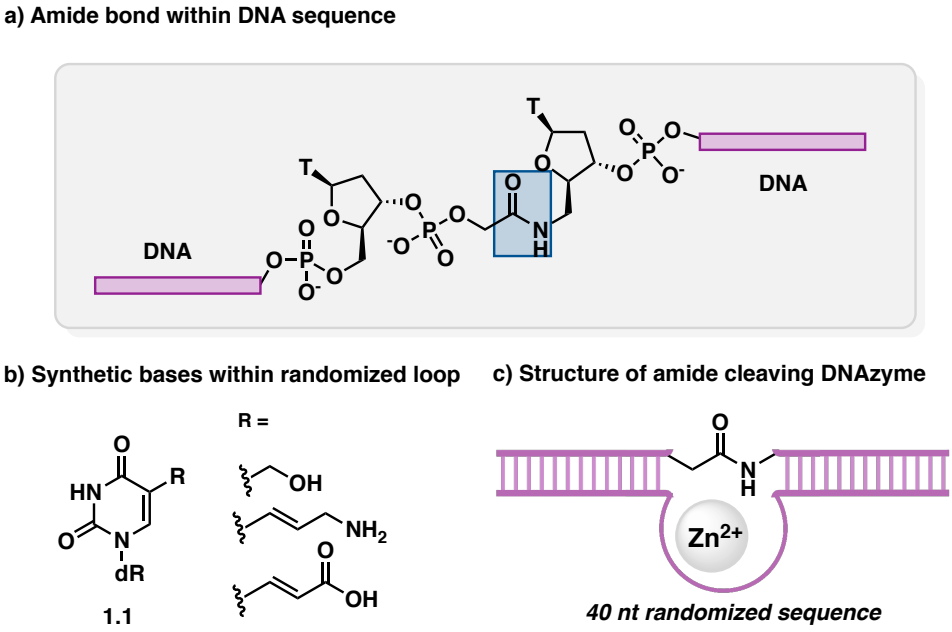

In these examples of DNA-transition metal catalysts, the metal is directly bound to specific binding pockets in ssDNA (*Figure 1.3c*), and the complexes have been shown to catalyze a range of different bond breaking and bond forming reactions, and most interestingly can be optimized for specific metal binding or substrate sequence selectivity through a few rounds of *in vitro* selection. While this process can lead to very active and specific catalysts, the types of reactions

performed by these catalysts are limited to nucleic acid and nucleic acid/peptide or small molecule derived substrates.

1.4 Intercalation of transition metal catalysts to DNA

While original efforts in the development of DNAzymes mainly focused on the breakage and formation of nucleic acid and nucleopeptide bonds, researchers have since pursued the discovery of nucleic-acid-metal complexes which perform more complex transformations. Toward this effort, it was found that the non-covalent interactions of metal complexes with nucleic acids can alter the reactivity of the metal complex through both electronic and steric affects, thereby expanding the potential utility of these complexes. Notably, there is extensive potential in utilizing hybrid catalysis which combine catalytic activity of transition metals with the chirality of these biological ligands. Furthermore, the modularity and ease of access to these biopolymers, like nucleic acids, allow for facile development of numerous metal complexes with various reactivity profiles. Specifically, this reactivity can be modulated by both the chirality of the DNA, as well as the ligand acceleration effects observed due to the π-stacking interactions with ligands intercalated between bases.

The supramolecular anchoring of transition-metal complexes to biomolecules has been explored extensively in the context of protein-transition metal hybrid catalysts since early reports by Whitesides in 1978.[11] However, reports in 2005 by Roelfes and Feringa showed that a Cu^{2+} ligand with a distal 9-aminoacridine moiety (**1.2**) could intercalate into dsDNA helix and catalyze a Diels-Alder reaction between azachalcone **1.3** cyclopentadiene **1.4** in water, with moderate enantioselectivities of the endo isomer (up to 49% ee) .[12] Since this seminal report, the repertoire of asymmetric reactions, catalyzed by intercalating ligands with dsDNA, has expanded to include

asymmetric Michael addition, Friedel-Crafts alkylation, electrophilic fluorination, hydrolytic kinetic resolution of epoxides, and cyclopropanation of α-diazo-β-keto sulfones, all with enhanced enantioselectivities up to 99% ee.

Figure 1.4 Cu-DNA complex formed through ligand intercalation and Cu-catalyzed Diels-Alder reaction.

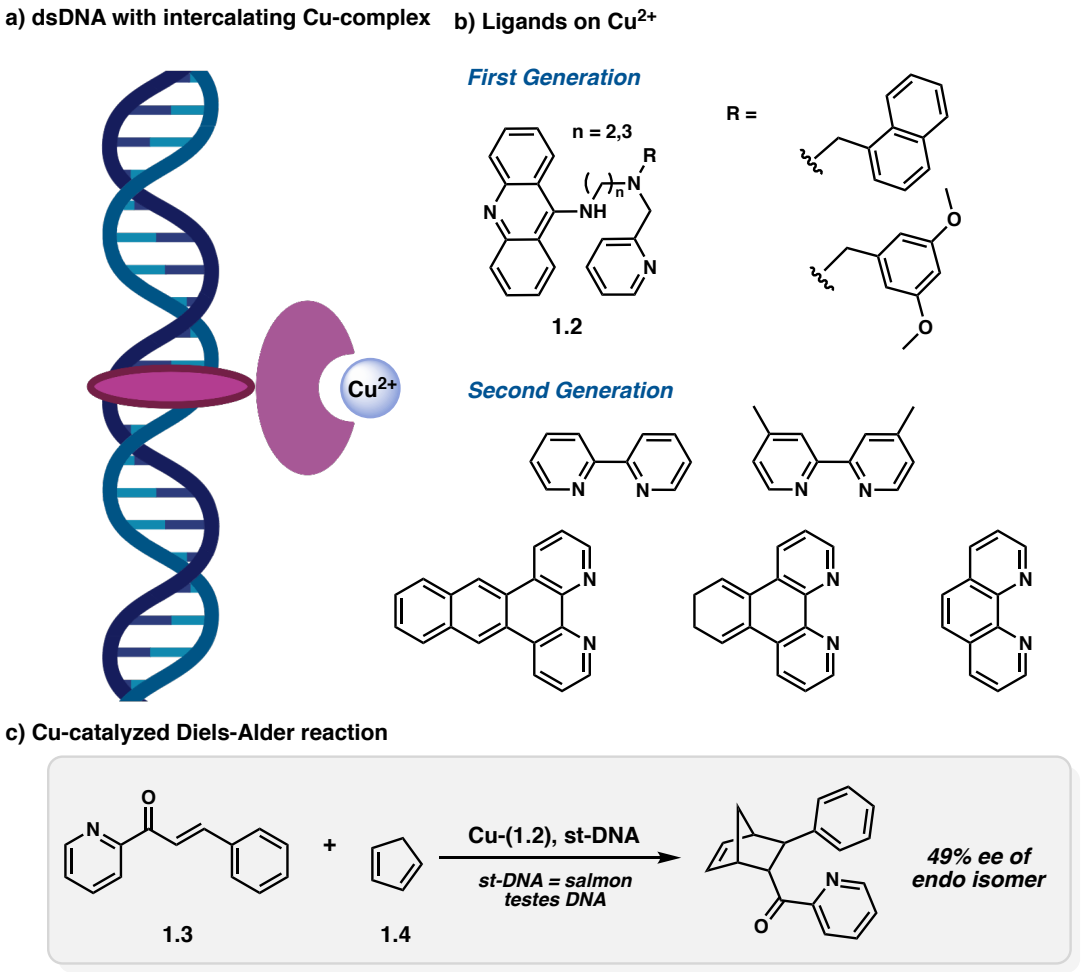

While the initial reports resulted in the formation of enantioenriched products, it was found the addition of dsDNA often led to losses in catalyst activity. However, further kinetic studies revealed that some of the Cu^{2+} catalysts (second generation ligands) experienced a ligand

acceleration in the presence of dsDNA and that this acceleration was highly sequence and intercalating-ligand dependent. Interestingly, this sequence preference and catalysis did not correspond to the binding constant of the copper complex with the DNA. For example, tighter binding copper complexes did not form the most reactive catalysts. Likely the microenvironment provided by the nucleobases within the DNA altered the electronics of the intercalating ligand on Cu^{2+}, resulting in a more active copper center.

In another example, the intercalation of metal-porphyrin complexes to G-quadruplexes resulted in the formation of catalysts capable of oxidation of small molecules.[13,14] These G-quadruplex heme hybrid catalysts exhibit peroxidase activity and have been shown to catalyze the reaction of luminol with hydrogen peroxide, producing a chemiluminescent response.[22] These initial reports led to further investigation of the activity of this DNA-Fe peroxidase catalyst and showed the potential application of this complex as a peroxide sensor. The combination of this oxidation catalyst with an aptamer sequence led Golub and coworkers to develop DNAzyme-Aptamer **1.5** capable of oxidizing small molecules such as dopamine **1.6** to form N-hydroxy-L-arginine (**1.7**) and aminochrome (**1.8**) to citrulline (**1.9**) selectively.[23] Specifically, known aptamers for these substrates, **1.6** and **1.8**, were paired with the peroxidase DNAzyme, bringing the substrate in proximity to the DNAzyme active site, allowing for substrate specific reactivity. This catalyst system utilizes a reactive Fe-heme within the G-quadruplex structure and an aptamer substrate binding site (**1.5**), resulting in a DNAzyme catalyst with substrate specificity that parallels that of protein enzyme catalysts.

Figure 1.5 G-quadruplex-Aptamer complex with Fe-heme cofactor with peroxidase activity.

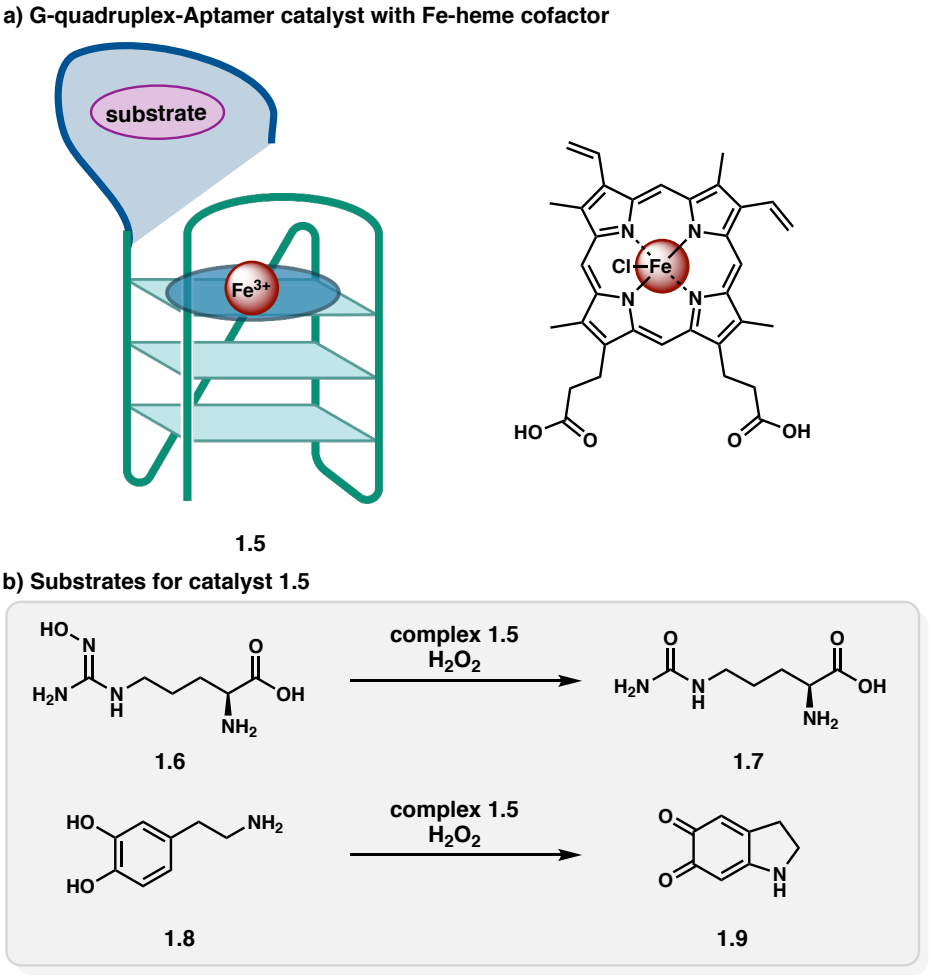

Overall, the non-covalent interactions between transition metal complexes and the secondary structures of DNA make for more active and efficient chiral catalysts. However, while the complex structure and electronic properties of DNA are useful in forming unique catalysts, the nonspecific interactions between these intercalating catalysts make it difficult to obtain high levels of control and predictability of the catalyst reactivity.

1.5 Covalent attachment of metal binding ligands to DNA

Another approach to forming hybrid metal-DNA catalysts is to covalently attach ligands to the DNA backbone. This has been shown to gain a greater level of control over the metal environment to induce enantioselectivity. In addition, there are a few examples of controlling the metal reactivity through hybridization to a specific sequence. In this way, transition metal reactivity is modulated by a specific nucleic acid analyte. While these reactions are of interest from a reactivity and catalyst control stand point, they have been proven more challenging to synthesize and have limitations in optimization as they require laborious synthetic modifications of nucleic acid sequences.

Alternatively, direct functionalization of nucleobases to incorporate metal binding motifs has proven successful in forming transition metal-DNA complexes. Phosphine and diene derived nucleosides have been used to form Pd(II)[15] and Ir(I)[16] DNAzymes, **1.10** and **1.11** respectively. Both complexes catalyze allylic amination reactions with modest to high levels of enantioselectivity (*Figure 1.6a*). While this initial approach led to the development of unique catalysts, the steric constraints of having the metal ligand be a nucleoside within a DNA strand resulted in a less active and optimizable catalysts. For example, Pd(II) complex **1.10** forms allylic amine **1.12** in >99% conversion, however, when incorporated into a trimer sequence (C-**1.10**-G), the conversion was reduced to 30%.

Figure 1.6 Palladium and Iridium DNA-complexes for asymmetric allylic amination.

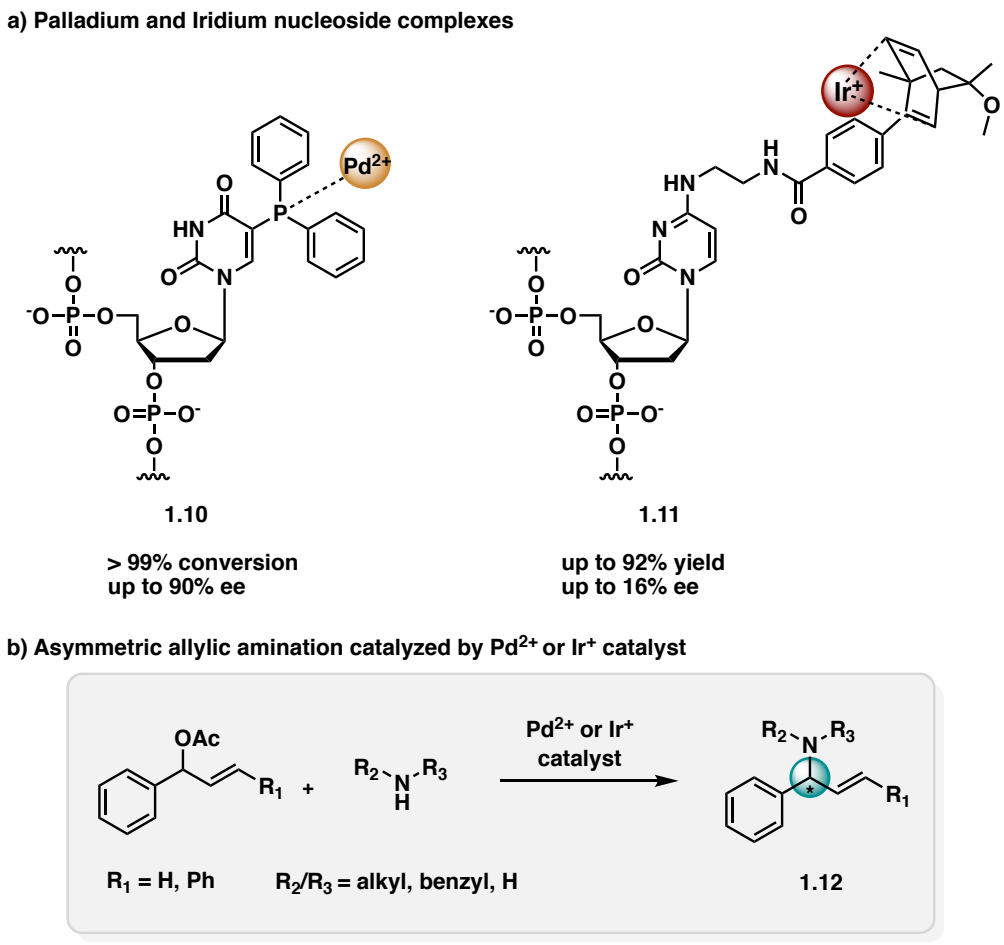

Another alternative approach to forming metal-DNAzymes with covalently bound ligands is through covalent attachment of ligand to the more synthetically accessible 5' or 3' ends of the nucleic acid sequence. A Cu^{2+}-bpy catalyst was designed using this concept such that three short nucleic acid sequences hybridize to form the intact complex. In this design, the metal is bound to a ligand in the center of the duplex, and is capable of catalyzing a Diels-Alder reaction with modest levels of enantioselectivity. The advantage of this approach is the ability to exchange sequence segments 2 (DNA2, **1.13**) and 3 (TEMPLATE, **1.14**) to optimize overall complex, making for a modular and easily optimized catalyst (*Figure 1.7a*).

In a similarly designed system, ligands can be attached to both the 5' end of one short nucleic acid sequence (**1.15**) and the 3' end of a complementary sequence (**1.16**). Upon hybridization, an active catalyst is formed (*Figure 1.7b*). This was initially applied to a DNAzyme system forming a Ni-salen complex that exhibits nuclease activity.[17] More recently, this has been adapted to form a diphenylphosphine Pd(II)-complex for reduction of a nonfluorescent diiodo-BODIPY (**1.17**) precursor to form a fluorescent BODIPY product (**1.18**), allowing for fluorescent detection of palladium ions in solution (*Figure 1.7c*).[18] Furthermore, this concept has been adapted to a Cu^{2+} complex that catalyzes the sequence selective amide cleavage of an ester peptide nucleic acid (PNA) bond.[19]

Figure 1.7 Metal-DNAzyme formation through covalent attachment of ligands to end of nucleic acid sequence and catalyst activation through hybridization.

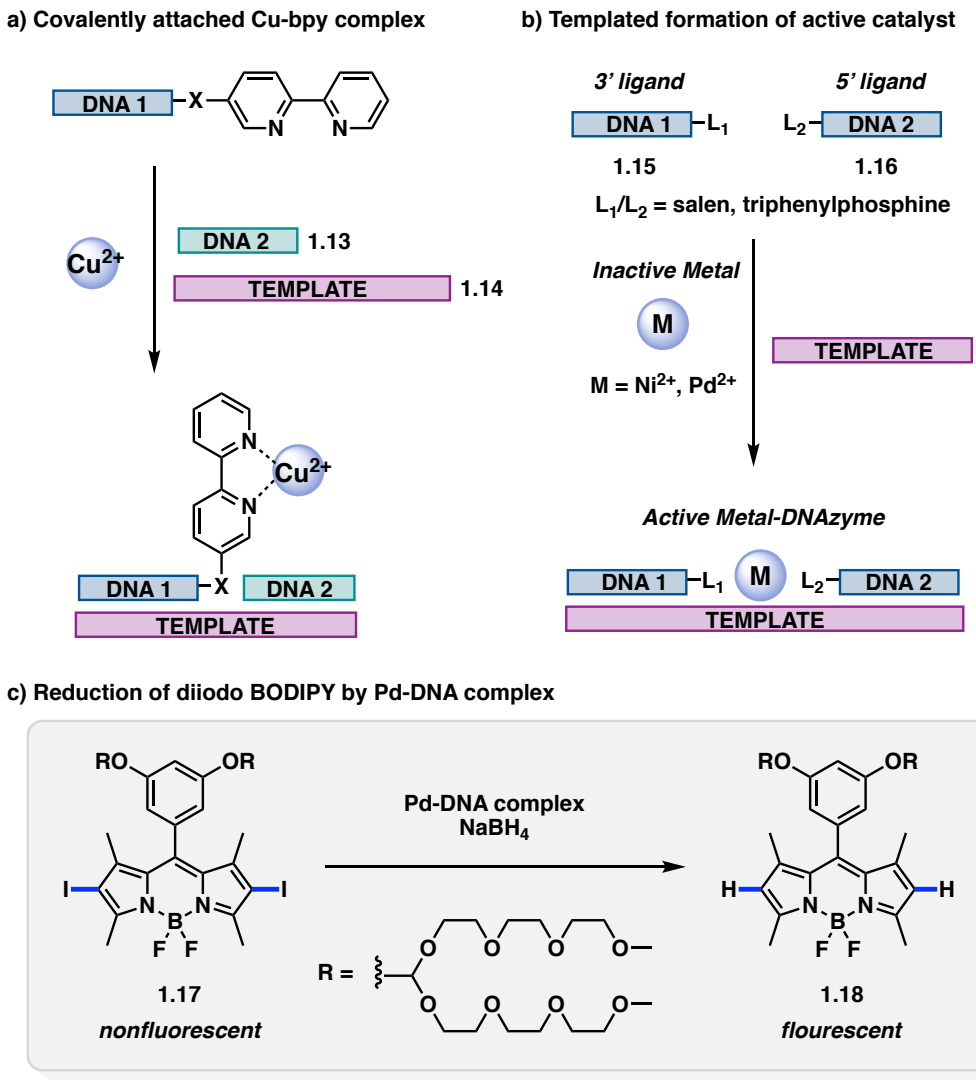

1.6 Conclusion

Metal-DNAzymes are capable of catalyzing a wide variety of reactions ranging from nucleic acid cleavage and ligation with biologically relevant metals, such as Zn^{2+} and Cu^{2+}, to asymmetric allylations with abiotic metals, such as Pd^{2+} and Ir^{+}. The three main approaches to forming catalytically active metal-DNAzymes include *in vitro* selection processes to identify a metal binding site, non-covalent complex formation through intercalating ligands, and covalent attachment of synthetic ligands to the limited synthetically accessible regions of nucleic acids.

While all approaches form catalytically active metalloDNAzymes with unique reactivity, there are often limitations. DNAzymes that are easily optimized through *in vitro* selection are formed from simple and cheap unmodified nucleic acids but suffer from limitations in substrate scope, as the catalyst only works with nucleic acid derived substrates. While the formation of catalytic metal-DNA complexes through covalent and non-covalent ligand attachment lead to more synthetically interesting reactions, these are often more expensive and challenging to optimize. Additionally, systems which employ non-covalent interactions, such as intercalation, are often inherently difficult to control and rationally design. The development of a transition metal catalyst formed through addition of an abiotic metal to simple, unmodified DNA could overcome the current limitations of metalloDNAzymes.

1.7 Notes and References

(1) F. H. Westheimer. Polyribonucleic acids as enzymes. *Nature* **1986**, *319*, 534–535.

(2) G. Garriga, A. M. Lambowitz, T. Inoue, T. R. Cech. Mechanism of rcognition of the 5' splice site in self-splicing group I introns. *Nature* **1986**, *322*, 86–89.

(3) For Reviews on DNA catalysts see: a) M. Hollenstein. DNA Catalysis: The Chemical Repertoire of DNAzymes. *Molecules* **2015**, *20*, 20777–20805. b) K. Hwnag, Q. Mou, R. J. Lake, M. Xion, B. Holland, Y. Lu. Metal-Dependent DNAzymes for the Quantitative Detection of Metal Ions in Living Cells: Recent Progress, Current Challenges, and Latest Results on FRET Ratiometric Sensors. *Inorg. Chem.* **2019**, *58*, 13696–13708. c) A. J. Boersma, R. P. MEgens, B. L. Feringa, G. Roelfes. DNA-based asymmetric catalysis. *Chem. Soc. Rev.* **2010**, *39*, 2083–2092. d) K. Hwang, P. Hosseinzadeh, Y. Lu. Biochemical and biophysical understanding of metal ion selectivity of DNAzymes. *Inorganica Chim. Acta* **2016**, *452*, 12–24. e) A. Rioz-Martinez, G. Roelfes. DNA-based hybrid catalysis. *Curr. Opin. Biotechnol.* **2015**, *25*, 80–87.

(4) E. A. Doherty, J. A. Doudna. Ribozyme Structures and Mechanisms. *Annu. Rev. Biochem.* 2001, 30, 457–475.

(5) a) N. Carmi, R. R. Breaker. Characterization of a DNA-Cleaving deoxyribozyme. *Bioorg. Med. Chem.* **2001**, *9*, 2589–2600. b) M. Chandra, A. Sachdeva, S. K. Silverman. DNA-catalyzed sequence-specific hydrolysis of DNA. *Nat. Chem. Biol.* **2009**, *5*, 718–729.

(6) For DNA ligation: A. Flynn-Charlebois, Y. Wang, T. K. Prior, I. Rashid, K. A. Hoadley, R. L. Coppins, A. C. Wolf, S. K. Silverman. Deoxyribozymes with 2'-5' RNA Ligase Activity. *J. Am. Chem. Soc.* **2003**, *125*, 2444–2454. For RNA ligation: W. E. Purtha, R. L. Coppins, M. K.

Smalley, S. K. Silverman. General Deoxyribozyme-Catalyzed Synthesis of Native 3'-5' RNA Linkages. *J. Am. Chem. Soc.* **2005**, *127*, 13124.

(7) W. Wang, L. P. Billen, Y. Li. Sequence Diversity, Metal Specificity, and Catalytic Proficiency of Metal-Dependent Phosphorylating DNA Enzymes. *Chem. Biol.* **2002**, *9*, 507–517.

(8) P. I. Pradeepkumar, C. Hobartner, D. A. Baum, S. K. Silverman. DNA-Catalyzed Formation of Nucleopeptide Linkages. *Angew. Chem. Int. Ed.* **2008**, *47*, 1753–1757.

(9) C. Zhou, J. L. Avins, P. C. Klauser, B. M. Brandsen, Y. Lee, S. K. Silverman. DNA-Catalyzed Amide Hydrolysis. **2016**, *138*, 2106–2109.

(10) C. E. Weinberg, Z. Weinber, C. Hammann. Novel ribozymes: discovery, catalytic mechanisms, and the quest to understand biological function. *Nucleic Acids Res.* **2019**, *47*, 9480–9494.

(11) M. E. Wilson, G. M. Whitesides. Conversion of a protein to a homogeneous asymmetric hydrogenation catalyst by site-specific modification with a diphosphinerhodium(I) moiety. *J. Am. Chem. Soc.* **1978**, *100*, 306–307.

(12) G. Roelfes, B. L. Feringa. DNA-Based Asymmetric Catalysis. *Angew. Chem., Int. Ed.* **2005**, *44*, 3230–3232.

(13) P. Ravascio, Y. F. Li, D. Sen. DNA-enhanced peroxidase activity of a DNA-hemin complex. *Chem. Biol.* **1998**, *5*, 505–517.

(14) E. Golub, H. B. Albada, W.-C. Liao, Y. Biniuri, I. Willner. Nucleoapzymes: Hemin/G-Quadruplex DNAzyme–Aptamer Binding Site Conjugates with Superior Enzyme-like Catalytic Functions. *J. Am. Chem. Soc.* **2016**, *138*, 164–172.

(15) L. Ropartz, N. J. Meeuwenoord, G. A. van der Marel, P. W. N. M van Leeuwen, A. M. Z. Slawin, P. C. J. Kamer. Phosphine containing oligonucleotides for the development of metallodeoxyribozymes. *Chem. Commun.* **2007**, 1556–1558.

(16) P. Fournier, R. Fiammengo, A. Jaschke. Allylic Amination by a DNA-Diene-Iridium(I) Hybrid Catalyst. *Angew. Chem. Int. Ed.* **2009**, *48*, 4426–4429.

(17) J. L. Czlapinski, T. L. Sheppard. Nucleic Acid Template-Directed Assembly of Metallosalen–DNA conjugates. *J. Am. Chem. Soc.* **2001**, *123*, 8616–8619.

(18) D. K. Prsuty, M. Kwak, J. Wildeman, A. Herrmann. Modular Assembly of a Pd Catalyst within a DNA Scaffold for the Amplified Colorimetric Detection of Nucleic Acids. *Angew. Chem. Int. Ed.* **2012**, *51*, 1894–11898.

(19) I. Boll, E. Jentzsch, F. Kramer, A. Mokhir Metal complex catalysis on a double stranded DNA template *Chem. Commun.* **2006**, 3447–3449.

CHAPTER TWO

Metal-Mediated Base Pairs Comprised of Au(I) Incorporated into Pyrimidine Mismatches

Unpublished Work: Sydnee Green, Hayden R. Montgomery, Tyler Benton, K. N. Houk, Hosea M. Nelson

2.1 Abstract

We report the formation of three Au(I) pyrimidine metal-mediated base pairs (MMBP) between a cytosine-cytosine, cytosine-thymine, and thymine-thymine mismatch. Incorporation of Au(I) into all three metal-mediated base pairs led to a large increase in thermal stability (7 °C – 33 °C) and can be observed through mass spectrometry. We found that the cytosine-Au(I)-cytosine led to the largest increase in thermal stability ever reported for a MMBP consisting of natural bases and incorporated two Au(I) ions per mismatch. In addition, we showed that these stable MMBP do not lead to a large change in helicity as shown by circular dichroism. These highly stable Au(I) bound DNA complexes have potential applications in nanomaterials and biocatalysis.

2.2 Introduction

Past studies of the interactions between transition metals and DNA have led to the development of metal-based therapeutics as well as advances in DNA-based nanotechnology.[1] Specifically, the discovery of metal-mediated base pairs (MMBP), metal-coordination complexes incorporated into DNA base pairs, have fueled many recent advances in new technologies and have enhanced our understanding of metal-DNA interactions.[2,3,4] The site-specific incorporation of transition metals has led to the development of new metal sensors, the improvement of charge

transfer through DNA, and the design of metal-responsive materials.[5] However, there are limited transition metals that can be incorporated into oligonucleotides. Additionally, most MMBPs rely on engineered synthetic bases.[2] Therefore, the exploration of new metals that can be incorporated into canonical bases is important for further developments of metalloDNA-based nanotechnology and therapeutics.

Currently, Ag(I) and Hg(II) are the only two metals that have been reported to coordinate specifically to canonical DNA mismatches.[6,7] Au(I), a metal sharing similar coordination and size to Ag(I) and Hg(II), is an ideal candidate for further investigating transition metal interactions with oligonucleotides.[8] Additionally, there is significant precedence for Au(I) as a medicinally relevant transition metal for treatment of diseases such as rheumatoid arthritis and cancer, lending to the extensive investigation of Au(I) and DNA interactions over the last four decades.[3, 9] The possibility of interstrand binding of Au(I) to double stranded DNA was originally proposed over three decades ago by Blank and Dabrowiak.[10] Further spectroscopic experiments suggested Au(III) and Au(I) binding to N7 of guanine as well as a dimeric Au(II) complex between two cytosine nucleosides.[11,12] However, despite numerous theoretical predictions and experimental data showing Au(I) interactions with nucleobases, the coordination of Au(I) within a DNA mismatch has never been reported.[13] This study discloses the first example of Au(I) incorporation into pyrimidine mismatches within a DNA duplex, facilitating the formation of the most stable metal-mediated base pair between canonical bases to date. We probed the formation of this highly stabilizing Au(I) metal-mediated base pair using thermal stability measurements, density functional theory (DFT) calculations, mass spectrometry (MS), and circular dichroism (CD) spectroscopy.

Figure 2.1 Formation of metal-mediated base pairs with pyrimidine mismatches and incorporation of Au(I) ions into duplex DNA containing mismatch.

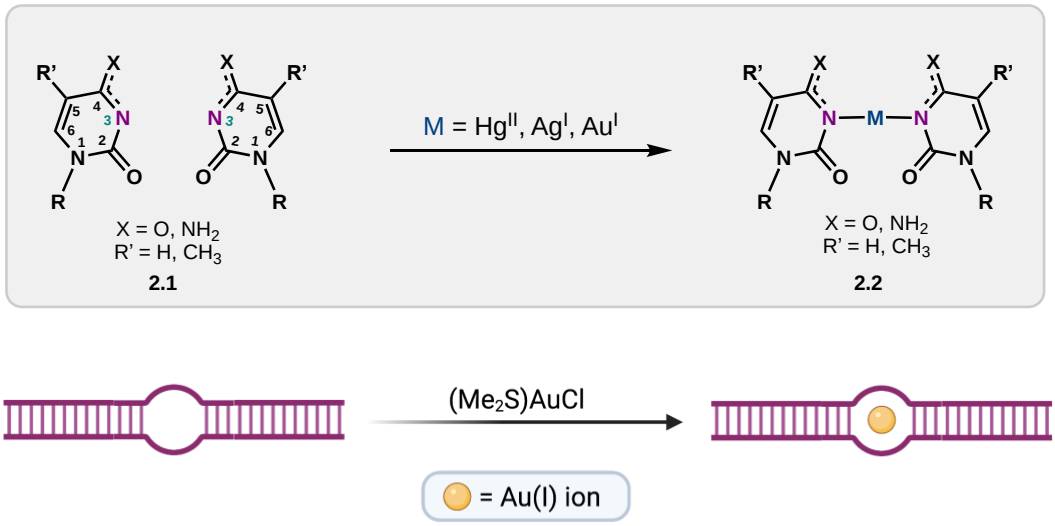

2.3 Thermal Denaturation Studies

In order to characterize Au(I) binding, we performed thermal denaturation studies to identify changes in the thermal stabilities of the mismatch-containing duplexes in the presence of Au(I). Common Au(I) complexes favor the coordination of one neutral donating ligand and one anionic ligand in a linear geometry.[14] Therefore, we hypothesized that binding between N3 of cytosine and the deprotonated N3 of thymine would be favorable. These interactions, in addition to the coordination geometries proposed for T–Hg(II)–C (**2.3**) and T–Ag(I)–C (**2.4**) MMBPs, led to the proposed structure of the T–Au(I)–C (**2.5**) metal mediated base pair shown in *Figure 2.2*.[15] Furthermore, crystal structure and NMR studies that show binding of Au(I) to deprotonated N3 of *1*-methylthymidine and N3 of cytosine are consistent with this structure. [12]

Figure 2.2 Proposed structure of T-Au(I)-C mismatch based on proposed structures of with Hg(II) and Ag(I). Calculated binding energy of each metal through N3 of cytosine and N3 of thymine. All the energy values are Gibb's free energies reported in kcal/mol. Geometries from B3LYP/6-31G(d)LANL2DZ. Energies are given in □G from B3LP/6311++G(2df,2pd)/SDD in H_2O (SMD model).

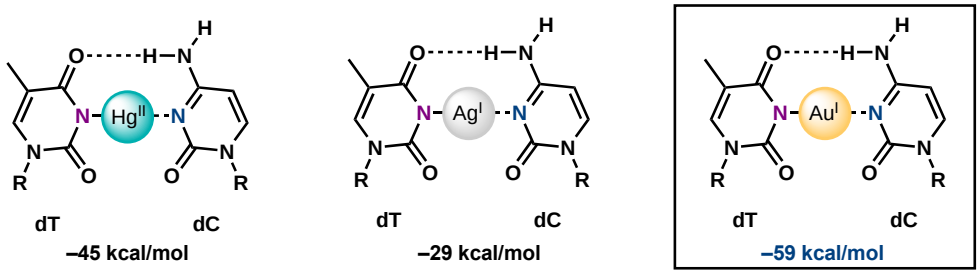

2.3 2.4 2.5

Table 2.1 T_m values for matches and pyrimidine mismatches.

			T_m (°C) with n equiv of $(Me_2S)AuCl$			
entry	duplex		n = 0	n = 1	n = 2	ΔT_m (°C)
1	5'-d(CCT TTC TCT CCC TC) 3'-d(GGA AAG AGA GGG AG)	CG1	55.6 ± 0.3	60.0 ± 0.5	—	4.4 ± 0.6[a]
2	5'-d(CCT TTC TAT CCC TC) 3'-d(GGA AAG ATA GGG AG)	AT1	52.4 ± 0.3	53.8 ± 0.3	—	1.4 ± 0.4
3	5'-d(CCT TTC TCT CCC TC) 3'-d(GGA AAG ATA GGG AG)	CT1	40.6 ± 0.7	47.3 ± 1.1	51.3 ± 0.6	10.7 ± 1.4
4	5'-d(CCT TTC TTT CCC TC) 3'-d(GGA AAG ATA GGG AG)	TT1	43.0 ± 0.4	53.2 ± 0.5	60.9 ± 0.7	17.9 ± 0.9
5	5'-d(CCT TTC TCT CCC TC) 3'-d(GGA AAG ACA GGG AG)	CC1	38.3 ± 0.9	35.2 ± 0.8 67.1 ± 1.4[b]	71 ± 1	33 ± 3

[a]Increase in CG1 due to known favorable interactions between gold, cytosine, and guanine.[10,11]

[b]Two values reported due to biphasic melting.

Thermal denaturation experiments show that the thermal stability of the cytosine-thymidine mismatched duplex, **CT1**, increases by 10.7 °C upon addition of two equivalents of Au(I) (Table 1, entry 3). This metal mediated base pair suggests the incorporation of approximately one Au(I). Moderate increases with additional Au(I) ions, as shown by thermal stability titration, due to nonspecific binding were also observed.[16] The addition of one equivalent of Au(I) leads to an increase in 7 °C with **CT1** compared to the duplex with no metal (entry 3). This increase is significant and not unlike common T_m changes associated with many metal-mediated base pairs.

Unlike the addition of Au(I) to **CT1**, the addition of Au(I) to **CC1** and **TT1** mismatched duplexes exhibit higher thermal stability than the respective control Watson-Crick AT and GC matched duplexes (entries 4–5). The addition of one equivalent of Au(I) to **TT1** increases the thermal stability by 10.2 °C (entry 4). This change in thermal stability is similar to reported T–Hg(II)–T metal mediated base pair containing a single T–T mismatch. The addition of excess Au(I), up to three equivalents, results in increased thermal stability. This is suggestive that it may be possible to incorporate multiple Au(I) atoms per mismatch, similar to Ag(I) incorporation into 4-thiothymine.[17]

In the case of **CC1**, we observe a large increase in thermal stability with the addition of two equivalents of Au(I), while the addition of excess Au(I) has minimal effect (entry 5). The biphasic properties of the thermal melting curves indicate direct formation of a doubly incorporated MMBP, behaving similarly to previously reported Ag(I) complexes.[18] The formation of a single Au(I) incorporated C–C mismatch does not appear to be present (*Figure 2.3c*). When 0.4, 1.0, and 1.4 equivalents of Au(I) are graphed to fit a biphasic curve, there are two T_m transitions. The early transition thermal stability corresponds to a mismatch duplex containing no gold ions, whereas the second transition has a very large thermal stability increase, likely due to

incorporation of two gold ions. This preference for binding of two Au(I) ions can be explained in part to the known aurophillic interaction between gold atoms.[19]

Figure 2.3 a) Incorporation of Au(I) ions into a duplex pyrimidine mismatch. Thermal denaturation curves for b) CT1, c) CT1, and d) CC1.

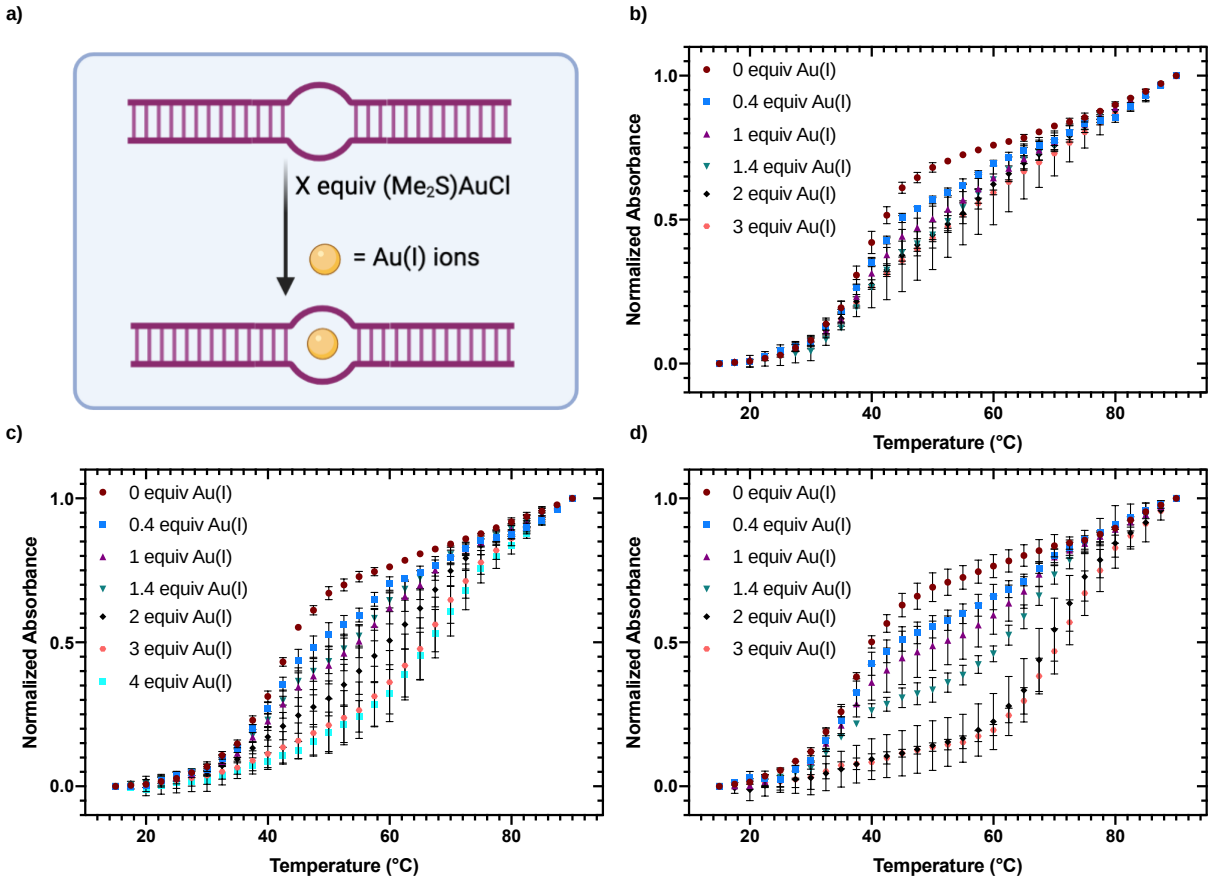

To the best of our knowledge, this is the largest increase in thermal stability from a metal mediated base pair containing canonical bases. Many other examples contain highly engineered bases and/or covalent bond formation.[20] Additionally, this exceptionally large increase in thermal stability is unique to Au(I). Other metals including Ni, Fe, and Cu, which have been previously reported to interact with nucleic acids, as well as Au(III) species and more stabilized Au(I) precursors did not affect the thermal stability of the pyrimidine mismatches.[21]

2.4 Proposed Structure of C-Au(I)-C Complex and pH Dependence

To elucidate potential binding modes of Au(I) to a C–C mismatch, the base-pairing energy of various *1*-methycytosine–Au(I) ions were calculated. *Figure 2.4* depicts the structures and corresponding base pairing energies (BE) of various possible 1-methylcytosine complexes with either one or two Au(I) ions. Complexes incorporating a single Au(I) ion have modest binding energies with the N3-Au(I)-N3 complex (**2.6**) preferred over all calculated possibilities. The lack of hydrogen bonding in the mono-Au complex allows for additional metal coordination without an energetic cost associated with breaking of the highly stabilizing hydrogen bonds present in canonical base pairs. Addition of a second Au(I) ion can then be incorporated either between the *4*-amino nitrogen (**2.7**) or the *2*-keto oxygen (**2.8**), with a preference for the later by nearly 10 kcal/mol. Displacement of a proton from a single *4*-amino group results in a more stable complex **2.9** and this effect is significantly more pronounced in the neutral, doubly deprotonated complex **2.10**.

Figure 2.4 Energy of C–Au(I)–C binding with 1 and 2 Au(I) ions bound.

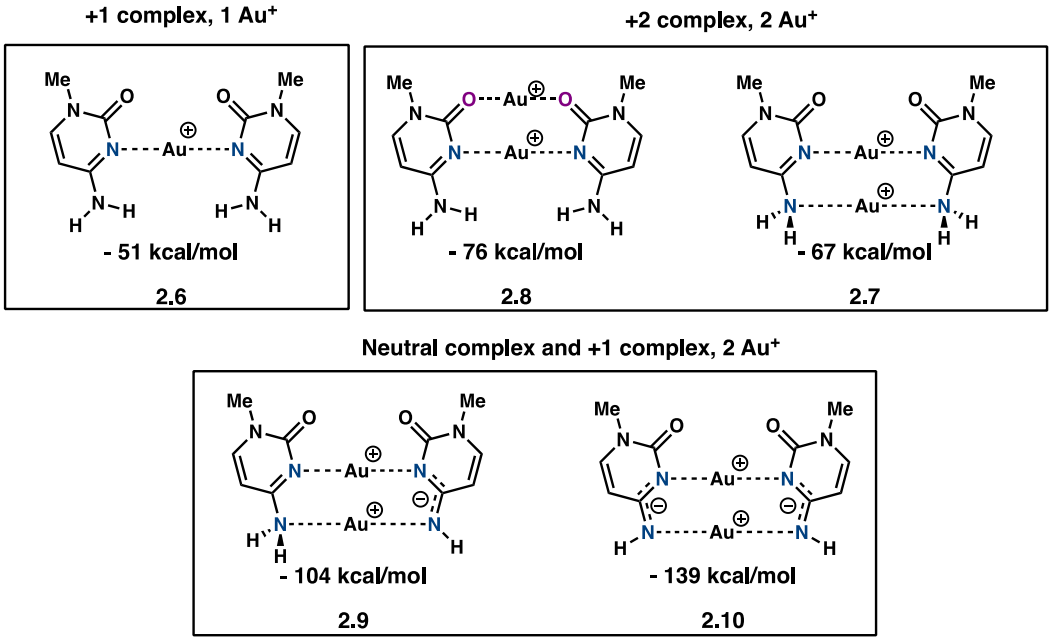

We hypothesized that the formation of cationic complex **2.9** and neutral complex **2.10**, resulting from the loss of one or two protons, would be highly pH dependent. Specifically, deprotonation of the exocyclic amines of cytosine, and binding to Au(I), should be favored under basic conditions. In turn, acidic conditions should disfavor this binding and result in loss of Au(I) binding. In fact, at pH 5.5 the increase in thermal stability is only 12.6 °C (*Figure 2.5a*), a loss of 20.4 °C of stabilization present at pH 7. Under basic conditions, at pH 8.5, the increase in thermal stabilization is 34 °C (*Figure 2.5b*), exhibiting no significant change from thermal stability at neutral pH 7. This is consistent with the formation of the cationic complex **2.8** (*Figure 2.4*), stabilized by the highly negative backbone of DNA. Previous NMR and IR studies suggest that Au(I) binds both N3 and the carbonyl of free cytidine. Therefore, the stability of the complex exhibiting this mode of binding would not be dramatically affected under basic conditions. Additionally, the known protonation of N3 of cytosine under acidic conditions is consistent with our result, as protonation would inhibit binding of Au(I), decreasing the stabilization effect.[22]

Figure 2.5 Thermal stability curves of CC1 in a) pH 5.5 and b) pH 8.5 phosphate buffer with no $(Me_2S)AuCl$ and 2 equivalents $(Me_2S)AuCl$.

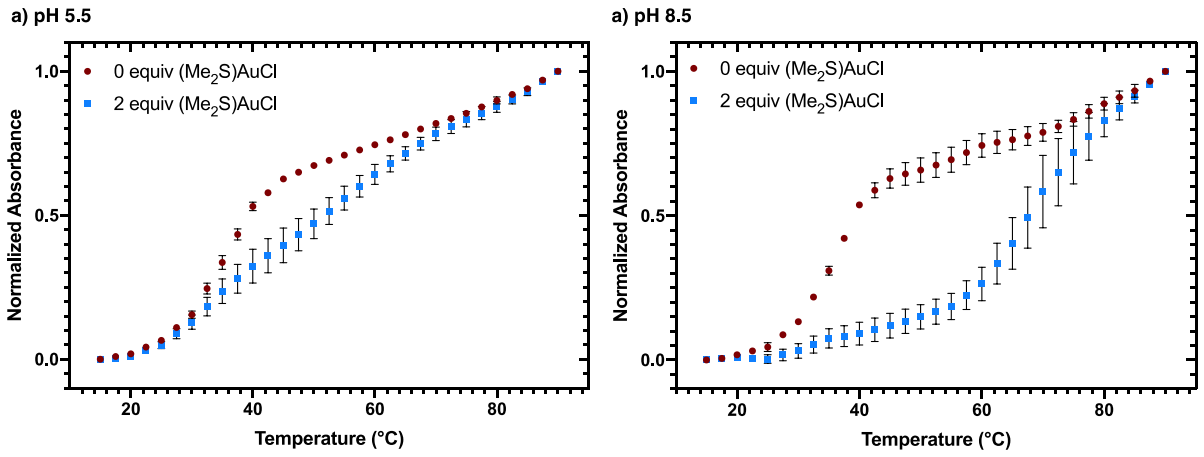

2.5 Mass Spectrometry

Highly specific metal mediated base pairs, such as thymine-Hg(II)-thymine, have been shown to form dimeric complexes with poly(thymine) sequences, such as 5'-TTTTT-3' (**T5**).[7] Based on the large increase in thermal stability, we proposed that poly(cytosine) sequences would also dimerize in the presence of Au(I) ions. Mass spectrometry experiments indicate formation of a base pair dimer in the presence of 5'-CCCCC-3' (**C5**), and 5 equivalents of Au(I), 1 equivalent per cytosine, wherein 5 and 6 Au(I) ions are coordinated, with the most intense peak containing 6 Au(I) adducts (*Figure 2.6a*). In the case of the **T5** sequence, only the mass for the single stranded sequence was observed as well as some nonspecific binding to the single stranded sequence (*Figure 2.6b*). In the presence of equimolar **T5** and **C5** sequences, only the mass corresponding to **C5** dimers is observed (*Figure 2.6c*). This is suggestive of specific binding to cytosine-cytosine mismatches with a binding affinity strong enough to hold together a sequence of complete mismatches. Further, in the presence of **G5 (**5'-GGGGG-3'), and **C5** there is a preference for formation of the **C5** dimers (*Figure 2.6d*), suggesting that this new MMBP is favored over the natural CG base pair.

Figure 2.6 Mass spectrum of a) C5 and b) T5 with and without 5 equivalents of (Me_2S)AuCl. c) Mass spectrum of C5 and T5 with 5 equivalents of (Me_2S)AuCl. d) Mass spectrum of C5 and G5 with 5 equivalents of (Me_2S)AuCl.

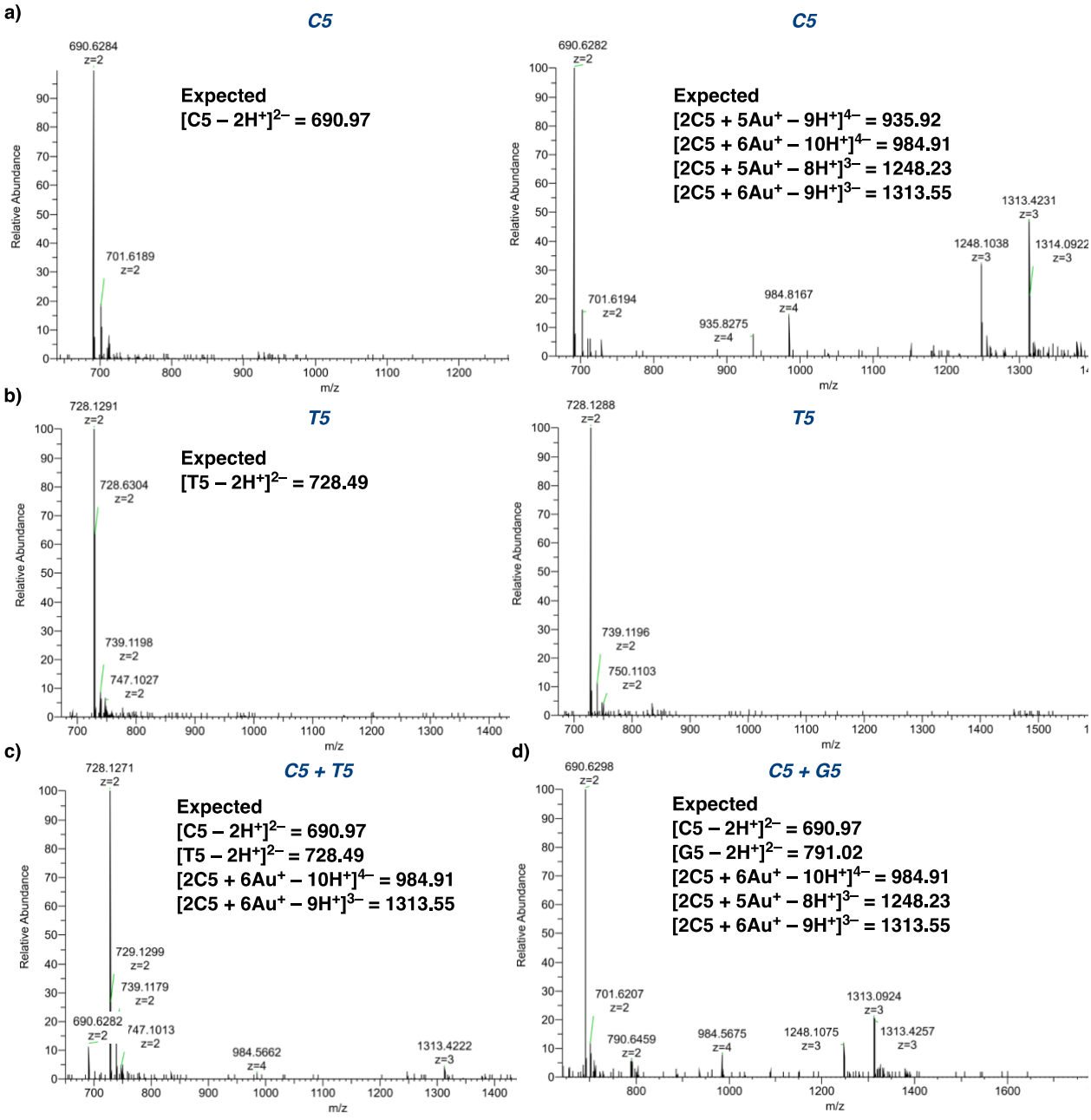

2.6 Circular Dichroism

While our experiments indicated the formation of a highly stabilized novel metal-mediated base pair, we sought to detect any structural changes to the DNA duplex upon addition of Au(I), as it is known that metal binding can cause changes to its helical structure. CD experiments show minimal change in the ellipticity profiles of duplexes containing a single C–C (**CC1**), C–T (**CT1**), or T–T (**TT1**) mismatch both before and after the addition of Au(I), suggesting that a single pyrimidine mismatch does not induce a significant deformation of the duplex (*Figure 2.7a-c*). However, duplexes containing multiple C–C mismatches show slight changes in spectrum upon addition of Au(I) (*Figure 2.7d*). Upon addition of Au(I) to a double C–C mismatched DNA duplex, **CC2**, the positive peak of the CD spectrum decreases in intensity and is shifted to a higher energy wavelength. In addition, the minimal changes in the CD spectrum show that it is unlikely to be forming a complex secondary structure, such as a G-quadruplex, in the presence of the cationic Au(I) atom.

Interestingly, the addition of $(Me_2S)AuCl$ to **C5** leads to an increase in helicity. The addition of 1 equivalent and 2 equivalents of gold per C–C mismatch corresponds to increases in helicity, with new peaks forming at about 250 nm and 270 nm (*Figure 2.7e*). The fully saturated duplex (2 Au(I) ions per mismatch) forms a helical duplex corresponding to a left-handed helix, contrary to the standard right-handed DNA duplex helix that arises under normal buffer conditions.[23]

Figure 2.7 CD spectrum of a) CC1, b) CT1, c) TT1 with no (Me_2S)AuCl and 1 equivalent (Me_2S)AuCl. d) CD spectrum of CC2 with 0, 1, 2, and 4 equivalents (Me_2S)AuCl. e) CD spectrum of C5 with 0, 1, and 2 equivalents of (Me_2S)AuCl per mismatch and representation of single stranded to Au(I) bound duplex upon addition of gold ions.

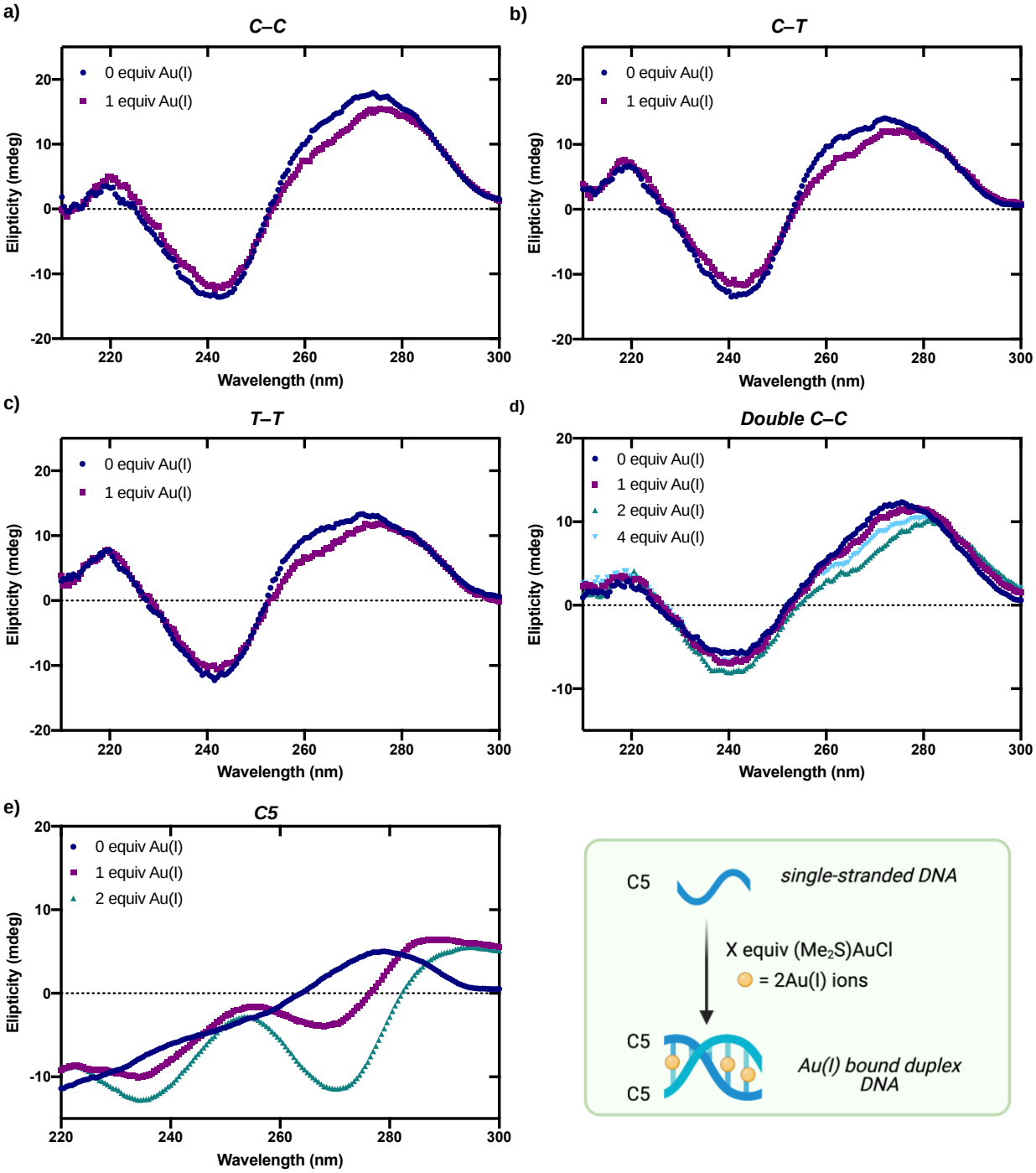

2.7 Conclusion

Over the last few decades, there have been many reports of MMBPs and extensive efforts have been dedicated to making these types of metal-DNA complexes into useful sensors, nanowires, and other devices for nanotechnology. However, only two metals have been previously shown to bind the bases of natural DNA mismatches. In this paper, we report on the first metal-mediated base pair containing Au(I) atoms with exquisite C–C mismatch selectivity. This highly stabilizing MMBP contains two Au(I) per mismatch and to the best of our knowledge, is the highest reported T_m increase for a MMBP composed of naturally occurring DNA bases. This new discovery adds to the repertoire of metal-mediated base pairs for the further development of nanotechnologies and biologically relevant therapeutics.

2.8 Experimental Section

2.8.1 Materials and Methods

All oligonucleotides were purchased through Integrated DNA Technology with standard desalting unless otherwise specified. Samples for thermal denaturation, mass spectrometry studies, and catalysis were prepared by heating the buffered DNA solution without metal at 90 °C in a heating block for 10 minutes then cooled to room temperature for 30 minutes. Once cool, the metal solution was added. In thermal denaturation experiments, all absorbances were measured at 260 nm using HP-8453 spectrophotometer with HP-89090A Peltier temperature controller from 15–90 °C at 5 °C min^{-1} with a hold time of 1 min. Relative absorbance, $A_{260nm}=(A_t–A_{15\,°C})/(A_{90\,°C}–A_{15\,°C})$, vs. temperature (°C) curves were fitted using GraphPad Prism 7.0c.

Table 2.1 DNA Sequences in Experiments.

Sequence Name	Sequence 1 (5'-3')	Sequence 2 (5'-3')
CTH	CGTTCTGTTTTCAGCACG	—
CCH	CGTCCTGTTTTCAGCACG	—
TTH	CGTTCTGTTTTCAGTACG	—
CT1	GAGGGACAGAAAGG	CCTTTCTTTCCCTC
CC1	GAGGGACAGAAAGG	CCTTTCTCTCCCTC
TT1	GAGGGATAGAAAGG	CCTTTCTTTCCCTC

TA1	GAGGGAAAGAAAGG	CCTTTCTTTCCCTC
GC1	GAGGGACAGAAAGG	CCTTTCTCTCCCTC
C5	CCCCC	—
T5	TTTTT	—
G5	GGGGG	—

2.8.2 Thermal Stability Studies

General Procedure for Sample Preparation for Thermal Stability Measurements

Solutions contained 3.5 μM DNA in buffer containing 0.75 mM sodium phosphate, pH 7, 150 mM $NaClO_4$ and 0 μM (0 eq) or 3.5 μM (1 eq) of $(Me_2S)AuCl$ (60:1 H_2O:MeOH v/v). DNA and buffer were heated at 90 °C for 10 minutes then allowed to cool to room temperature over 45 minutes. After the solution was cooled, $(Me_2S)AuCl$ (210 μM stock solution in methanol) was added and the resulting solution was incubated at room temperature for 5 min before performing experiments. The reported data is based on 3 trials and graphed on GraphPad Prism 7.0c.

Au(III) Precursors with Each Pyrimidine Mismatch Duplex (CT, CC, TT)

Figure 2.8 Relative absorbance, $A_{260nm}=(A_t-A_{15\,°C})/(A_{90\,°C}-A_{15\,°C})$, vs. temperature (°C) curves for pyrimidine-mismatch-containing oligonucleotides, a) CT1, b) CC1, and c) TT1 with and without 1 equivalent of $AuCl_3$.

a) CT1

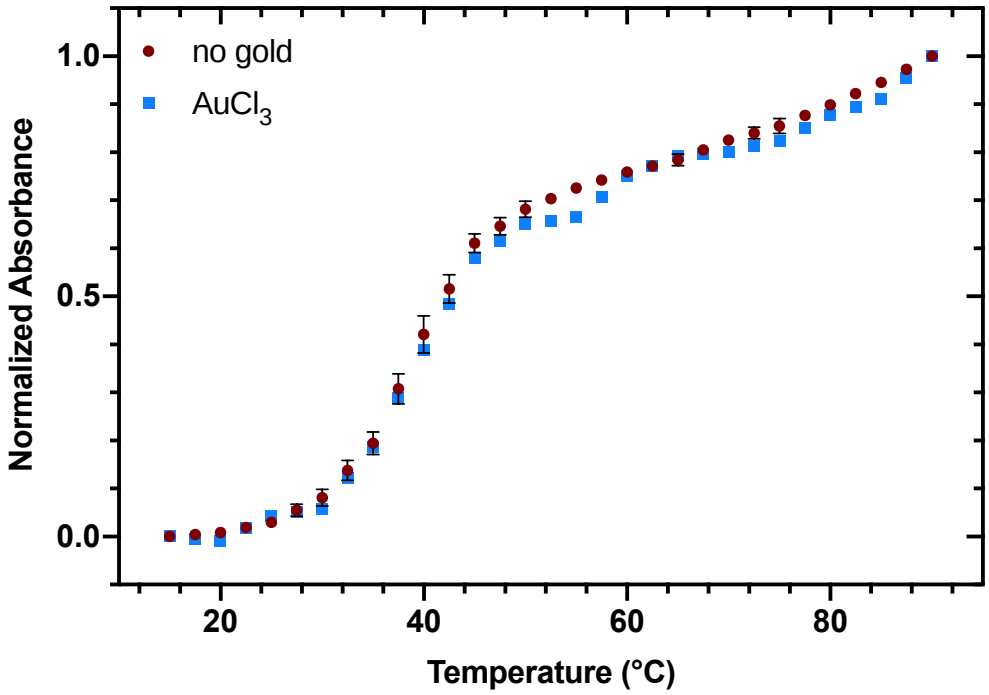

b) CC1

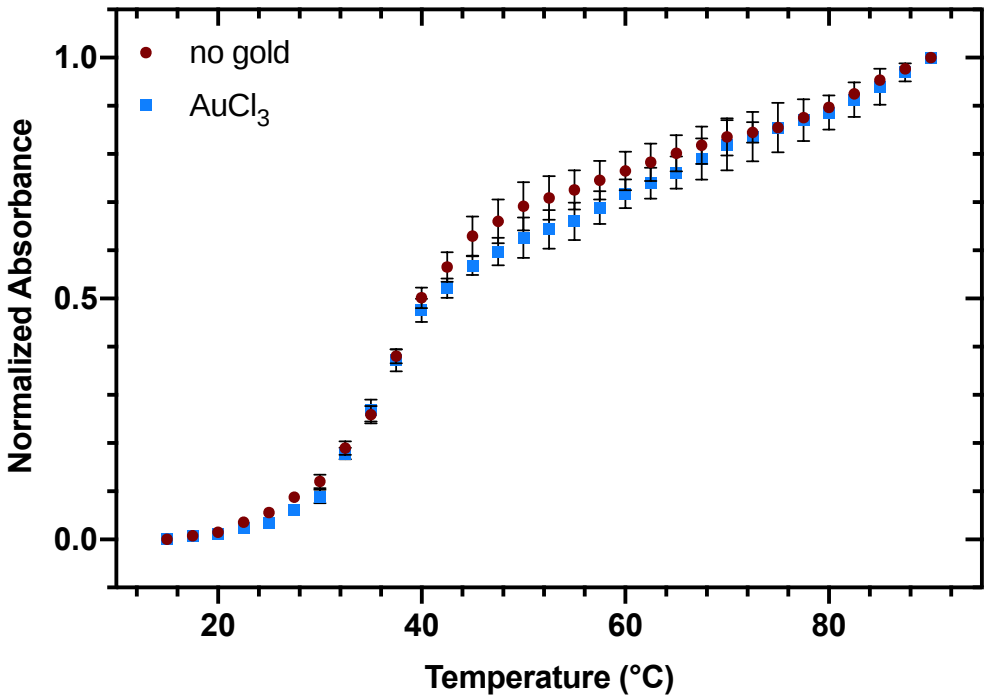
no gold
AuCl3
Normalized Absorbance
1.0
0.5
0.0
20
40
60
80
Temperature (°C)

c) TT1

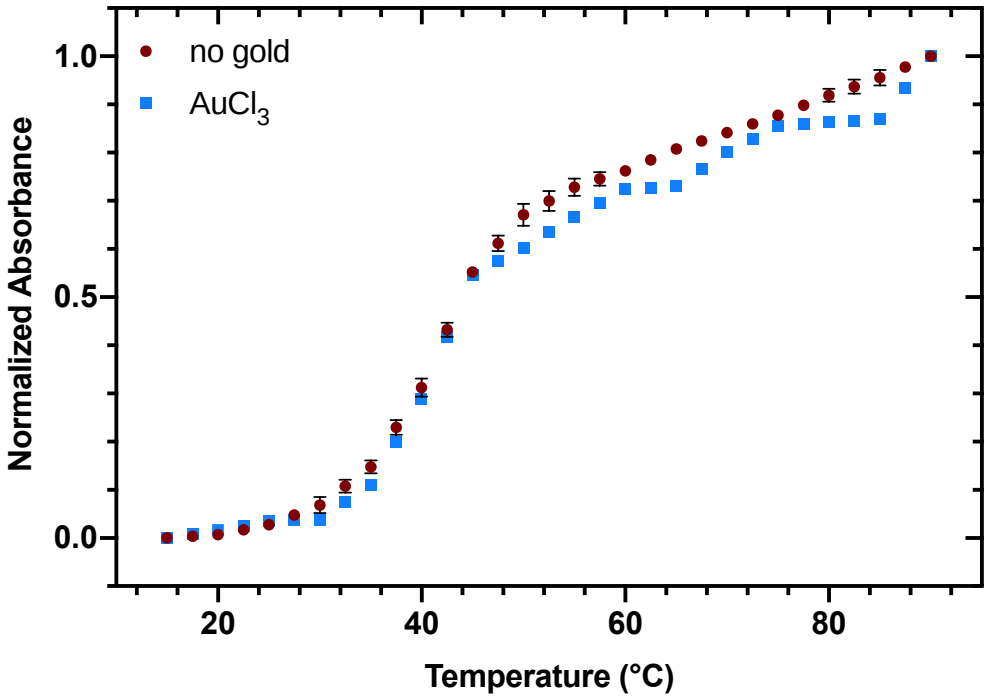
no gold
AuCl3
Normalized Absorbance
1.0
0.5
0.0
20
40
60
80
Temperature (°C)

Table 2.2 Thermal denaturation values for CT1, CC1 and TT1 with $AuCl_3$

Thermal Denaturation – CT1, CC1, TT1				
Sequence	**0 equiv T_m (°C)**	**1 equiv T_m (°C)**	**ΔT_m (°C)**	**Error**
CT1	40.6	41.2	0.6	1.4
CC1	38.3	37.8	0.5	2.0
TT1	43.3	43.8	0.5	1.2

Melting temperatures calculated from the thermal denaturation profiles of pyrimidine-mismatch-containing oligonucleotides in the presence of various concentrations of $(Me_2S)AuCl$. Melting temperatures and error calculated using the sigmoidal dose-response feature in GraphPad Prism 7.0c.

Other Metals with Pyrimidine Mismatched Hairpins and CT1 Duplex

Figure 2.9 Relative absorbance, $A_{260nm}=(A_t-A_{15\,°C})/(A_{90\,°C}-A_{15\,°C})$, vs. temperature (°C) curves for pyrimidine-mismatch-containing oligonucleotides, a) MTCH, b) MCCH, and c) MTTH with and without 1 equivalent of CuCl, $CuCl_2$, $NiCl_2$, $FeCl_3$, and $(Me_2S)AuCl$.

a) MTCH

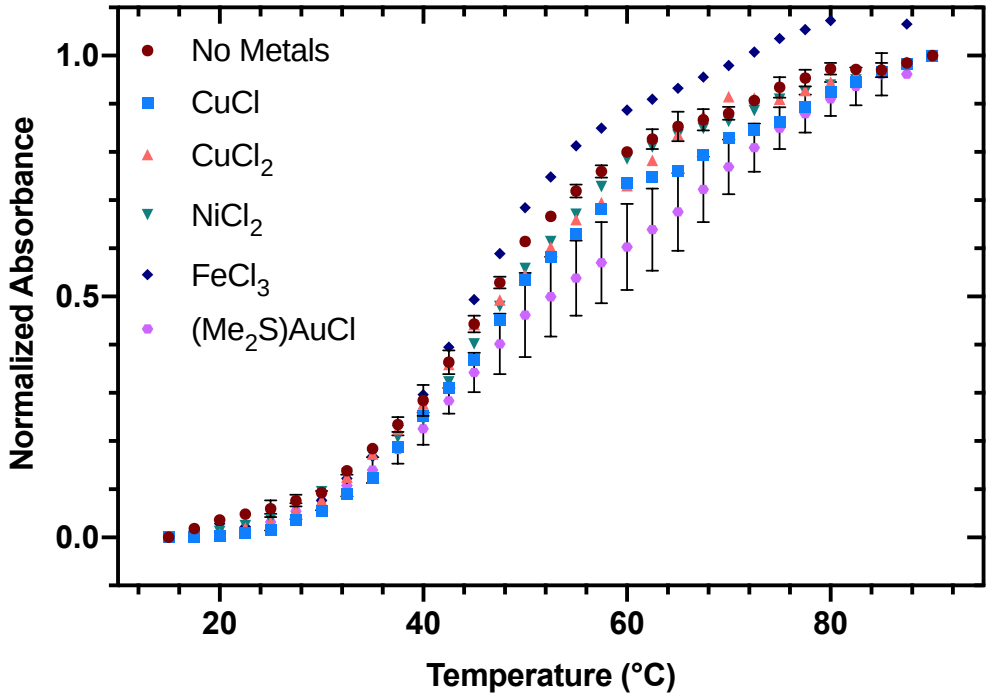

b) MCCH

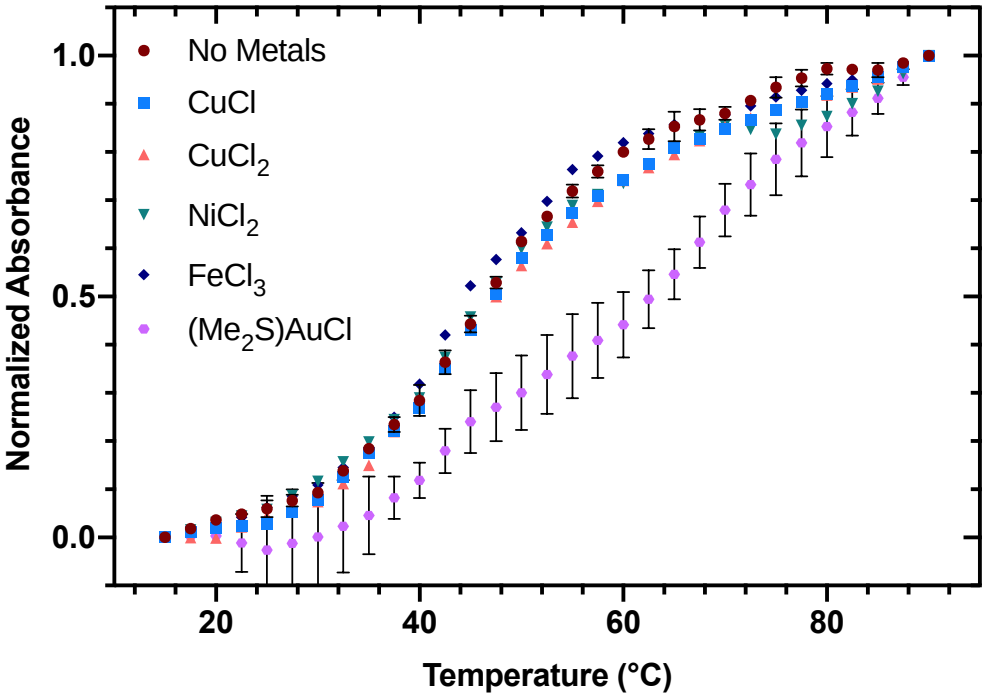
No Metals
CuCl
CuCl2
NiCl2
FeCl3
(Me2S)AuCl
Normalized Absorbance
1.0
0.5
0.0
20
40
60
80
Temperature (°C)

c) MTTH

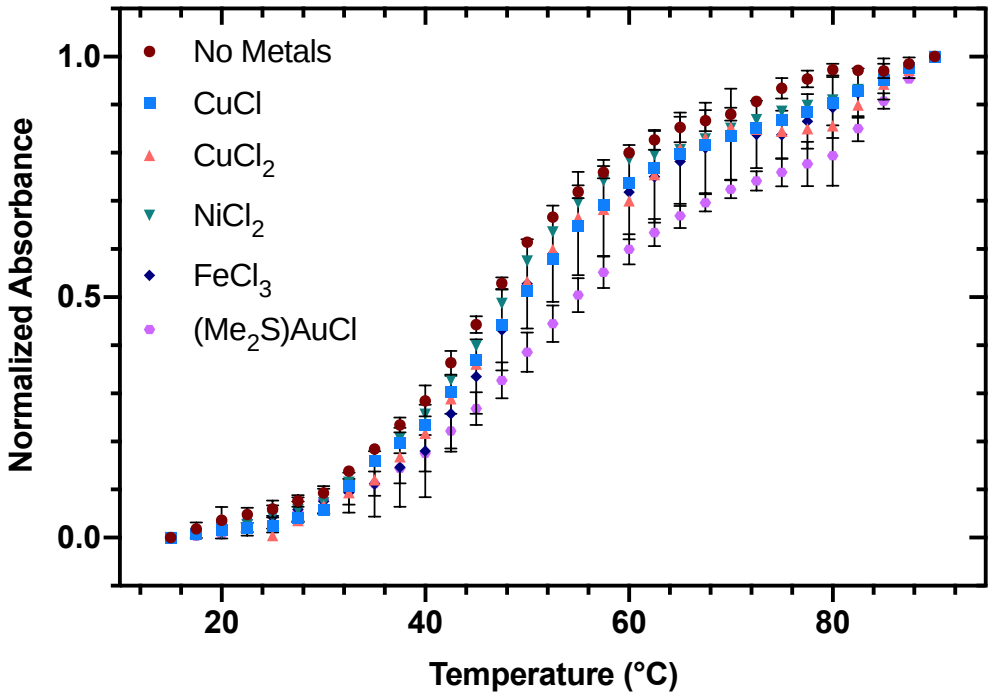
No Metals
CuCl
CuCl2
NiCl2
FeCl3
(Me2S)AuCl
Normalized Absorbance
1.0
0.5
0.0
20
40
60
80
Temperature (°C)

Table 2.3 Thermal denaturation values for CT1, CC1 and TT1 with $AuCl_3$

Thermal Denaturation – CT1, CC1, TT1						
Sequence	**No Metal**	**CuCl**	**$CuCl_2$**	**$NiCl_2$**	**$FeCl_3$**	**(Me_2SAuCl)**
CT1	46.2	48.2	47.2	47.4	46.0	53.1
CC1	46.3	46.4	46.4	44.9	44.1	63.7
TT1	46.3	48.3	48.1	46.7	49.2	54.5

Melting temperatures calculated from the thermal denaturation profiles of pyrimidine-mismatch-containing oligonucleotides in the presence of various concentrations of (Me_2S)AuCl. Melting temperatures and error calculated using the sigmoidal dose-response feature in GraphPad Prism 7.0c.

Table 2.4 Error of thermal denaturation values (from *Table 2.4*) for CT1, CC1 and TT1.

Thermal Denaturation – CT1, CC1, TT1						
Sequence	**No Metal**	**CuCl**	**$CuCl_2$**	**$NiCl_2$**	**$FeCl_3$**	**(Me_2SAuCl)**
CT1	0.3	0.6	0.4	0.3	0.5	2.2
CC1	0.3	0.5	0.5	0.7	0.4	2.6
TT1	0.3	0.5	0.6	0.5	0.7	0.9

Melting temperatures calculated from the thermal denaturation profiles of pyrimidine-mismatch-containing oligonucleotides in the presence of various concentrations of (Me_2S)AuCl. Melting temperatures and error calculated using the sigmoidal dose-response feature in GraphPad Prism 7.0c.

pH Dependence of CT1 Duplex with and without $(Me_2S)AuCl$

Figure 2.10 Relative absorbance, $A_{260nm}=(A_t-A_{15\,°C})/(A_{90\,°C}-A_{15\,°C})$, vs. temperature (°C) curves for pyrimidine-mismatch-containing oligonucleotide CT1 at a) pH 5.5 and b) pH 8.5.

a) pH 5.5

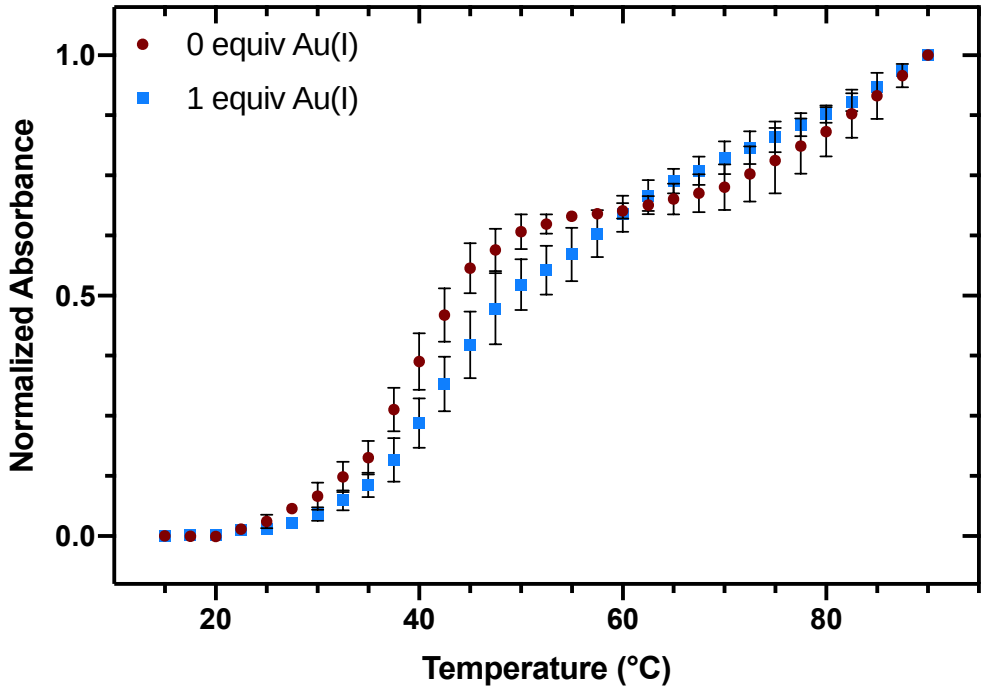

b) pH 8.5

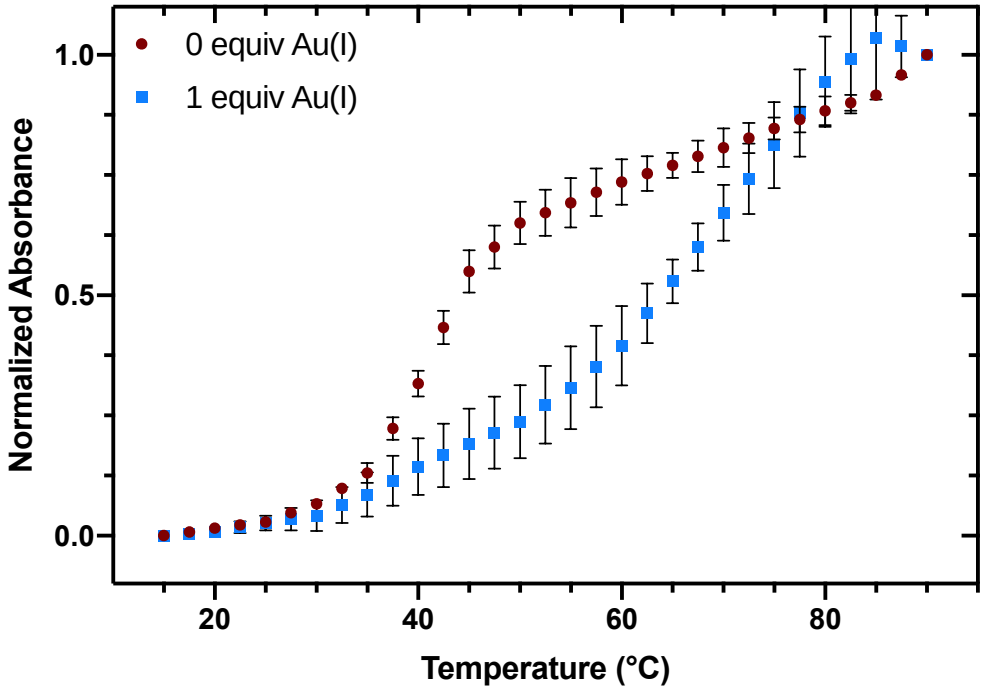

Table 2.5 Thermal denaturation values for CT1 with and without $(Me_2S)AuCl$

Thermal Denaturation – CT1, CC1, TT1				
pH	**0 equiv T_m (°C)**	**1 equiv T_m (°C)**	**ΔT_m (°C)**	**Error**
5.5	40.4	48.0	7.6	1.4
8.5	43.1	67.6	24.5	1.5

Melting temperatures calculated from the thermal denaturation profiles of pyrimidine-mismatch-containing oligonucleotides in the presence of various concentrations of $(Me_2S)AuCl$. Melting temperatures and error calculated using the sigmoidal dose-response feature in GraphPad Prism 7.0c.

Control Sequences (GC and TA match) with and without (Me_2S)AuCl

Figure 2.11 Relative absorbance, $A_{260nm}=(A_t-A_{15\,°C})/(A_{90\,°C}-A_{15\,°C})$, vs. temperature (°C) curves for pyrimidine-mismatch-containing oligonucleotides, a) GC1 and b) TA1 with and without 1 equivalent of (Me_2S)AuCl.

a) GC1

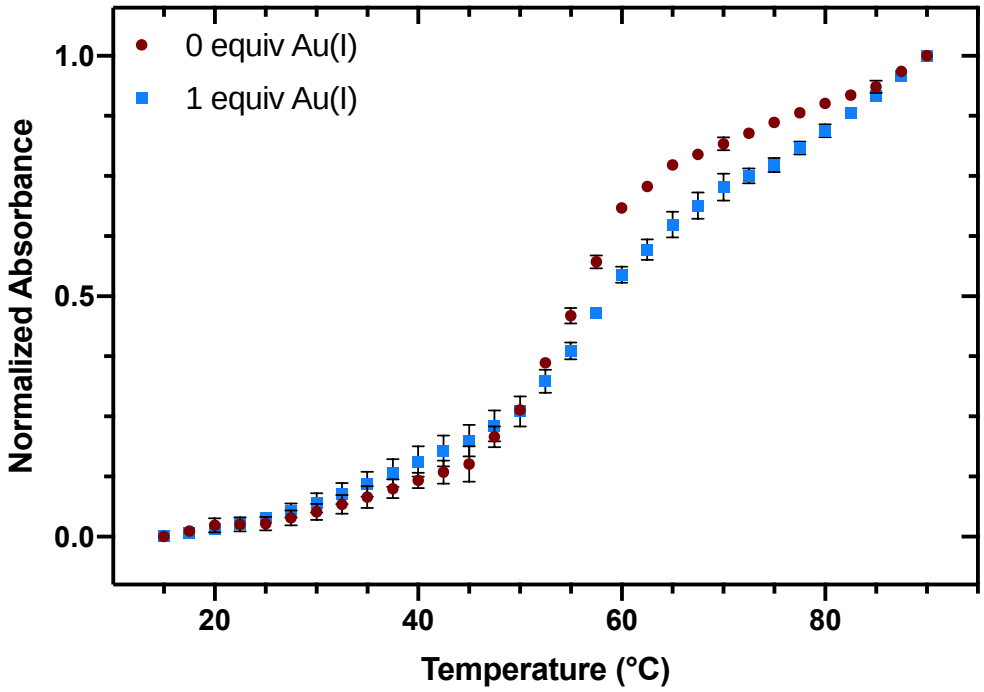

b) TA1

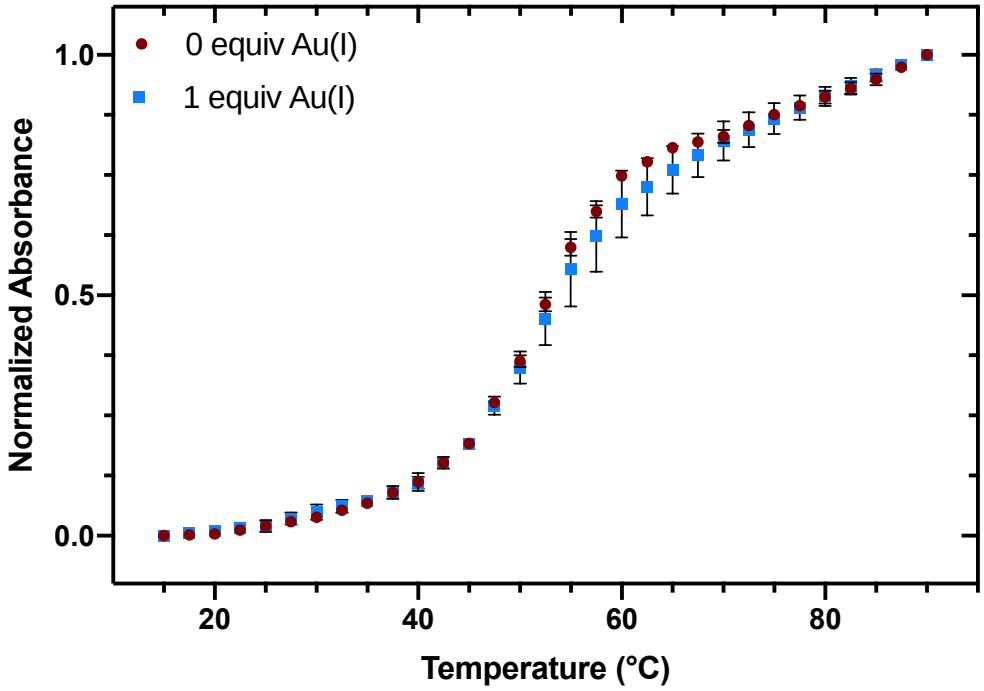

Table 2.6 Thermal denaturation values for GC1 and TA1

Thermal Denaturation – GC1 and TA1				
Sequence	**0 equiv T_m (°C)**	**1 equiv T_m (°C)**	**ΔT_m (°C)**	**Error**
GC1	55.6	60.0	4.4	1.4
TA1	52.4	53.8	1.4	0.9

Melting temperatures calculated from the thermal denaturation profiles of pyrimidine-mismatch-containing oligonucleotides in the presence of various concentrations of $(Me_2S)AuCl$. Melting temperatures and error calculated using the sigmoidal dose-response feature in GraphPad Prism 7.0c.

Melting Temperature vs Equivalents of (Me_2S)AuCl

Figure 2.12 Melting temperature (°C) vs equivalents of (Me_2S)AuCl with a) CT1, b) CC1, and c) TT1.

a) CT1

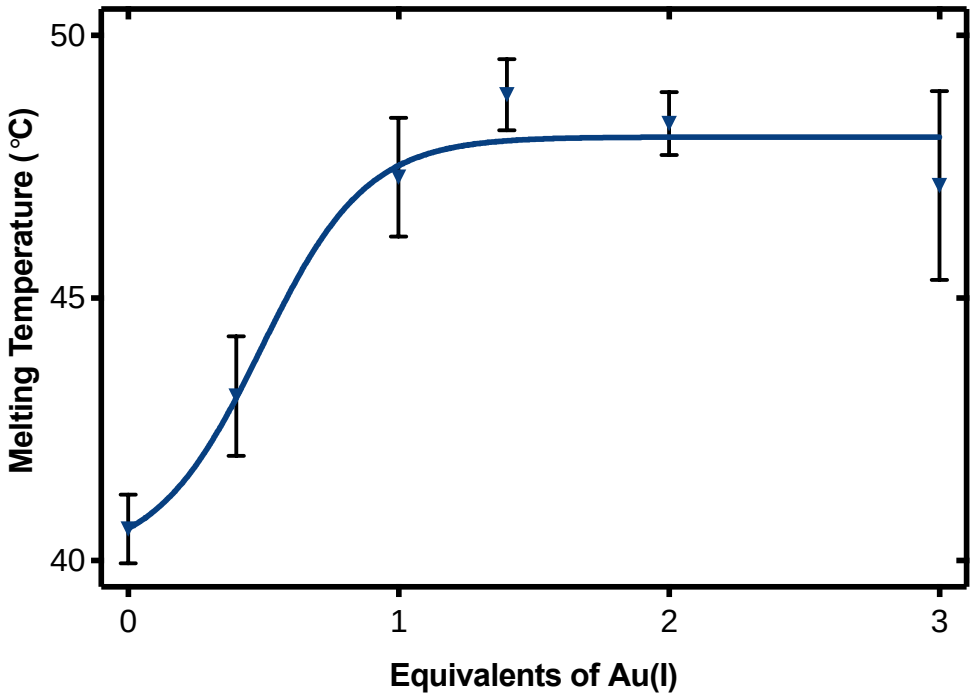

b) CC1

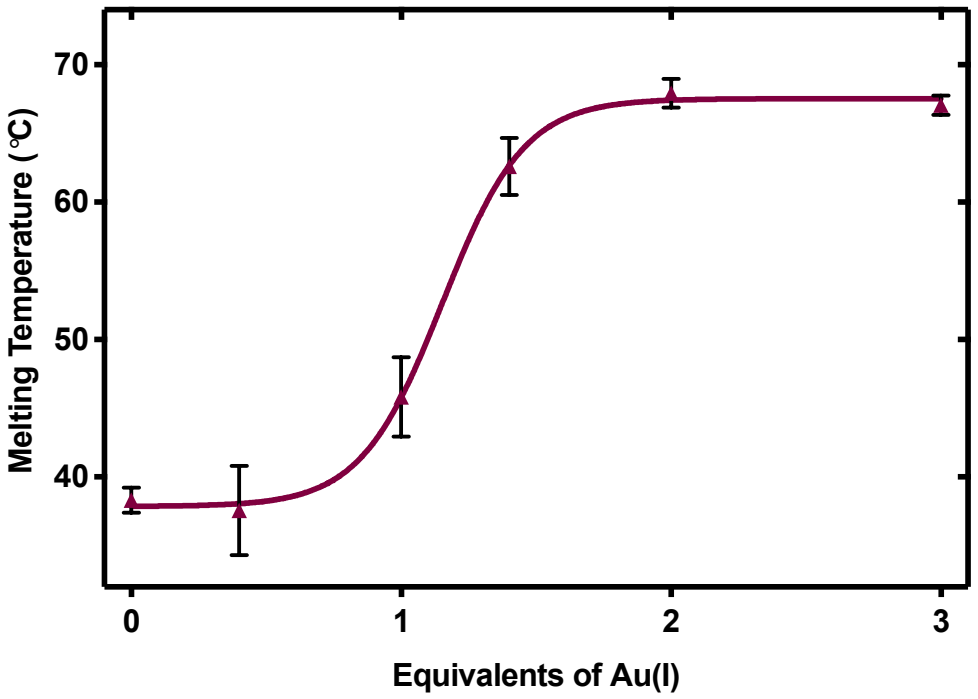
Melting Temperature (°C)
70
60
50
40
0
1
2
3
Equivalents of Au(I)

c) TT1

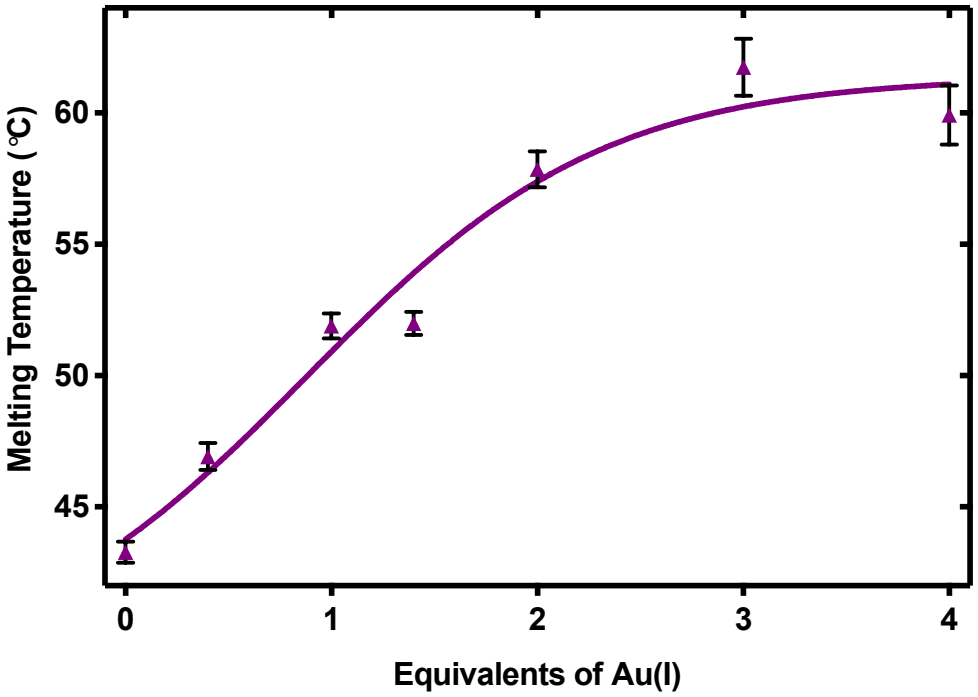
Melting Temperature (°C)
60
55
50
45
0
1
2
3
4
Equivalents of Au(I)

2.8.3 UV Absorbance

General Procedure for UV Absorbance Titration Experiment

Solutions contained 3.5 μM DNA in buffer containing 0.75 mM sodium phosphate, pH 7, 150 mM $NaClO_4$ and 0 μM (0 equivalents) multiple equivalents of $(Me_2S)AuCl$ (60:1 H_2O:MeOH v/v).

Figure 2.13 Absorbance at 300 nm versus equivalents of $(Me_2S)AuCl$ per cytosine base in sequence.

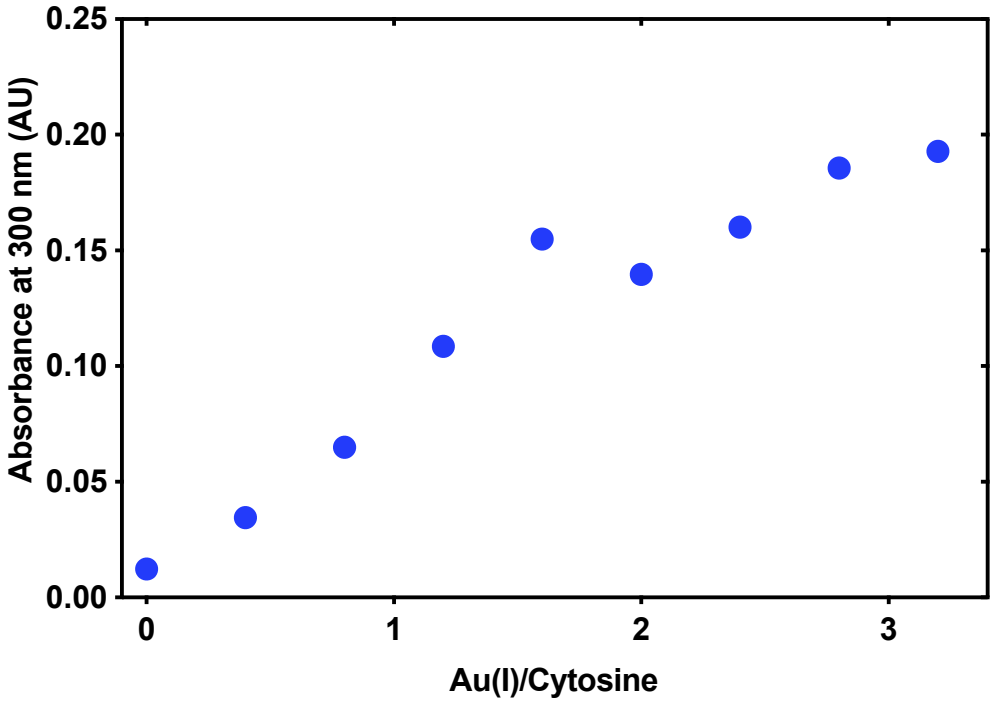

Table 2.7 Thermal denaturation values for GC1 and TA1

Au(I) equivalencies/per Cytosine	**Absorbance (300 nm)**
0	0.012
0.4	0.034
0.8	0.065
1.2	0.11
1.6	0.15
2.0	0.14
2.4	0.16
2.8	0.19
3.2	0.19

2.8.4 Mass Spectrometry

General Procedure for Sample Preparation for Mass Spectrometry Experiments

Solutions contained 5 mM C5, T5, G5, or A5 and 5 mM to 25 mM of $(Me_2S)AuCl$ in 0.3% NH_4OH in 1:1 H2O:MeOH *v/v*. For experiments containing duplex DNA CC1 and TT1, 5 mM of duplex was formed by annealing duplex in water by heating at 90 °C for 10 minutes and then cooling for 45 minutes before adding $(Me_2S)AuCl$ to a final concentration of 5 mM in 50 mM NH_4OAc in 4:1 H_2O:MeOH *v/v*. Solution containing DNA and $(Me_2S)AuCl$ were mixed and data was collected within one hour on MS. Mass spectrometry data was collected on a Thermo Scientific Q Exactive Plus Hybrid Quadrupole-Orbitrap Mass Spectrometer using negative ionization mode.

Figure 2.14 Mass Spectrometry of CT1 a) without and b) with1 equivalent of (Me_2SAuCl)

a) CT1

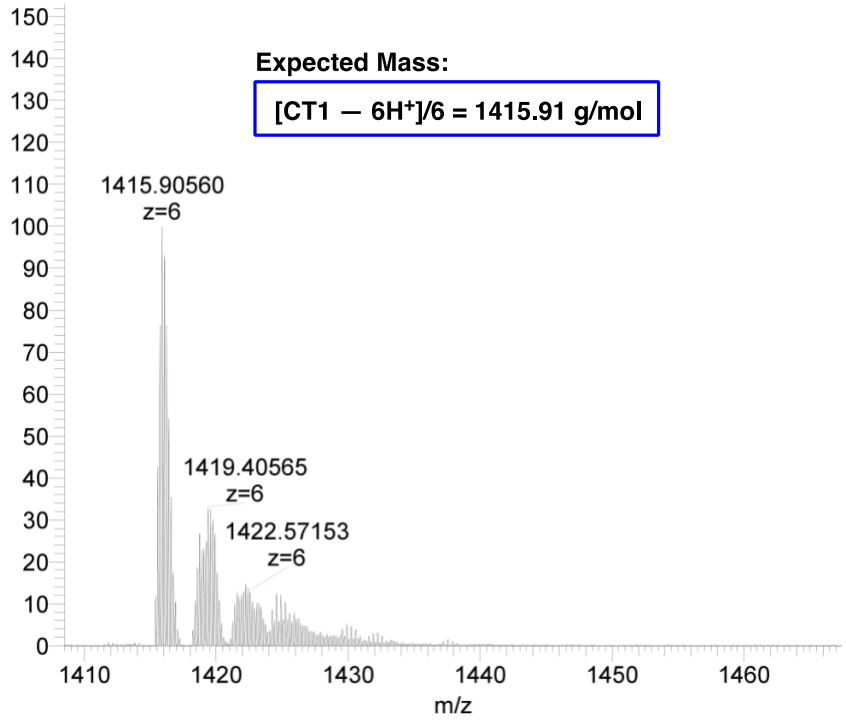

b) CT1 + 1 equivalent $(Me_2S)AuCl$

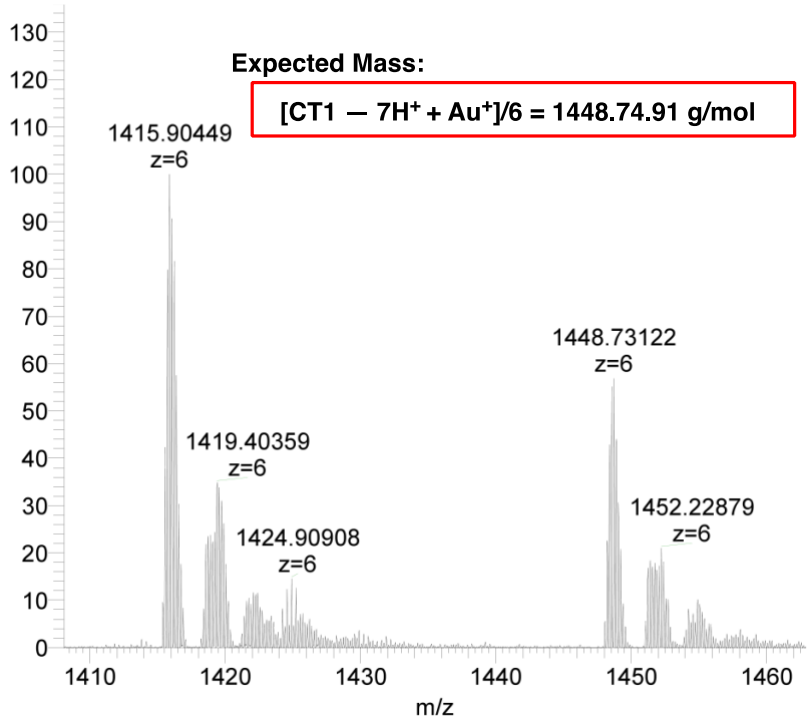

2.8.5 Circular Dichroism

General Procedure for Sample Preparation for Circular Dichroism Spectroscopy

Solutions contained 3.5 μM DNA in buffer containing 0.75 mM sodium phosphate, pH 7, 150 mM $NaClO_4$ and 0 μM (0 equivalents) or 3.5 μM (1 equivalents) of $(Me_2S)AuCl$ (60:1 H_2O:MeOH *v/v*). DNA and buffer were heated at 90 °C for 10 minutes then allowed to cool to room temperature over 45 minutes. After the solution was cooled, 5 μl of $(Me_2S)AuCl$ (210 μM stock solution in methanol) was added and the resulting solution was incubated at room temperature for 5 min before performing experiments. The data was graphed on GraphPad Prism 7.0.

2.8.6 Computational Studies

All density functional theory (DFT) calculations were performed using Gaussian 09 revision D.01.[24] Geometry optimizations and frequency calculations were performed using the functional B3LYP with the 6-31G(d) basis set for all non-metals and the LANL2DZ effective core potential for Au, Ag, and Hg, in implicit water solvent using the SMD continuum solvation model.[25] Single-point energy corrections were calculated with the 6-311++G(2df,2pd) basis set for all non-metals and the SDD effective core potential for Au, Ag, and Hg, in water solvation (SMD).[26] Dispersion corrections using D3(BJ), consisting of the D3 method developed by Grimme along with the Becke−Johnson damping scheme, were applied to all calculations.[27] Gibbs free energies were calculated with vibrational entropy contributions using the GoodVibes python script, in which the vibrational frequencies are corrected by a quasi-harmonic approximation for entropy with a free-rotor description for frequencies below 100 cm^{-1}, as proposed by Grimme.[28] Normal mode analysis of the harmonic vibrational frequencies confirmed that optimized structures are minima (no imaginary frequency). All 3D rendering of stationary points was generated using CYLview.[29] *1*-methylthymine and *1*-methylcytosine were used as the model nucleobases for all calculations.

Figure 2.15 Optimized structures of the C–T metal mediated base pairs showing key bond lengths and structural differences. Left is Au, middle right is Ag, and right is Hg.

Energies.

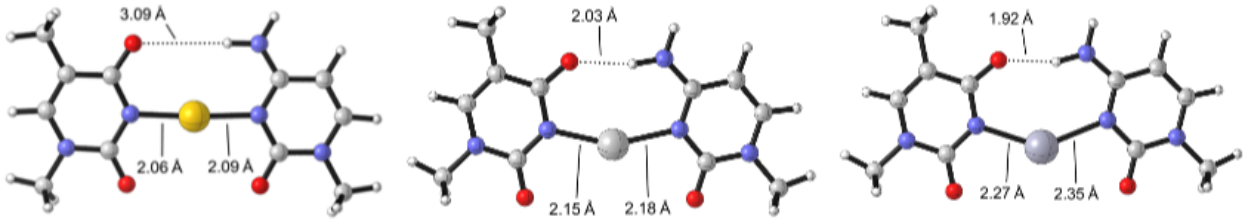

For the following tables, **E** corresponds to the electronic energy, **ZPE** to the zero-point energy correction, **H** to enthalpy, **T•S** entropy, **T•qh-S** quasi-harmonic corrected entropy, **G(T)** uncorrected Gibbs energy, and **qh-G(T)** to the quasi-harmonic Gibbs energy (calculated using a standard state of 1 atmosphere of pressure and at 298.15K). Values are given in atomic units. **SPC** indicates single point corrected energy. Overall calculation method: B3LYP-D3(BJ)/SDD-6-311++G(2df,2pd)/SMD(H_2O)//B3LYP-D3(BJ)/LANL2DZ-6-31G(d)/SMD(H_2O)

Table 2.8 Optimization level SCF energies in addition to ZPE and entropy corrections of all pertinent species used for this study.

Optimization/frequency calculation method: B3LYP-D3(BJ)/LANL2DZ-6-31G(d)/SMD(H_2O)

Structure	E	ZPE	T•S	T•qh-S
Thymine anion	-492.994207	0.129584	0.042885	0.042603
Ag (I)	-146.859656	0	0.018966	0.018966
Au (I)	-135.581849	0	0.019831	0.019831
Cytosine	-434.286064	0.126526	0.040988	0.04083
C–Ag–T	-1073.01804	0.260984	0.073707	0.06972
C–Au–T	-1062.71006	0.261439	0.074086	0.069948
C–Hg–T	-969.862223	0.26139	0.075102	0.070725
Hg (II)	-153.186096	0	0.019867	0.019867

Table 2.9 Single-point corrected energies of all pertinent species used for this study.

Single-point correction method: B3LYP-D3(BJ)/SDD-6-311++G(2df,2pd)/SMD(H_2O)

Structure	E (SPC)	H (SPC)	G(T) (SPC)	qh-G(T) (SPC)
Thymine anion	-493.196659	-493.057693	-493.10058	-493.100297
Ag (I)	-146.859656	-146.857296	-146.87626	-146.876262
Au (I)	-135.581849	-135.579489	-135.59932	-135.59932
Cytosine	-434.4576	-434.322427	-434.36342	-434.363258
C–Ag–T	-1074.59864	-1074.316016	-1074.3897	-1074.385735
C–Au–T	-1063.36986	-1063.086825	-1063.1609	-1063.156773
C–Hg–T	-1080.95165	-1080.668803	-1080.7439	-1080.739528
Hg (II)	-153.186096	-153.183736	-153.2036	-153.203603

Cartesian Coordinates

(Optimized with B3LYP-D3(BJ)/LANL2DZ-6-31G(d)/SMD(H_2O) using Gaussian 09.)

Thymine anion

Charge: –1

Cartesian coordinates

C	-2.414779	1.359558	0.000000
H	-3.245782	0.658200	-0.000191
N	-1.170421	0.593075	-0.000064
C	0.022763	1.270509	-0.000035
H	-0.057990	2.353203	-0.000069
C	1.214358	0.627998	0.000011
C	2.528455	1.351197	-0.000004
H	2.381609	2.436510	-0.000102
H	3.131224	1.088701	0.878976
H	3.131284	1.088551	-0.878898
C	1.185032	-0.834793	0.000103
O	2.271400	-1.484509	0.000099
N	-0.012506	-1.486605	0.000024
C	-1.184796	-0.817398	-0.000060

O	-2.298494	-1.402699	-0.000069
H	-2.474584	1.992553	-0.891191
H	-2.474709	1.992216	0.891424

There are no imaginary frequencies.

Cytosine

Charge: 0

Cartesian coordinates

N	-1.115249	0.437812	-0.000083
C	-0.261991	1.497645	-0.000089
H	-0.718707	2.480411	-0.000174
C	1.084911	1.316368	-0.000010
H	1.767646	2.156352	0.000043
C	1.551525	-0.034435	0.000063
N	2.875662	-0.280302	0.001019
H	3.209191	-1.234170	-0.002130
H	3.546055	0.475125	-0.002437
N	0.723631	-1.083996	-0.000041
C	-0.619870	-0.884709	-0.000032
O	-1.442415	-1.820405	-0.000091
C	-2.565220	0.627692	-0.000052
H	-3.005760	0.169114	-0.888436
H	-3.005672	0.169545	0.888604
H	-2.777866	1.696908	-0.000286

There are no imaginary frequencies.

C–Au–T

Charge: 0

Cartesian coordinates

N	-4.378615	-0.733764	-0.033827
C	-4.967433	0.483764	0.124306
H	-6.049947	0.488334	0.157695
C	-4.231310	1.619327	0.230948
H	-4.698214	2.586973	0.356153
C	-2.814246	1.500613	0.174167
N	-2.040502	2.583111	0.273221
H	-2.462499	3.494787	0.390520
N	-2.236706	0.285671	0.017664
C	-2.991569	-0.863387	-0.096668
O	-2.480884	-1.978953	-0.248369
C	-5.174275	-1.959088	-0.163899
H	-4.979144	-2.427430	-1.130846

H	-4.912713	-2.657481	0.633301
H	-6.228373	-1.694893	-0.089925
Au	-0.162668	0.050221	-0.032583
C	4.498962	-2.649810	0.266887
H	4.242879	-3.291770	-0.579323
N	3.865925	-1.337164	0.122919
C	4.617279	-0.190476	0.040713
H	5.690377	-0.337472	0.080368
C	4.059829	1.038407	-0.080093
C	4.871489	2.297614	-0.163861
H	5.941728	2.074009	-0.124526
H	4.667779	2.841969	-1.093936
H	4.631524	2.978993	0.661470
C	2.609663	1.128629	-0.113952
O	2.012830	2.225130	-0.205091
N	1.895778	-0.054906	-0.039247
C	2.479092	-1.290485	0.073484
O	1.818994	-2.344129	0.135200
H	4.164356	-3.129167	1.189846
H	5.579040	-2.509478	0.301769
H	-1.029583	2.507545	0.230246

There are no imaginary frequencies.

C–Ag–T

Charge: 0

Cartesian coordinates

N	-4.583339	-0.373602	-0.022519
C	-4.902011	0.952041	-0.021406
H	-5.960012	1.184236	-0.031036
C	-3.944725	1.915448	-0.010222
H	-4.202483	2.966330	-0.011374
C	-2.582588	1.490348	0.002445
N	-1.589931	2.385518	0.011266
H	-1.816618	3.371125	0.006318
N	-2.279080	0.176178	0.006957
C	-3.248520	-0.787194	-0.000814
O	-2.978103	-1.998861	0.010190
C	-5.620294	-1.408771	-0.028739
H	-5.474156	-2.074250	-0.881574
H	-5.574433	-1.992386	0.893612
H	-6.592008	-0.922127	-0.107380
C	5.133636	-2.033646	-0.024864
H	4.951309	-2.690677	-0.878274
N	4.170555	-0.932325	-0.021435

C	4.585753	0.375895	-0.021954
H	5.660139	0.521171	-0.034576
C	3.717310	1.417785	-0.009268
C	4.159548	2.850968	-0.010892
H	5.251345	2.923277	-0.020148
H	3.771684	3.384759	-0.887189
H	3.787060	3.381472	0.874018
C	2.298332	1.106620	0.004517
O	1.423707	2.014464	0.012680
N	1.927392	-0.214605	0.009264
C	2.812853	-1.247172	0.001092
O	2.456111	-2.443394	0.011921
H	5.049162	-2.618409	0.894810
H	6.138478	-1.617436	-0.097859
H	-0.603741	2.111840	0.015014
Ag	-0.203710	-0.501887	0.017515

There are no imaginary frequencies.

C–Hg–T

Charge: +1

Cartesian coordinates

N	-4.621843	-0.106421	0.004889
C	-4.874372	1.234588	0.011567
H	-5.919917	1.516686	0.016125
C	-3.874673	2.154211	0.012746
H	-4.081703	3.216220	0.019017
C	-2.533142	1.666445	0.006846
N	-1.492115	2.497867	0.010521
H	-1.658181	3.495632	0.014697
N	-2.302278	0.338915	-0.002323
C	-3.309649	-0.581955	-0.007267
O	-3.085797	-1.803256	-0.021286
C	-5.709116	-1.089595	-0.002950
H	-5.675772	-1.676280	-0.923822
H	-5.608761	-1.758994	0.853473
H	-6.656711	-0.555170	0.057608
C	5.301765	-1.743523	0.006493
H	5.151756	-2.412083	-0.843954
N	4.286932	-0.688607	-0.000016
C	4.636508	0.640146	-0.002963
H	5.702805	0.835566	-0.004483
C	3.720267	1.640972	-0.004570
C	4.091476	3.094487	-0.008337
H	5.178232	3.220178	-0.007360

H	3.686096	3.604081	-0.890919
H	3.683985	3.608795	0.870535
C	2.315877	1.266139	-0.004598
O	1.396602	2.123052	-0.009873
N	2.020968	-0.072847	0.001172
C	2.950133	-1.069204	0.009518
O	2.639475	-2.276269	0.023808
H	5.241612	-2.324767	0.930162
H	6.284527	-1.278501	-0.067178
H	-0.522969	2.163689	0.002879
Hg	-0.174242	-0.663274	-0.002082

There are no imaginary frequencies.

2.9 Notes and References

(1) B. Jash, J. Müller. Metal-Mediated Base Pairs: From Characterization to Application. J. *Chem. Eur. J.* **2017**, *23*, 17166-17178.

(2) (a) J. Muller. Metal-Ion-Mediated Base Pairs in Nucleic Acids. *Eur. J. Inorg. Chem.* **2008**, 3749–3763. (b) W. He, R. M. Franzini, C. Achim. Metal-containing nucleic acid strcutres based on synergetic hydrogen and coordination bonding. *Prog. Inorg. Chem.* **2007**, *55*, 545–611. (c) D. A. Megger, N. Megger, J. Muller. Metal-mediated base pairs in nucleic acids with purine- and pyrimidine-derived nucleosides. *Met. Ions Life Sci.* **2012**, *10*, 295–317. (d) Y. Takezawa, M. Shionoya. Metal-Mediated DNA Base Pairing: Alternatives to Hydrogen-Bonded Watson-Crick Base Pairs. *Acc. Chem. Res.* **2012**, *45*, 2066–2076. (e) J. Muller. Meteal-mediated base pairs in parallel-stranded DNA. *Beilstein J. Org. Chem.* **2017**, *13*, 2671–2681. (f) A. Molter, F. Mohr. Gold complexes containing organoselenium and organotellurium ligands. *Coordination Chemistry Reviews* **2010**, *254*, 19-45. (g) H. Mei, I. Röhl, F. Seela. Ag^{+}-Mediated DNA Base Pairing: Extraordinarily Stable Pyrrolo-dC-Pyrrolo-dC Pairs Binding Two Silver Ions. *J. Org. Chem.* **2013**, *78*, 9457-9463.

(3) A. Lopez, J. Liu. Self-Assembly of Nucleobase, Nucleoside and Nucleotide Coordination Polymers: From Synthesis to Applications. *ChemNanoMat*, **2017**, *3*, 670-684.

(4) (a) H. Urata, E. Yamaguchi, T. Funai, Y. Matsumira, S.-I. Wada. Incorporation of Thymine Nucleotides by DNA Polymerases through T-Hg^{II}-T Base Pairing. *Angew. Chem. Int. Ed.* **2010**, *49*, 6516-6519. (b) T. Funai, Y. Miyazaki, M. Aotani, E. Yamaguchi, O. Nakagawa, S.-I. Wada. Ag(I) ion mediated formation of a C-A mispair by DNA polymerases. *Angew. Chem. Int. Ed.* **2012**, *51*, 6464-6466.

(5) (a) D. B. Hall, J. K. Barton. Sensitivity of DNA-Mediated Electron Transfer to the Intervening π-Stack: A Probe for the Integrity of the DNA Base Stack. *J. Am. Chem. Soc.*, **1997**, *119*, 5045-5046.

(6) A. Ono, S. Cao, H. Togashi, M. Tashiro, T. Fujimoto, T. Machinami, S. Oda, Y. Miyake, I. Okamoto, Y. Tanaka. Specific interactions between silver(I) ions and cytosine-cytosine pairs in DNA duplexes. *Chem. Commun.* **2008**, 4825-4827.

(7) J. Kondo, T. Yamada, C. Hirose, I. Okamoto, Y. Tanaka, A. Ono. Crystal structure of metallo DNA duplex containing consecutive Watson-Crick-like T-Hg(II)-T base pairs. *Angew. Chem. Int. Ed.* **2014**, *53*, 2385-2388. (b) Miyake, Y.; Togashi, H.; Tashiro, M.; Yamaguchi, H.; Oda, S.; Kudo, M.; Tanaka, Y.; Kondo, Y.; Sawa, R.; Fujimoto, T.; Machinami, T.; Ono, A. Mercury^{II}-Mediated Formation of Thymine-Hg^{II}-Thymine Base Pairs in DNA Duplexes. *J. Am. Chem. Soc.* **2006**, *128*, 2172-2173.

(8) (a) A. Bayler, A. Schier, G. A. Bowmaker, H. Schmidbaur. Gold Is Smaller than Silver. Crystal Structures of [Bis(trimesitylphopshine)gold(I)] and [Bis(trimethylphosphine)silver(I)] Tetrafluoroborate. *J. Am. Chem. Soc.* **1996**, *118*, 7006-7007. (b) M. C. Gimeno, P. G. Jones, A. Laguna, C. Sarroca. 1,1'-Bis(diphenylthiophosphoryl)ferrocene as a *trans*- chelating ligand in gold(I) and silver(I) complexes. *J. Chem. Soc. Dalton Trans.* **1995**, 3563-3564.

(9) (a) I. Ott. On the medicinal chemistry of gold complexes as anticancer drugs. *Coord. Chem. Rev.*, **2009**, *253*, 1670-1681. (b) E. R. T. Tiekink. Gold derivatives for the treatment of cancer. *Crit. Rev. Oncol. Hematol.*, **2002**, *42*, 225-248.

(10) C. E. Blank, J. C. Dabrowiak. Absorption and Circular Dichroism Studies of a Gold (I)-DNA Complex. *J. Inorg. Biochem.*, **1984**, *21*, 21-29.

(11) N. Hadjiliadis, G. Pneumatikakis, R. Basosi. Gold complexes of purine and pyrimidine nucleosides. *J. Inorg. Biochem.* **1981**, *14*, 115-126.

(12) (a) M. Bressan, R. Ettorre, P. Rigo. NMR studies of the interaction between cytosine and gold complexes. *J. Mag. Reson.*, **1977**, *26*, 43-47. (b) R. Faggiani, H. E. Howard-Lock, C. J. L. Lock, M. A. Turner. The reaction of chloro(triphenylphosphine)gold(I) with 1-methylthymine. *Can. J. Chem.* **1987**, *65*, 1568-1575. (c) Y. Rosopulos, U. Nagel, W. Beck. Metallkomplexe mit biolgisch wchtigen Liganden, XXIV. Allyl-Palladium(II)- und Triphenylphosphan-Gold(I)-Komplexe mit Nucleobasen und Nucleosiden. *Chem. Ber.* **1985**, *118*, 931-942.

(13) For computational studies see: M. K. Shukla, M. Dubey, E. Zakar, J. Leszczynski. DFT Investigation of the Interaction of Gold Nanoclusters with Nucleic Acid Base Guanine and the Watson-Crick Guanine Cytosine Base Pair. *J. Phys. Chem. C*, **2009**, *113*, 3960-3966.

(14) H. Urata, E. Yamaguchi, Y. Nakamura, S.-I. Wada. Pyrimidine-pyrimidine base pairs stabilized by silver(I) ions. *Chem. Comm.* **2011**, *47*, 941-943.

(15) See Section 2.8.6

(16) (a) P. Schwerdtfeger, H. L. Hermann, H. Schmidbaur. Stability of the Gold(I)-Phosphine Bond. A Comparison the other Group 11 Elements. *Inorg. Chem.*, **2003**, *42*, 1334-1342. (b) M. A. Carvajal, J. J. Novoa, S. Alvarez. Choice of Coordination Number in d^{10} Complexes of Group 11 Metals. *J. Am. Chem. Soc.*, **2004**, *126*, 1465-1477.

(17) I. Okamoto, T. Ono, R. Sameshima, A. Ono. Metal ion-binding properties of DNA duplexes containing thiopyrimidine base pairs. *Chem. Commun.* **2012**, *48*, 4347-4349.

(18) A. Ono, H. Torigoe, Y. Tanaka, I. Okamoto. Binding of metal ions by pyrimidine base pairs in DNA duplexes. *Chem. Soc. Rev.* **2011**. *40*, 5855-5866.

(19) (a) H. Schmidbaur. The fascinating implications of new results in gold chemistry. *Gold Bull.* **1990**, *23*, 11-21. (b) F. Scherbaum, A. Grohmann, B. Huber, C. Kruger, H. Schmidbaur. "Aurophilicity" as a Consequence of Relativistic Effects: The Hexakis(triphenylphosphineaurio)methane Dication $[(Ph_3PAu)_6C]^{2+}$. *Angew. Chem. Int. Ed. Engl.* **1988**, *27*, 1544-1546. (c) P. Pyykko. Strong Closed-Shell Interactions in Inorganic Chemistry. *Chem. Rev.* **1997**, *97*, 597-636. (d) Y. Jiang, S. Alvarez, R. Hoffmann. Dinuclear and polymeric gold(I) complexes. *Inorg. Chem.* **1985**, *24*, 749-757. (e) R. Narayanaswamy, M. A. Young, E. Parkhurst, M. Ouellette, M. E. Kerr, D. M. Ho, R. C. Elder, A. E. Bruce, M. R. Bruce. Synthesis, structure, and electronic spectroscopy of neutral dinuclear gold(I) complexes. Gold(I)-gold(I) interactions in solution and in the solid state. *Inorg. Chem.* **1993**, *32*, 2506-2517.

(20) G. H. Clever, K. Polborn, T. Carell. A highly DNA-duplex-stabilizing metal-salen base pair. *Angew. Chem. Int. Ed.*, **2005**, *44*, 7204-7208.

(21) See Section 2.8.2

(22) T. Brown, G. A. Leonard, E. D. Booth. Influence of pH on the conformation and stability of mismatch base-pairs in DNA. *J. Mol. Biol.*, **1990**, *212*, 437-440.

(23) J. Kypr, I. Kejnovska, D. Rencuik, M. Vorlickova. Circular dichroism and conformational polymorphism of DNA. *Nucleic Acids Res*, **2009**, *37*, 1713-1725.

(24) Gaussian 09, Revision D.01, M. J. Frisch, G. W. Trucks, H. B. Schlegel, G. E. Scuseria, M. A. Robb, J. R. Cheeseman, G. Scalmani, V. Barone, B. Mennucci, G. A. Petersson, H. Nakatsuji, M. Caricato, X. Li, H. P. Hratchian, A. F. Izmaylov, J. Bloino, G. Zheng, J. L. Sonnenberg, M. Hada, M. Ehara, K. Toyota, R. Fukuda, J. Hasegawa, M. Ishida, T. Nakajima, Y. Honda, O. Kitao, H. Nakai, T. Vreven, J. A. Montgomery Jr., J. E. Peralta, F. Ogliaro, M. Bearpark, J. J. Heyd, E. Brothers, K. N. Kudin, V. N. Staroverov, T. Keith, R. Kobayashi, J. Normand, K.

Raghavachari, A. Rendell, J. C. Burant, S. S. Iyengar, J. Tomasi, M. Cossi, N. Rega, J. M. Millam, M. Klene, J. E. Knox, J. B. Cross, V. Bakken, C. Adamo, J. Jaramill o, R. Gomperts, R. E. Stratmann, O. Yazyev, A. J. Austin, R. Cammi, C. Pomelli, J. W. Ochterski, R. L. Martin, K. Morokuma, V. G. Zakrzewski, G. A. Voth, P. Salvador, J. J. Dannenberg, S. Dapprich, A. D. Daniels, O. Farkas, J. B. Foresman, J. V. Ortiz, J. Cioslowski, D. J. Fox, Gaussian, Inc., Wallingford CT, 2010.

(25) (a) A. D. Becke. Density-functional thermochemistry. III. The role of exact exchange. *J. Chem. Phys.* **1993**, 98, 5648–5652. (b) C. Lee, W. Yang, R. G. Parr. Development of the Colle-Salvetti correlation-energy formula into a functional of the electron density. *Phys. Rev. B: Condens. Matter Mater. Phys.* **1988**, 37, 785–789. (c) A. D. Becke. A new mixing of Hartree-Fock and local density-functional theories. *J. Chem. Phys.* **1993**, 98, 1372–1377. (d) P. J. Stephens, F. J. Devlin, C. F. Chabalowski, M. J. Frisch. Ab Initio Calculation of Vibrational Absorption and Circular Dichroism Spectra Using Density Functional Force Fields. *J. Phys. Chem*. **1994**, 98, 11623−11627.

(26) (a) M. Dolg, U. Wedig, H. Stoll, H. Preuss. Energy-adjusted ab initio pseudopotentials for the first-row transition elements. *J. Chem. Phys*. **1987**, 86, 866−872. (b) D. Andrae, U. Haüßermann, M. Dolg, H. Stoll, H. Preu. Ab initio energy-adjusted pseudopotentials for the noble gases Ne through Xe: Calculation of atomic dipole and quadrupole polarizabilities. *Theor. Chem. Acc.* **1990**, 77, 123−141.

(27) (a) S. Grimme, J. Antony, S. Ehrlich, H. Krieg. A consistent and accurate ab initio parametrization of density functional dispersion correction (DFT-D) for the 94 elements H-Pu. *J. Chem. Phys.* 2010, 132, 154104. (b) E. R. Johnson, A. D. Becke. A post-Hartree-Fock model of intermolecular interactions. *J. Chem. Phys*. **2005**, 123, 024101. (c) E. R. Johnson, A. D. Becke.

A post-Hartree-Fock model of intermolecular interactions: Inclusion of higher-order corrections. *J. Chem. Phys.* **2006**, 124, 174104. (d) S. Grimme, S. Ehrlich, L. Goerigk. Effect of the Damping Function in Dispersion Corrected Density Functional Theory. *J. Comput. Chem*. **2011**, 32, 1456−1465.

(28) (a) S. Grimme. Supramolecular Binding Thermodynamics by Dispersion-Corrected Density Functional Theory. *Chem. Eur. J.* **2012**, *18*, 9955; (b) I. Funes-Ardoiz, R. S. Paton. (**2016**). GoodVibes*: GoodVibes 2.0.2* DOI: 10.5281/zenodo.595246.

(29) C. Y. Legault, CYLView, 1.0b (Université de Sherbrooke, 2009); www.cylview.org.

CHAPTER THREE

Regulating Transition Metal Catalysis Through Interference by Short RNAs

Adapted From: Sydnee A. Green, Hayden R. Montgomery, Tyler Benton, Neil J. Chan, Hosea M. Nelson, *Angew., Chem. Int. Ed*, **2019**, *58*, 16400–16404.

3.1 Abstract

We report the discovery of a Au(I)-DNA hybrid catalyst that is compatible with biological media and whose reactivity can be regulated by small complementary nucleic acid sequences. The development of this catalytic system was enabled by the discovery of a C–Au(I)–T metal-mediated base pair. In the Au(I)-DNA catalyst's latent state, the Au(I) ion is sequestered by the mismatch such that it is coordinatively saturated, rendering it catalytically inactive. Upon addition of an RNA or DNA strand that is complementary to the latent catalyst's oligonucleotide sequence, catalytic activity is induced leading to a 7-fold increase in formation of a fluorescent product, forged through a Au(I)-catalyzed hydroamination reaction. Moreover, we demonstrate that regulation of this abiotic chemical reactivity is highly sequence selective, as 1-nucleotide and 2-nucleotide mismatched complements underperform the perfect complement. Further development of this catalytic system will expand not only the chemical space available to synthetic biological systems but also allow for temporal and spatial control of transition metal catalysis through gene transcription.

3.2 Introduction

The use of biocatalysis in synthetic chemistry is emerging as a powerful strategy for the construction of complex molecules.[1, 2] Protein enzymes, utilized in isolated form,[3, 4] as part of constructed artificial pathways,[5, 6] or encapsulated within cells programmed to express them,[7, 8] often form reaction products efficiently and stereoselectively under mild conditions. While many of the recently developed biocatalytic transformations are mechanistically similar to native biochemical processes, several reported systems feature distinctly abiotic transformations, where the products of the reactions arise through a mechanism hitherto unknown in biology. Examples include Ru-catalyzed olefin metathesis reactions in the artificial active site of an evolved streptavidin protein[9] and Ir- and Fe-catalyzed metal-carbenoid and nitrenoid insertion reactions from evolved P450 enzymes.[10, 11, 12] In these systems, abiotic chemical reactivity is developed through directed evolution,[13] construction of novel metalloenzymes *via* transmetalation reactions,[14] a posttranslational metalation,[15] or some combination thereof.[16] It is doubtless that as these strategies improve, the availability of protein enzymes that catalyze novel abiotic transformations will advance in unison. However, chemical concepts allowing for control of biocatalytic reactions by biological stimuli, a goal that would lead to advances in synthetic biology and chemical biology, have yet to be explored fully.[17, 18]

Inspired by current hypotheses concerning the role of ribozymes in biogenesis,[19, 20] the stimuli-responsiveness of riboswitches and molecular beacons, and the well-established propensity of late transition metals to bind nucleic acids in a sequence selective manner,[21, 22] our group recently became interested in the development of biocatalytic systems composed of nucleic acids and transition metals that mediate chemical reactions. Here, we envisioned the application of metal-mediated base pairs[23] (MMBPs) comprised of catalytically relevant transition metal centers

and duplex DNA composed exclusively of canonical nucleobases. Specifically, toehold-stem-loop oligonucleotide hairpins could be designed with MMBPs such that the metal reactivity would be regulated through outer sphere, sense/antisense interactions with small RNA/DNA. Here, strand displacement reactions would dictate the coordination sphere of the reactive metal center and influence substrate binding events (*Figure 3.1a*). In this scenario, chemical transformations mediated by transition metal species could then be "controlled" by inherently biological molecules. The successful demonstration of this concept could open the door to genotype-specific transition metal catalysis and the development of new biosynthetic pathways that feature transformations with no biological equivalent. Here we report the initial steps toward achieving this goal. We find that an unprecedented Au(I) MMBP is formed through the treatment of DNA hairpins possessing a C–T mismatch with an appropriate Au(I) precursor (*Figure 3.1b*). Importantly, the rate at which this organometallic complex mediates an abiotic hydroamination reaction is dramatically increased when exposed to short strands of sequence-complementary DNA or RNA. This study represents an early example of an organometallic catalyst that can be regulated by biological stimuli.

Figure 3.1 a) Incorporation of metal ions into DNA hairpin containing mismatch and modulation of metal reactivity using hybridization. b) Au(I) addition to C–T mismatch.

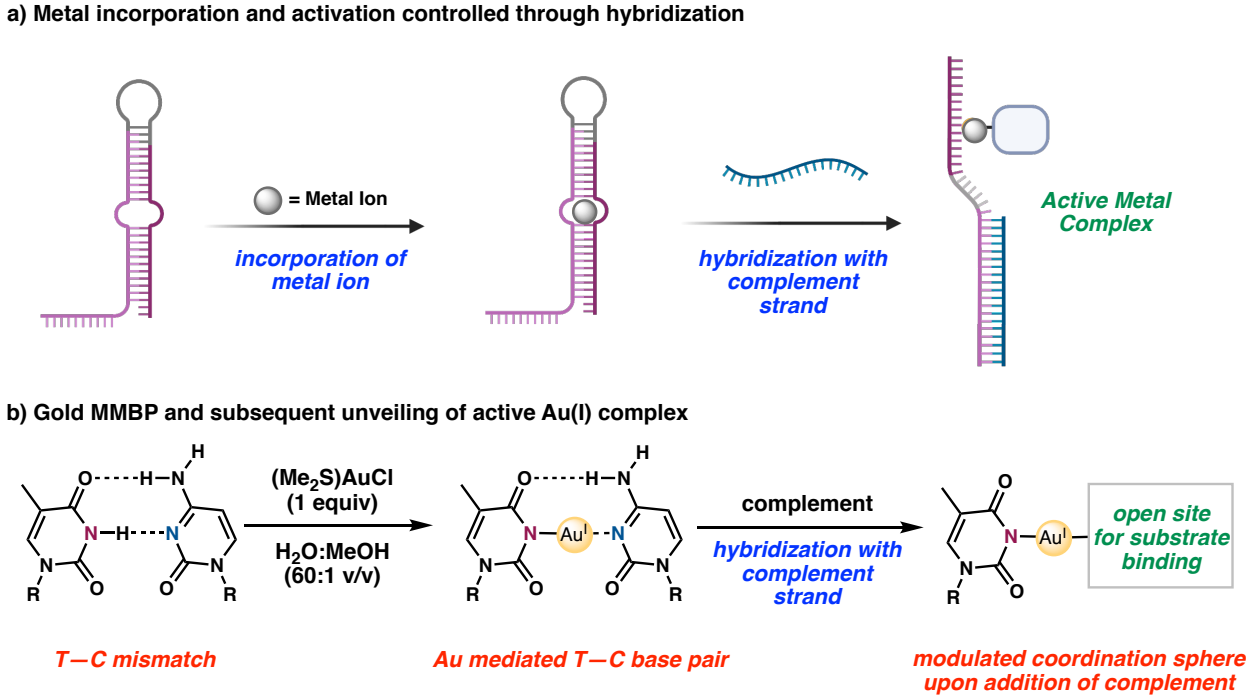

3.3 Fluorescent Response Following Addition of Complement

Having previously designed a sequence-specific transition metal binding motif through formation of a Au(I)-mediated base pair, we moved forward with investigations of its catalytic properties. We hypothesized that the hairpin containing a C–T mismatch in the stem (**3.1**) would bind one equivalent of Au(I) (refer to Chapter Two) to form latent DNA-Au complex **3.2** (*Figure 3.2a*). Upon exposure to a short, complementary DNA or RNA sequence, strand displacement would interfere with the Au–base bonds of the stable MMBP, forming an active complex **3.3**. We assessed the catalytic activity of this complex using pro-fluorophore **3.4**, which cyclizes to form fluorescent BODIPY **3.5** through a Au-catalyzed hydroamination reaction, allowing for high throughput sequence optimization using a simple plate reader (*Figure 3.2b*).

Figure 3.2 a) Addition of Au(I) into hairpin **TCH5** and formation of active duplex following complement addition. b) Fluorescent BODIPY product formed through Au(I)-catalyzed hydroamination reaction. c) Kinetics of inactive catalyst 3.2 and active catalyst 3.3

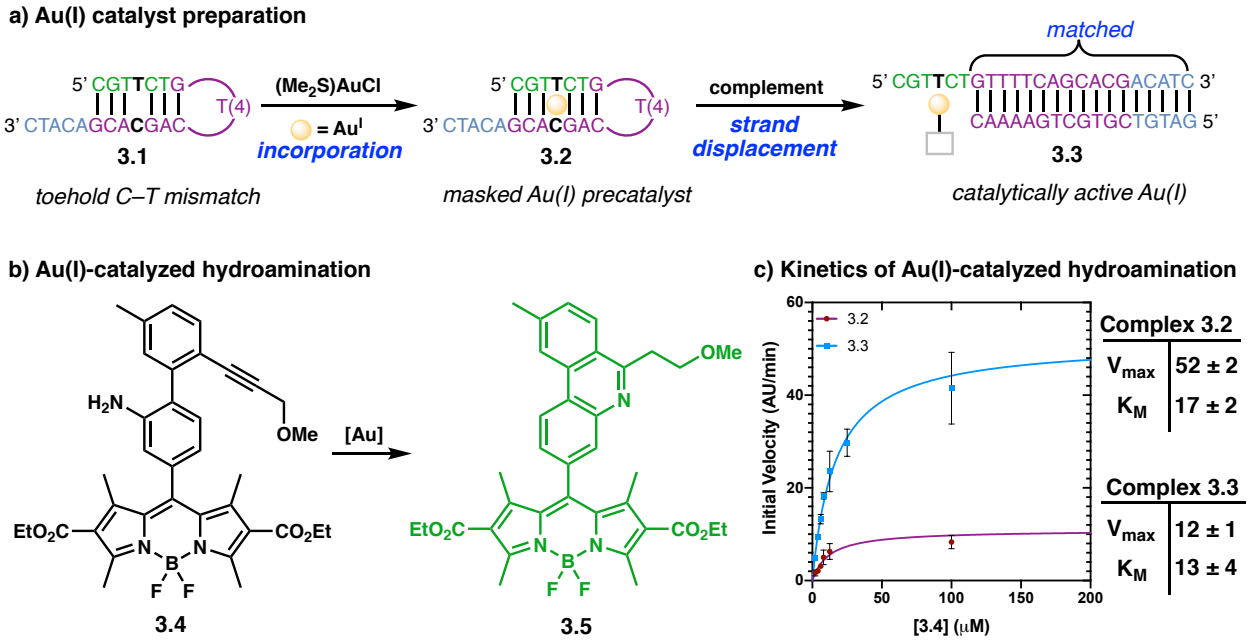

We were pleased to find that treatment of latent DNA-Au catalyst **3.2** with 1 equivalent of a complementary short oligo (**cTCH5**) increases the fluorescence of a solution containing pro-fluorophore **7** by approximately 700% when compared to the reaction containing no complement. Fluorescence based kinetics show that the initial rate of hydroamination with active complex **3.3** are significantly higher than that of complex **3.2**. Interestingly, both putative complexes have similar substrate affinity (K_M = 16 □M), suggesting that this affinity is inherent to the Au(I) center. However, the initial rates are dramatically increased upon addition of the complement strand, wherein more Au(I) is accessible, resulting in a higher effective catalyst concentration. The background fluorescence induced by latent catalyst **3.2** may be due to unbound Au(I) or Au(III) formed through decomposition of precatalyst **3.2** in solution.[24] In previous thermal stability

studies, we determined that Au(III) does not bind C–T mismatches, but does catalyze the formation of fluorophore **3.5** (refer to Chapter Two) .

3.4 FRET Probe Control

To further support that the observed reactivity was due to the modulation of the Au(I)-mediated base pair in a sequence-specific manner, we carried out further control experiments. First, we sought to confirm that a hairpin bearing a Au-mediated base pair could undergo strand-displacement reactions, analogous to canonical structured oligonucleotides, despite the inclusion of strong Au-base bonds. A FRET probe was designed to probe this key elementary step. Fluorescein (**3.6**) was appended to the 5' end of hairpin **3.2** and a distal quencher dabcyl (**3.7**) was appended to the 3' end, forming FRET probe **3.8** (*Figure 4a-b*). Here, strand displacement with a complementary sequence would yield fluorescent duplex **3.9.**[25] Gratifyingly, the addition of complement to either probes containing a Au(I) MMBP or a mismatch without Au(I) resulted in an increase in fluorescence due to spatial separation between the donor and quencher (*Figure 3.3c*). This result confirms that stabilization of the duplex due to strong Au(I)-base bonds does not hinder strand displacement reactions.

Figure 3.3 a) On and off state of molecular beacon. b) Structures of the fluorophore (FAM) and quencher on molecular beacon. c) Fluorescence of molecular beacon on (**3.9**) and off (**3.8**) state with and without Au(I)

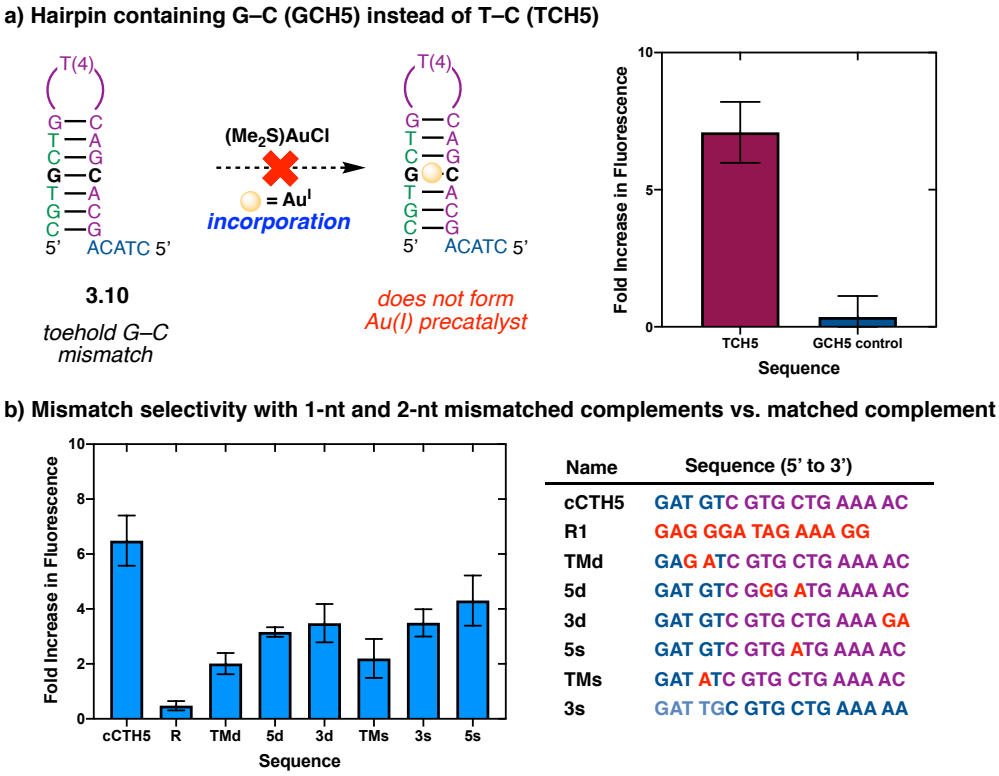

3.5 G–C Hairpin Control and Mismatch Selectivity

To further support the need for a mismatch to form inactive complex **3.2** comprised of a Au(I) metal-mediated base pair, we designed the same hairpin sequence that contains a G–C match **3.10** instead of a C–T mismatch. Exposure of a solution of (Me_2S)AuCl and **3.10** (a G–C base pair instead of a C–T mismatch in complex **3.2**) to the complement strand (**cTCH5**) did not result in an increase of fluorescence (*Figure 3.4a*). This suggests that a precatalytic complex analogous to precatalyst **3.2** is not formed here; formation of such complexes are contingent of a mismatch in the stem. Moreover, when the complementary strand (**cTCH5**) was replaced with non-

complementary, purine-rich, random DNA sequence **R1**, there is no significant activation of the latent DNA-Au catalyst **3.2**, as minimal increase in fluorescence is observed (*Figure 3.4b*). In sequence-selectivity experiments, the highest increase in fluorescence is exhibited in the presence of the exact complementary sequence (**cTCH5**), whereas addition of complements possessing single (1-nt) or double (2-nt) mismatches (**TMs**/**3s**/**5s** and **TMd**/**3d**/**5d**, respectively) result in lower fluorescence intensity, with the 2-nt mismatched sequence **TMd** resulting in the lowest levels of fluorescence (*Figure 3.4b*). This further supports our hypothesis that complement hybridization is required to form the active catalyst.

Figure 3.4 a) Addition of Au(I) to non-mismatched hairpin and fold increase in fluorescence upon addition of complement. b) Fold increase in fluorescence with matched and mismatched complementary sequences.

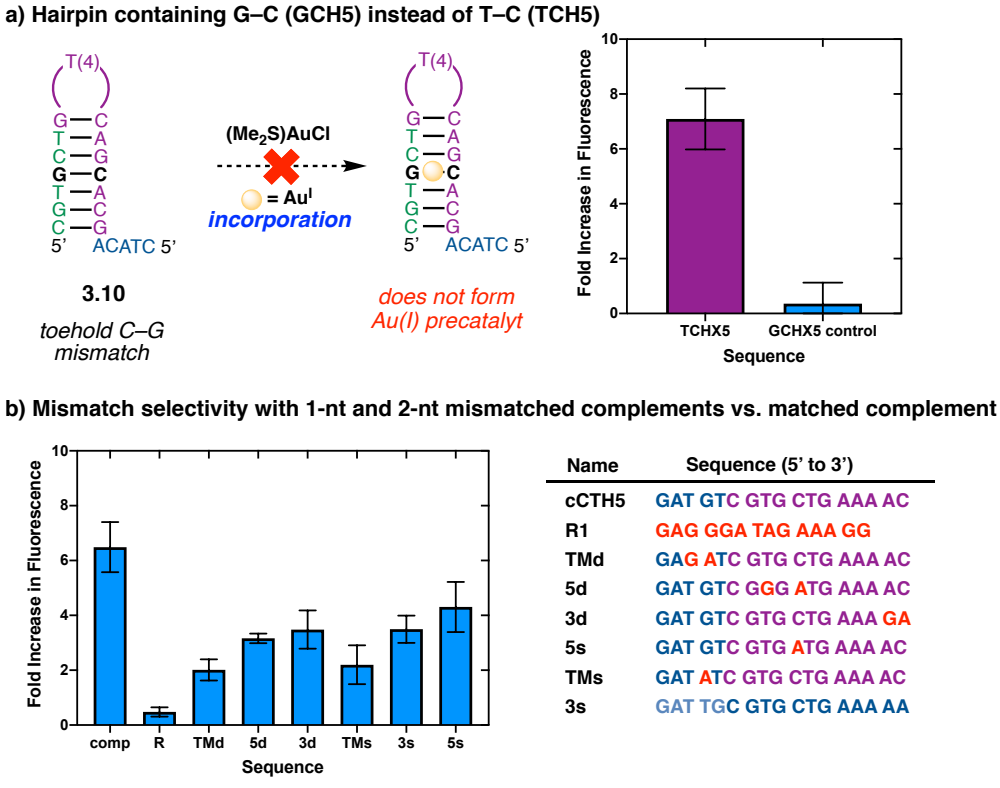

3.6 Biological Conditions

Excited by our initial results and sequence selectivity, we wanted to see if we could for the active complex **3.3** in the presence of biological conditions. Biological systems contain many potential ligands for metal binding, leading to difficulties developing biocompatible complexes and controlling abiotic metal reactivity under physiological conditions. Specifically, Au(I) and Au(III) have been shown to readily form nanoparticles in the presence of small biomolecules, such as short nucleic acids, amino acids, and sugars.[26] To assess the stability and reactivity of complex **3.2** under biological conditions, we exposed our catalyst system to mixtures of nucleic acids and biologically relevant solutions. We were pleased to find that the addition of a mixture of random sequence **R1** and complement **cTCH5** to latent catalyst **3.2**, led to a 1.5-fold increase in fluorescence, a significant increase in reactivity when compared to complex **3.2** alone (*Figure 3.5a*). In addition, complex **3.3** showed significant catalytic activity under conditions containing urine or saliva solutions, with nearly a 2-fold and 4-fold increase in yield respectively. This result is especially remarkable due to the fact that these solutions contain albumin, an enzyme with a considerable amount of sulfur containing residues,[27] and urea, a small molecule well known to denature DNA.[28] These examples suggest that Au(I) binding to hairpin **3.1** protects the metal ion from non-productive binding to nucleic acids, proteins, and small biomolecules. These findings suggest that control of the reactivity of species such as latent catalyst **3.2** can be achieved in biologically relevant environments.

In living organisms, it is known that small RNA sequences selectively bind to complementary nucleotide acids and promote nucleotide degradation *via* the recruitment of active enzymes. These systems in which small RNA sequences modulate gene expression have been utilized as biological tools and therapeutics.[29] We envisioned an analogous system in which our

DNA-Au complex could be regulated by small RNA sequences, ultimately controlling the chemical reactivity of transition metal DNAzymes. Gratifyingly, the addition of a short complementary RNA strand (**RcTCH5**) to latent Au-DNA catalyst **3.2** results in nearly a 600% increase in yield, akin to the DNA-based complement (**cTCH5**) (*Figure 3.5b*). This increase in fluorescence, likely due the formation of a hybrid DNA-RNA complex, demonstrates that there is potential for the use of this type of system to perform catalytic reactions in response to gene transcription.

Figure 3.5 a) Fold increase in fluorescence in various biological solutions, including random nucleic acid sequences, synthetic urine, and synthetic saliva. b) Fold increase in fluorescence with DNA complement (cTCH5) and RNA complement (RcTCH5).

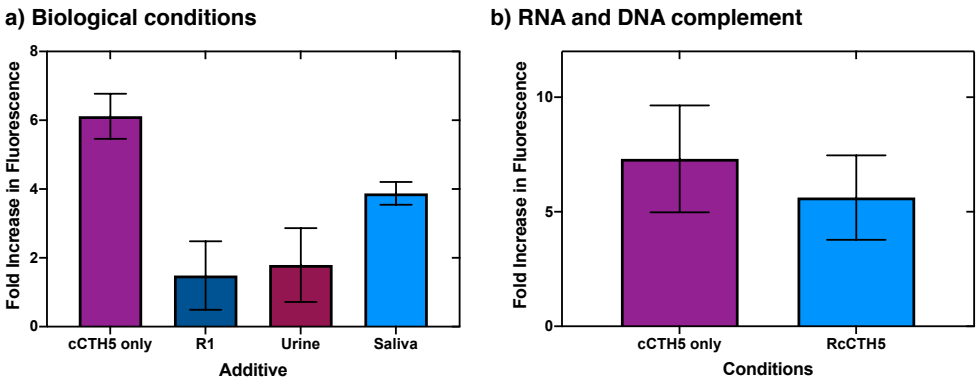

3.7 Conclusion

The synergy of synthetic catalysts and biomolecules remains underdeveloped in chemistry and biology. There are several potential applications for such biocommunicative organometallic species, including the development of chemical biology probes capable of signal amplification through catalyst turnover, the ability to treat diseases through gene-specific cytotoxic reactions

and catalytic formation of therapeutics in targeted cells, the construction of artificial biosynthetic pathways possessing abiotic chemical transformations, and the catalytic modification of biomolecules. This work represents an early proof-of-principle study where the innately abiotic reactivity of a transition metal catalyst can be regulated through interactions with native biological molecules such as DNA and RNA.

3.8 Experimental Section

3.8.1 Materials and Methods

Unless stated otherwise, reactions were performed in flame-dried glassware under an atmosphere of nitrogen. Benzene, THF, dichloromethane, and dimethylformamide were degassed and dried in a JC Meyer solvent system. SilicaFlash P60 silicagel (230–400 mesh) was used for flash chromatography. NMR spectra were recorded on a Bruker AV-300 (1H), Bruker AV-400 (1H, 13C), Bruker DRX-500 (1H), and Bruker AV-500 (1H, 13C). 1H NMR spectra are reported relative to $CDCl_3$ (7.26 ppm). All oligonucleotides were purchased through Integrated DNA Technology with standard desalting unless otherwise specified. Samples for thermal denaturation, mass spectrometry studies, and catalysis were prepared by heating the buffered DNA solution without metal at 90 °C in a heating block for 10 minutes then cooled to room temperature for 30 minutes. Once cool, the metal solution was added. In thermal denaturation experiments, all absorbances were measured at 260 nm using HP-8453 spectrophotometer with HP-89090A Peltier temperature controller from 15–90 °C at 5 °C min^{-1} with a hold time of 1 min. Relative absorbance, $A_{260nm}=(A_t–A_{15\,°C})/(A_{90\,°C}–A_{15\,°C})$, vs. temperature (°C) curves were fitted using GraphPad Prism 7.0c. Fluorescence experiments were recorded on a Tecan Infinite M1000 Pro plate reader with the following conditions: 480 nm excitation, 510 nm emission, 8 mm excitation and emission bandwidth, 50 flashes with a frequency of 400 Hz, and a 10 ms delay time. Fluorescence data was collected on a JASCO-J715 CD spectrophotometer with a scan rate of 20 nm/min from 200 nm to 300 nm with 3 accumulations. Mass spectrometry data was collected on a Thermo Scientific Q Exactive Plus Hybrid Quadrupole-Orbitrap Mass Spectrometer using negative ionization mode.

3.8.2 Thermal Stability Measurements

Thermal stability measurements. Solutions of 3.5 □M mismatch-containing DNA were prepared in 0.75 mM phosphate buffer, pH 7.0, and 150 mM $NaClO_4$. Samples were annealed at 90 °C in a heating block for 10 minutes and allowed to cool to room temperature over 30 minutes. One equivalent (3.5 mM) of $(Me_2S)AuCl$ was added in methanol such that the solution contained 60:1 H_2O:MeOH (v/v). Melting temperature profiles were recorded using HP-8453 spectrophotometer with HP-89090A Peltier temperature controller from 15–90 °C at 5 °C min^{-1} with a hold time of 1 min. Relative absorbance at 260 nm, $A_{260nm}=(A_t–A_{15\,°C})/(A_{90\,°C}–A_{15\,°C})$, vs. temperature(°C) curves were fitted using GraphPad Prism 7.0c

Table 3.1 Sequences used in thermal denaturation experiments.

Sequence Name	Hairpin (5'-3')
CTH	CGTTCTGTTTTCAGCACG
TAH	CGTTCTGTTTTCAGAACG
GCH	CGTGCTGTTTTCAGCACG
TCH3	CGTTCTGTTTTCAGCACGACA
cTCH3	TGTCGTGCTGAAAAC

Thermal denaturation profiles TCH3 and TCH3 + cTCH3 in the presence of $(Me_2S)AuCl$

Figure 3.6 Relative absorbance, $A_{260nm}=(A_t–A_{15\,°C})/(A_{90\,°C}–A_{15\,°C})$, vs. temperature (°C) curves for pyrimidine-mismatch-containing oligonucleotides, a) CTH b) TAH c) CGH in the presence of $(Me_2S)AuCl$. Solutions contained 3.5 □M DNA in buffer containing 0.75 mM sodium phosphate, pH 7, 150 mM $NaClO_4$ and 0 and 1 equivalent $(Me_2S)AuCl$ (60:1 H_2O:MeOH v/v).

a) TCH3

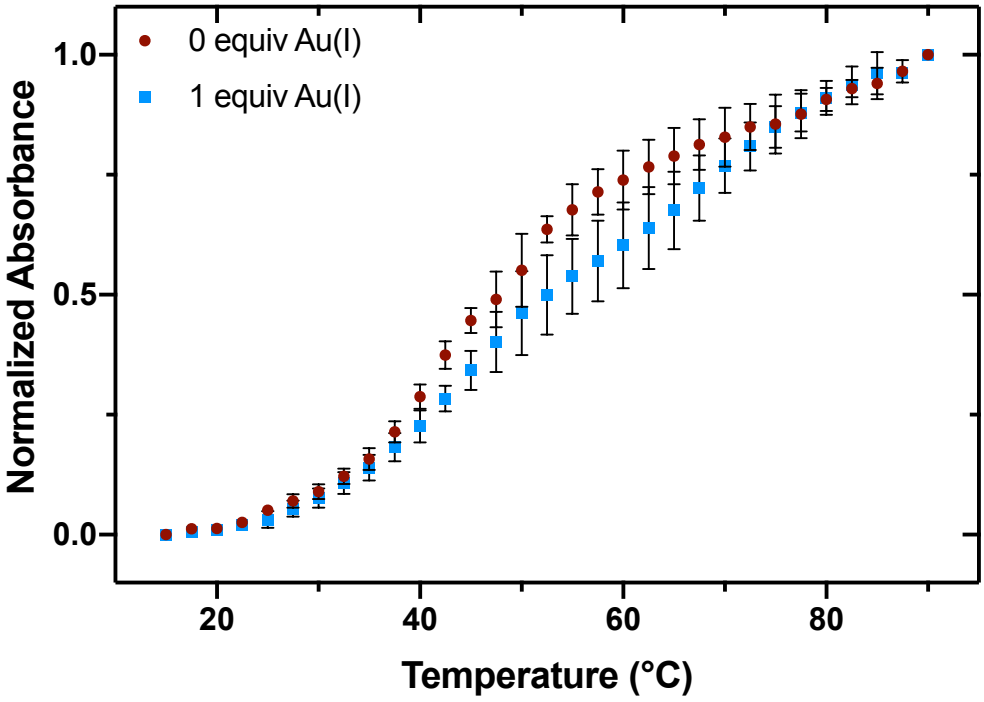

b) TCH3 + cTCH3

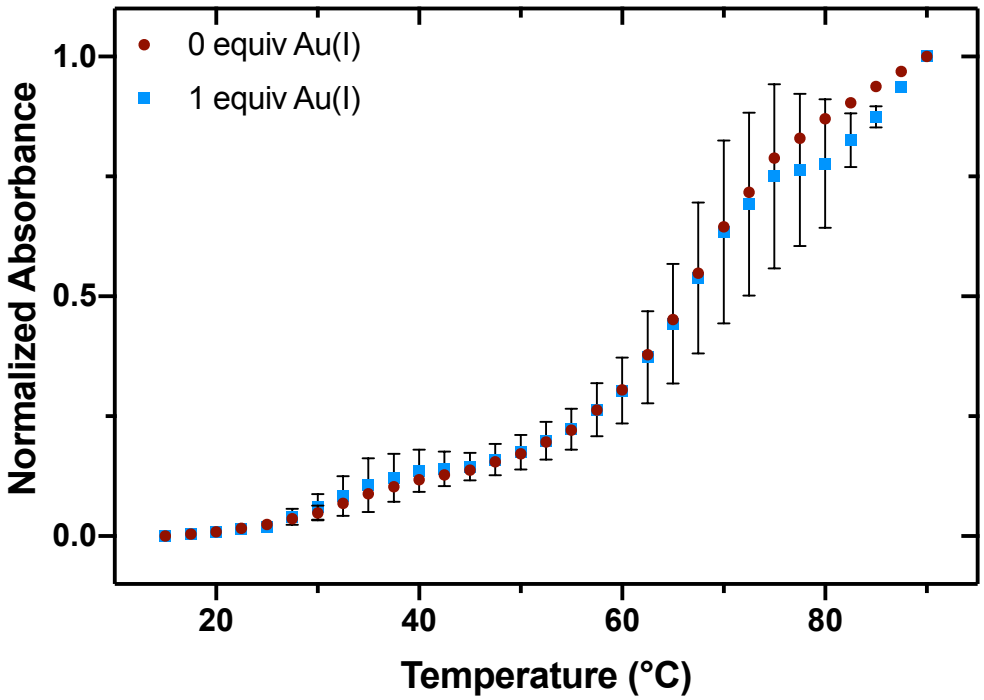
0 equiv Au(I)
1 equiv Au(I)
Normalized Absorbance
1.0
0.5
0.0
20
40
60
80
Temperature (°C)

c) GCH

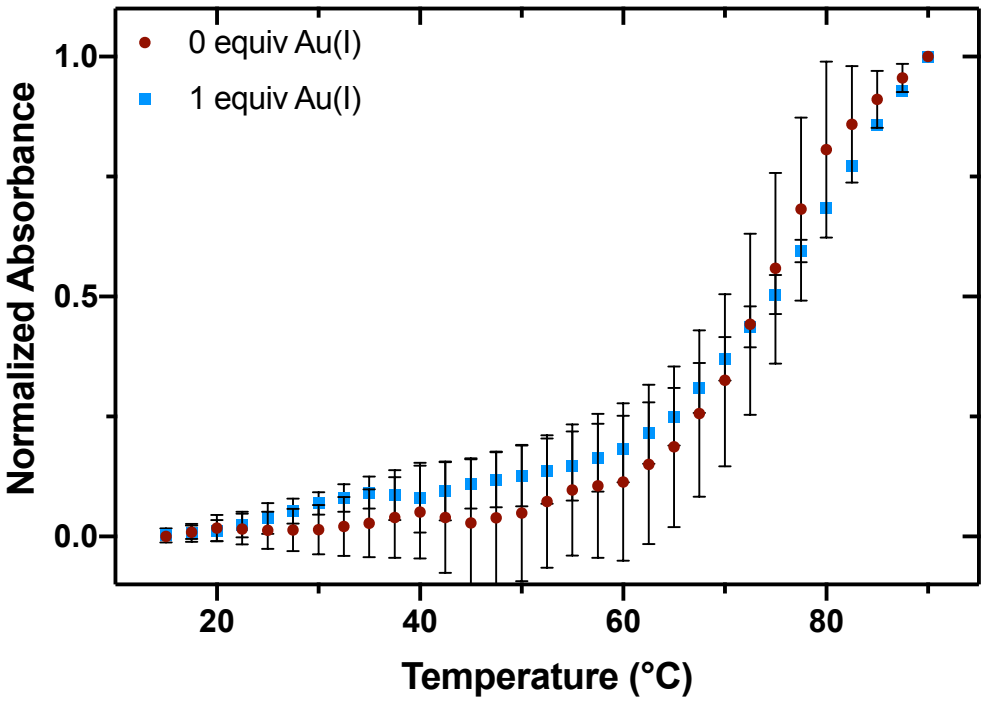

Table 3.2 Thermal denaturation values for control sequences CTH, TAH, AND GCH

Thermal Denaturation – CTH, TAH, and GCH				
Sequence	**0 equiv T_m (°C)**	**1 equiv T_m (°C)**	**□T_m (°C)**	**Error**
CTH	45.9	56.6	10.7	2.5
TAH	67.9	69.2	1.3	6.9
GCH	74.7	84.4	9.7	9.0

Melting temperatures calculated from the thermal denaturation profiles of pyrimidine-mismatch-containing oligonucleotides in the presence of various concentrations of $(Me_2S)AuCl$. Melting temperatures and error calculated using the sigmoidal dose-response feature in GraphPad Prism 7.0c.

Thermal denaturation profiles of TCH3 and TCH3 + complement

Figure 3.7 Relative absorbance, $A_{260nm}=(A_t–A_{15\,°C})/(A_{90\,°C}–A_{15\,°C})$, vs. temperature (°C) curves for pyrimidine-mismatch-containing oligonucleotides, a) TCH3 and TCH3 + complement in the presence of $(Me_2S)AuCl$. Solutions contained 3.5 μM DNA in buffer containing 0.75 mM sodium phosphate, pH 7, 150 mM $NaClO_4$ and 0 and 1 equivalent $(Me_2S)AuCl$ (60:1 H_2O:MeOH v/v).

a) TCH3

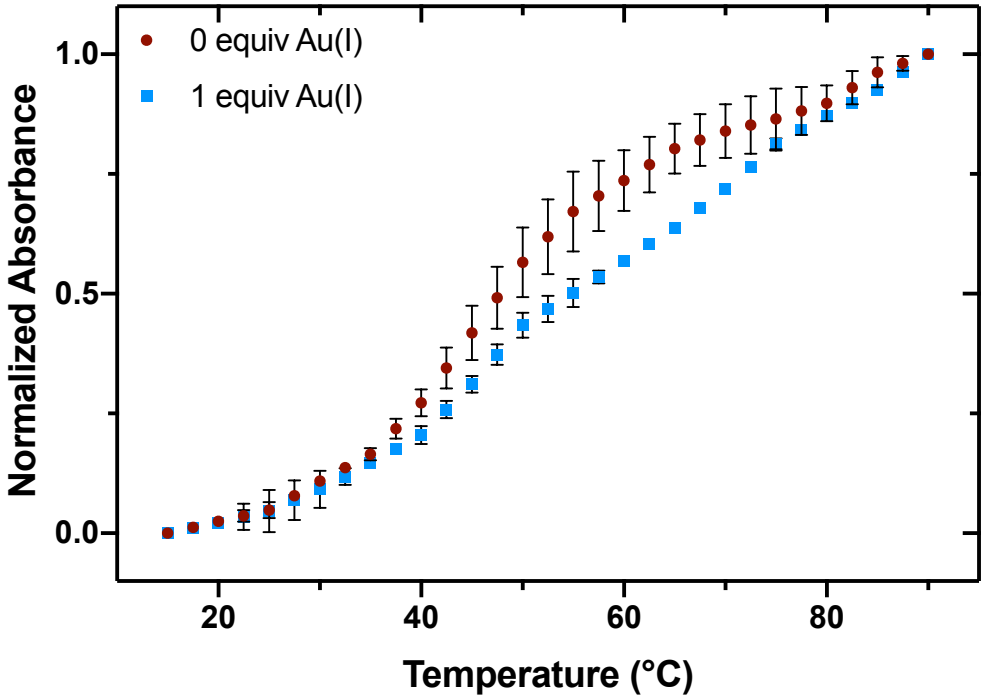

b) TCH3 + complement

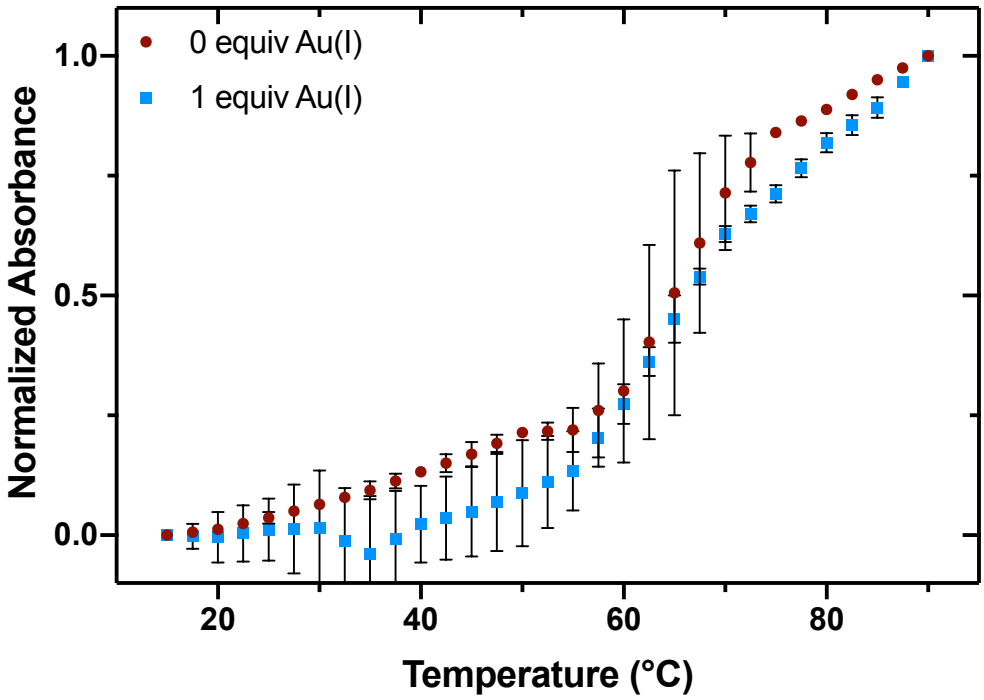

Table 3.3 Thermal denaturation values for control sequences TCH3 and TCH3 + cTHC3

Thermal Denaturation – CTH, TAH, and GCH				
Sequence	**0 equiv T_m (°C)**	**1 equiv T_m (°C)**	**ΔT_m (°C)**	**Error**
TCH3	46.7	56.6	10.7	2.5
TCH3 + cTCH3	66.1	66.9	1.3	6.9

Melting temperatures calculated from the thermal denaturation profiles of pyrimidine-mismatch-containing oligonucleotides in the presence of various concentrations of $(Me_2S)AuCl$. Melting temperatures and error calculated using the sigmoidal dose-response feature in GraphPad Prism 7.0c.

3.8.3 Circular Dichroism (CD)

General Procedure for Sample Preparation for Circular Dichroism Spectroscopy

Solutions contained 3.5 μM DNA in buffer containing 0.75 mM sodium phosphate, pH 7, 150 mM $NaClO_4$ and 0 μM (0 equiv) or 3.5 μM (1 equiv) of $(Me_2S)AuCl$ (60:1 H_2O:MeOH v/v). DNA and buffer were heated at 90 °C for 10 minutes then allowed to cool to room temperature over 45 minutes. After the solution was cooled, 5 μl of $(Me_2S)AuCl$ (210 μM stock solution in methanol) was added and the resulting solution was incubated at room temperature for 5 min before performing experiments. The reported data is based on 3 trials and graphed on GraphPad Prism 7.0c.

Figure 3.8 CD spectra of TCH duplex in the presence of 0 equiv (0 eq) or 1 equiv (1 eq) $(Me_2S)AuCl$.

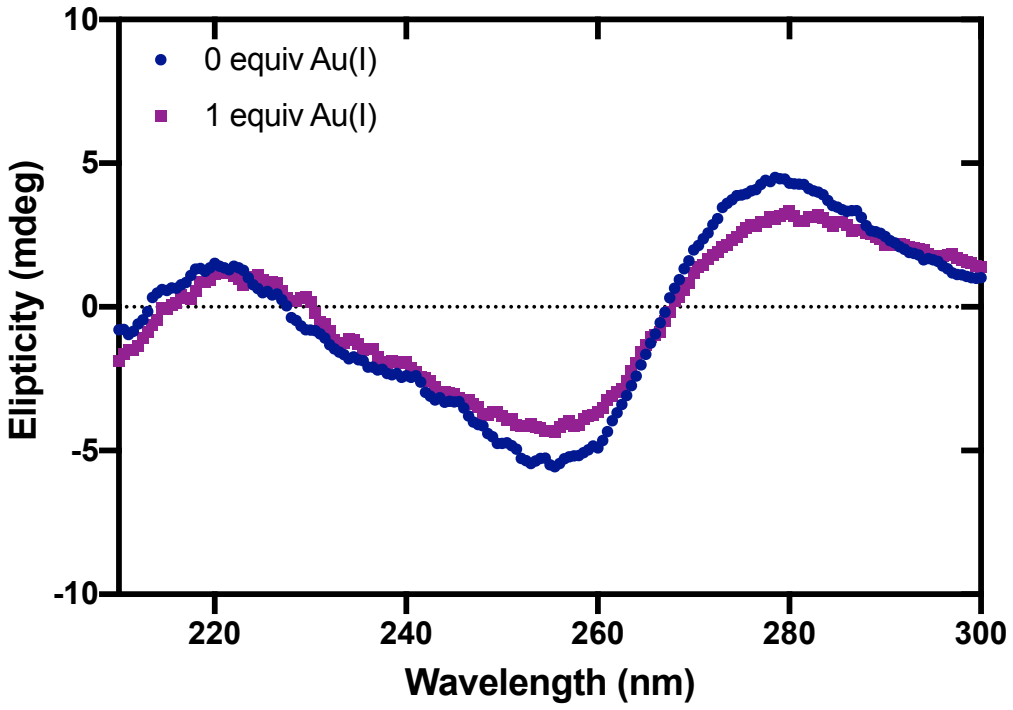

Figure 3.9 CD spectra of TAH hairpin in the presence of 0 equiv (0 eq) or 1 equiv (1 eq) Me_2SAuCl.

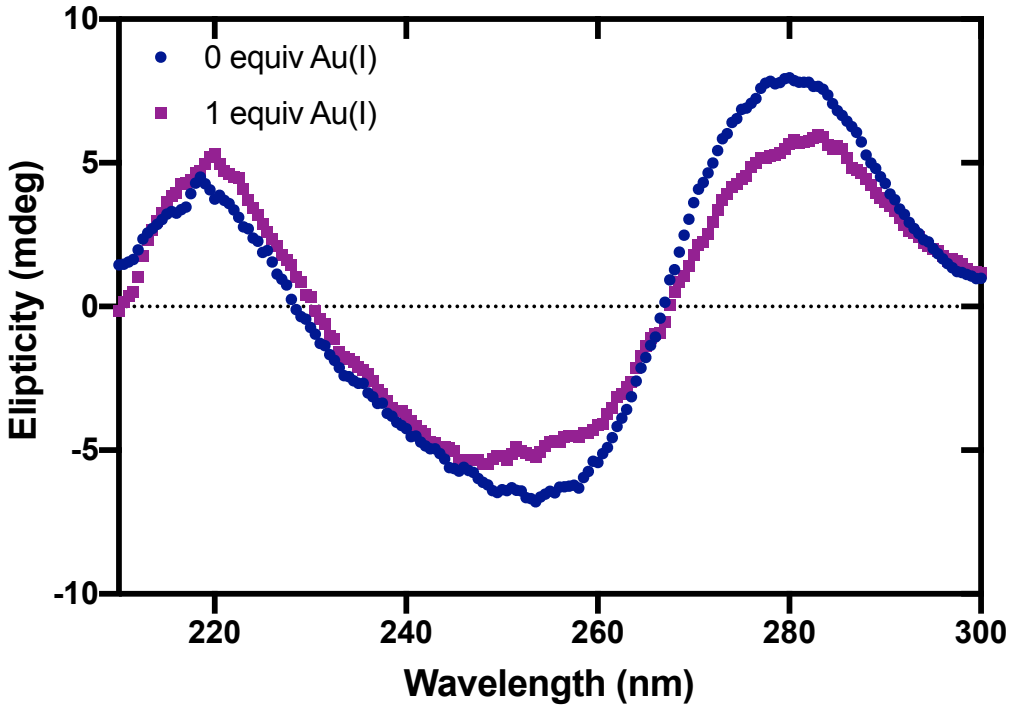

3.8.4 DNA-Au(I) Hydroamination Reactions

Fluorescent DNA-Au(I) hydroamination reactions. Samples for catalysis were prepared by heating the buffered DNA solution without metal at 90 °C in a heating block for 10 minutes. Solutions were cooled to room temperature over 30 minutes. Then one equivalent (2.38 μl, 420 μM stock solution) of $(Me_2S)AuCl$ as a solution in acetone was added. Following the addition of the gold solution, the complement sequence was added and the solution was allowed to incubate at room temperature for 5 minutes. Then a solution of BODIPY **3.4** in ethanol was added resulting in a final solution containing (1:1:0.02 H_2O:EtOH:$(CH_3)_2CO$). Reactions contain 10 μM DNA hairpin, 10 μM complement sequence, 250 mM $NaClO_4$, and 40 μM BODIPY **3.4**. Positive control contains no DNA. Negative control contains no DNA nor $(Me_2S)AuCl$. No complement reactions: 0 equivalents of complement sequence added to reaction. 1 equivalent of complement: 1 equivalent (10 □M) complement sequence added to reaction. Progress of reactions was determined by fluorescence intensity. All fluorescence values reported in arbitrary units (AU). A standard curve containing various concentrations of BODIPY **3.5** was used to calculate a yield of product (60 μM, 30 μM, 15 μM, 7.5 μM, 3.25 μM, 1.63 μM, and 0.81 μM).

Figure 3.10 Gold catalyzed hydroamination reaction.[30]

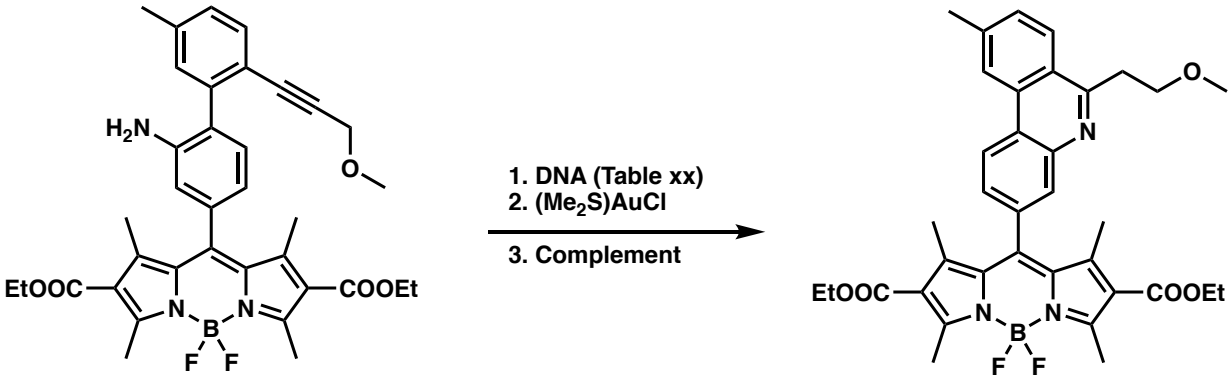

3.4 **3.5**

Table 3.4 Sequences used in catalysis experiments.

Sequence Name	Hairpin (5'-3')
TCH5	CGTTCTGTTTTCAGCACGACATC
cTCH5	GATGTCGTGCTGAAAAC
cTCH5-5s	GATGTCGTGATGAAAAC
cTCH5-5d	GATGTCGGGATGAAAAC
cTCH5-3s	GATGTCGTGCTGAAAAA
cTCH5-3d	GATGTCGTGCTGAAAGA
cTCH5-TMs	GATATCGTGCTGAAAAC
cTCH5-TMd	GAGATCGTGCTGAAAAC

Rc-TCH5	GAUGUCGUGCUGAAAAC
GCH5	CGTGCTGTTTTCAGCACGACATC
TTH5	CGTTCTGTTTTCAGTACGACATC
CCH5	CGTCCTGTTTTCAGCACGACATC
TCH3	CGTTCTGTTTTCAGCACGACA
TCH7	CGTTCTGTTTTCAGCACGACATCAG
cTCH3	TGTCGTGCTGAAAAC
cTCH7	CTGATGTCGTGCTGAAAAC

3.8.4.1 Fluorescence Data

Figure 3.12 Fluorescence intensity of TCH5 with (1 equiv) and without (0 equiv) complement.

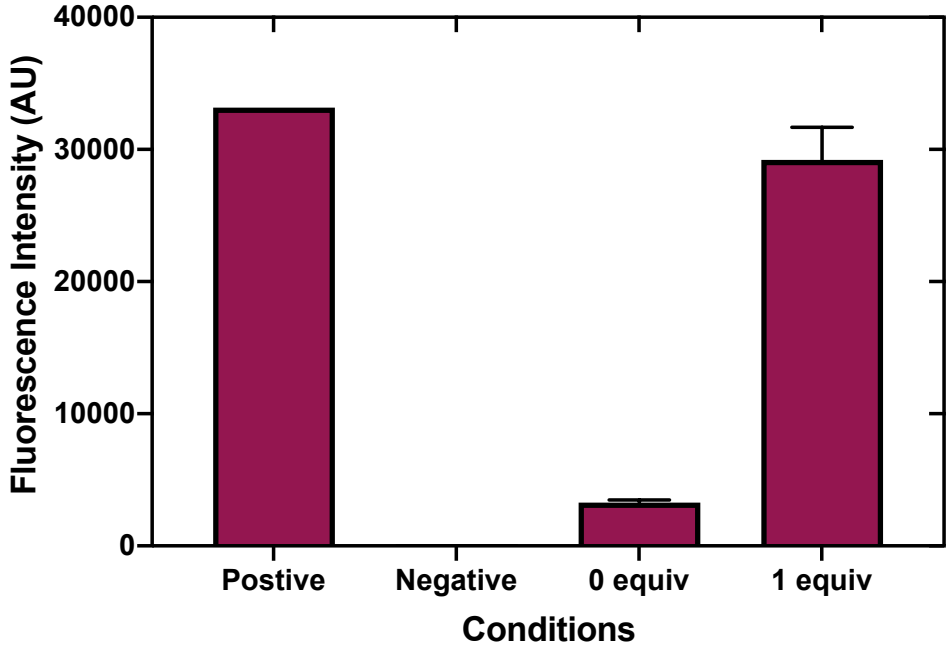

Table 3.5 Fluorescence intensity of TCH5 with (1 equiv) and without (0 equiv) complement.

Conditions	Mean	Std. Dev.
Positive	33160	__
Negative	116	__
0 equivalents	3275	210
1 equivalent	29205	2466

Figure 3.13 Fluorescence intensity with and without complement after background subtraction.

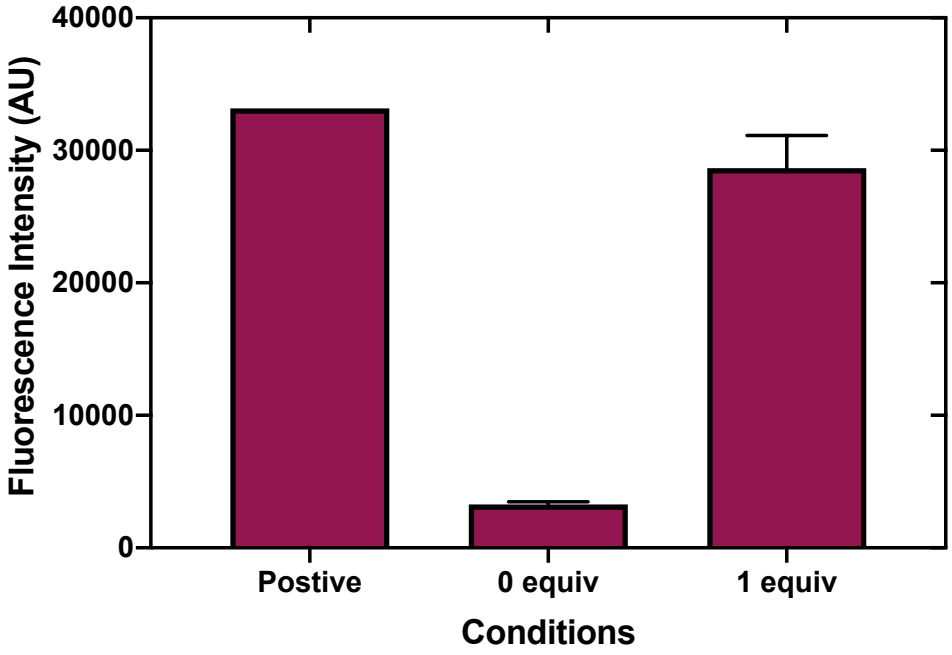

Figure 3.14 Percent yield of standard conditions with no complement and with 1 equivalent of complement.

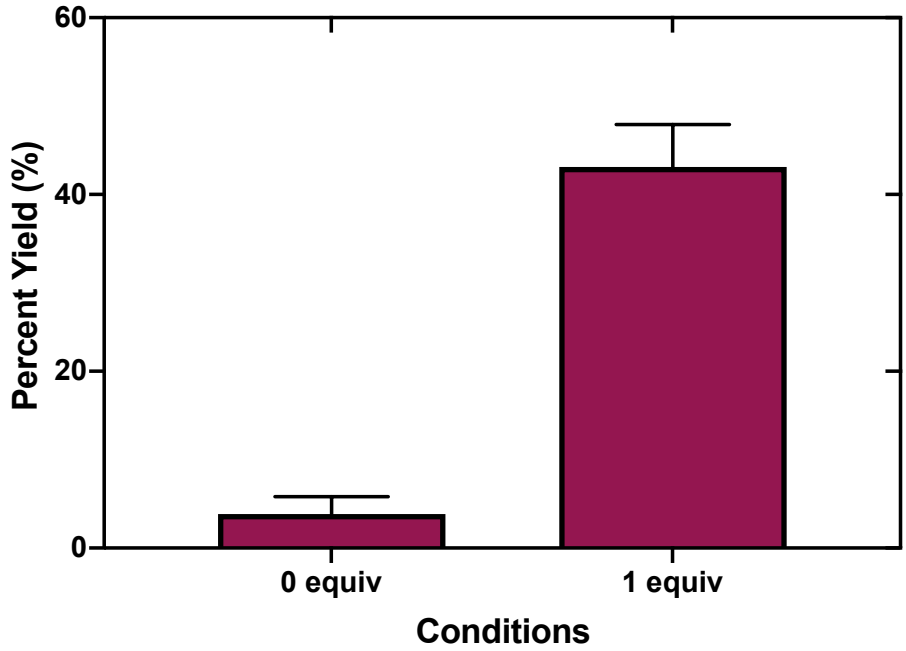

Figure 3.16 Fluorescence intensity of reactions containing TCH5 with matched and mismatched complements background subtracted at 62.5 mM sodium perchlorate condition.

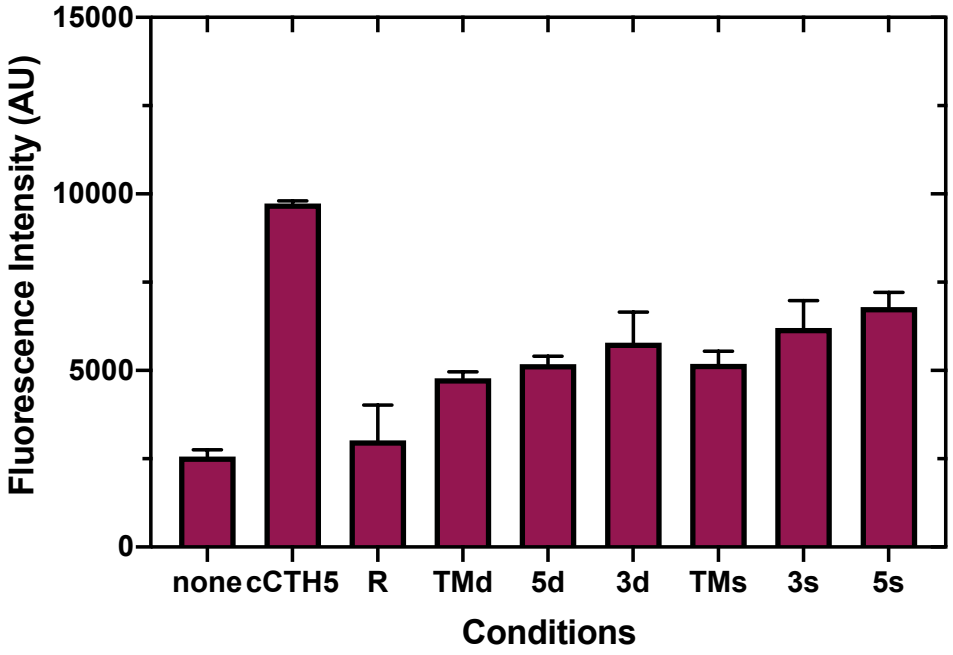

Table 3.6 Fluorescence intensity of reactions containing TCH5 with matched and mismatched complements background subtracted at 62.5 mM sodium perchlorate condition.

Conditions	Mean	Std. Dev.
none	2562	190
cTCH5	9725	81
R	3017	999
cTCH5-TMd	4778	186
cTCH5-5d	5180	220

cTCH5-3d	5787	865
cTCH5-TMs	5190	359
cTCH5-5s	6208	770
cTCH5-3s	6795	416

Figure 3.17 Fold increase in fluorescence o reactions containing f TCH5 with matched and mismatched complements at 62.5 mM sodium perchlorate condition.

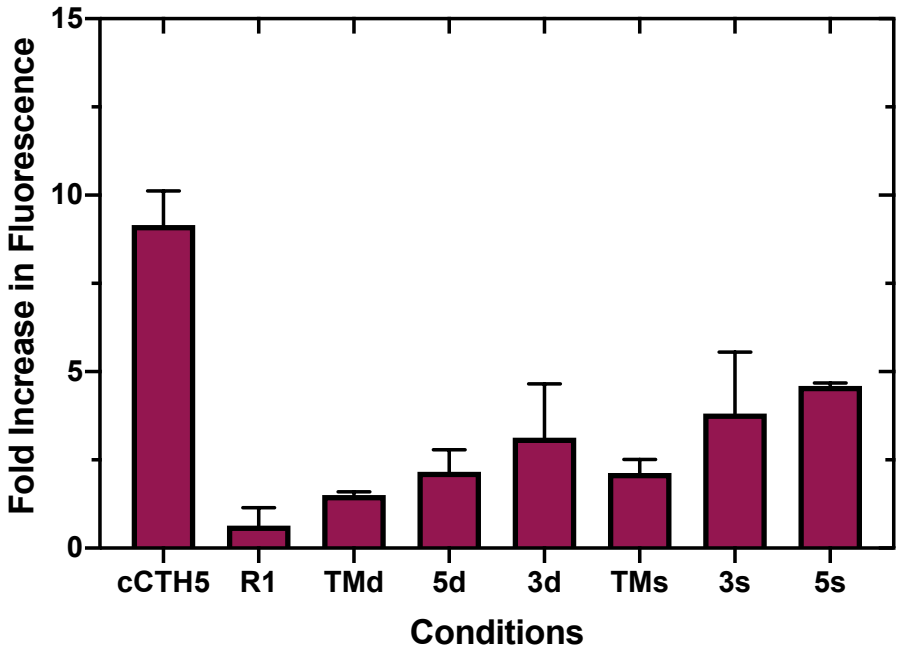

Figure 3.18 Percent yield reactions containing TCH5 with matched and mismatched complements at 62.5 mM sodium perchlorate condition.

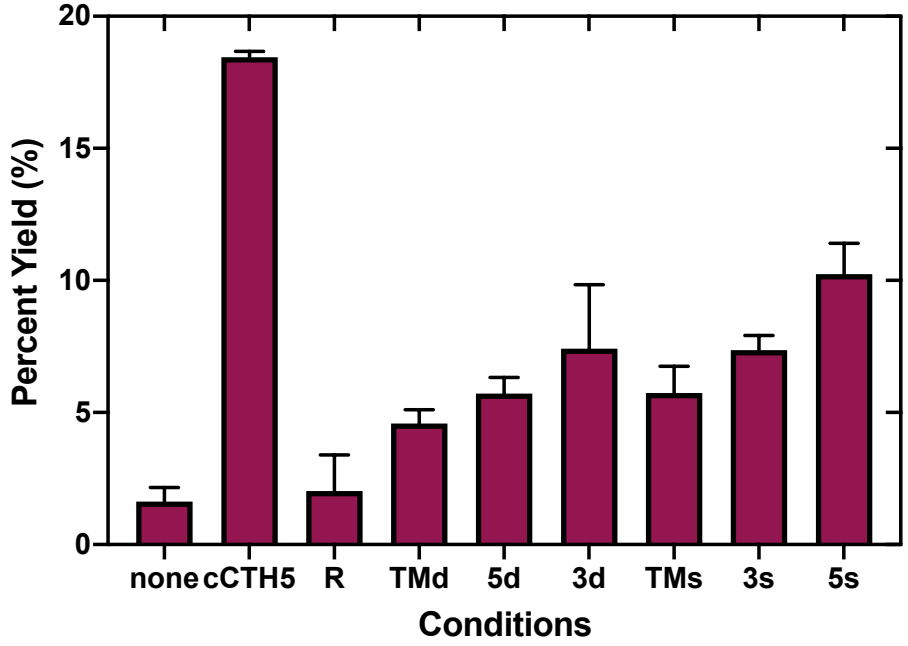

Figure 3.19 Fluorescence intensity of reactions containing TCH5 with matched and mismatched complements background subtracted at 250 mM sodium perchlorate condition.

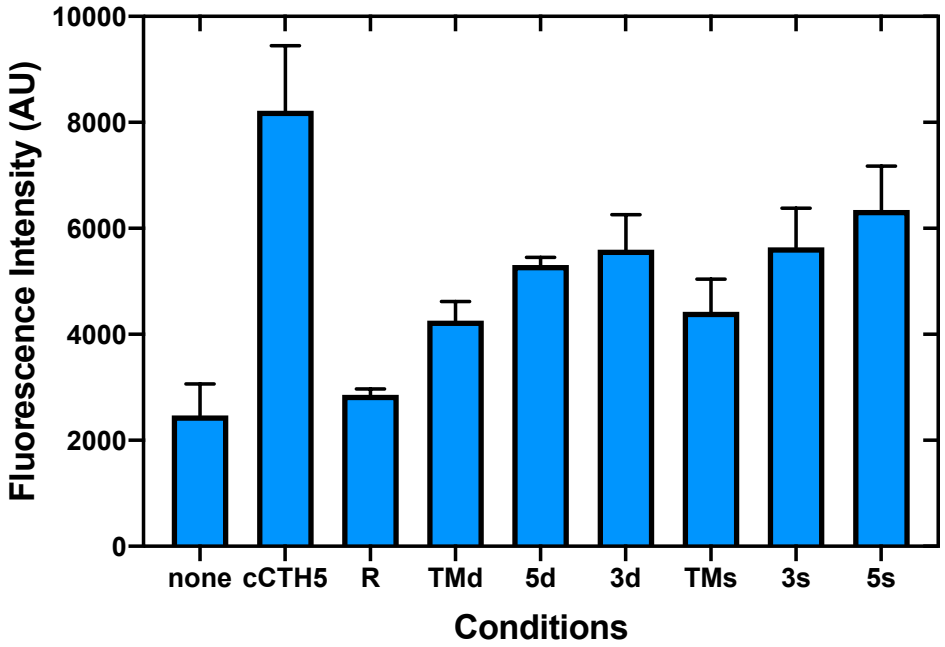

Table 3.7 Fluorescence intensity of reactions containing TCH5 with matched and mismatched complements background subtracted at 250 mM sodium perchlorate condition.

Conditions	Mean	Std. Dev.
none	2469	594
cTCH5	8221	1229
R	2860	107
cTCH5-TMd	4260	357
cTCH5-5d	5308	145
cTCH5-3d	5599	659
cTCH5-TMs	4424	620
cTCH5-5s	5642	740
cTCH5-3s	6347	827

Figure 3.20 Fold increase in fluorescence of reactions containing TCH5 with matched and mismatched complements background subtracted at 250 mM sodium perchlorate condition.

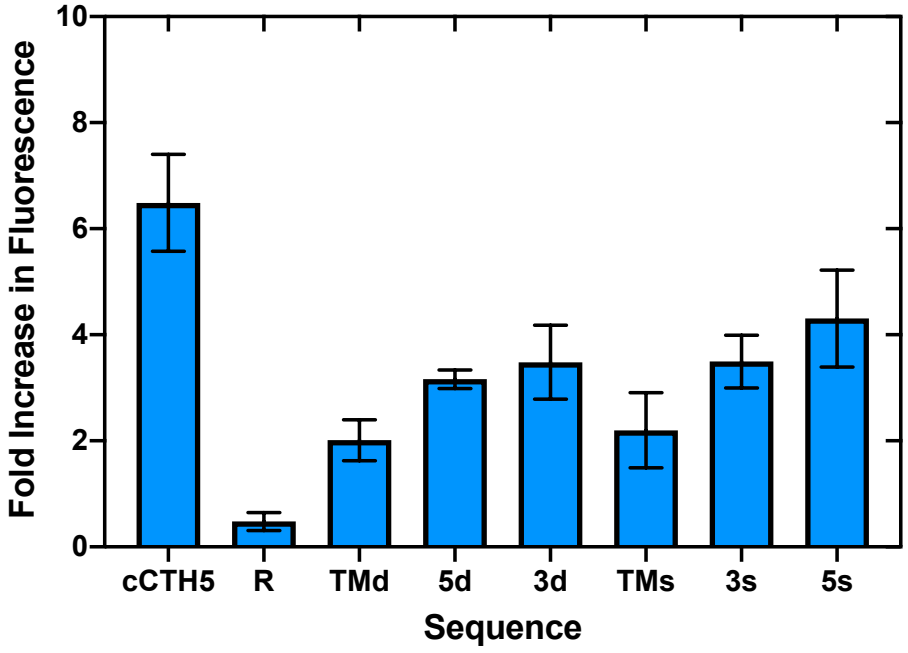

Figure 3.21 Percent yield of reactions containing TCH5 with matched and mismatched complements background subtracted at 250 mM sodium perchlorate condition.

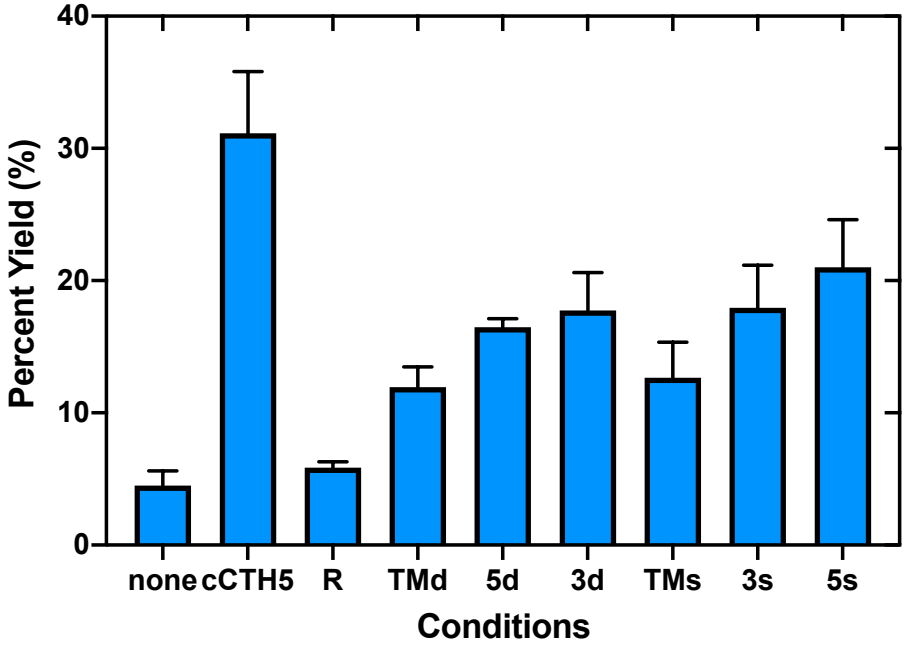

Figure 3.22 Fluorescence intensity of reactions containing TCH5 with and without DNA and RNA complement at 62.5 mM sodium perchlorate condition.

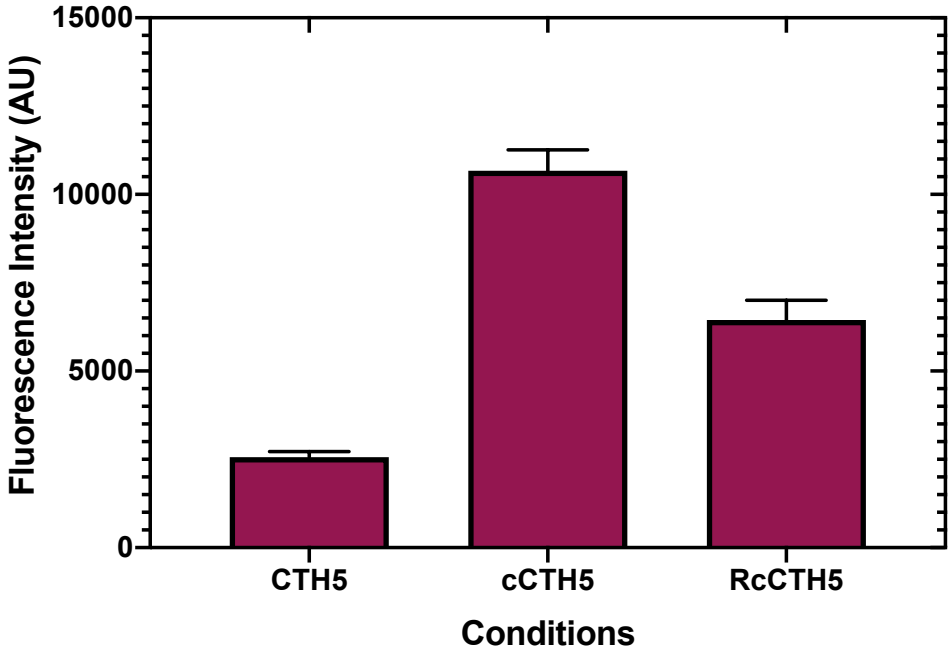

Table 3.8 Fluorescence intensity of reactions containing TCH5 with and without DNA and RNA complement at 62.5 mM sodium perchlorate condition.

Conditions	Mean	Std. Dev.
CTH5	2562	155
cCtH5	10670	590
RcCTH5	6446	556

Figure 3.23 **Fold** increase in fluorescence of reactions containing TCH5 with and without DNA and RNA complement at 62.5 mM sodium perchlorate condition.

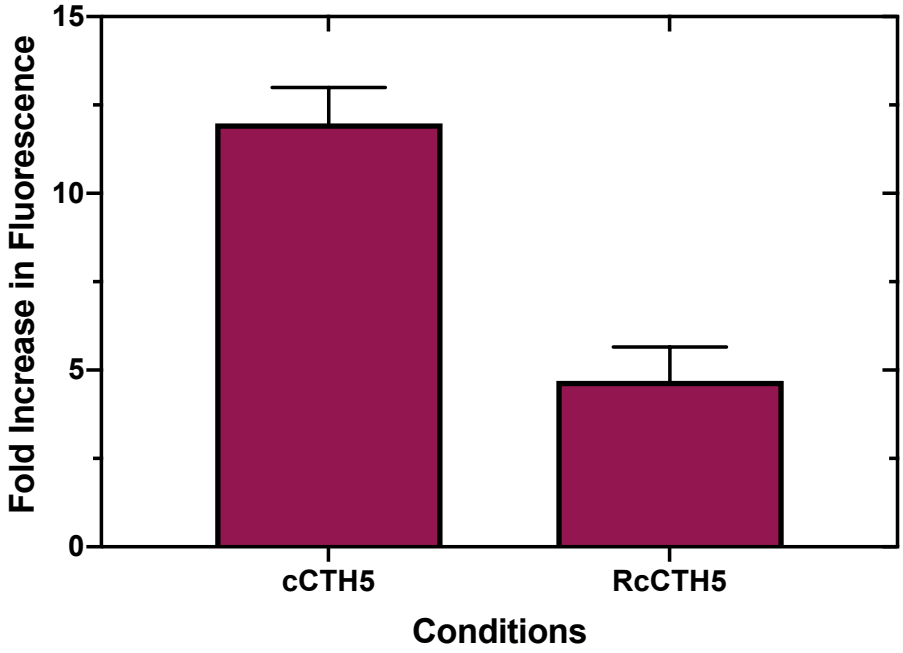

Figure 3.24 Percent yield of reactions containing TCH5 with and without DNA and RNA complement at 62.5 mM sodium perchlorate condition.

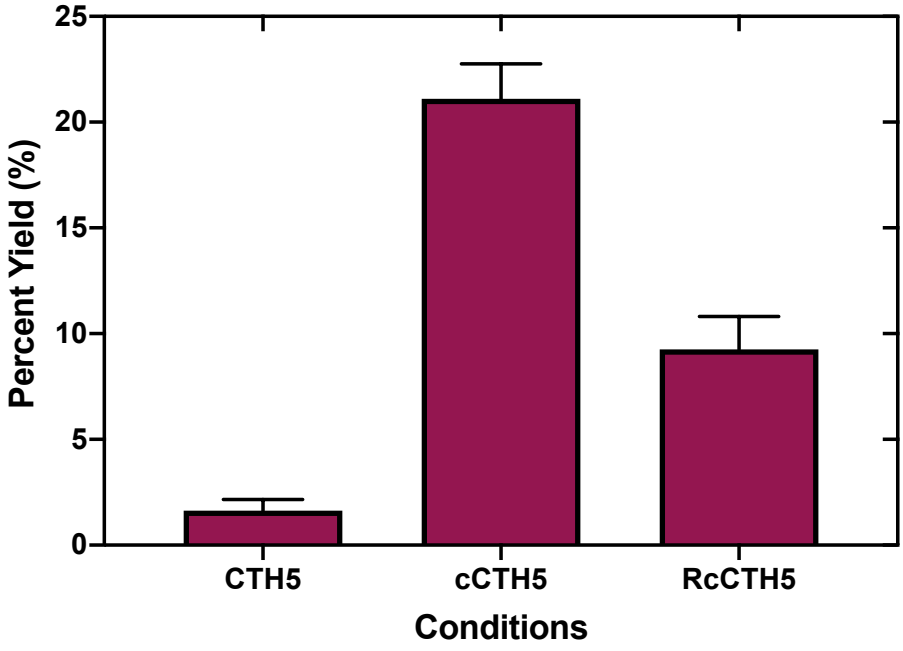

Figure 3.25 Fluorescence intensity of reactions containing TCH5 with and without DNA and RNA complement at 250 mM sodium perchlorate condition.

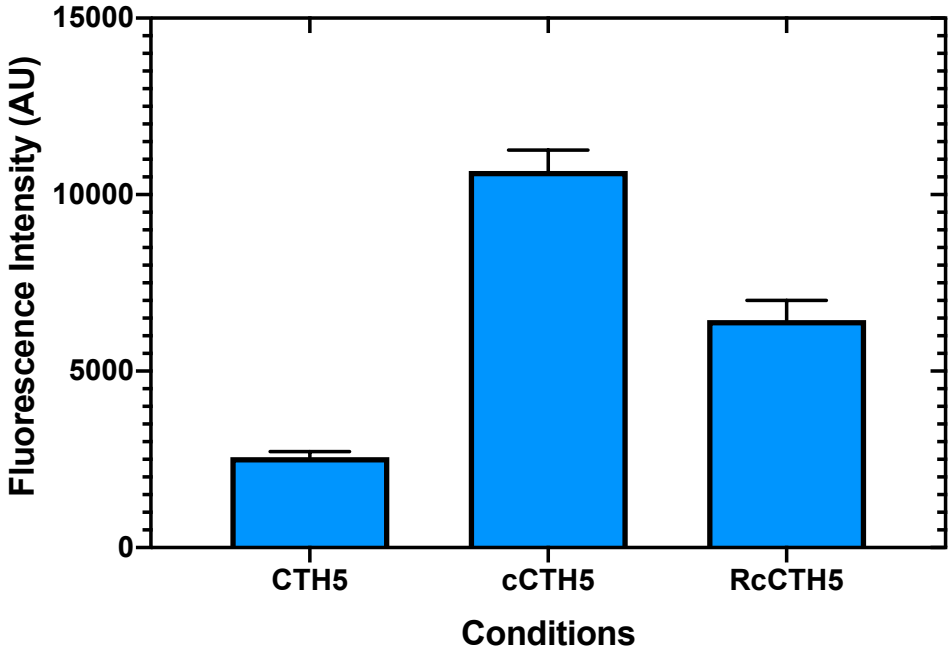

Table 3.9 Fluorescence intensity of reactions containing TCH5 with and without DNA and RNA complement at 250 mM sodium perchlorate condition.

Conditions	Mean	Std. Dev.
CTH5	2469	485
cCtH5	8221	921
RcCTH5	6153	971

Figure 3.26 Fold increase in fluorescence of reactions containing TCH5 with and without DNA and RNA complement at 250 mM sodium perchlorate condition.

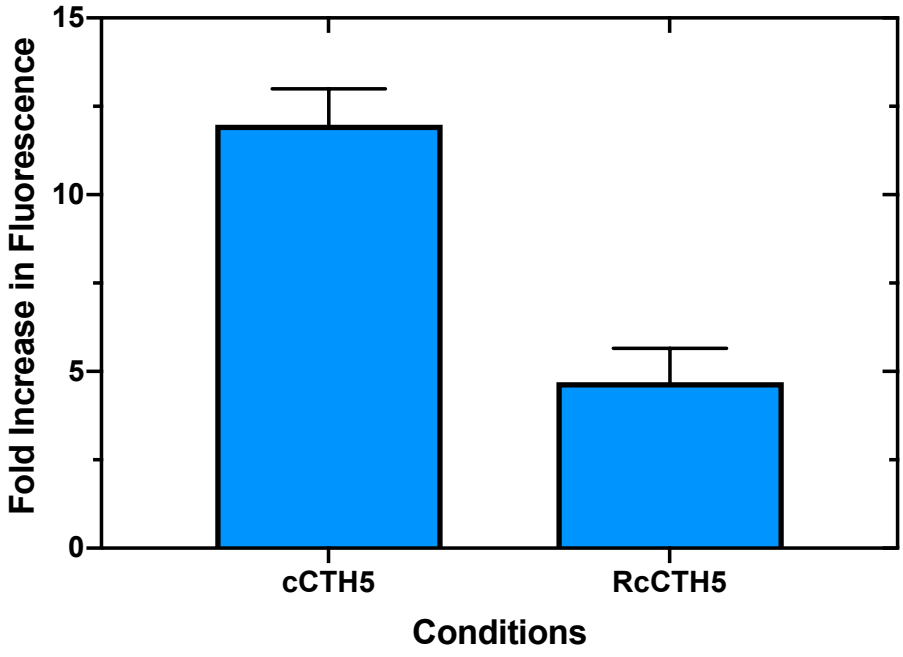

Figure 3.27 Percent yield of reactions containing TCH5 with and without DNA and RNA complement at 250 mM sodium perchlorate condition.

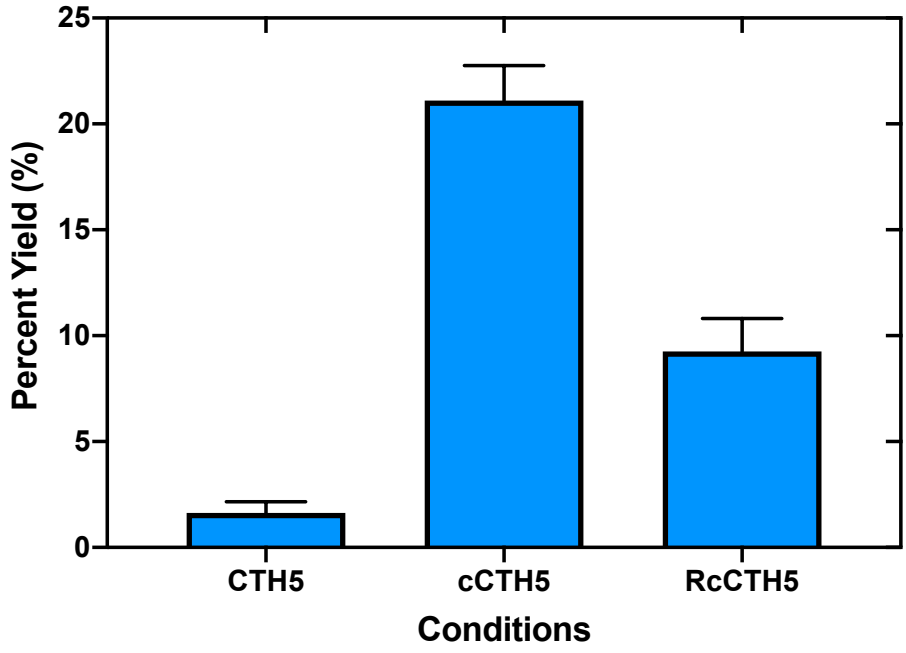

Figure 3.28 Fluorescence intensity of TCH5, CCH5, and TTH5 with and without 1 equivalent of complement.

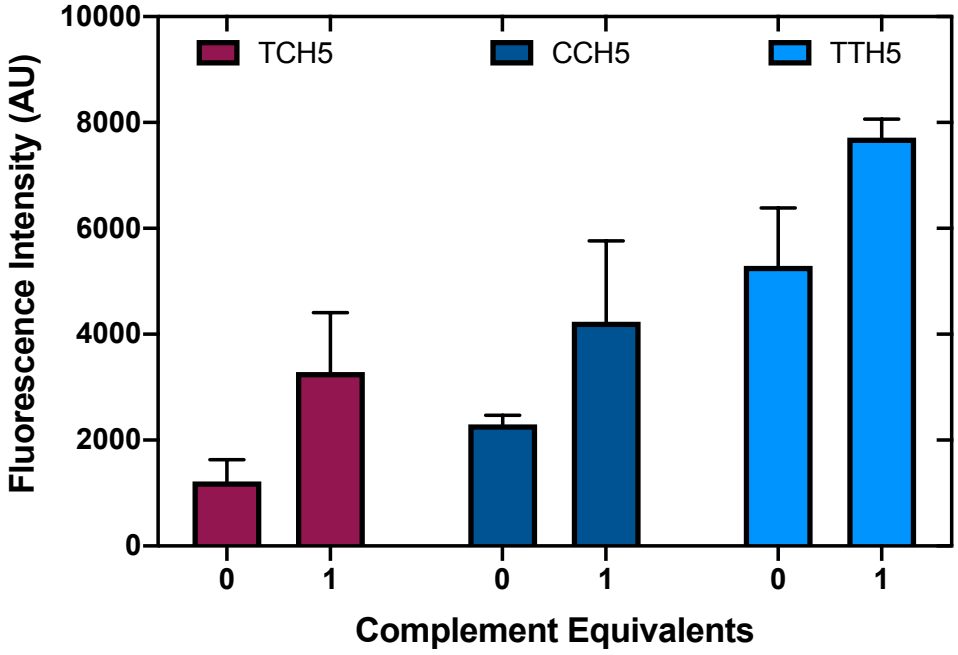

Table 3.10 Fluorescence intensity of TCH5, CCH5, and TTH5 with and without 1 equivalent of complement.

Hairpin	Complement Equiv.	Mean	Std. Dev.
TCH5	0	1220	413
TCH5	1	3289	1118
CCH5	0	2298	174
CCH5	1	4236	1529
TTH5	0	5291	1097
TTH5	1	7716	347

Figure 3.29 Fluorescence intensity of TCH3, TCH5, and TCH7 with and without 1 equivalent of complement.

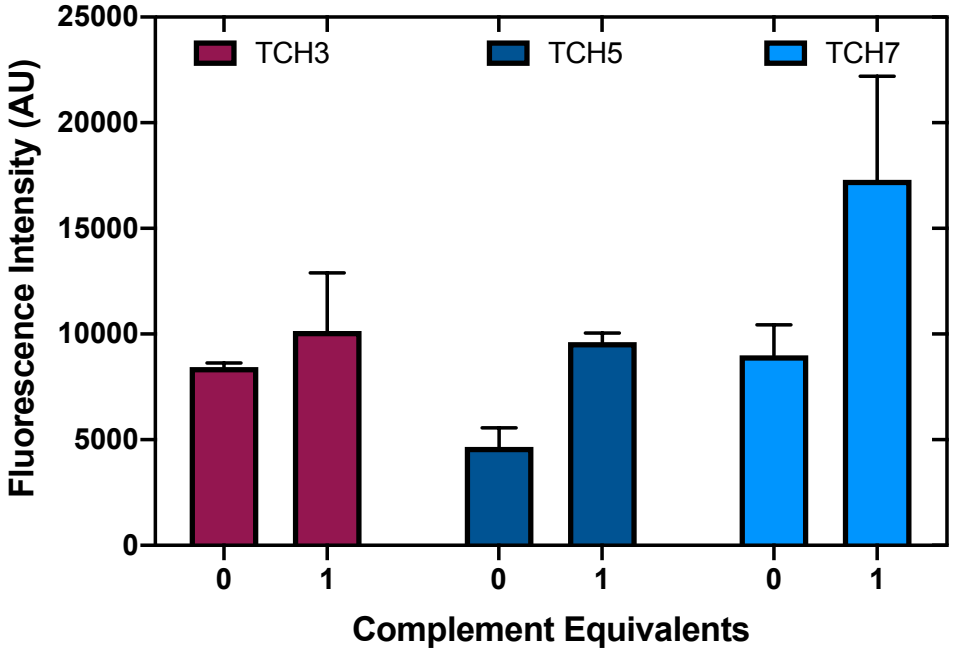

Table 3.11 Fluorescence intensity of TCH3, TCH5, and TCH7 with and without 1 equivalent of complement.

Hairpin	Complement Equiv.	Mean	Std. Dev.
TCH3	0	8439	199
TCH3	1	10148	2753
TCH5	0	4661	897
TCH5	1	9614	437
TCH7	0	8992	1441

TCH5	1	17301	4896

Figure 3.30 Fluorescence intensity of reactions containing TCH5 mixed with different gold precursors with and without 1 equivalent of complement.

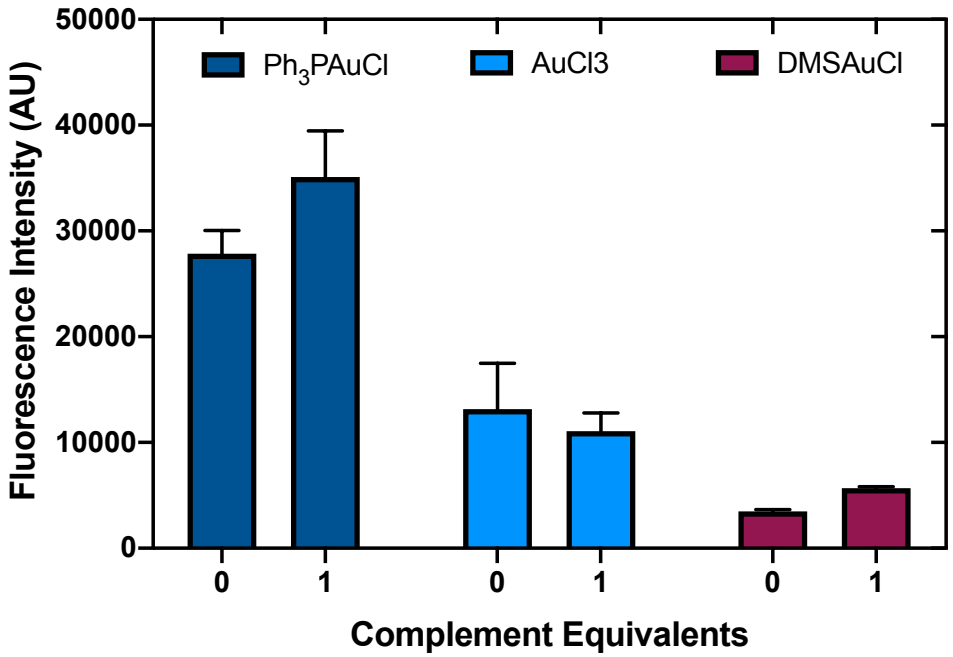

Table 3.12 Fluorescence intensity of reactions containing TCH5 mixed with different gold precursors with and without 1 equivalent of complement.

Au Precursor	Complement Equiv.	Mean	Std. Dev.
DMSAuCl	0	3477	183
DMSAuCl	1	5673	134
PPh_3AuCl	0	27849	2194

PPh_3AuCl	1	35099	4371
$AuCl_3$	0	13153	4343
$AuCl_3$	1	11061	1742

Figure 3.31 Fluorescence intensity of reaction containing GCH5 and TCH5 with and without 1 equivalent of complement.

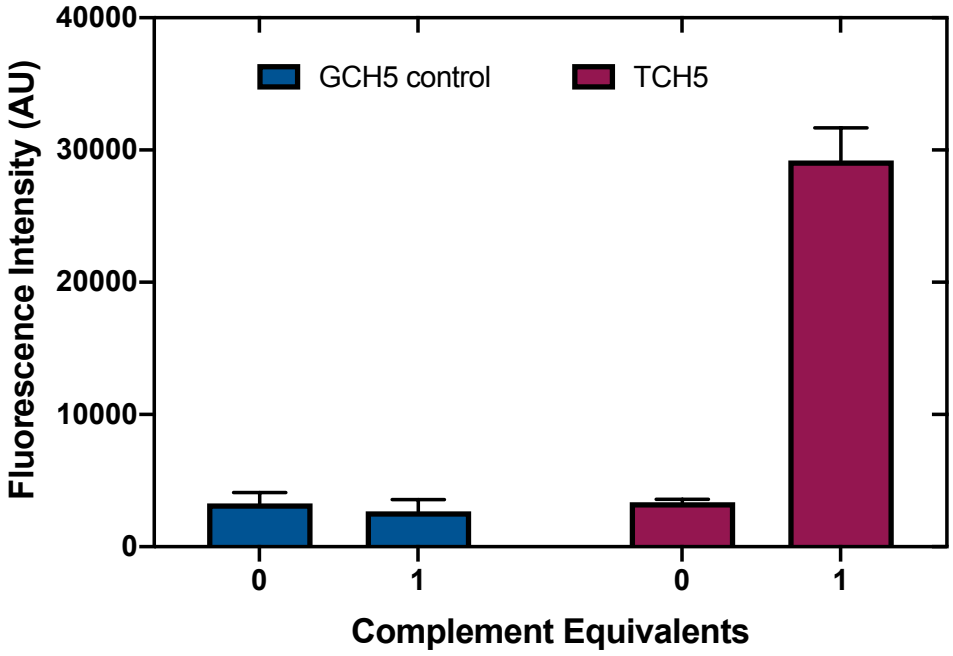

Figure 3.32 Fluorescence intensity of just (Me_2S)AuCl, TCH5, and TCH5 with complement all with one equivalent of R1 added to standard reaction conditions.

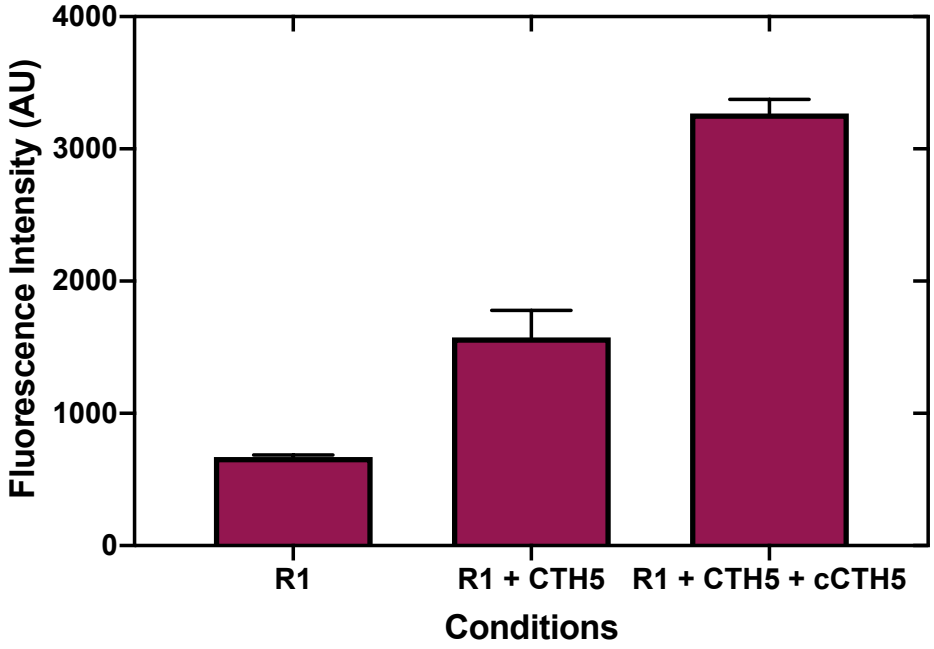

Table 3.13 Fluorescence intensity of just (Me_2S)AuCl, TCH5, and TCH5 with complement all with one equivalent of R1 added to standard reaction conditions.

Condition	Mean	Std. Dev.
R1	669	17
R1 + CTH5	1574	205
R1 + CTH5 + cCTH5	3269	105

Preparation of experiments containing biologically relevant fluids

Solutions contain 10 μM DNA hairpin, 10 μM complement sequence, and 62.5 mM $NaClO_4$ and 40 μM BODIPY **7** with 10 uM R1, or 30 % solutions of synthetic saliva (Artificial Saliva for Medical and Dental Research purchased through Pickering Laboratories) or synthetic urine (300 mM urea, 60 mM KCl, 128 mM NaCl, 30 mM Na_3PO_4, 15 mM creatine, and 1 μM albumin powder).

Figure 3.33 Fluorescence intensity of reactions containing TCH5 with and without complement under urine conditions.

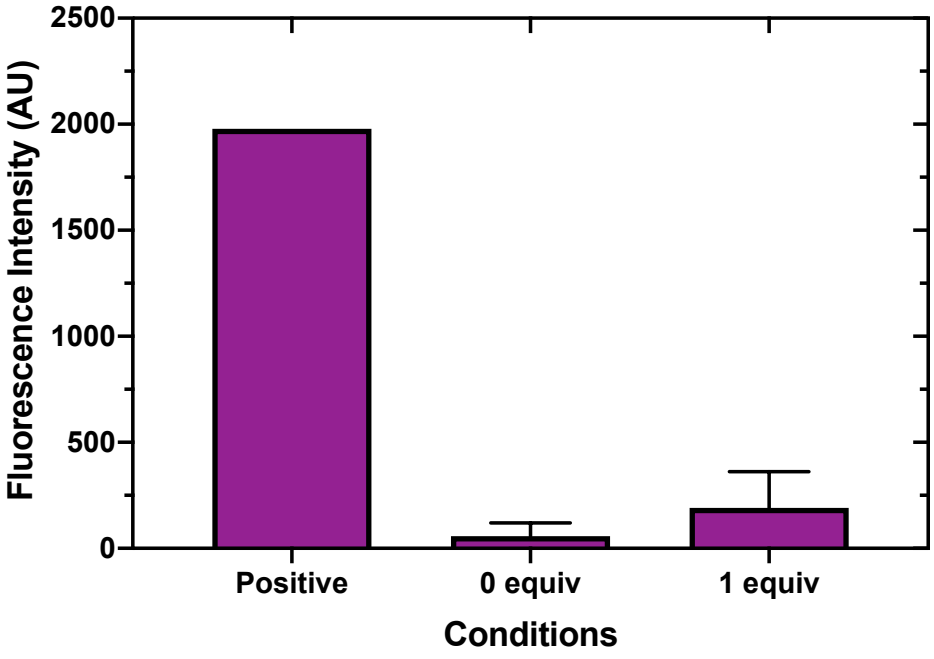

Table 3.14 Fluorescence intensity of reactions containing TCH5 with and without complement under urine conditions.

Condition	Mean	Std. Dev.
Positive	1979	__
0 equiv complement	57	63
1 equiv complement	191	171

Figure 3.34 Fluorescence intensity of reactions containing TCH5 with and without complement under saliva conditions.

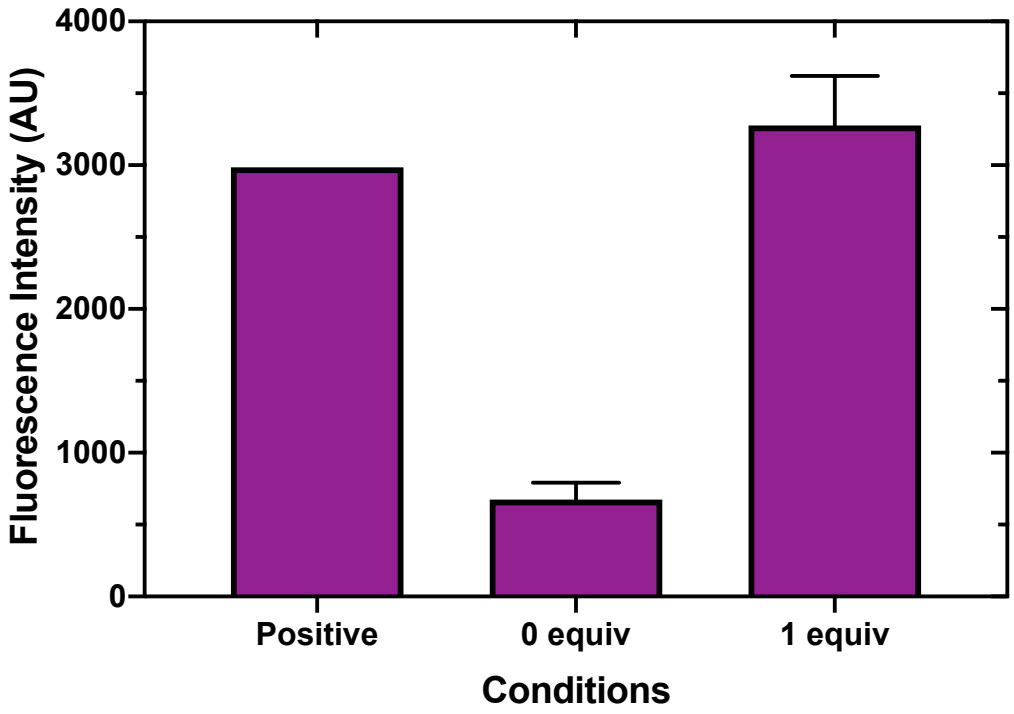

Table 3.15 Fluorescence intensity of reactions containing TCH5 with and without complement under saliva conditions.

Condition	Mean	Std. Dev.
Positive	2986	__
0 equiv complement	676	117
1 equiv complement	3278	344

3.8.5 Synthesis

Preparation of BODIPY (3.2)

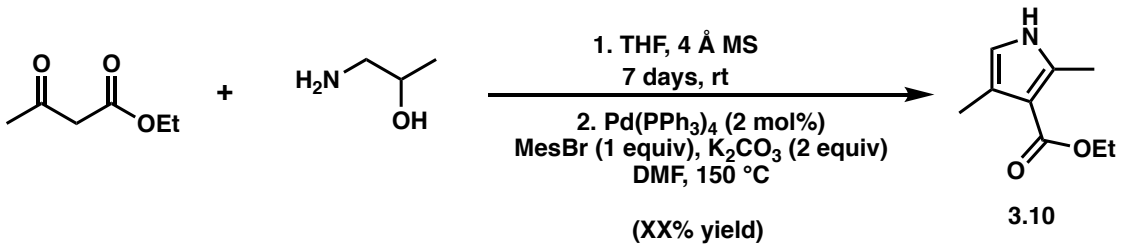

3,5-dimethyl-4-(ethoxycarbonyl)pyrrole (3.11): Synthesized according to reported literature. Purified by flash chromatography to obtain 3.10 as a yellow oil in 75% yield of product over two steps. NMR spectra match those reported in literature[31].

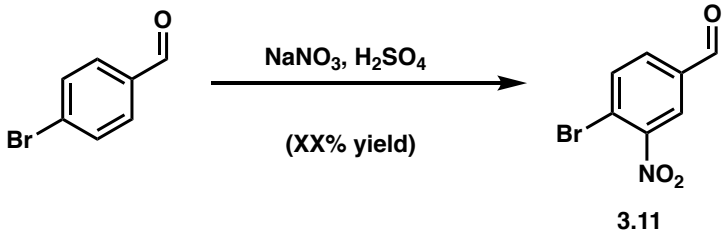

4-bromo-3-nitrobenzaldehyde (3.12): Synthesized from 4-bromobenzaldehyde according to reported literature. Purified by recrystallization in ethanol to obtain 87% yield of product. NMR spectra match those reported in literature[32].

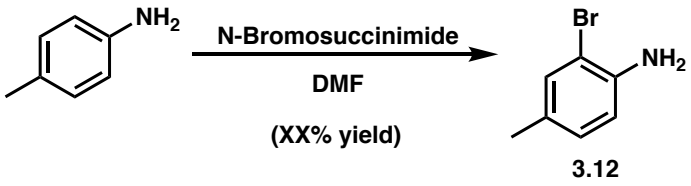

2-bromo-4-methylaniline (3.13): Synthesized from 4-methylaniline according to reported literature. Purified by flash chromatography in 3:1 Hexanes:EtOAc to obtain 58% yield of a yellow oil. NMR spectra match those reported in literature[33].

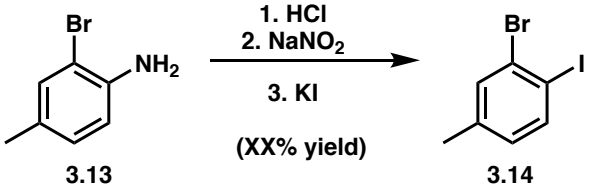

2-bromo-4-methyl-iodobenzene (3.14): Synthesized according to reported literature. Purified by flash chromatography in 20:1 Hexanes:EtOAc to obtain 78% yield of product NMR spectra match those reported in literature[4].

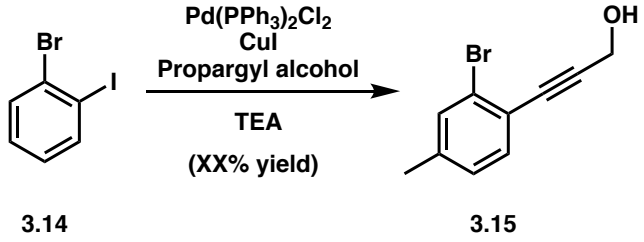

3-(2-bromo-4-methylphenyl)prop-2-yn-1-ol (3.15): Synthesized from 2-bromo-4-methyliodobenzene according to reported literature. Purified by flash chromatography in 1:1 Hexanes: DCM with 0-10% EtOAc to obtain 85% yield of product. NMR spectra match those reported in literature[1].

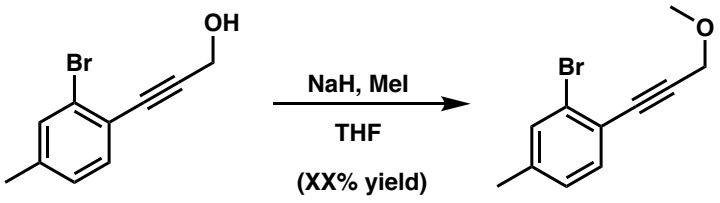

3.15 3.16

2-bromo-1-(3-methoxyprop-1-ynyl)-4-methylbenzene (3.16): Synthesized from 3-(2-bromo-4-methylphenyl)prop-2-yn-1-ol according to reported literature. Purified by flash chromatography in 5:1 Hexanes:EtOAc to obtain 92% yield of product NMR spectra match those reported in literature[1].

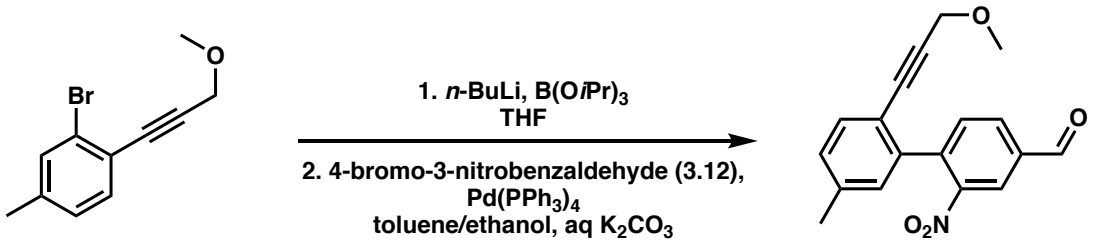

3.16 3.17

2'-(3-methoxyprop-1-yn-1-yl)-5'-methyl-2-nitro-[1,1'-biphenyl]-4-carbaldehyde (3.17): Synthesized from 4-bromobenzaldehyde according to reported literature. Purified by column chromatography to obtain 52% yield over two steps. NMR spectra match those reported in literature[1].

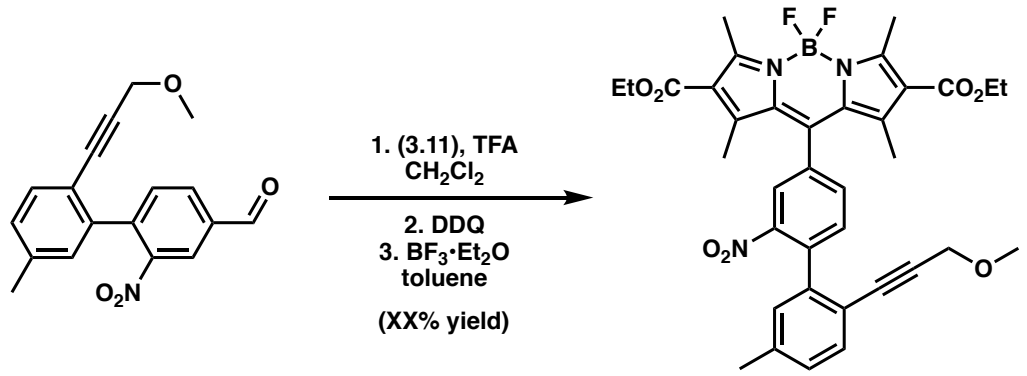

3.17 3.18

2,8-bis(ethoxycarbonyl)-5,5-difluoro-10-(2'-(3-methoxyprop-1-yn-1-yl)-5'-methyl-2-nitro-[1,1'-biphenyl]-4-yl)-1,3,7,9-tetramethyl-5H-dipyrrolo[1,2-c:2',1'-f][1,3,2]diazaborinin-4-ium-5-uide (3.18): Synthesized according to reported literature. Purified by flash chromatography in 1:1 Hexanes:DCM with 3% EtOAc to obtain 45% yield of product NMR spectra match those reported in literature[1].

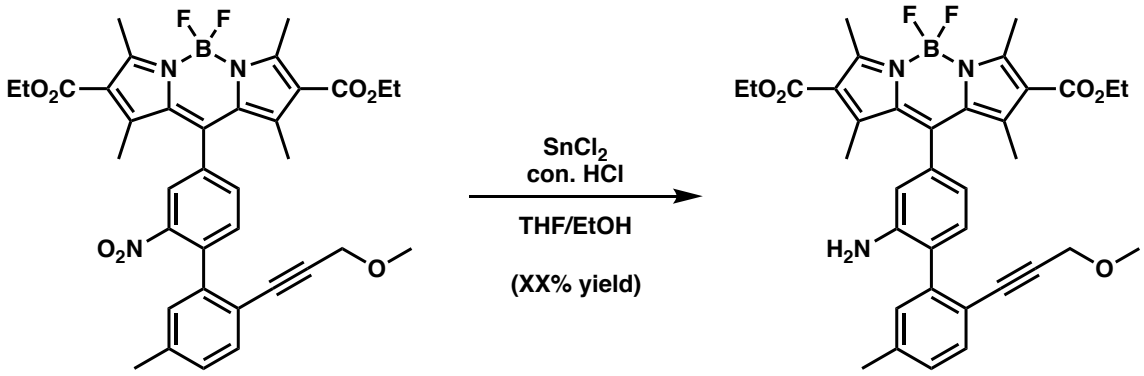

3.18 3.19

2,8-bis(ethoxycarbonyl)-5,5-difluoro-10-(6-)2-methoxyehtyl)-9-methylphenanthridin-3-yl)-1,3,7,9-tetramethyl-5H-dipyrrolo[1,2-c:2',1'-f][1,3,2]diazaborninin-4-ium-5-uide (3.19): Synthesized according to reported literature. Purified by flash chromatography in 1:1 Hexanes: DCM with 2% EtOAc to obtain 34% yield of product NMR spectra match those reported in literature[1].

3.9 Spectra Relevant to Chapter Two:

Regulating Transition Metal Catalysis Through Interference by Short RNAs

Adapted From: Sydnee A. Green, Hayden R. Montgomery, Tyler Benton, Neil J. Chan, Hosea M. Nelson, *Angew., Chem. Int. Ed*, **2019**, *58*, 16400–16404

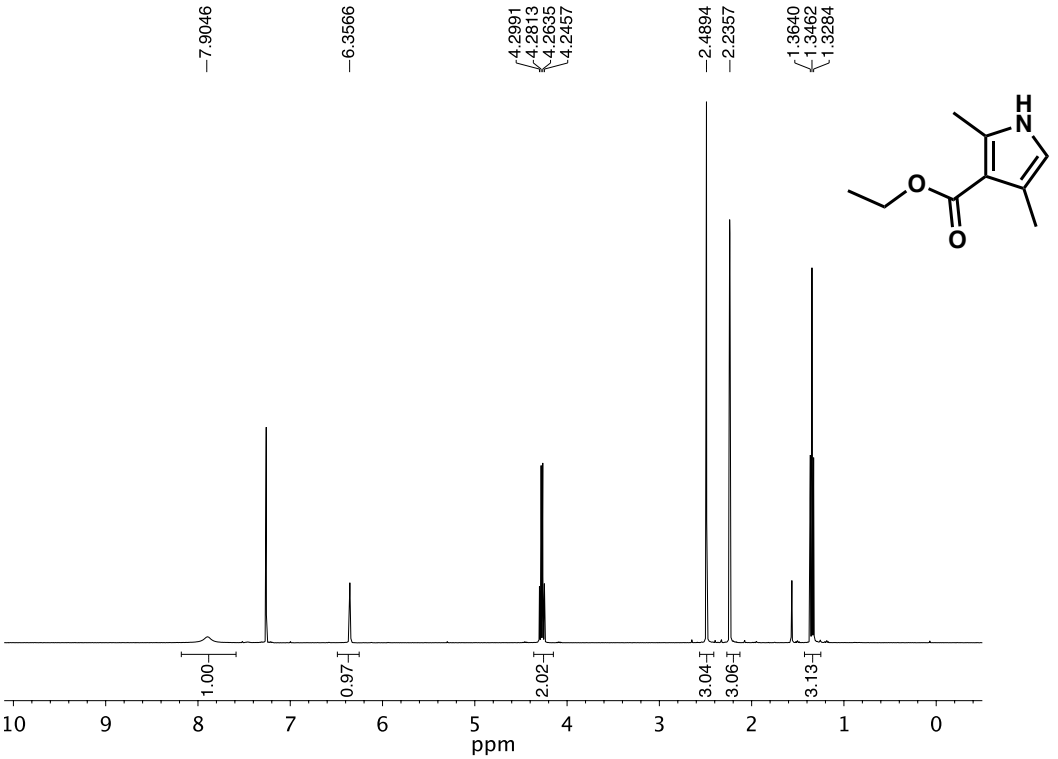

Figure 3.35 [1]H NMR (400 MHz, CDCl3) of compound **3.11**.

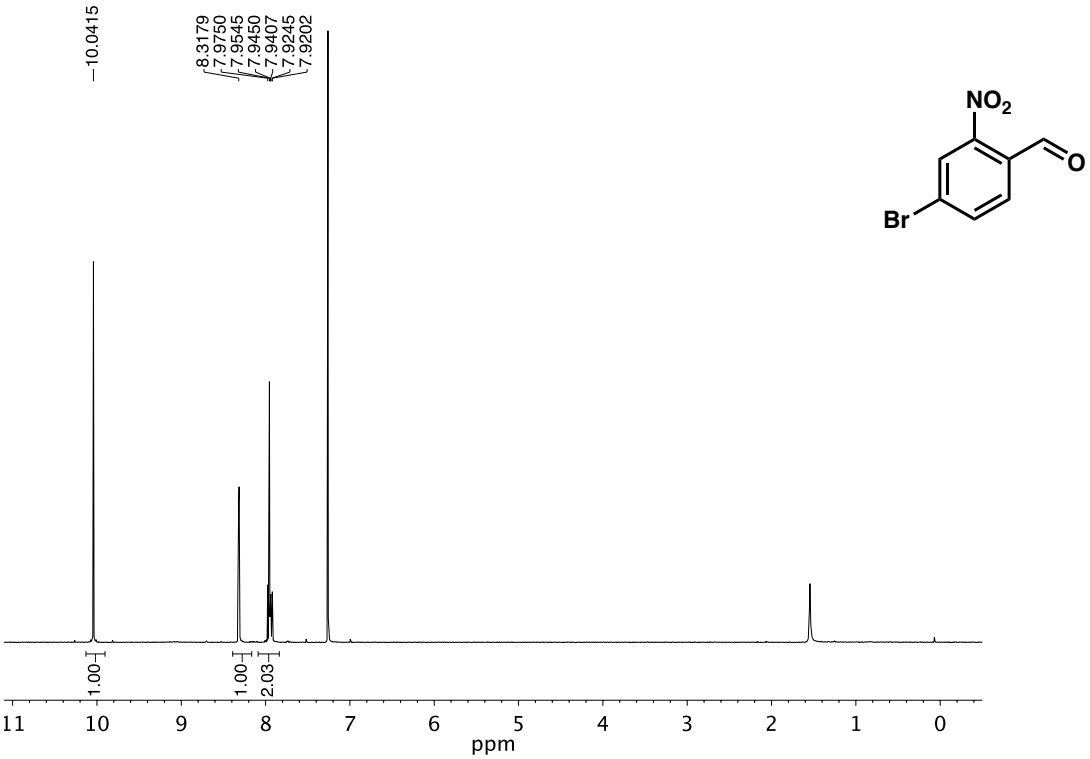

Figure 3.36 [1]H NMR (400 MHz, CDCl3) of compound **3.12**.

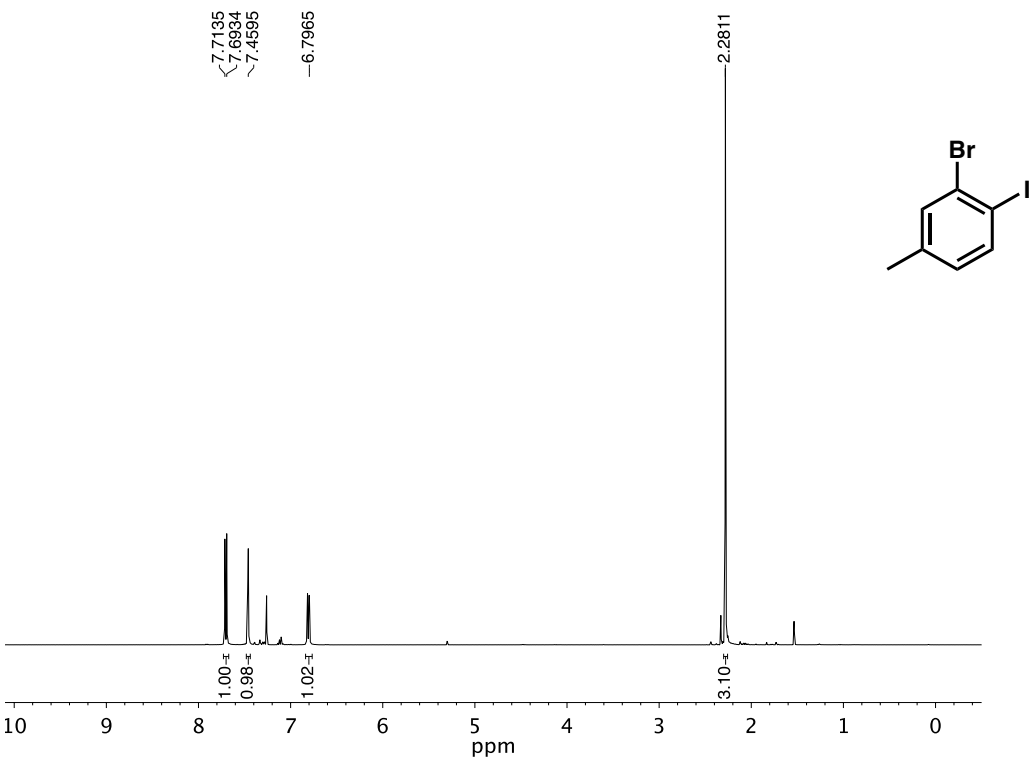

Figure 3.37 [1]H NMR (400 MHz, CDCl3) of compound **3.14**.

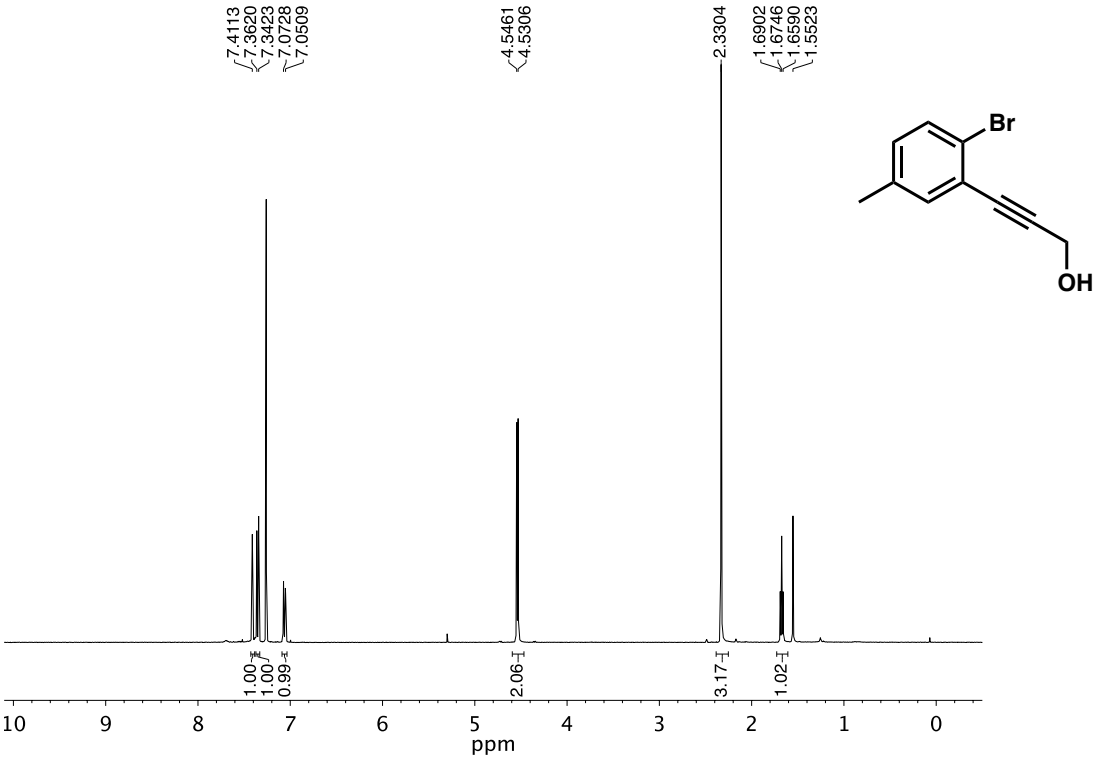

Figure 3.38 [1]H NMR (400 MHz, CDCl3) of compound **3.15**.

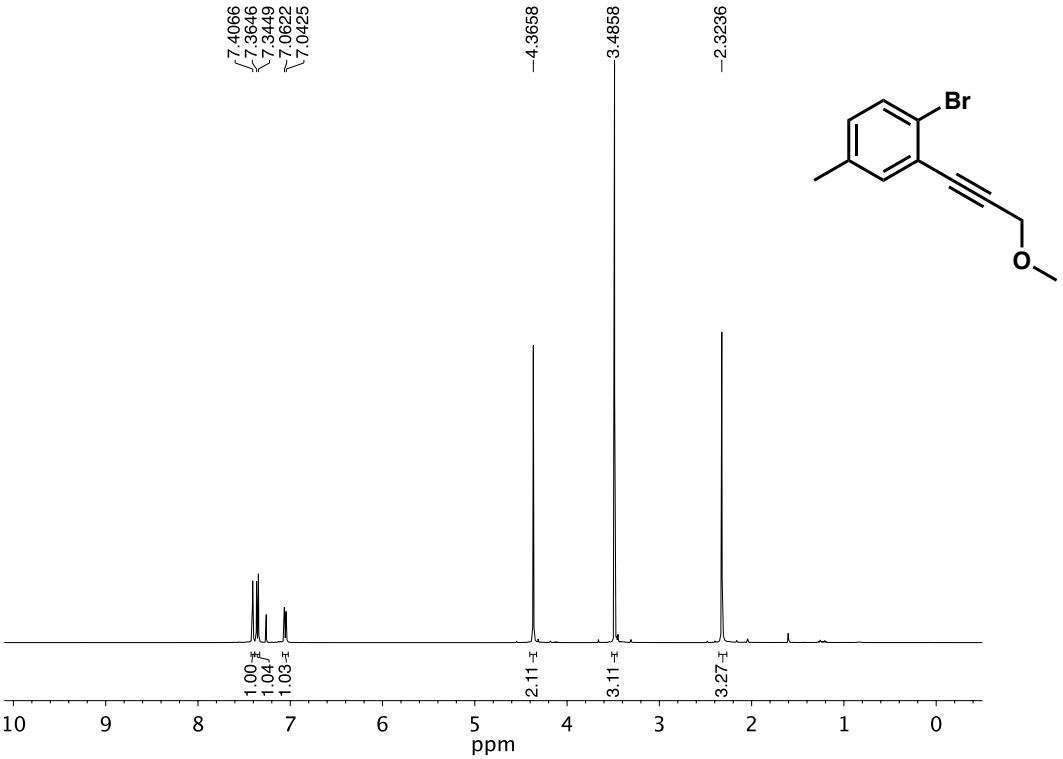

Figure 3.39 [1]H NMR (400 MHz, CDCl3) of compound **3.16**.

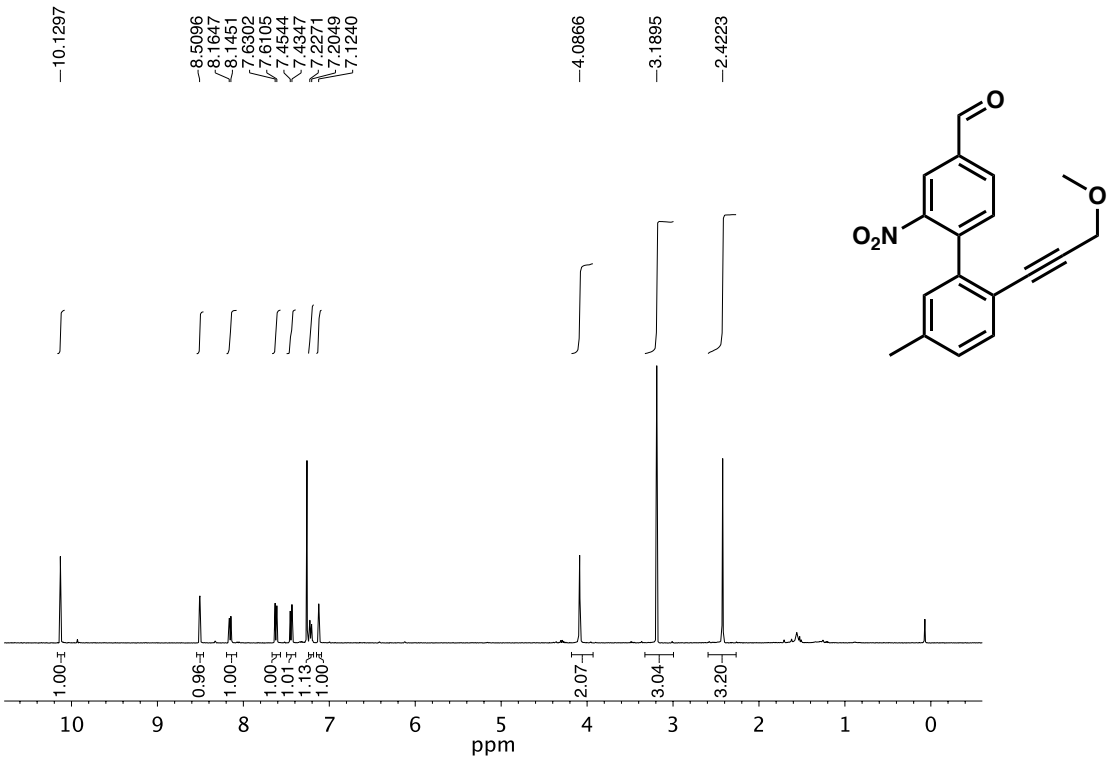

Figure 3.40 [1]H NMR (400 MHz, CDCl3) of compound **3.17**.

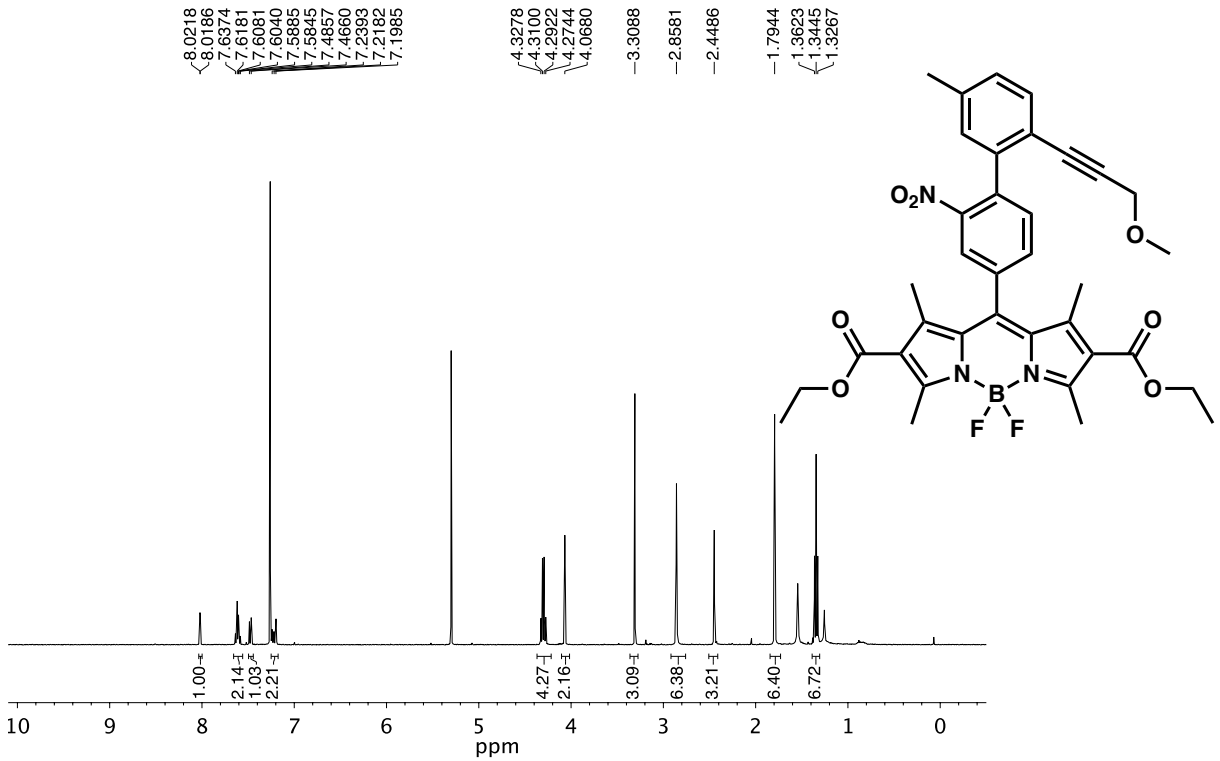

Figure 3.41 [1]H NMR (400 MHz, CDCl3) of compound **3.18**.

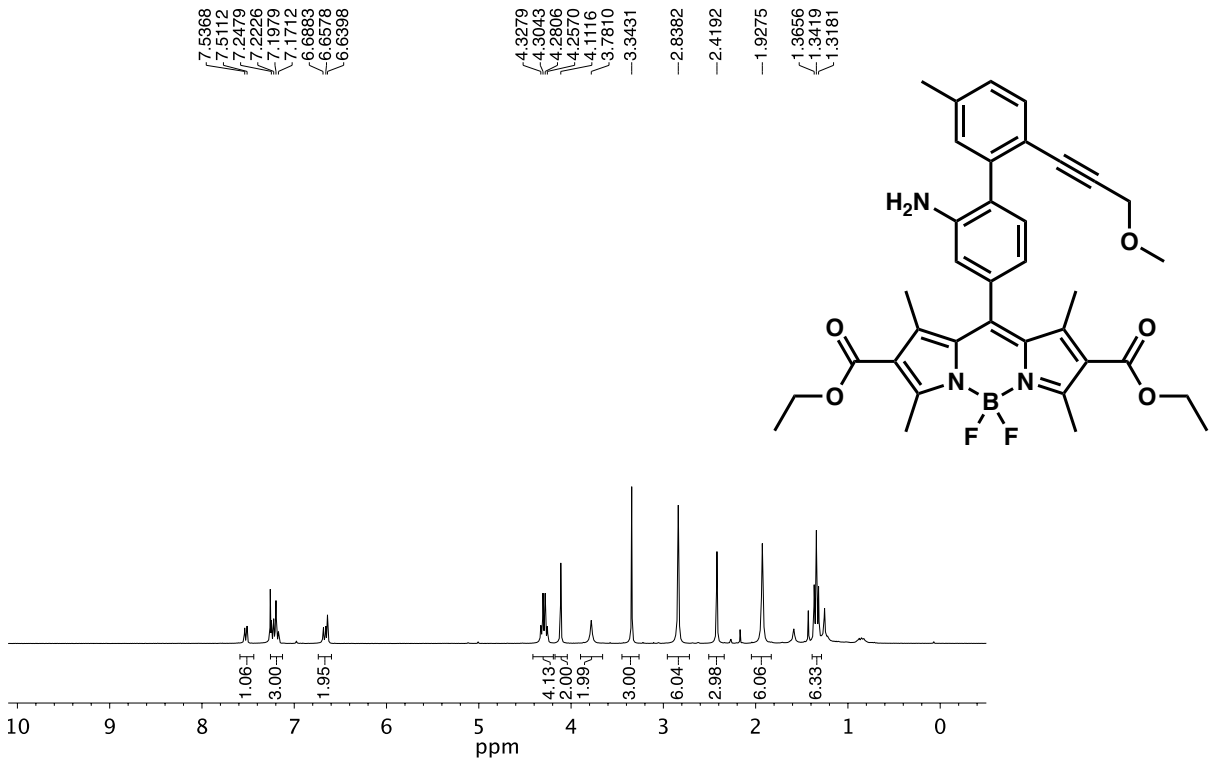

Figure 3.42 [1]H NMR (400 MHz, CDCl3) of compound **3.19**

3.10 Notes and References

(1) T. Hudlicky, J. W. Reed. Applications of biotransformations and biocatalysis to complexity generation in organic synthesis. *Chem. Soc. Rev.* **2009***, 38*, 3117–3132.

(2) K. M. Koeller, C. H. Wong. Enzymes for chemical synthesis. *Nature* **2001**, *409*, 232–240.

(3) F. C. Huang L. F Lee, R. S. Mittal, P. R. Ravikumar, J. A. Chan, C. J. Sih, E. Caspi, C. R. Eck. Preparation of (R)- and (S)-mevalonic acids. *J. Am. Chem. Soc.* **1975**, *97*, 4144–4145.

(4) G. M. Whitesides, C.-H. Wong. Enzymes as catalysts in synthetic organic chemistry. *Angew. Chem., Int. Ed.* **1985**, *24*, 617–718.

(5) W.-D. Fessner, C. Walter. "Artificial metabolisms" for the asymmetric one-pot synthesis of branched-chain saccharides. *Angew. Chem., Int. Ed.* **1992**, *31*, 614–616.

(6) J. H. Schrittwieser, S. Vilkogne, H. Hall, W. Kroutil. Artificial biocatalytic linear cascades for preparation of organic molecules. *Chem. Rev.* **2018**, *118*, 270–348.

(7) M. D. Mihovilovic, G. Chen, S. Wang, B. Kyte, F. Rochon, M. M. Kayser, J. D. Stewart. Asymmetric Baeyer−Villiger Oxidations of 4-Mono- and 4,4-disubstituted cyclohexanones by whole cells of engineered Escherichia coli. *J. Org. Chem.* **2001**, *66*, 733–73.

(8) J. Wachtmeister, D. Rother. Recent advances in whole cell biocatalysis techniques bridging from investigative to industrial scale. *Curr. Opin. Biotechnol.* **2016**, *42*, 169–177.

(9) M. Jeschek, R. Reuter, T. Heinisch, C. Trindler, J. Klehr, S. Panke, T. R. Ward. Directed evolution of artificial metalloenzymes for in vivo metathesis. *Nature* **2016**, *537*, 661–665.

(10) H. M. Key, P. Dydio, D. S. Clark, J. F. Hartwig. Abiological catalysis by artificial haem proteins containing noble metals in place of iron. *Nature* **2016**, *534*, 534–537.

(11) P. Dydio, H. M. Key, H. Hayashi, D. S. Clark, J. F Hartwig. Chemoselective, enzymatic C-H bond amination catalyzed by a cytochrome P450 containing an Ir(Me)-PIX cofactor. *J. Am. Chem. Soc.* **2017**, *139,* 1750–1753.

(12) P. S. Coelho, E. M. Brustad, A. Kanna, F. H. Arnold. Olefin Cyclopropanation via Carbene Transfer Catalyzed by Engineered Cytochrome P450 Enzymes. *Science* **2013**, *339*, 307–310.

(13) K. Chen, F. H.Arnold. Enzyme engineering for nonaqueous solvents: random mutagenesis to enhance activity of Subtilisin E in polar organic media. *Nat. Biotechnol.* **1991**, *9*, 1073–1077.

(14) P. Dydio, H. M. Key, A. Nasarenko, J. Y.-E. Rha, V. Seyedkaemi, D. S. Clark, J. F. Hartwig. An artificial metalloenzyme with the kinetics of native enzymes. *Science* **2016**, *354*, 102–106.

(15) M. E. Wilson, G. M. Whitesides. Conversion of a protein to a homogeneous asymmetric hydrogenation catalyst by site-specific modification with a diphosphinerhodium(I) moiety. *J. Am. Chem. Soc.* **1978**, *100*, 306–307.

(16) A. Illie, M. T. Reetz. Directed evolution of artificial metalloenzymes. *Isr. J. Chem.* **2015**, *55*, 51–60.

(17) A. J. Boersma, J. E. Klijn, B. L. Feringa, G. Roelfes. DNA-based asymmetric catalysis: sequence-dependent rate acceleration and enantioselectivity. *J. Am. Chem. Soc*. **2008**, *130*, 11783–11790.

(18) D. K. Prusty, M. Kwak, J. Wildeman, A. Herrmann. Modular assembly of a Pd catalyst within a DNA scaffold for the amplified colorimetric and fluorimetric detection of nucleic acids. *Angew. Chem., Int. Ed.* **2012**, *51*, 11894 –11898.

(19) G. F. Joyce. RNA evolution and the origins of life. *Nature* **1989**, *338*, 217–224.

(20) P. G. Higgs, N. Lehman. The RNA world: molecular cooperation at the origins of life. *Nat. Rev. Genet.* **2015**, *16*, 7–17.

(21) J. K. Barton. Metal/Nucleic Acid Interactions. *Bioinorganic Chemistry*. University Press, **455** (1994).

(22) W. Zhou, R. Saran, J. Liu. Metal sensing in DNA. *Chem. Rev.* **2017**, *117*, 8272–8325.

(23) Takezawa, Y. & Shionoya M. Metal–mediated DNA base pairing: alternatives to hydrogen –bonded Watson–Crick base pairs. *Acc. Chem. Res.* **2012**, *45*, 2066–2076.

(24) M. Kumar, J. Jasinski, G. B. Hammond, B. Zu. Alkyne/alkene/allene–induced disproportionation of cationic gold(I) catalyst. *Chem. Eur. J.* **2014**, *20*, 3113–3119.

(25) S. A. E. Marras, F. R. Kramer, S. Tyagi. Efficiencies of fluorescence resonance energy transfer and contact—mediated quenching in oligonucleotide probes. *Nucleic Acids Res.* **2002**, *30*, e122.

(26) O. V. Kharissova, H. V. R. Dias, B. I. Kharisov, B. O. Pèrez, V. M. J. Pèrez. The greener synthesis of nanoparticles. *Trends Biotechnol.* **2013**, *31*, 240–248.

(27) D. C. Carter, J. X. Ho. Structure of serum albumin. *Adv. Protein Chem.* **1994**, *45*, 153–176.

(28) T. T. Herskovits. Nonaqueous solutions of DNA; denaturation by urea and its methyl derivatives. *Biochemistry* **1963**, *2*, 335–340.

(29) M. T. McManus, P. A. Sharp. Gene silencing in mammals by small interfering RNAs. *Nat. Rev. Genet.* **2002**, *3*, 737–747.

(30) J. Wang, Q. Wu, Y. Min, Y. Liu, Q. A. Song. A novel fluorescent probe for Au(III)/Au(I) ions based on an intramolecular hydroamination of a Bodipy derivative and its application in bioimaging. *Chem. Commun.* **2012**, *48*, 744–746.

(31) Y. Aoyagi, T. Mizusaki, M. Shishikura, T. Komine, T. Yoshinaga, H. Inaba, A. Ohta, K. Takeya. Efficient synthesis of pyrroles and 4,5,6,7-tetrahydroindoles via palladium-catalyzed oxidation of hydroxyenamines. *Tetrahedron* **2006**, *62*, 8533–8538.

(32) C. L. Huang, T. Weng, F. C. Chen. Synthesis of biflavonyl ethers. *J. Heterocycl Chem.* **1970**, *7*, 1189–1190.

(33) J. Lv, Q. Liu, J. Tang, F. Perdih, K. Kranjc, A facile synthesis of indolo[3,2,1-*jk*]carbazoles *via* palladium-catalyzed intramolecular cyclization. *Tetrahedron Lett.* **2012**, *53*, 5248–5252.

CHAPTER FOUR

Chemocatalytic Amplification Probes Composed of a C–C Mismatch Enable Transcriptionally-Regulated Au(I) Catalysis *in vitro* and *in vivo*

Adapted From: Sydnee A. Green, Benjamin Wigman, Sepand K. Nistanaki, Hayden R. Montgomery, Christopher G. Jones, Hosea M. Nelson **2020**, *ChemRxiv. Preprint.*

https://doi.org/10.26434/chemrxiv.12915761.v2

4.1 Abstract

Here we report a novel Au(I)-DNAzyme that is activated by DNA and RNA in a highly sequence-specific manner and that is compatible with complex biological matrices. The active Au(I)-DNAzyme catalyzes the formation of a fluorescent molecule with >10 turnovers. This functional allostery, resulting in chemocatalytic signal amplification, is competent in complex biological settings, including within recombinant *E. coli* cells, where the catalytic activity of the Au(I)-DNAzyme is regulated by transcription of an inducible plasmid in cell lysates and whole cells. This optimized system highlights the potential for the use of chemocatalytic amplification probes to detect RNA transcripts *in vitro* and *in vivo*.

4.2 Introduction

While transition metal catalysis has become a powerful and efficient tool in synthetic chemistry, its application in biology has trailed behind, as synthetic transition metal complexes struggle to avoid deleterious reactions with the diverse chemical functionalities present in biological media. The biocatalytic community has made great strides toward overcoming this challenge, demonstrating that engineering of wild-type metalloenzymes can lead to biocatalysts

that mediate abiotic chemical transformations such as insertion and other metal-carbenoid reactions.[1,2] In fewer examples, novel metalloenzymes with non-native metal centers have been reported, in some cases capable of mediating transformations well beyond the scope of wild-type biochemical transformations.[3,4] Organometallic complexes have also found use in biological settings, although rarely employed catalytically.[5,6]

Our group has become interested in developing transition metal catalysts that are not only functional under the challenges presented in biological conditions, but also regulated by gene transcription. In this scenario, we envisioned genotype-specific catalysis, where bioconjugation reactions and activation of pro-drugs or reporter molecules could be controlled temporally and spatially through transcriptional upregulation. Moreover, akin to biochemical amplification regimes such as polymerase chain reaction (PCR), we envisioned that signal amplification could be achieved through this chemical catalysis, allowing for detection of infinitesimally-small quantities of gene transcripts for applications in chemical biology, genetics, and diagnostics. To this end, we previously reported an example of a novel Au(I)-DNAzyme that performs abiotic hydroamination reactions under highly sequence specific upregulation by short RNA or DNA fragments (*Figure 4.1*).[7] In our initial study, we provided proof-of-principle, but were not able to demonstrate efficacy in biological matrices as our Au(I)-DNA catalyst proved to be poorly compatible with biological media. Herein we report the development of a new chemocatalytic amplification probe (CAP) featuring a novel metal-binding motif comprised of a Au(I)-mediated cytosine–cytosine (C–C) base pair with unprecedented thermal and biological stability. We show that this new Au(I)-DNA catalyst is capable of catalyzing hydroarylation reactions of alkynes in response to gene transcription in cellular extracts and inside living *E. coli* cells.

Figure 4.1 Activation of Au(I)-CAP with complementary DNA or RNA fragments.

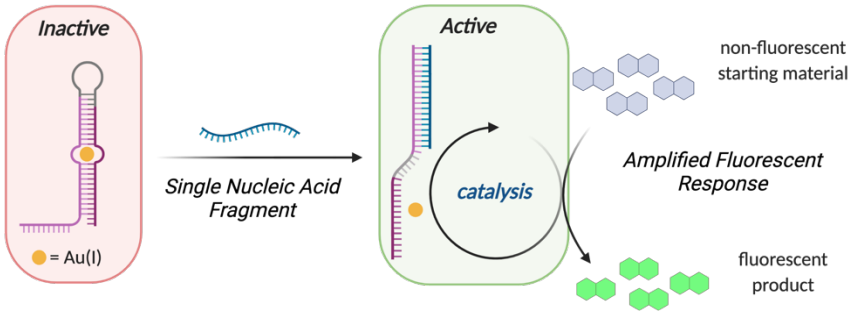

4.3 Catalytic Amplification Probe formed through a C–C mismatch

Encouraged by the strong binding of Au(I) to C–C mismatches (Chapter Two), which implied a potential for greater stability in complex chemical environments, we attempted to incorporate Au(I) into a hairpin sequence to forge a Au(I)-DNA catalyst. We envisioned that two Au(I) ions could be incorporated into a hairpin sequence containing a single C–C mismatch (**CC15-5** 5'-CGT TCT GTT TTC ACA GAA CGA CAT CAG AGA GTA GG-3'), providing a coordinatively saturated metal complex (Chapter Two). Addition of a complementary nucleic acid strand induces strand displacement revealing a coordination site on the metal (*Figure 4.2a*). Presumably, binding of alkyne **4.1** to this coordination site initiates cyclization to a fluorescent coumarin product **4.2** (*Figure 4.2b*).[8] In initial experiments, we were pleased to find that upon addition of 1 equivalent of complement there was an 8- or 10-fold increase in fluorescence with 1 μM or 250 nM of complex **4.3**, respectively (*Figure 4.2c*). In addition, activation of a 250 nM solution of the Au(I)-DNA complex with one catalytic equivalent of complement initiated nearly 13 catalytic turnovers based on the concentration of Au(I) added. Importantly, without addition of the complementary nucleic acid strand, there was approximately 0.1 turnovers (*Figure 4.2d*). This finding, though representing modest turnover numbers (TON) from a chemistry perspective,

revealed the opportunity to achieve superior sensitivity to our previously reported C–T system due to a dramatic decrease in background reactivity of the probe in the absence of a transcriptional activator (increased signal-to-noise ratio), likely due to less gold leaching in the more stable C–Au(I)–C metal-mediated base pair.

Figure 4.2 a) inactive DNA-Au complex and formation of active complex following addition of complement. b) Au(I)-catalyzed hydroarylation for formation of fluorescent coumarin product **4.2**. c) Fluorescence intensity and fold increase in fluorescence with 1 μM and 250 nM complex **4.3**. d) Amplification factor ([**4.2**]/[**4.3**]) of reaction containing 250 nM of complex **4.3**.

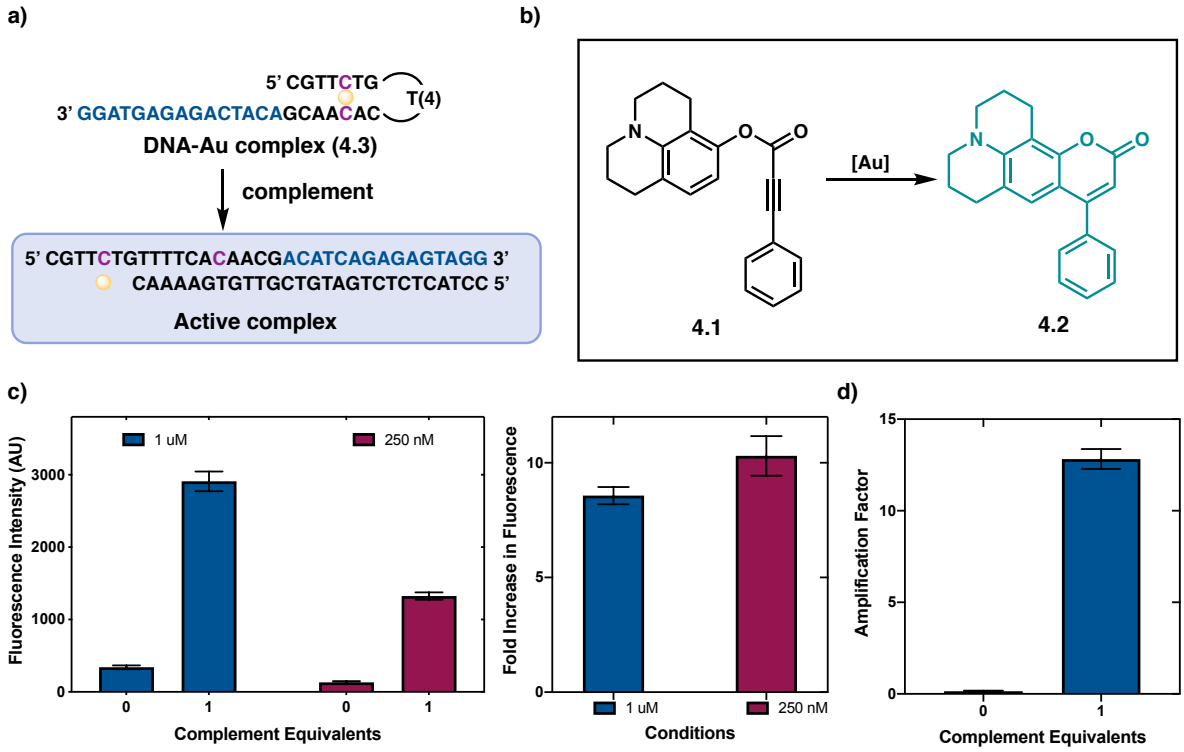

4.4 Detection Sensitivity Compared to Molecular Beacon

With the heightened sensitivity of this probe compared to our previously reported system (250 nM detection *vs.* 10 μM detection), we were compelled to compare the sensitivity of our CAP complexes to molecular beacons routinely used for sensing nucleic acids. Molecular beacons are often used in conjunction with PCR for quantitative detection of nucleic acids.[9,10] These FRET-based probes provide a single fluorescent output for every complementary nucleic acid that is hybridized, hence there is a need for amplification through PCR or other means to increase the amount of detectable nucleic acid present to meet the beacon's limit of detection (250 nM in our hands).[11] We hypothesized that our catalytic platform could overcome this inherent limitation given its ability to amplify signal through the catalytic production of >10 equivalents of fluorophore in response to a single hybridization event. Ultimately, this would allow entry to a more sensitive gene detection platform with improved limits of detection. Indeed, in direct comparison at 1 μM, addition of one equivalent of complementary sequence led to a 13-fold increase (fold increase = [fluorescence with complement]/[fluorescence with no complement]) in fluorescence with the Au(I)-CAP, compared to less than a 2-fold increase with the FRET-based molecular beacon. At complement concentrations lower than one equivalent respective to probe, our Au(I)-CAP maintained over a 4-fold increase in fluorescence, whereas the detection limit of the molecular beacon was ~0.25 μM, above which there was only a 1.3-fold increase in fluorescence (*Figure 4.3*). Interestingly, addition of excess complementary sequence to our CAP complex **4.3** results in lower levels of fluorescence. This is likely due to the decrease in gold activity with excess nucleic acids available to non-specifically sequester gold ions (Chapter Three).

Figure 4.3 a) Molecular beacon hairpin and duplex. b) Fold increase in fluorescence upon addition of various complement concentrations with 1 μM **4.3** and **4.4**.

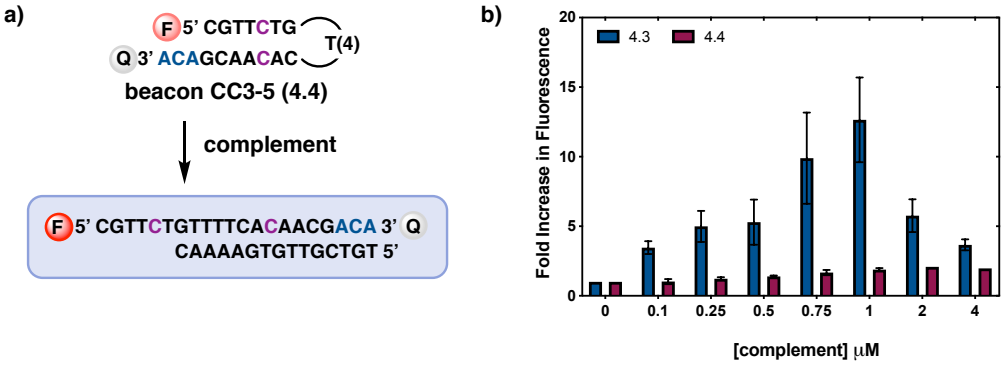

4.5 CAP System in *E. coli* Cell Lysates and Whole Cells

The increased sensitivity of our CAP system inspired us to explore its ability to detect mRNA directly produced through transcription. The direct (PCR-free) detection of mRNA or DNA in cell lysates could contribute to several areas, including diagnostics and forensics, by lowering detection limits. We initially attempted to detect mRNA extracted from recombinant *E. coli* cells. We transformed competent *E. coli* cells with a plasmid containing our complement (gene **CC15-5**) and a T7 *lac* promoter. As an appropriate control, we transformed a group of cells with the plasmid that did not contain gene **CC15-5**.[12] The cell lysates of both cell lines were incubated with our CAP at 1 μM and profluorophore **4.1** at 200 μM for 12 hours and subjected to confocal microscopy to visualize fluorescence (*Figure 4.4a*). We observed that the cell lysate of the cells expressing the complement exhibited nearly a 3-fold increase in fluorescence when compared to the control cell lysate (*Figure 4.4b*).

Figure 4.4 a) Cell lysate experimental design and b) fluorescence intensity of cell lysates.

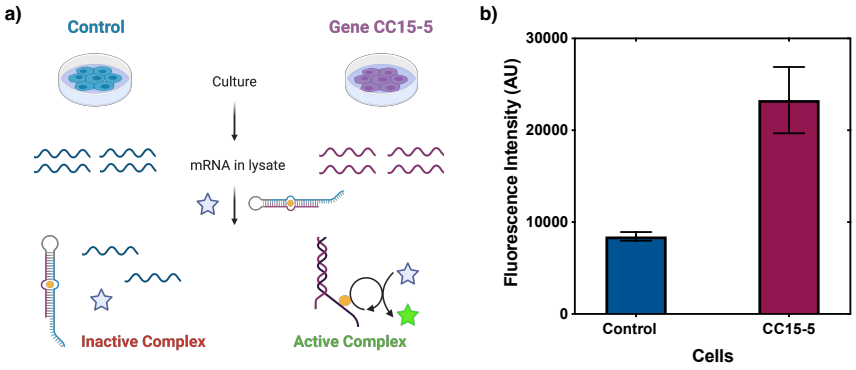

To further assess the ability of our catalyst to perform in biologically relevant conditions, we incorporated the HP-Au(I) complex directly into competent *E. coli* cells using heat shock (*Figure 4.5*).[13] After a three-hour incubation of *E. coli* transformed with gene **CC15-5** plasmids with 1 μM of the HP-Au(I) complex, followed by stringent washing, and a subsequent overnight incubation with profluorophore **4.1**, we observed that the cells expressing the complementary sequence (*Figure 4.5b*) were more fluorescent than the cells containing the control plasmid (*Figure 4.5c*). These results further demonstrate the ability of this novel Au(I)-DNA complex to catalyze abiotic chemical transformations *in cellulo* in response to gene transcription, highlighting the potential for this technology to be used as a highly sensitive diagnostic tool for detection of nucleic acid material in both biotechnological and clinical applications.

Figure 4.5 a) Reaction scheme of *E. coli* whole cells reacted with with Au(I)-CAP catalyst. b) Fluorescence microscopy of cells expressing gene CC15-5. c) Fluorescence microscopy of cells expressing control gene. d) Fluorescence intensity of cells after lysing once the reaction is complete. e) Histogram of fluorescence in images from (b) and (c).

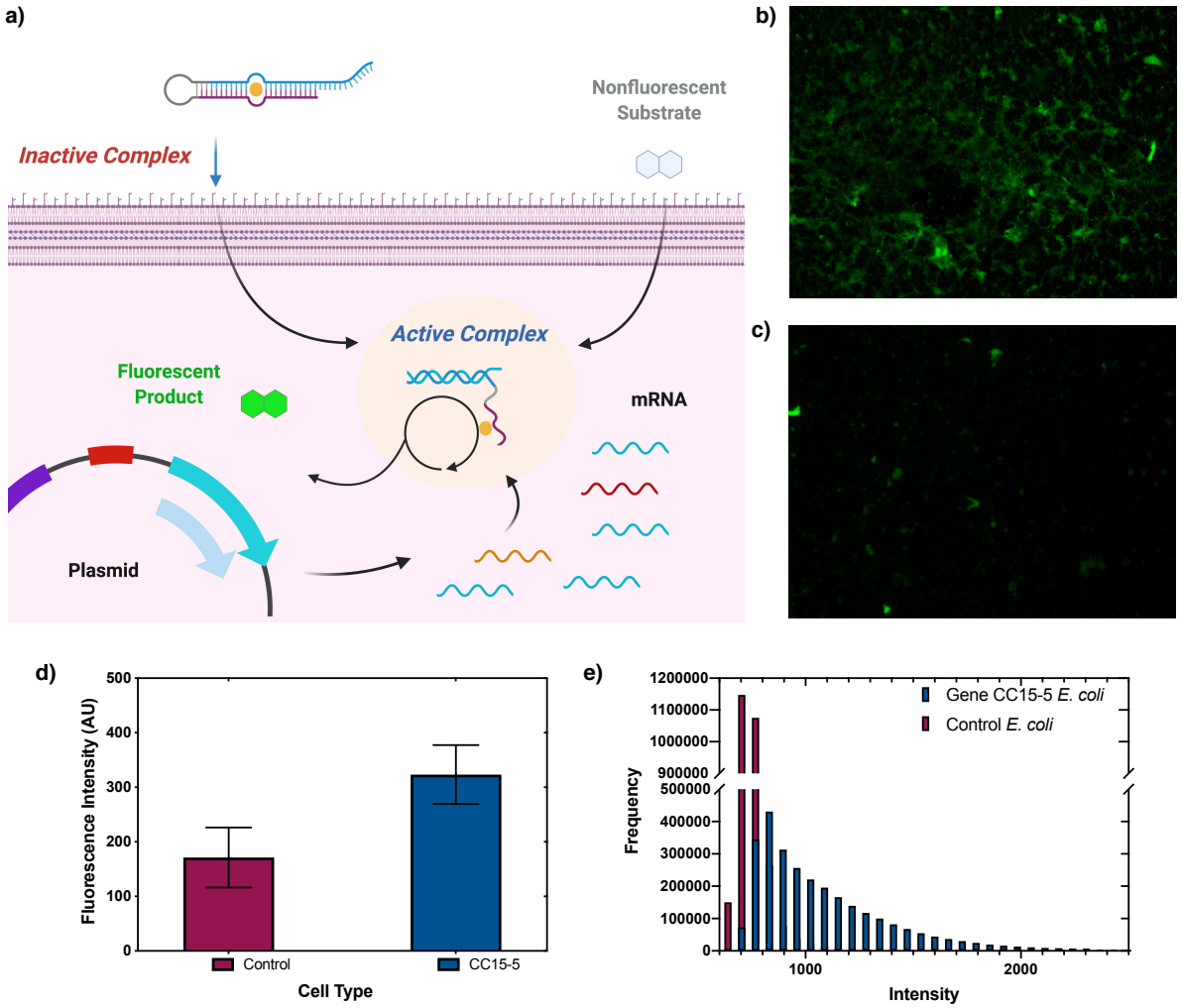

4.6 Conclusion

In conclusion, we have discovered and developed a novel C–C metal-mediated base pair, wherein the incorporation of two equivalents of Au(I) ions results in an unprecedented level of thermal stabilization (ΔT_m = 33 ºC). We have demonstrated that, despite the inherent stability of

these Au(I)-DNA complexes, they are able to effectively hybridize to low concentrations of complementary nucleic acid strands, and activate the catalytic activity of the Au(I) metal center. These findings permitted the detection of low concentrations of mRNA in complex biological matrices such as cell lysates and whole cells, and were competitively more sensitive than standard molecular beacon technologies. This system shows promise as an inexpensive method for the detection nucleic acids.

4.7 Experimental Section

4.7.1 Materials and Methods

Unless stated otherwise, reactions were performed in flame-dried glassware under an atmosphere of nitrogen. Benzene, THF, dichloromethane, and dimethylformamide were degassed and dried in a JC Meyer solvent system. SilicaFlash P60 silicagel (230–400 mesh) was used for flash chromatography. NMR spectra were recorded on a Bruker AV-300 (1H), Bruker AV-400 (1H, 13C), Bruker DRX-500 (1H), and Bruker AV-500 (1H, 13C). 1H NMR spectra are reported relative to $CDCl_3$ (7.26 ppm). All oligonucleotides were purchased through Integrated DNA Technology with standard desalting unless otherwise specified. Samples for thermal denaturation, mass spectrometry studies, and catalysis were prepared by heating the buffered DNA solution without metal at 90 °C in a heating block for 10 minutes then cooled to room temperature for 30 minutes. Once cool, the metal solution was added. In thermal denaturation experiments, all absorbances were measured at 260 nm using HP-8453 spectrophotometer with HP-89090A Peltier temperature controller from 15–90 °C at 5 °C min^{-1} with a hold time of 1 min. Relative absorbance, $A_{260nm}=(A_t–A_{15\,°C})/(A_{90\,°C}–A_{15\,°C})$, vs. temperature (°C) curves were fitted using GraphPad Prism 7.0c. Fluorescence experiments were recorded on a Tecan Infinite M1000 Pro plate reader with the following conditions: 480 nm excitation, 510 nm emission, 8 mm excitation and emission bandwidth, 50 flashes with a frequency of 400 Hz, and a 10 ms delay time. Fluorescence data was collected on a JASCO-J715 CD spectrophotometer with a scan rate of 20 nm/min from 200 nm to 300 nm with 3 accumulations. Mass spectrometry data was collected on a Thermo Scientific Q Exactive Plus Hybrid Quadrupole-Orbitrap Mass Spectrometer using negative ionization mode.

4.7.2 DNA-Au(I) Freidel-Crafts Reactions *in vitro*

General Procedure

Hairpin-Au(I) complex made at 50 uM and stored at 4 °C for up to 2 days. The solution was left to incubate for 30 min at room temperature to allow for complete formation of metal-mediated base pair before added to any experiments. Further dilutions were made to desired stock concentration for reaction. Following hairpin addition to the reaction, the complement sequence was added and the solution was allowed to equilibrate for 10 minutes before adding it to a solution of alkyne **2** in 40% ethanol resulting in a final solution containing (3:2 H_2O:EtOH). Reactions contain 250 nM DNA hairpin, 250 nM complement sequence, 125 mM $NaClO_4$ and 200 μM alkyne **2**. All other conditions/concentrations vary depending on experiment. Positive control contains no DNA. Negative control contains no DNA nor $(Me_2S)AuCl$. No comp (0 equiv): 0 equivalents of complement sequence added to reaction. Comp (1 equiv): 1 equivalent (250 nM) complement sequence added to reaction. Progress of reactions was determined by fluorescence intensity. All fluorescence values reported in arbitrary units. Fold increase in fluorescence was calculated based on equation $FI = (F_{1\ eq} – F_{0\ eq})/(F_{0\ eq})$. Yields were calculated using a standard curve of product coumarin derivative **1** at known concentrations ranging from 3.25 μM to 60 μM, this was then fit to a line in excel and the equation was used to calculate the yield of fluorescent product for each reaction.

Figure 4.6 Gold catalyzed Friedel-Crafts reaction.

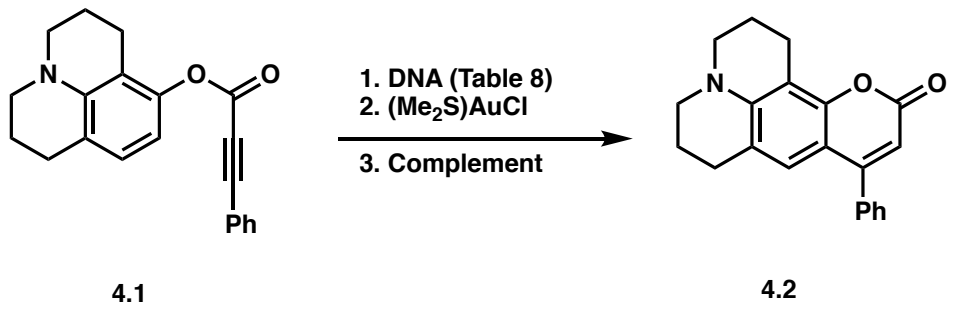

4.1 4.2

Table 4.1 Sequences used in catalysis and *E. coli* cell experiments (section 4).

Sequence Name	Hairpin (5'-3')
CC15-5	GCTTCTGTTTTCACAACGACATCAAGAGAGTAGGG
CCBeacon	GCTTCTGTTTTCACAACGACA
CC comp	CCTACTCTCTGATGTCGTTGTGAAAAC
CC comp RNA	CCUACUCUCUGAUGUCGUUGUGAAAAC

4.7.2.1 Data

Figure 4.7 Fluorescence of CC15-5 at 1 μM or 250 nM with no complement (0) or 1 equivalent complement (1).

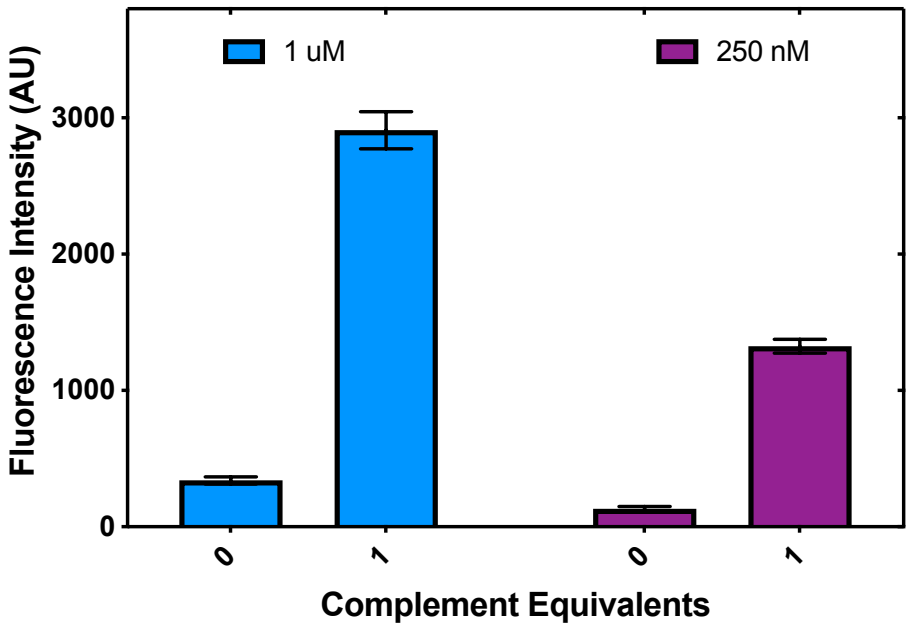

Table 4.2 Fluorescence values of CC15-5 at 1 μM or 250 nM with no complement (0) or 1 equivalent complement (1).

[Hairpin]	[Complement]	Mean	Std. Dev.
1 μM	0 μM	340	26
1 μM	1 μM	2910	136
250 nM	0 nM	133	16
250 nM	250 nM	1324	51

Figure 4.8 Turnover of CC15-5 at 1 μM or 250 nM with no complement (0) or 1 equivalent complement (1).

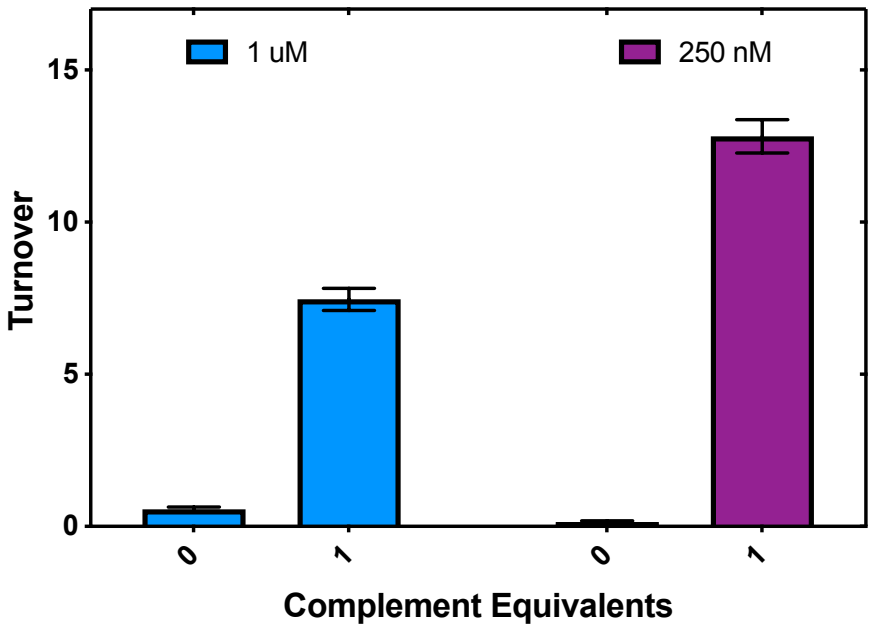

Table 4.3 Turnover values of CC15-5 at 1 μM or 250 nM with no complement (0) or 1 equivalent complement (1).

[Hairpin]	[Complement]	Mean	Std. Dev.
1 μM	0 μM	0.6	0.1
1 μM	1 μM	7.5	0.4
250 nM	0 nM	0.1	0.1
250 nM	250 nM	12.8	0.5

Figure 4.9 Fluorescence of CC15-5 (250 nM) with no complement (0) or 1 equivalent complement (1) with $(Me_2S)AuCl$ (blue) or $HAuCl_4$ (purple).

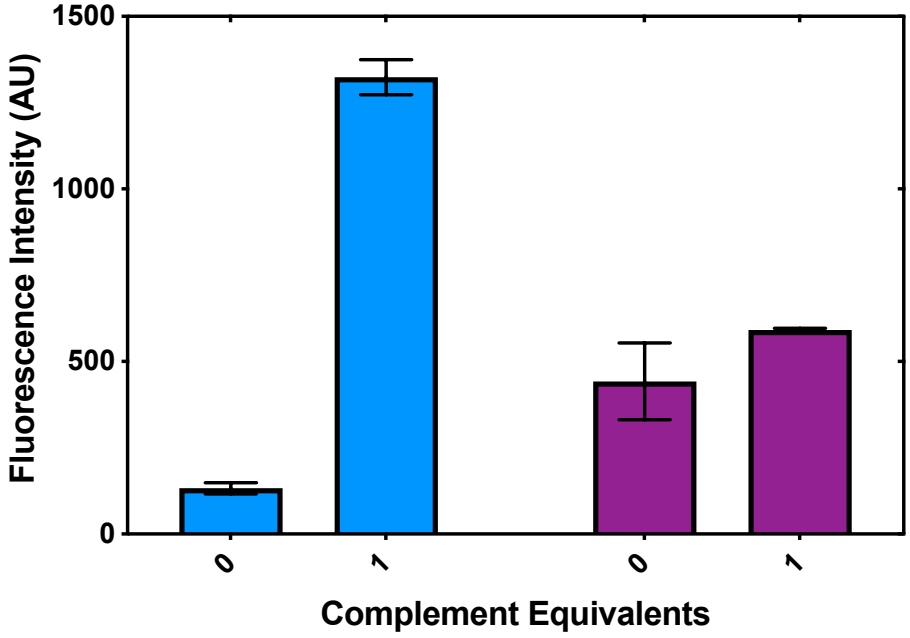

Table 4.4 Fluorescence of CC15-5 (250 nM) with no complement (0) or 1 equivalent complement (1) with $(Me_2S)AuCl$ (blue) or $HAuCl_4$ (purple).

Au(I) Precursor	Complement Equiv	Mean	Std. Dev.
$(Me_2S)AuCl$	0	133	16
$(Me_2S)AuCl$	1	1324	51
$HAuCl_4$	0	442	111
$HAuCl_4$	1	591	5

Figure 4.10 Fluorescence of CC15-5 (1 μM) with no complement (0) or 1 equivalent complement (1) with $(Me_2S)AuCl$ (blue) or $HAuCl_4$ (purple).

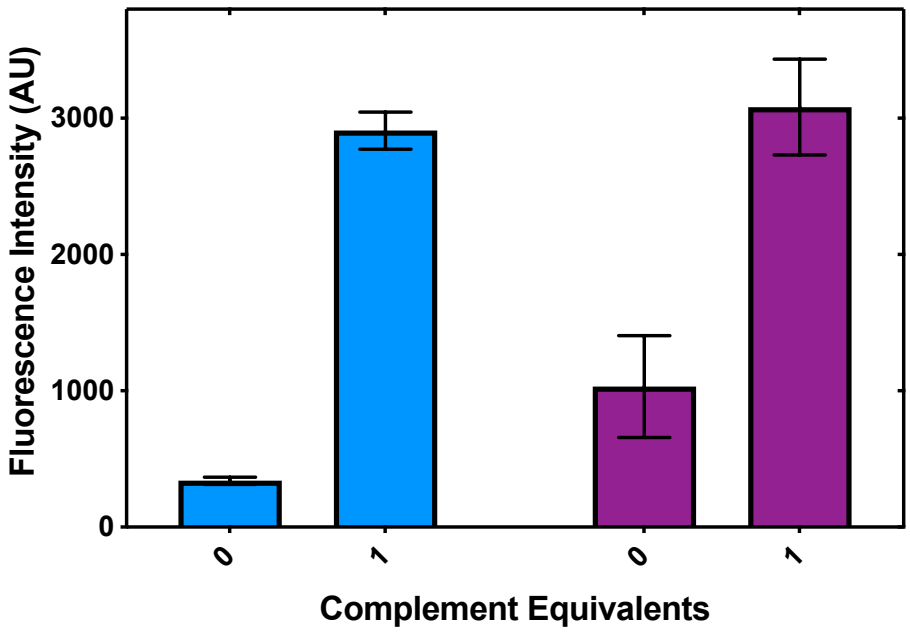

Table 4.5 Fluorescence of CC15-5 (1 μM) with no complement (0) or 1 equivalent complement (1) with $(Me_2S)AuCl$ (blue) or $HAuCl_4$ (purple).

Au(I) Precursor	Complement Equiv	Mean	Std. Dev.
$(Me_2S)AuCl$	0	340	26
$(Me_2S)AuCl$	1	2910	136
$HAuCl_4$	0	1031	373
$HAuCl_4$	1	3081	351

Figure 4.11 Fluorescence of CC15-5 (1 μM) with varying concentrations of CC comp and CC comp RNA.

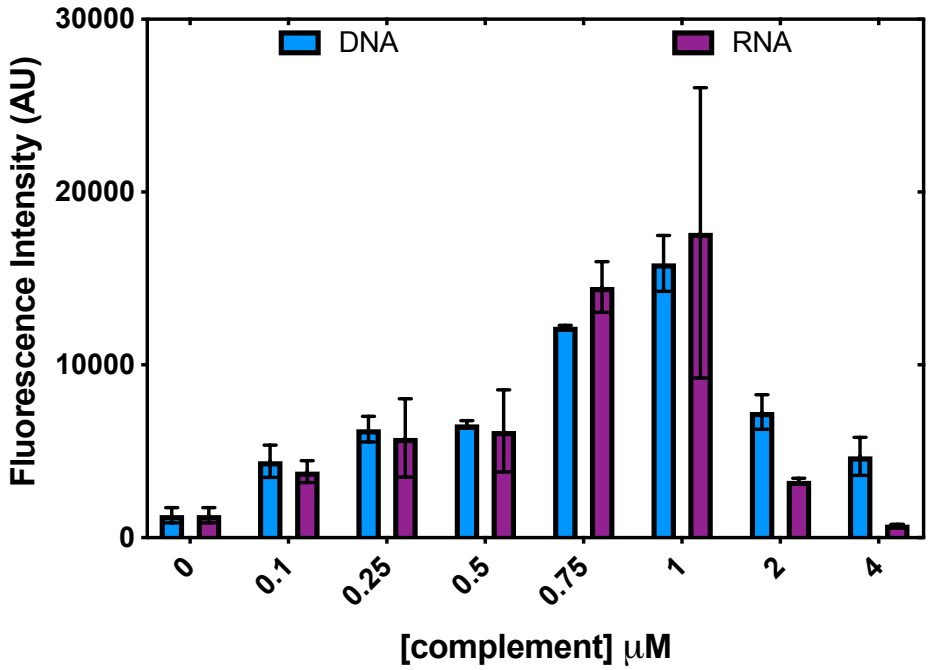

Table 4.6 Fluorescence of CC15-5 (1 μM) with various equivalents of DNA complement.

[Complement]	Mean	Std. Dev.
0 μM	1308	442
0.1 μM	4430	933
0.25 μM	6280	746
0.5 μM	6558	216
0.75 μM	12211	86

1 μM	15871	1614
2 μM	7271	1002
4 μM	4702	1101

Table 4.7 Fluorescence of CC15-5 (1 μM) with various equivalents of RNA complement.

[Complement]	Mean	Std. Dev.
0 μM	1308	442
0.1 μM	3826	635
0.25 μM	5777	2261
0.5 μM	6163	2368
0.75 μM	14503	1466
1 μM	17640	8403
2 μM	3293	147
4 μM	766	6

Figure 4.12 Fluorescence of CC beacon (1 μM) with varying concentrations of CC comp.

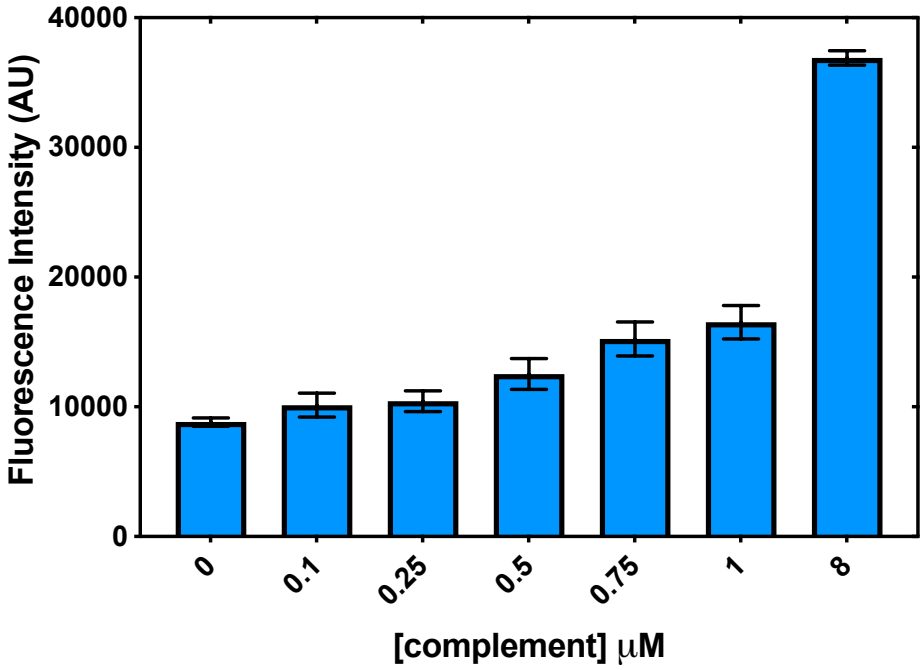

Table 4.8 Fluorescence of CC beacon (1 μM) with various equivalents of DNA complement.

[Complement]	Mean	Std. Dev.
0 μM	8828	327
0.1 μM	10132	913
0.25 μM	10443	800
0.5 μM	12528	1186
0.75 μM	15226	1308

1 μM	16523	1289
8 μM	36898	556

4.7.3 DNA-Au(I) Friedel-Crafts Reactions *in cellulo* and in lysates

Cell transformation and expression

Gene CC15-5 (5'-GTTTTCACAACGACATCAGAGAGTAGGTTAGT-3') was cloned into pET24a, which had been digested with NdeI and XhoI, by Gibson assembly. The sequence was verified by DNA sequencing (Genewiz). pGeneCC15-5 and pControl (pET24a) were grown in LB broth, 500 ml for pGeneCC15-5 and 250 ml for pControl, at 37 °C. RNA expression was induced with 1 mM IPTG when the cells reached an OD600 of ~ 0.5. Cell growth was continued at 37 °C for 4 hours and the cells then harvested (50 ml conical tubes) by centrifugation using JS5.3 rotor (10 minutes at 6.8K). Cell pellets were diluted in LB buffer and re-aliquoted such that the pellets would be OD_{600} = 10 in 1 ml of buffer.

Figure 4.13 Insertion of Gene CC15-5 into pET24a plasmid for transformation into *E. coli* cells. Gene CC15-5 cell line contains plasmid with inserted Gene CC15-5 and Control cell line was transformed with original pET24a plasmid.

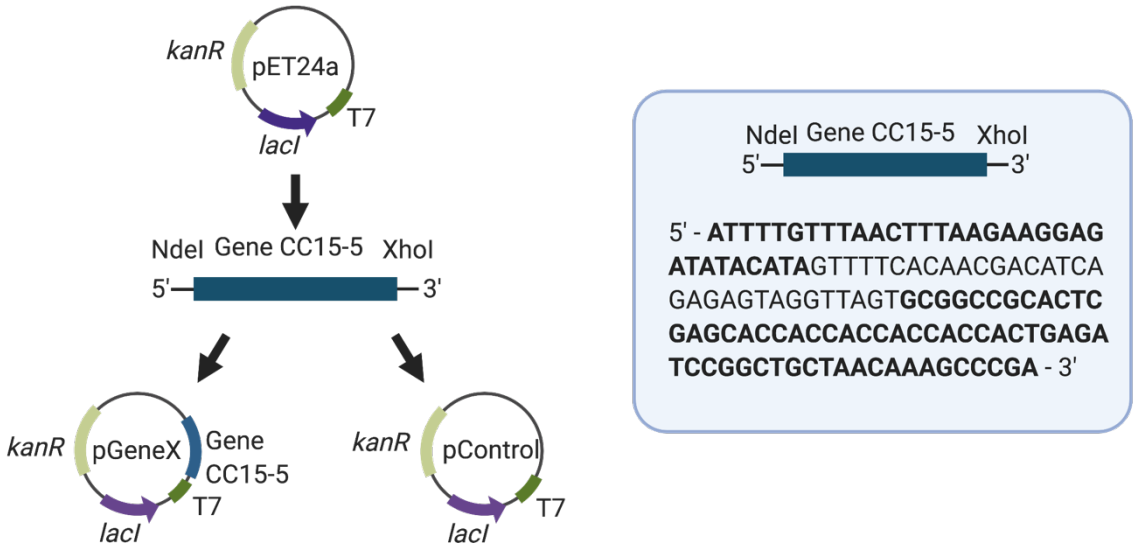

Lysate Experiments

To each cell aliquot (Gene CC15-5 and Control *E. coli* cells) was added 1 ml of lysis buffer (1.5% isoamyl alcohol, 750 mM sodium perchlorate, and 40% EtOH) or 1 ml other lysing conditions (Phenol-Chloroform or TRIzol). The cells were then sonicated for 30 minutes. Following sonication, cells were aliquoted into reaction tubes and fluorescent probe and CC15-5-Au(I) complex was added. Final concentrations (1 μM CC15-5-Au(I) complex, 200 υM probe 1, 50% EtOH, 125 mM sodium perchlorate).

Whole Cell Experiments

Competent gene CC15-5 and control *E. coli* cell aliquots were diluted in 1 ml of TB buffer (Millipore Sigma). The cells were vortexed until monodispersed in tubes and then 200 ul added

to 0.6 ml epitubes. To these tubes were added CC15-5-Au(I) complex (10 μM) in TB buffer such that the final concentration was 5 μM CC15-5-Au(I) complex and cell OD_{600} = 5 in 400 μl TB buffer. After 1 hour incubation at 37 °C, the cells were centrifuged for 10 minutes and washed with TB buffer (x3). Then solution containing 100 μM probe 1 (in 100 μl TB buffer, 1% DMSO) was added to pelleted cells and incubated overnight at 37 °C. Following incubation, cells were washed and dehydrated using 40% EtOH for visualization.

4.7.3.1 Data

Figure 4.14 Cell lysates (Gene CC15-5 and control) using Phenol-Chloroform extraction.[14]

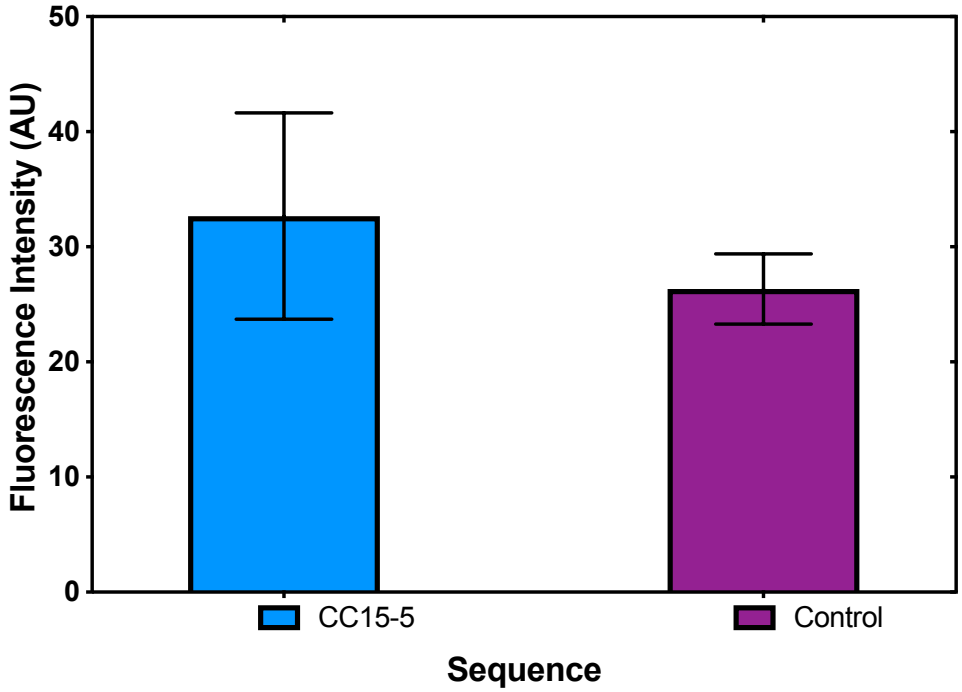

Table 4.9 Fluorescence values of CC15-5 (1 μM) with cell lysates (Phenol-Chloroform extraction) with Gene CC15-5 and Control gene.

Gene	Mean	Std. Dev.
CC15-5	33	9
Control	26	3

Figure 4.15 TRIzol extraction of cell lysates with 25 mM, 12.5 mM, and 6.25 mM.[15]

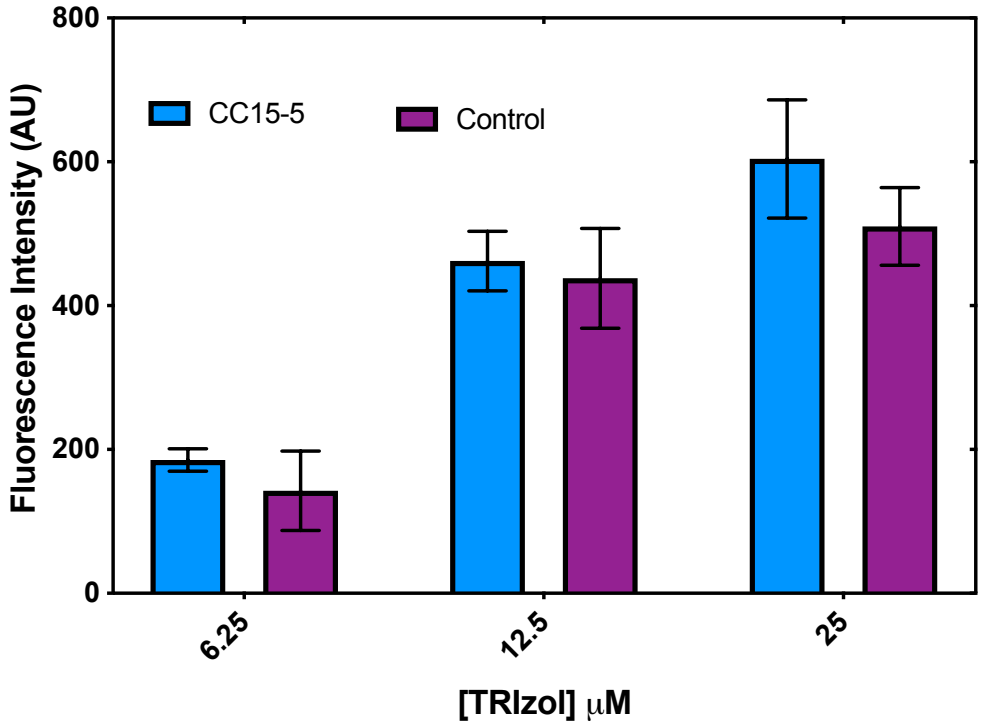

Table 4.10 Fluorescence values of CC15-5 (1 μM) with cell lysates (Phenol-Chloroform extraction) with Gene CC15-5 and Control gene.

[TRIzol] μM	Gene	Mean	Std. Dev.
6.25	CC15-5	185	16
12.5	CC15-5	462	42
25	CC15-5	604	82
6.25	Control	143	55
12.5	Control	438	69

25	Control	510	54

Figure 4.16 Fluorescence of CC15-5 (1 μM) with cells lysed with 2% Isopropyl alcohol in various concentrations of sodium perchlorate.

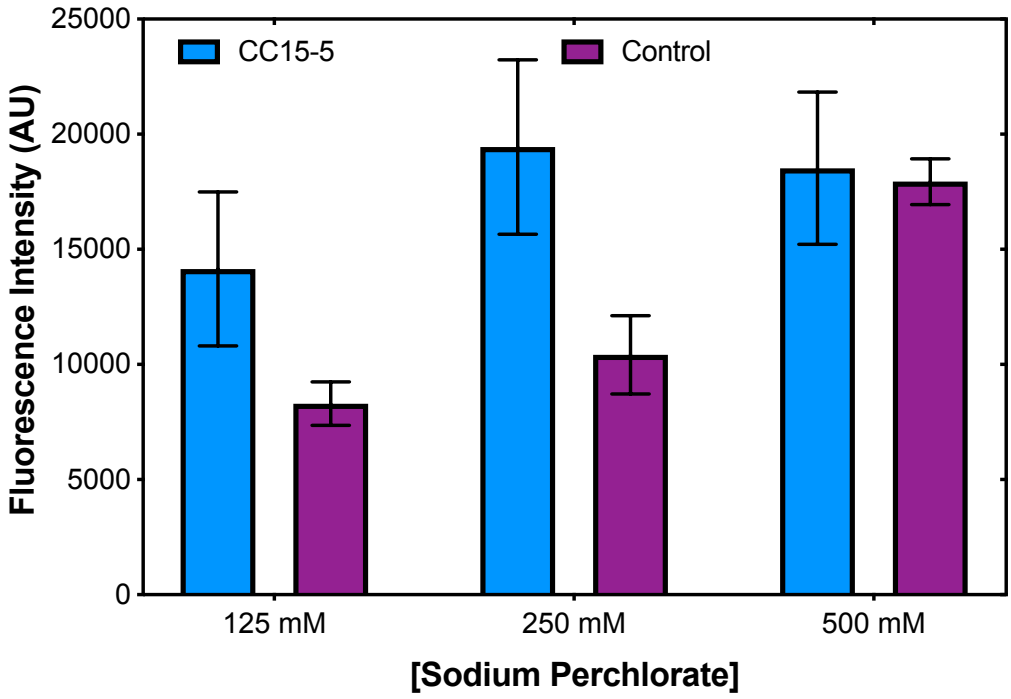

Table 4.11 Fluorescence values of CC15-5 (1 μM) with cells lysed with 2% Isopropyl alcohol in various concentrations of sodium perchlorate.

[Sodium Perchlorate] mM	Gene	Mean	Std. Dev.
125	CC15-5	14149	3347
250	CC15-5	19443	3783

500	CC15-5	18523	3306
125	Control	8289	948
250	Control	10419	1698
500	Control	17940	994

Figure 4.17 Fluorescence of CC15-5 (1 μM) with cells lysed with 250 mM sodium perchlorate with various percentages of isopropyl alcohol.

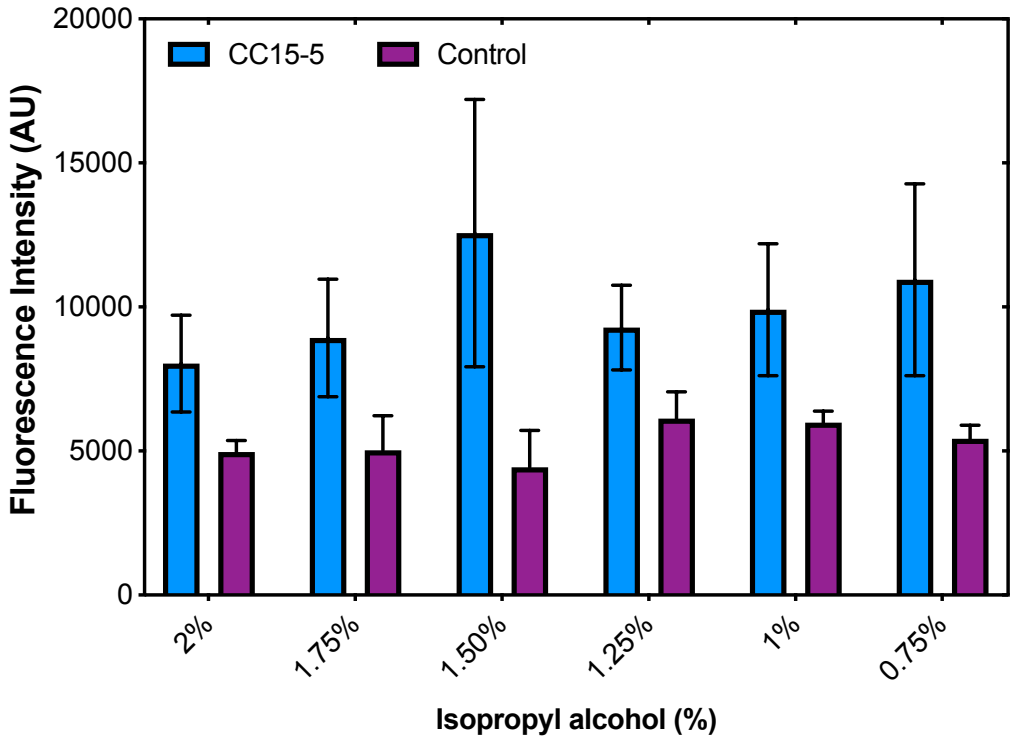

Table 4.12 Fluorescence values of CC15-5 (1 μM) with cells lysed with 2% Isopropyl alcohol in various concentrations of sodium perchlorate.

Isopropyl alcohol (%)	Gene	Mean	Std. Dev.
2	CC15-5	8034	1679
1.75	CC15-5	8927	2039
1.5	CC15-5	12569	4639
1.25	CC15-5	9287	1468
1	CC15-5	9905	2290
0.75	CC15-5	10946	3331
2	Control	4958	400
1.75	Control	5012	1203
1.5	Control	4426	1280
1.25	Control	6116	929
1	Control	5980	400
0.75	Control	5411	478

Figure 4.18 Fluorescence of CC15-5 (1 μM) with cells lysed with 1.5% isopropyl alcohol with various concentrations of sodium perchlorate.

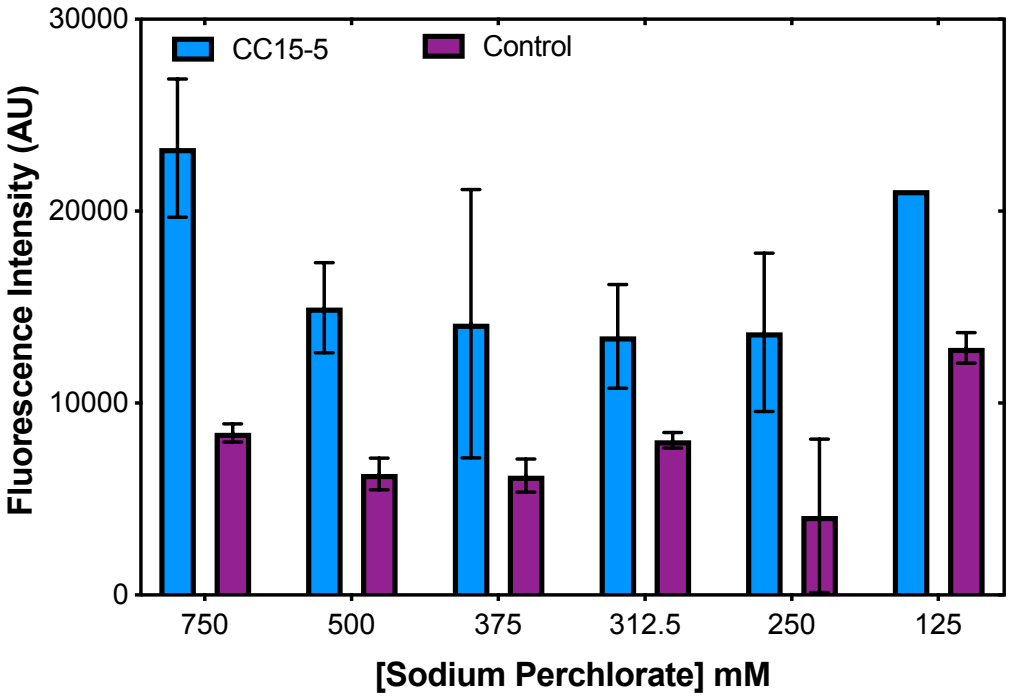

Table 4.13 Fluorescence values of CC15-5 (1 μM) with cells lysed with 2% Isopropyl alcohol in various concentrations of sodium perchlorate.

[Sodium Perchlorate] mM	Gene	Mean	Std. Dev.
750	CC15-5	23285	3603
500	CC15-5	14973	2346
375	CC15-5	14135	6993
312.5	CC15-5	13476	2702

250	CC15-5	13691	4125
125	CC15-5	21096	—
750	Control	8447	472
500	Control	6308	824
375	Control	6225	866
312.5	Control	8063	406
250	Control	4120	3999
125	Control	12876	790

Figure 4.14 a) Brightfield and fluorescence of pGeneCC15-5 cell line with CC15-5 Au(I)-CAP b) histogram of fluorescence and brightfield.

a)

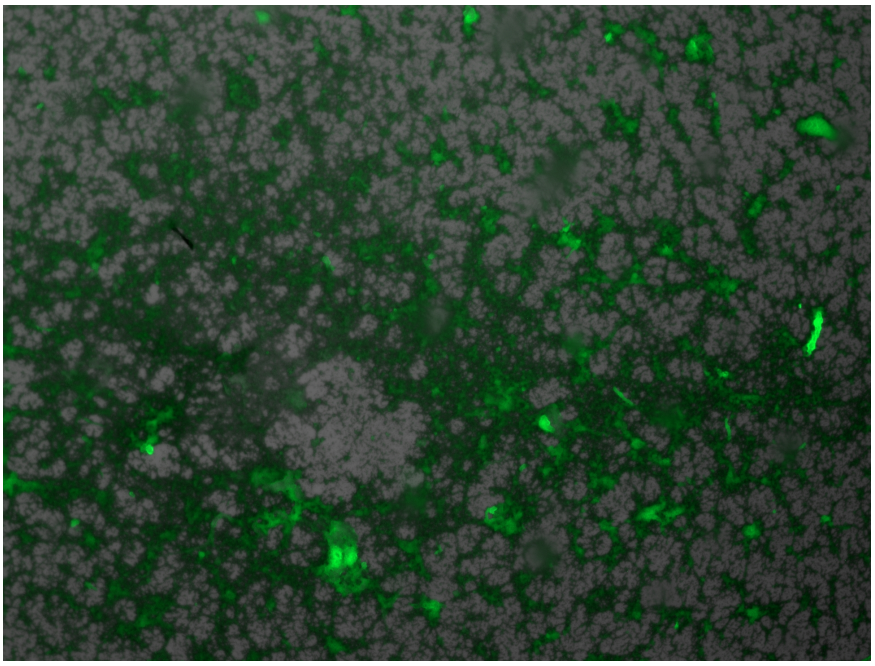

b)

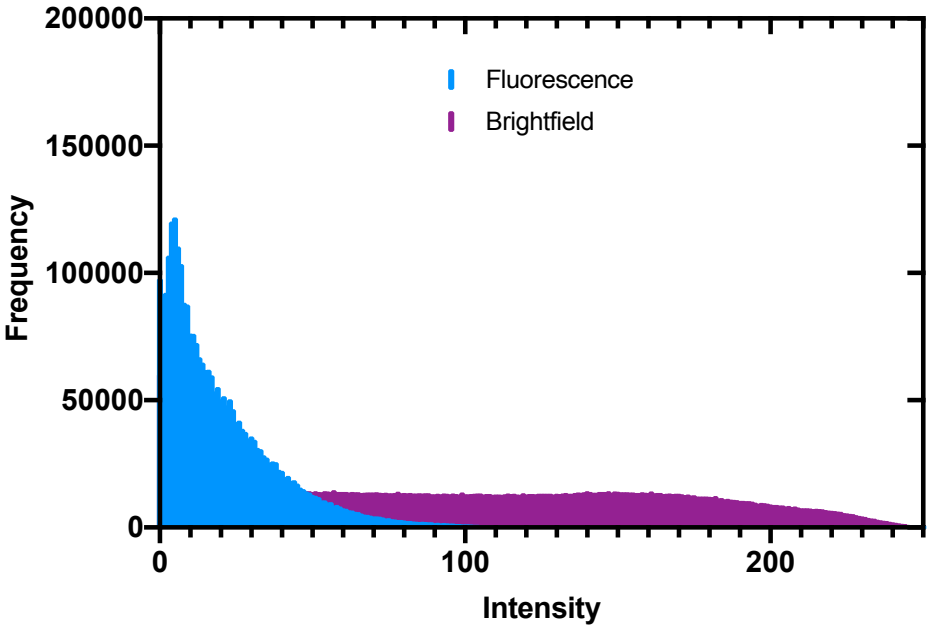

Figure 4.15 a) Brightfield and fluorescence of pControl cell line with CC15-5 b) histogram of fluorescence and brightfield

a)

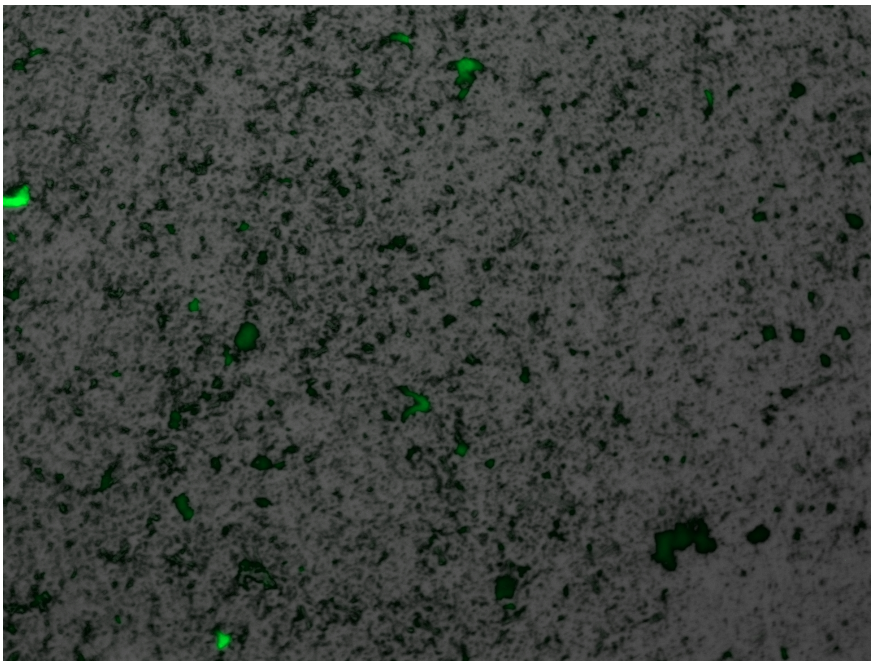

b)

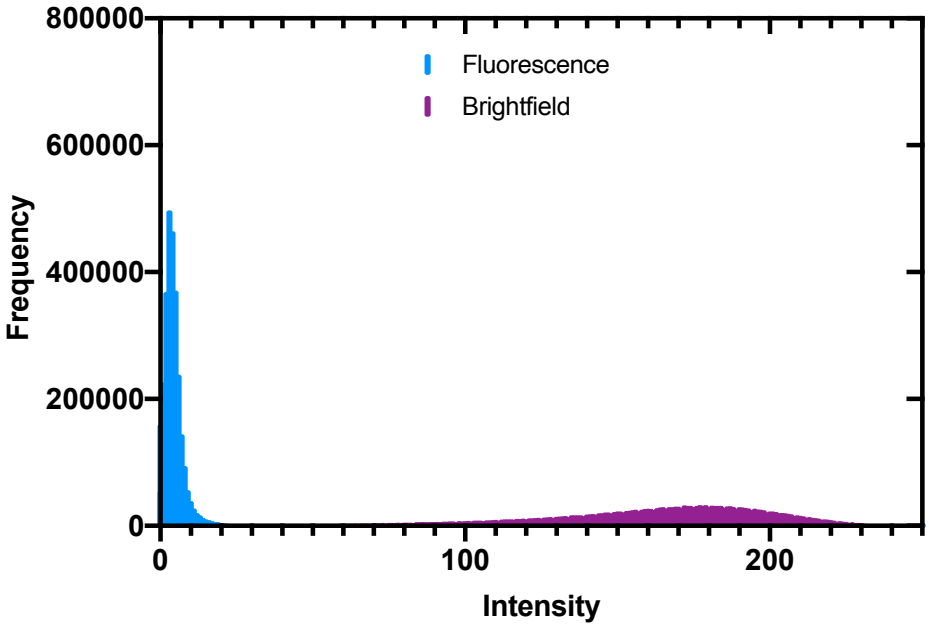

Figure 4.16 a) Brightfield and fluorescence of pGeneCC15-5 cell line with $(Me_2S)AuCl$ only b) histogram of fluorescence and brightfield

a)

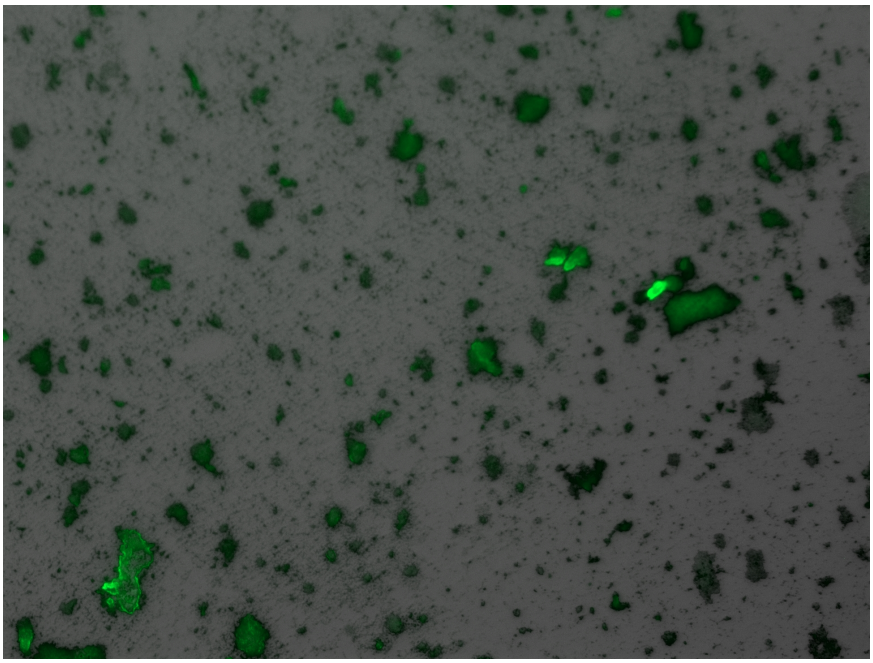

b)

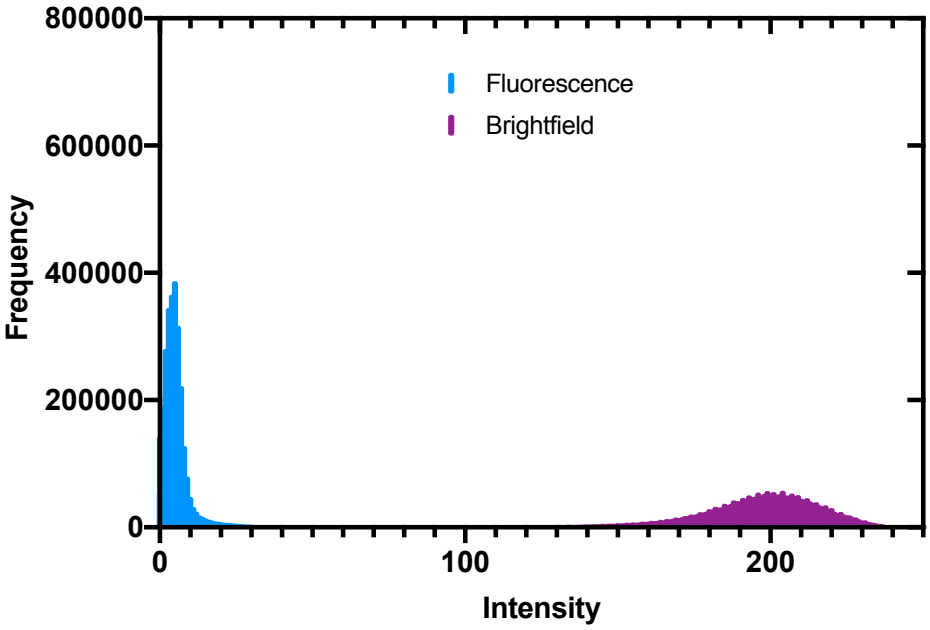

Figure 4.17 a) Brightfield and fluorescence of pControl cell line with $(Me_2S)AuCl$ only b) histogram of fluorescence and brightfield.

a)

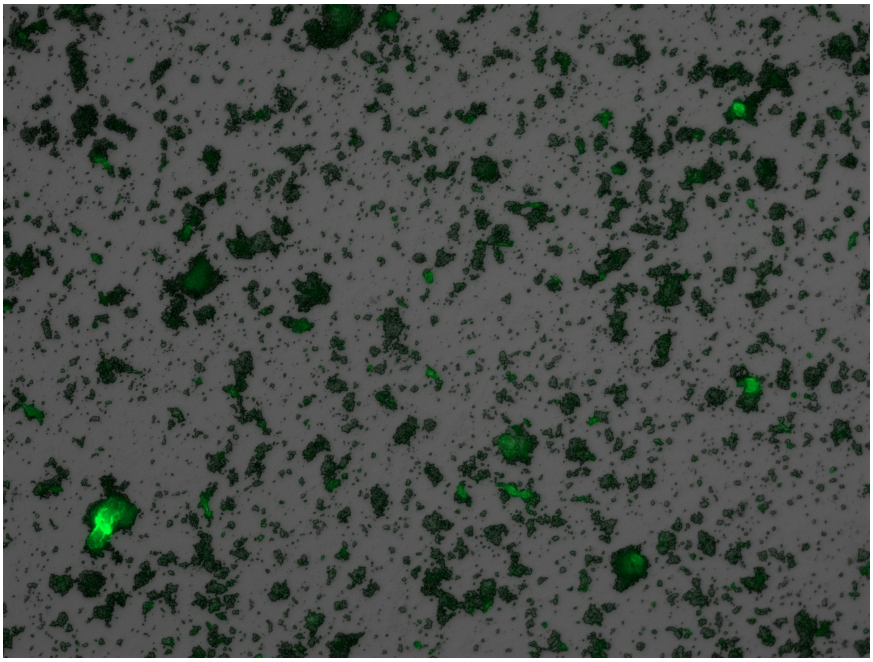

b)

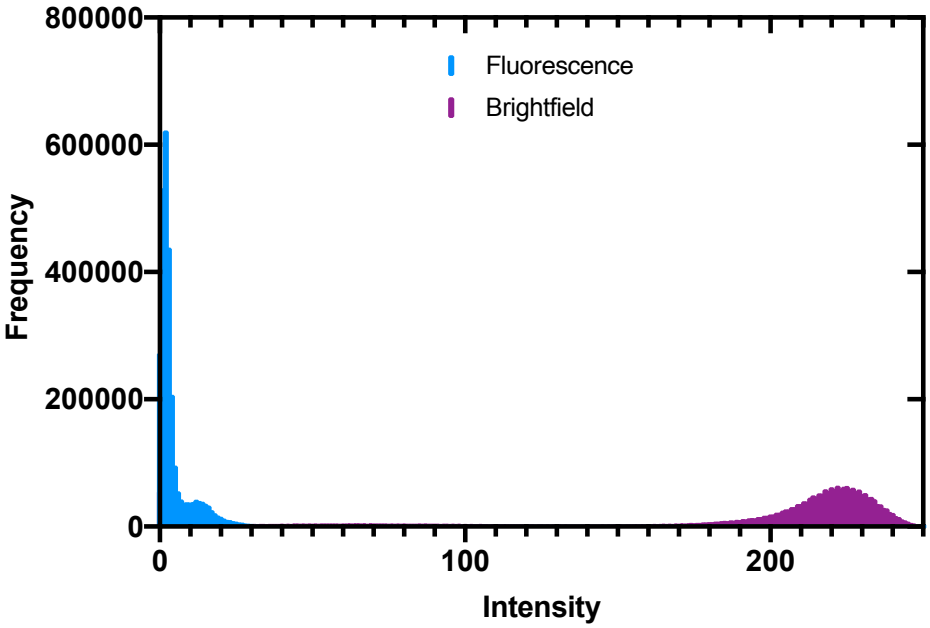

4.7.4 Synthesis

Preparation of Profluorophore 4.1

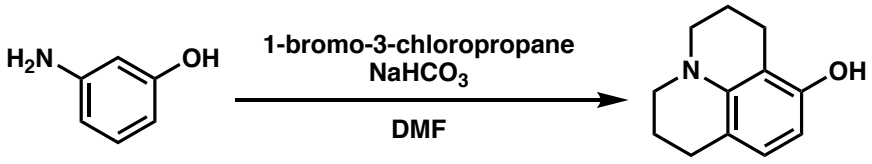

4.5

2,3,6,7-tetrahydro-1*H*,5*H*-pyrido[3,2,1-i*j*]quinoline-8-ol (4.5): Synthesized according to reported literature. Purified by flash chromatography to obtain **4.5** as a white solid in 52% yield of product. NMR spectra match those reported in literature[16].

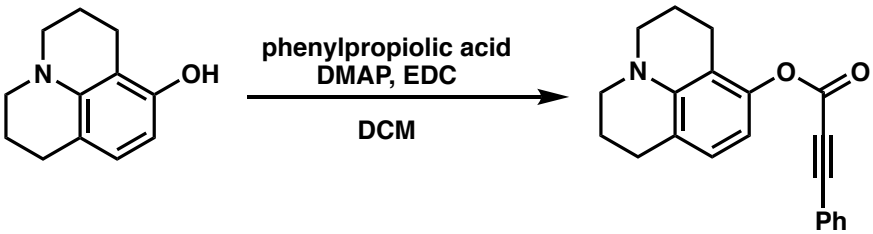

4.5 4.1

2,3,6,7-tetrahydro-1*H*,5*H*-pyrido[3,2,1-i*j*]quinoline-8-ol (4.1): Synthesized according to reported literature. Purified by flash chromatography to obtain **4.1** as a yellow solid in 64% yield of product. NMR spectra match those reported in literature.[14]

4.8 Spectra Relevant to Chapter Four:

Chemocatalytic Amplification Probes Composed of a C–C Mismatch Enable Transcriptionally-Regulated Au(I) Catalysis *in vitro* and *in vivo*

Adapted From: Sydnee A. Green, Benjamin Wigman, Sepand K. Nistanaki, Hayden R. Montgomery, Christopher G. Jones, Hosea M. Nelson **2020**, *ChemRxiv. Preprint.*

https://doi.org/10.26434/chemrxiv.12915761.v2

Figure 4.18 [1]H NMR (400 MHz, CDCl3) of compound **4.5**.

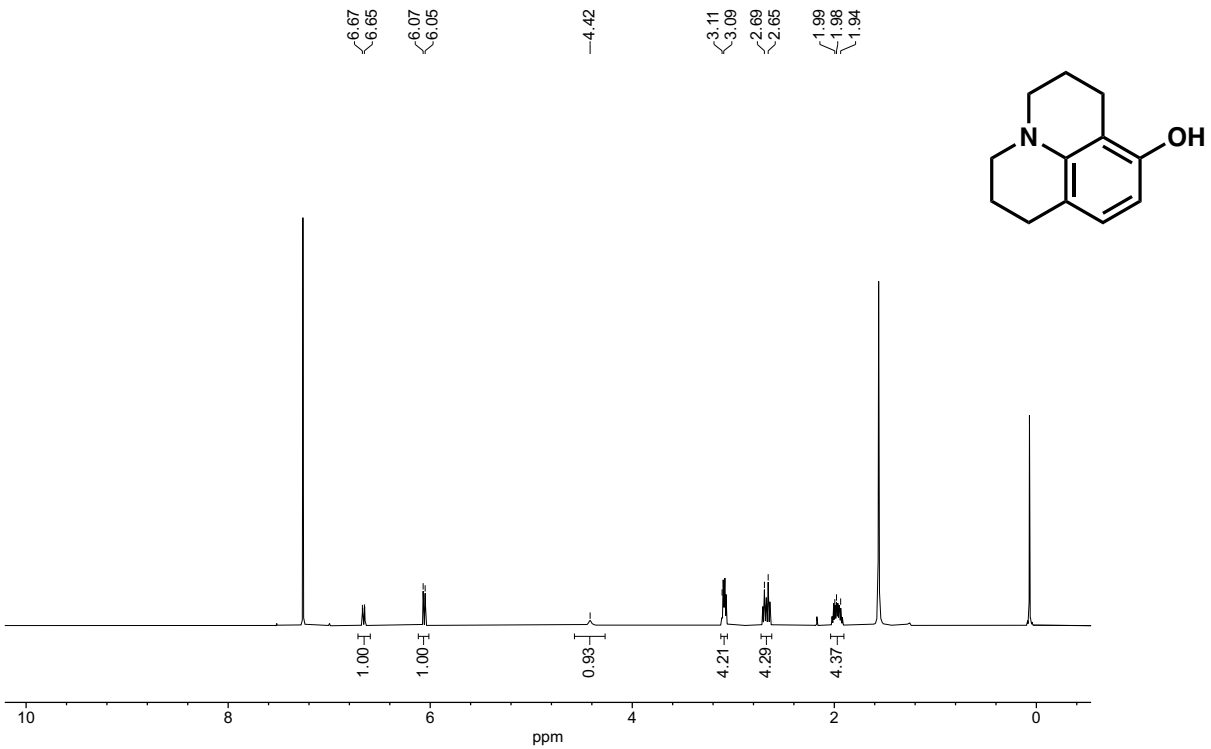

Figure 4.19 1H NMR (400 MHz, CDCl3) of compound **4.1**.

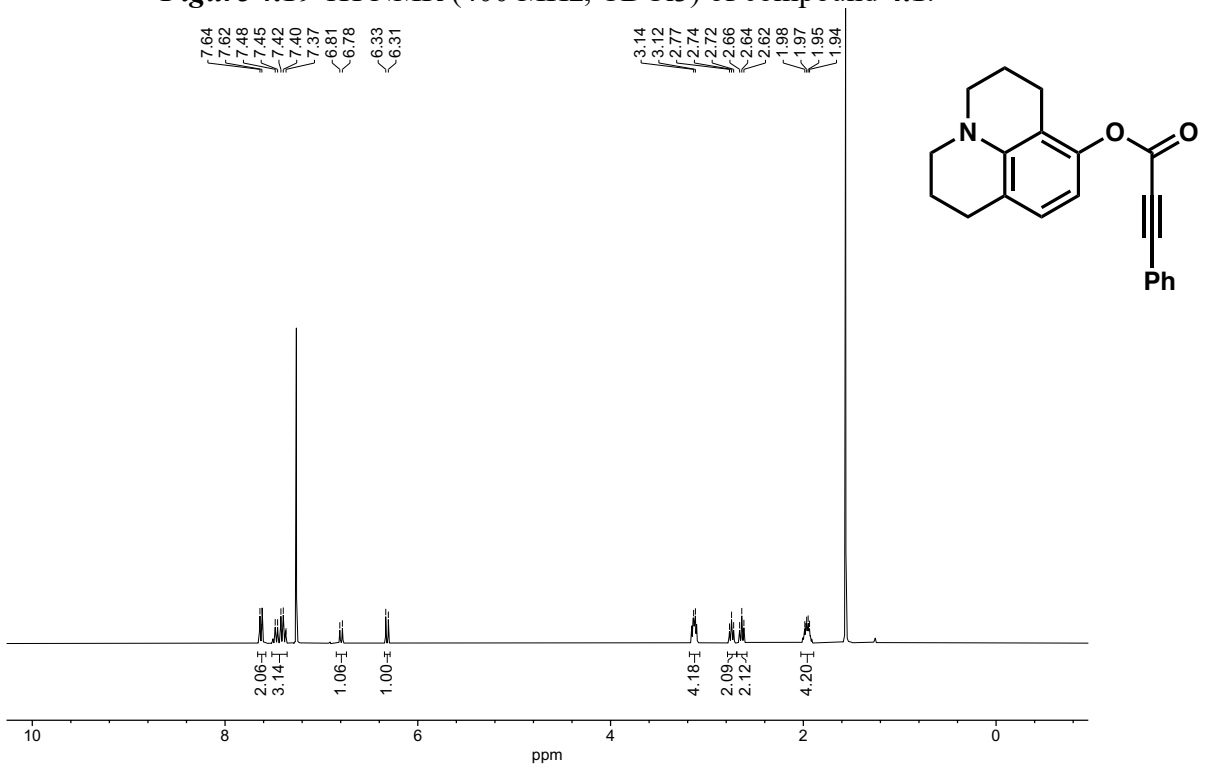

4.7 Notes and References

(1) H.-T. Hsu, B. M. Trantow, R. M. Waymouth, P. A. Wender, Bioorthogonal Catalysis: A General Method To Evaluate Metal-Catalyzed Reactions in Real Time in Living Systems Using a Cellular Luciferase Reporter System. *Bioconjugate Chem.* **2016**, *27*, 376-382.

(2) K. Chen, F. H. Arnold, Engineering new catalytic activities in enzymes. *Nat. Catal.* **2020**, *3*, 203–213.

(3) M. T-. Gamasa, M. M-. Calvo, J. R. Couceiro, J. L. Mascareñas, Transition metal catalysis in the mitochondria of living cells. *Nat. Comm.* **2016**, *7*, 12538.

(4) F. Schwizer *et al.*, Artificial metalloenzymes: reaction scope and optimization strategies. *Chem. Rev.* **2018**, *118*, 142–231.

(5) E. V. Vinogradova, C. Zhang, A. M. Spokoyny, B. L. Pentelute, & S. L. Buchwald, Organometallic palladium reagents for cysteine bioconjugation. *Nature* **2015**, *526*, 687–691.

(6) C .Streu, E. Meggers, Ruthenium-induced allylcarbamate cleavage in living cells. *Angew. Chem. Int. Ed.* **2006**, *45*, 5645–5648.

(7) S. A. Green, H. R. Montgomery, N. J. Chan, T. R. Benton, H. M. Nelson Regulating transition-metal catalysis through interference by short RNAs. *Angew. Chem. Int. Ed.* **2019**, *58*, 16400–16404.

(8) J.H. Do, H.N. Kim, Yoon, J., Kim, J. S., H.–J. Kim, A rationally designed fluorescence turn-on probe for the Gold(III) ion. *Org. Lett.* **2010**, *12*, 932–934.

(9) S. Tyagi, F.R. Kramer, Molecular beacons: probes that fluoresce upon hybridization. *Nat. Biotechnol*. **1996**, *14*, 303–308.

(10) G. Leone, B. van Gemen, C.D. Schoen, H. van Schijndel, F.R. Kramer, Molecular beacon probes combined with amplification by NASBA enable homogeneous, real-time detection of RNA. *Nucleic Acids Res.* **1998**, *26*, 2150–2155.

(11) Y. Kim, D. Sohn, W. Tan, Molecular beacons in biomedical detection and clinical Diagnosis. *Int. J. Clin. Exp. Pathol.* **2008**, *1*, 105–116.

(12) C. Johnston, B. Martin, G. Fichant, P. Polard, J.-P. Claverys, Bacterial transformation: distribution, shared mechanisms and divergent control. *Nat. Rev. Microbiol.* **2014**, *12*, 181–196.

(13) C. Xi, M. Balberg, S.A. Boppart, L. Raskin, Use of DNA and peptide nucleic acid molecular beacons for detection and quantification of rRNA in solution and in whole cells. *Appl. Environ. Microbiol*. **2003**, *69*, 5673–5678.

(14) J. Sambrook, D. W. Russel. Purification of Nucleic Acids by Extraction with Phenol:Chloroform. *Cold Spring Harb Protoc* **2017** doi:10.1101/pdb.prot093450.

(15) D. C. Rio, M. Ares Jr., G. J. Hannon, T. W. Nilsen. Purification of RNA Using TRIzol (TRI Regent). *Cold Spring Harb Protoc* **2010** doi:10.1101/pdb.prot5439.

(16) S. Lui, W.-H. Wang, Y.-L. Dang, Y. Fu, R. Sang. Rational Design and Efficient Synthesis of a Fluorescent-Labeled Jasmonate. *Tetrahedron Lett.* **2012**, *53*, 4235–4239.

CHAPTER FIVE

Chemocatalytic Amplification Probes for the Femtomolar Detection of SARS-CoV-2 Fragments

Adapted From: Sydnee A. Green, Benjamin Wigman, Sepand K. Nistanaki, Hayden R. Montgomery, Christopher G. Jones, Hosea M. Nelson **2020**, *ChemRxiv. Preprint.*

https://doi.org/10.26434/chemrxiv.12915761.v2

5.1 Abstract

At the outset of our previous chemocatalytic amplification probe (CAP) studies, we were met with the emergence of the COVID-19 pandemic and saw the need for a fast and cheap nucleic acid-based diagnostic. We demonstrate the potential of our transition metal oligonucleotide complexes as a highly sensitive and selective hybridization probe, permitting the detection of attomolar concentrations (*ca.* 60 molecules/mL) of SARS-CoV-2 RNA gene fragments in simulated biological matrices with ≥85% accuracy. Notably, this sensitive detection platform avoids expensive and poorly-scalable biochemical components (e.g., post-synthetically modified oligonucleotides or enzymes) and instead utilizes small molecule fluorophores, inexpensive Au salts and oligonucleotides composed of canonical bases. This discovery highlights promising opportunities to perform abiotic catalysis in complex biological settings under transcriptional regulation, as well as a chemocatalytic strategy for PCR-free, direct-detection of RNA and DNA.

5.2 Introduction

In late 2019, the world was met with a new coronavirus, SARS-CoV-2, that began spreading rapidly until it was officially declared a global pandemic by the World Health

Organization in early 2020.[1] While the initial polymerase chain reaction (PCR) COVID-19 diagnostic test was authorized in the United States in late January 2020, access to testing for the general population was very limited.[2,3] Given the remarkable sensitivity of our previous Au(I)-CAP system for the detection of genetic information under biologically relevant conditions, we reasoned that the application of this technology to viral diagnostics could address an unmet biomedical need, and in fact, it has been reported that the best way to limit the spread of COVID-19 is through rapid and reliable testing of the general population.[4,5,6]

The current testing platform introduced by the Centers for Disease Control (CDC) relies on resource intensive reverse transcription/qPCR to amplify the viral RNA to meet the minimum detection limit of the FRET-based hybridization probe used in the COVID-19 test kit.[7] The process requires cumbersome procedures, sensitive reagents, and advanced molecular biology instrumentation, thereby limiting rapid deployment of low-cost tests on a large scale, with limited opportunity for point-of-care testing.[8] Given these limitations, and the need for accurate, sensitive, and cost-efficient COVID-19 diagnostics,[9] we felt responsible to translate our newly developed catalytic system toward a COVID-19 diagnostics platform. The observed signal amplification and superior sensitivity of our system over standard molecular beacon platforms highlighted a strategic opportunity to contribute to the field during this unprecedented time.

Figure 5.1 Comparison of molecular beacon in standard PCR to CAP-Au(I) catalyst.

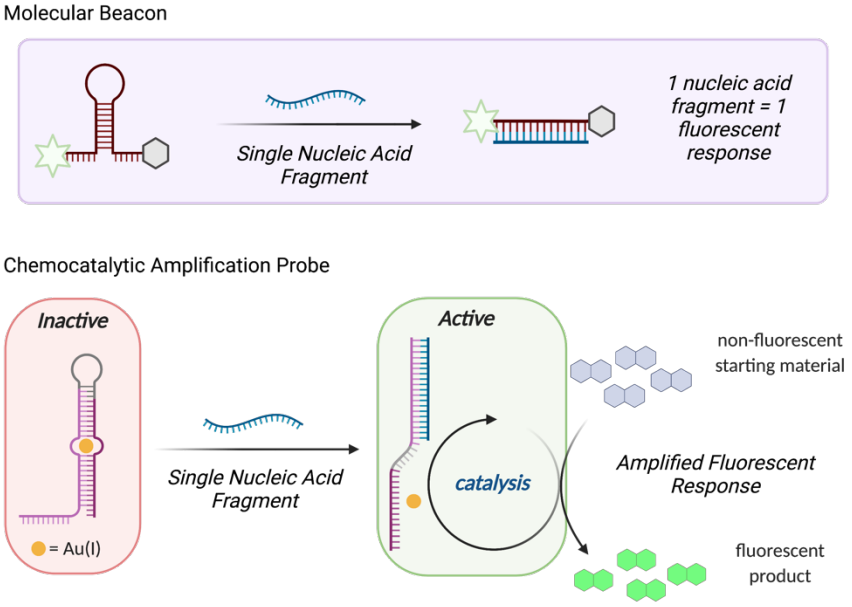

5.3 Probe Design and Initial Sequences

In initial efforts, we designed several Au(I)-CAPs complementary to various portions of the SARS-CoV-2 N gene viral transcript DNA. Building on the design principles that were discovered in previous experiments, all three initial hairpins contained a poly-T loop, consisting of 4 adjacent thymines (Chapter Three and Four).[10] In addition, the C–C mismatch was surrounded by A–T matches on either side, as this would lead to the most stable metal-mediated base pair.[11] Finally a toehold length of between 15 and 30 nucleotides was incorporated, as previous studies showed that a longer toehold would result in the formation of the active duplex, despite the high stability of the C–Au(I)–C mismatch employed in the initial CAP complex (*Figure 5.2a*).

Exposing these new hairpin sequences to our previous standard conditions (Chapter Four), we found that all three hairpins (dHP1, dHP2, dHP3) led to a significant increase in fluorescence when added 1 equivalent complement (1 μM) (*Figure 5.2b*). However, only dHP1 resulted in significant increases in fluorescence when exposed to lower concentrations of complement down

to 1 nM (*Figure 5.2c*). While this initial hit would require further optimization to get down to more relevant concentration of SARS-CoV-2 related nucleic acids (aM–fM), it was already more sensitive than reported molecular beacons.[12]

Figure 5.2 a) Probe sequences and design requirements (red = polyT loop, green = mismatch region, purple = toehold). b) Fluorescence intensity of initial sequences. c) Fold increase in fluorescence of initial sequences.

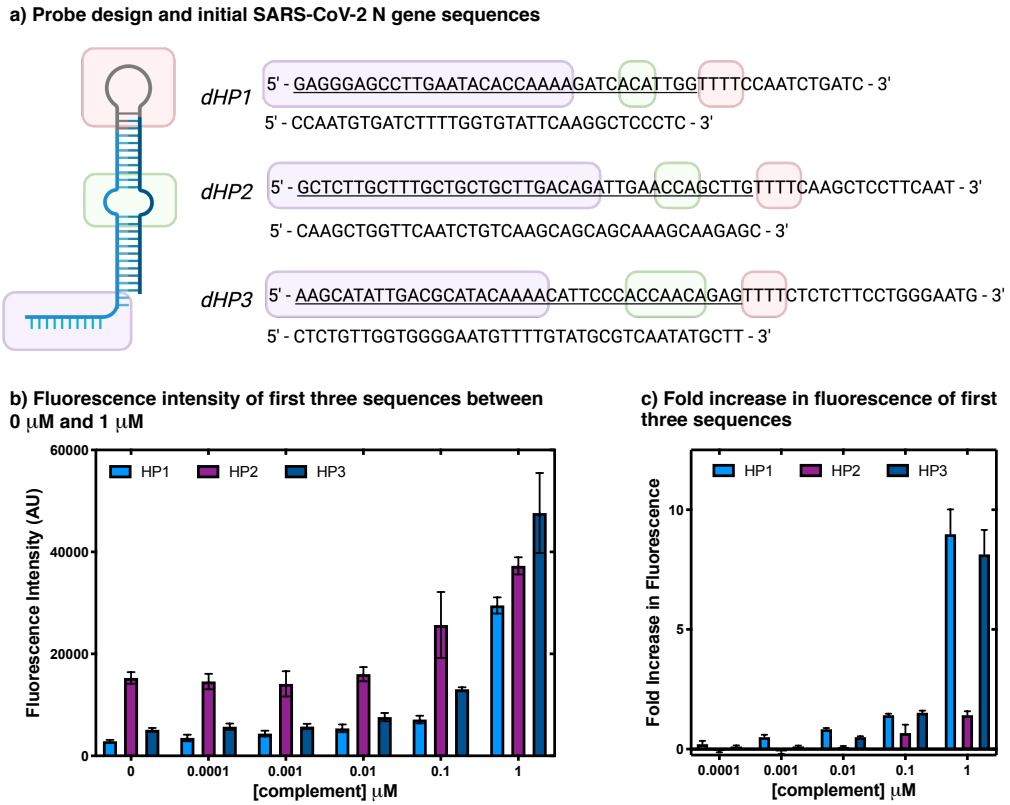

5.4 Optimization to Increase Sensitivity of Detection

Further optimization of our initial hairpin, dHP1, resulted in increased sensitivity down to the low aM range. We found that lowering the concentration of our Au(I)-CAP complex down to 100 nM, resulted in a decrease in background (no complement added) and increased the sensitivity

at lower concentrations. In addition, a change in buffer from only 150 mM sodium perchlorate to include a synthetic saliva solution that contains various phosphate and chloride salts lowered the background and variation in fluorescence values and provided more consistent results and an increase in sensitivity. Interestingly, we found that this sequence outperforms the current molecular beacon used in the current CDC test (2019-nCOV_N1 probe – FAM, BHQ-1) in the direct detection complementary transcripts (250 nM in our hands without PCR amplification, showing significant differences down to 19 nM) by an astounding 10^7-fold increase in sensitivity.

Figure 5.3 Fluorescence intensity of CDC N1 probe at 250 nM with various concentrations of complement (a) and HP1-Au(I) complex at 100 nM with various concentrations of complement (b).

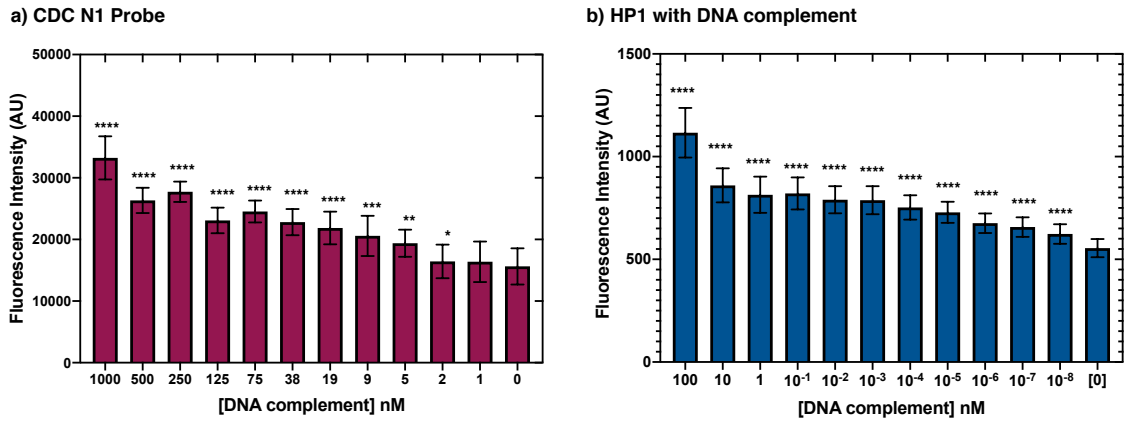

In addition, examination of hairpin structures that hybridize to the N gene of the viral genome, hairpin **rHP6** (5'-AGT CGC AGC ACA GCT CGC TGG TCC AGA ACT GAT TTT TCA CTT CTG G-3') resulted in a significant increase in fluorescence when exposed to 100 nM of the complementary RNA sequence with 95% accuracy, using a limit of detection (LOD) threshold analogous to FDA regulations.[13] Further comparison of the mean intensities using one-

way ANOVA and the Tukey-Kramer Honestly Significant Difference (HSD) test ($p < 0.0001$) however, show a significant difference in mean intensities down to 10 fM (*Figure 5.4a*) when compared to conditions without the complementary sequence. Given these promising initial experiments, we were eager to see if the **rHP6** Au(I)-CAP would be compatible with conditions relevant to real human samples. Interestingly, conducting these experiments in a solution of synthetic saliva containing 10 mg/mL of random sequence DNA (salmon testes DNA) showed an increase in sensitivity, with >95% of the values above the threshold for 1 fM of complementary RNA fragment (*Figure 5.4b*).

Figure 5.4 a) Fluorescence intensity of 100 nM 100 nM rHP6-Au(I) at standard condition (125 mM sodium perchlorate) b) Fluorescence intensity of 100 nM rHP6-Au(I) with synthetic saliva.

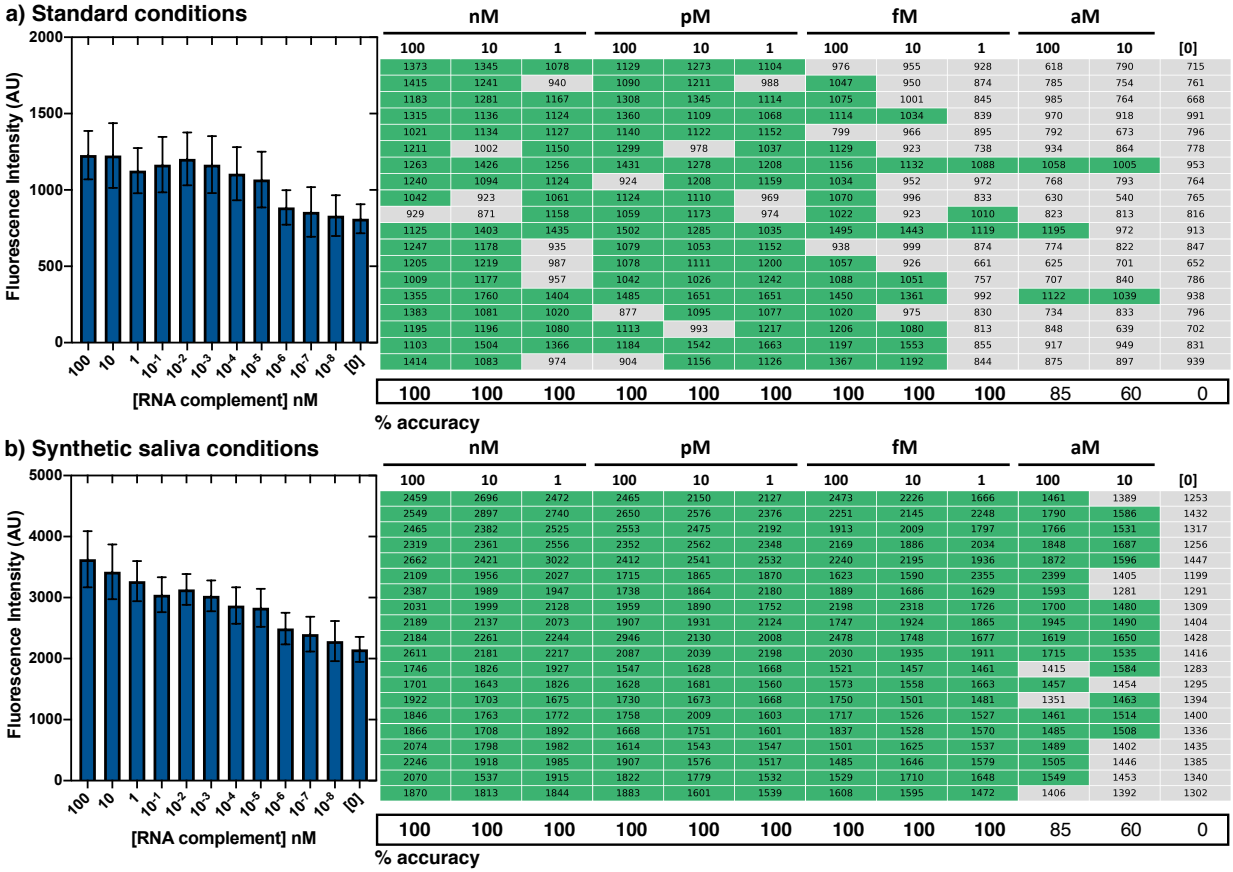

a) Standard conditions	nM			pM			fM			aM		
	100	10	1	100	10	1	100	10	1	100	10	[0]
	1373	1345	1078	1129	1273	1104	976	955	928	618	790	715
	1415	1241	940	1090	1211	988	1047	950	874	785	754	761
	1183	1281	1167	1308	1345	1114	1075	1001	845	985	764	668
	1315	1136	1124	1360	1109	1068	1114	1034	839	970	918	991
	1021	1134	1127	1140	1122	1152	799	966	895	792	673	796
	1211	1002	1150	1299	978	1037	1129	923	738	934	864	778
	1263	1426	1256	1431	1278	1208	1156	1132	1088	1058	1005	953
	1240	1094	1124	924	1208	1159	1034	952	972	768	793	764
	1042	923	1061	1124	1110	969	1070	996	833	630	540	765
	929	871	1158	1059	1173	974	1022	923	1010	823	813	816
	1125	1403	1435	1502	1285	1035	1495	1443	1119	1195	972	913
	1247	1178	935	1079	1053	1152	938	999	874	774	822	847
	1205	1219	987	1078	1111	1200	1057	926	661	625	701	652
	1009	1177	957	1042	1026	1242	1088	1051	757	707	840	786
	1355	1760	1404	1485	1651	1651	1450	1361	992	1122	1039	938
	1383	1081	1020	877	1095	1077	1020	975	830	734	833	796
	1195	1196	1080	1113	993	1217	1206	1080	813	848	639	702
	1103	1504	1366	1184	1542	1663	1197	1553	855	917	949	831
	1414	1083	974	904	1156	1126	1367	1192	844	875	897	939
% accuracy	100	100	100	100	100	100	100	100	100	85	60	0

b) Synthetic saliva conditions	nM			pM			fM			aM		
	100	10	1	100	10	1	100	10	1	100	10	[0]
	2459	2696	2472	2465	2150	2127	2473	2226	1666	1461	1389	1253
	2549	2897	2740	2650	2576	2376	2251	2145	2248	1790	1586	1432
	2465	2382	2525	2553	2475	2192	1913	2009	1797	1766	1531	1317
	2319	2361	2556	2352	2562	2348	2169	1886	2034	1848	1687	1256
	2662	2421	3022	2412	2541	2532	2240	2195	1936	1872	1596	1447
	2109	1956	2027	1715	1865	1870	1623	1590	2355	2399	1405	1199
	2387	1989	1947	1738	1864	2180	1889	1686	1629	1593	1281	1291
	2031	1999	2128	1959	1890	1752	2198	2318	1726	1700	1480	1309
	2189	2137	2073	1907	1931	2124	1747	1924	1865	1945	1490	1404
	2184	2261	2244	2946	2130	2008	2478	1748	1677	1619	1650	1428
	2611	2181	2217	2087	2039	2198	2030	1935	1911	1715	1535	1416
	1746	1826	1927	1547	1628	1668	1521	1457	1461	1415	1584	1283
	1701	1643	1826	1628	1681	1560	1573	1558	1663	1457	1454	1295
	1922	1703	1675	1730	1673	1668	1750	1501	1481	1351	1463	1394
	1846	1763	1772	1758	2009	1603	1717	1526	1527	1461	1514	1400
	1866	1708	1892	1668	1751	1601	1837	1528	1570	1485	1508	1336
	2074	1798	1982	1614	1543	1547	1501	1625	1537	1489	1402	1435
	2246	1918	1985	1907	1576	1517	1485	1646	1579	1505	1446	1385
	2070	1537	1915	1822	1779	1532	1529	1710	1648	1549	1453	1340
	1870	1813	1844	1883	1601	1539	1608	1595	1472	1406	1392	1302
% accuracy	100	100	100	100	100	100	100	100	100	85	60	0

5.5 RNAse P Gene Control

Similar to previously reported COVID-19 detection assays, we designed a Au(I)-CAP complex to detect transcripts of the human RNAse P gene as a positive control for RNA extraction.[14, 15] We found that this Au(I)-CAP (**Hs_RPP30** 5'-CCG CGC AGA GCC TTC AGG TCA GAA TTT TTT CTC ACC T-3') has exceptional sensitivity and low background reactivity. Akin to our hairpin complex for the SARS-CoV-2 N gene (**rHP6**), we were able to detect femtomolar (10 fM, ≥95% accuracy) concentrations of the human RNAse P gene transcript after 2 hours (*Figure 5.5a*). Importantly, we found that the addition of short nucleic acid fragments that are non-complementary to **rHP6** or **Hs_RPP30** do not result in an increase in fluorescence; Only the addition of the complementary sequence leads to the formation of fluorescent product and therefore selective detection of short nucleic acids can be achieved through this system, as the addition of a short MERS related nucleic acid sequence does not result in a concentration dependent increase in fluorescence (*Figure 5.5b*).

Figure 5.5 **a)** Control experiments with Hs_RPP30 hairpin and complement and b) rHP6 sequence with MERS wrong complement.

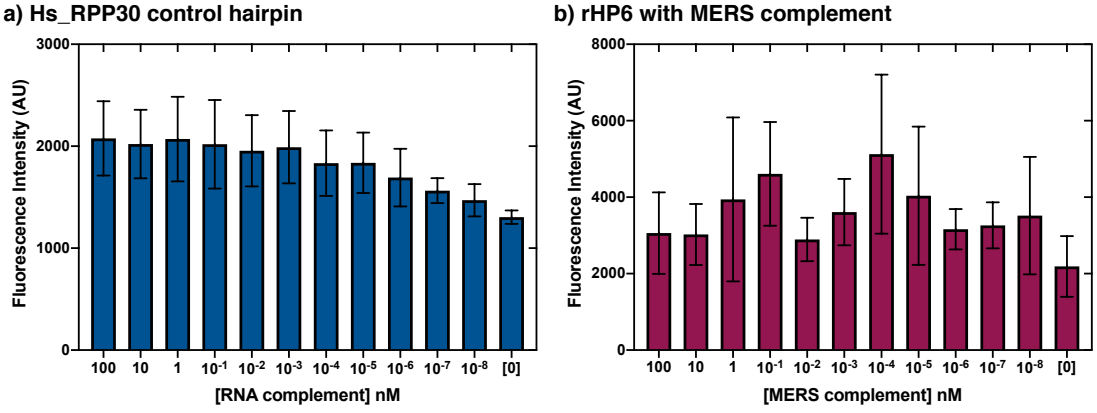

5.6 Kinetic Experiments of rHP6 and dHP1

Kinetic experiments of **rHP6** revealed a significant increase in fluorescence of the solutions containing complement within the first several hours, Figure 5.6 shows the change in each concentration's probability distribution over time. After the first 60 minutes there is no overlap between 100 nM and the no complement reaction, meaning that all of the values at 100 nM have surpassed the LOD threshold after 60 minutes (*Figure 5.6a*). After only 180 minutes, the fluorescence values of the reactions containing 100 fM of complement have very little overlap with the no complement reactions and are near the LOD (*Figure 5.6b*). While at early time points, the fluorescence is fairly low, after 36 hours, the fluorescence differences are visible to the eye under long wave UV irradiation using an inexpensive hand-held TLC lamp (*Figure 5.6c*). Longer reaction times resulted in an increase in the background from the experiment containing no complement. This background is likely due to leaching of gold and decomposition of the hairpin-Au complex.

Figure 5.6 Probability density of rHP6 reactions at a) 60 minutes and b) 180 minutes. c) Fluorescence of rHP6 reactions after 36 hours with various concentrations of complement added.

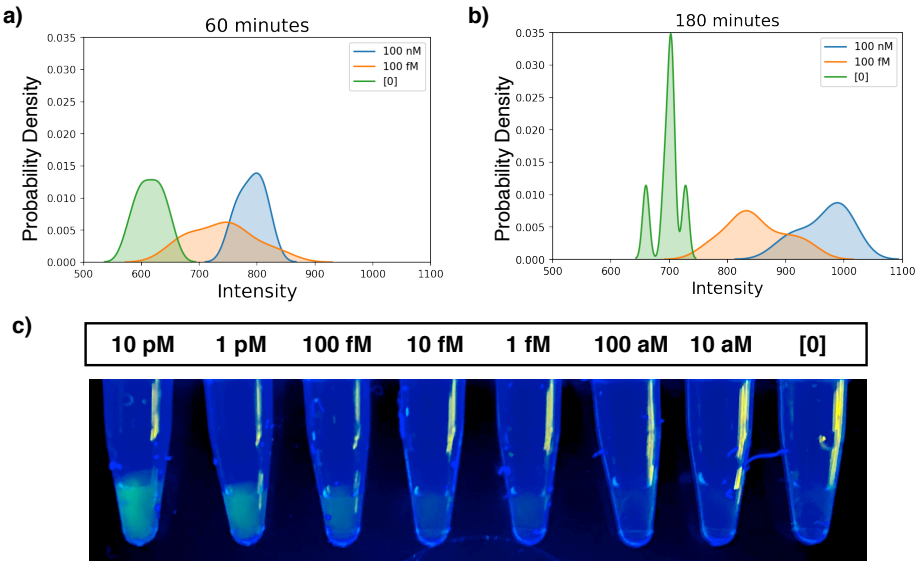

5.7 Heat Inactivated Virus in Saliva

To further validate our method as a diagnostic tool for detection of SARS-CoV-2, we added our **rHP6** hairpin-Au(I) complex and profluorophore **4.1 (**Chapter Four**)** to saliva samples (human pooled saliva from Innovative Research) spiked with heat-inactivated virus (concentration quantified using qPCR). Interestingly, there was a significant increase in fluorescence in healthy saliva samples spiked with approximately 550 copies (55 copies/□L) compared to the reaction containing only non-contaminated saliva after 24 hours (*Figure 5.7*). These results highlight the potential ability of this Au(I)-DNA catalytic system to be used directly with saliva samples from individuals infected with SARS-CoV-19.

Figure 5.7 Au(I)-CAP system (rHP6 sequence) with SARS-CoV-2 heat inactivated virus in human saliva.

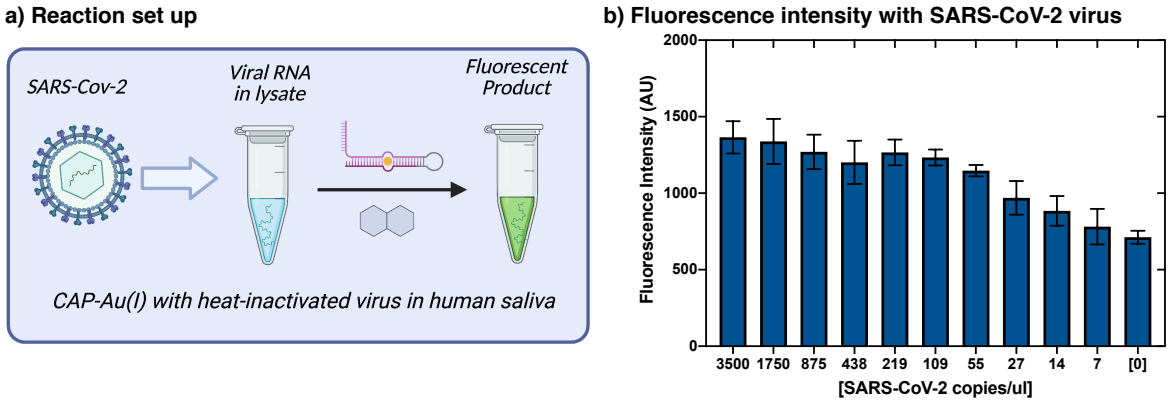

5.8 Catalytic Amplification with PCR and RPA Amplification

The sensitivity of this Au(I)-CAP system down to 14-27 copies/ml without the need for nucleic amplification is unprecedented for detection of nucleic acids. However, this would only allow for the detection of SARS-CoV-2 in individuals with very high viral loads and is higher than standard PCR assays for COVID detection (approx. 1 copy/ml).[16] We thought we could merge our Au(I)-CAP system with standard nucleic acid amplification methods, such as PCR and recombinase polymerase amplification (RPA), to obtain very low detection of COVID viral fragments.

Initially we designed primers for PCR and RPA that would amplify a SARS-CoV-2 N gene fragment that is complementary to our rHP6-Au(I) complex. Following standard protocols for amplification of these fragments with the respective amplification methods,[17] our Au(I)-CAP probe and profluorophore substrate were added directly to amplification reactions. Interestingly, we found that signal amplification through our Au(I)-CAP system, along with a standard PCR and

RPA nucleic acid amplification methods led to the detection of SARS-CoV-2 down to 0.1 and 1 copy/ml, respectively (*Figure 5.8*). While these results are only slightly more sensitive than standard PCR or amplification methods on their own, they don't require expensive, modified molecular beacons as do standard qPCR reactions.

Figure 5.8 PCR and RPA amplification methods with rHP6 Au(I)-CAP system.

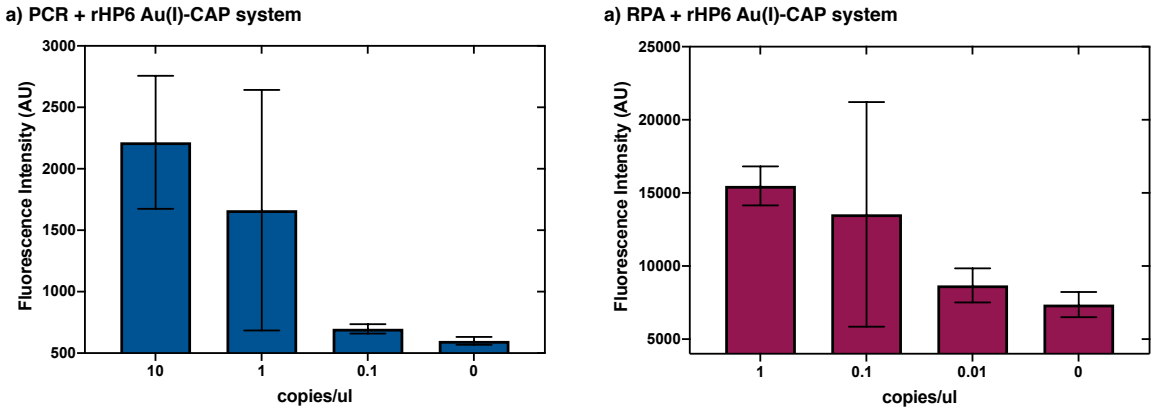

5.9 Conclusion

In conclusion, we have demonstrated the early development of a COVID-19 detection method, which culminated in the ability to detect femtomolar to attomolar concentrations of viral RNA fragments with ≥85% accuracy. Often methods to detect genetic information require expensive enzymes, probes, or instrumentation, however, we have demonstrated the detection of femtomolar concentrations of short nucleic acid transcripts with simple coumarin probes and inexpensive gold salts that could ultimately lead to the development of a cheap and accessible point-of-care viral diagnostics test. In addition, we have shown that this catalytic amplification system can be paired with a nucleic acid amplification system to achieve very low detection of SARS-CoV-2 fragments. We believe this system has potential to be a complementary method to nucleic acid amplification in the detection of nucleic acids.

5.10 Experimental Section

5.10.1 Materials and Methods

Unless stated otherwise, reactions were performed in flame-dried glassware under an atmosphere of nitrogen. Benzene, THF, dichloromethane, and dimethylformamide were degassed and dried in a JC Meyer solvent system. SilicaFlash P60 silicagel (230–400 mesh) was used for flash chromatography. NMR spectra were recorded on a Bruker AV-300 (1H), Bruker AV-400 (1H, 13C), Bruker DRX-500 (1H), and Bruker AV-500 (1H, 13C). 1H NMR spectra are reported relative to $CDCl_3$ (7.26 ppm). All oligonucleotides were purchased through Integrated DNA Technology with standard desalting unless otherwise specified. Samples for thermal denaturation, mass spectrometry studies, and catalysis were prepared by heating the buffered DNA solution without metal at 90 °C in a heating block for 10 minutes then cooled to room temperature for 30 minutes. Once cool, the metal solution was added. In thermal denaturation experiments, all absorbances were measured at 260 nm using HP-8453 spectrophotometer with HP-89090A Peltier temperature controller from 15–90 °C at 5 °C min^{-1} with a hold time of 1 min. Relative absorbance, $A_{260nm}=(A_t–A_{15\,°C})/(A_{90\,°C}–A_{15\,°C})$, vs. temperature (°C) curves were fitted using GraphPad Prism 7.0c. Fluorescence experiments were recorded on a Tecan Infinite M1000 Pro plate reader with the following conditions: 480 nm excitation, 510 nm emission, 8 mm excitation and emission bandwidth, 50 flashes with a frequency of 400 Hz, and a 10 ms delay time. Fluorescence data was collected on a JASCO-J715 CD spectrophotometer with a scan rate of 20 nm/min from 200 nm to 300 nm with 3 accumulations. Mass spectrometry data was collected on a Thermo Scientific Q Exactive Plus Hybrid Quadrupole-Orbitrap Mass Spectrometer using negative ionization mode.

5.10.3 Experiments with SARS-CoV-2 Transcripts

General Procedure

All experiments were performed with lights off/lights lowered and any solution containing Au(I) was left strictly in the dark (wrapped in tinfoil). All pipette tips were RNAse and DNAse free. Unless stated otherwise, all water was nuclease free. Experiments were performed with either no saliva conditions: 125 mM sodium perchlorate, 200 μM probe 5.1 (for synthesis, see Chapter 5), 100 nM Hairpin-Au(I) complex, in 40% EtOH or synthetic saliva conditions: 125 mM sodium perchlorate, 200 μM probe 1, 100 nM Hairpin-Au(I) complex, 40% EtOH, 4% synthetic saliva and 10 μg/ml. A 50 ml concentrated saliva solution consisted of 100 mg of methyl-p-hydroxybenzoate, 500 mg sodium carboxymethyl cellulose, 31.3 mg KCl, 3.0 mg $MgCl_2•6H_2O$, 8.3 mg $CaCl_2•2H_2O$, 40.2 mg K_2HPO_4, and 16.3 mg KH_2PO_4.

Figure 5.9 Profluorophore used to monitor reaction.

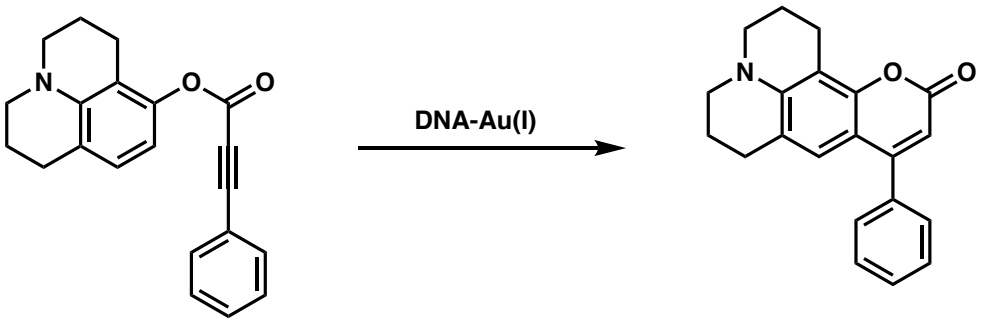

5.1

Table 5.1 Sequences used in COVID-19 catalysis experiments.

Sequence	Hairpin (5'-3')
rHP6	ACTCGCAGCACAGCTCGCTGGTCCAGAACTGATTTTTCACTTCTGG
rHP6 complement (DNA)	AAATCAGTTCTGGACCAGCGAGCTGTGCTGCGACT
rHP6 complement (RNA)	AAAUCAGUUCUGGACCAGCGAGCUGUGCUGCGACU
dHP1	GAGGGAGCCTTGAATACACCAAAAGATCACATTGGTTTTCCAATCTGATC
dHP1 complement	CCAATGTGATCTTTTGGTGTATTCAAGGCTCCCTC
dHP2	GCTCTTGCTTTGCTGCTGCTTGACAGATTGAACCAGCTTGTTTTCAAGCTCCTTCAAT
dHP2 complement	CAAGCTGGTTCAATCTGTCAAGCAGCAGCAAAGCAAGAGC
dHP3	AAGCATATTGACGCATACAAACATTCCCACCAACAGAGTTTTCTCTCTTCCTGGGAATG
dHP3 complement	CTCTGTTGGTGGGAATGTTTTGTATGCGTCAATATGCTT
Hs_RPP30	CCGCGCAGAGCCTTCAGGTCAGAATTTTTTCTCACCT

Hs_RPP30 Complement (DNA)	TTCTGACCTGAAGGCTCTGCGCGG
Hs_RPP30 Complement (RNA)	TTCTGACCTGAAGGCTCTGCGCGG
2019-NCoV_N1	FAM-ACCCCGCATTACGTTTGGTGGACC-BHQ1
2019-NCoV_N1 complement	GGTCCACCAAACGTAATGCGGGGTG
MERS complement	GGATGGCATCGTTGGGTCCATGAAGATGGCGC

5.10.3.1 Data

Figure 5.10 Fluorescence values for rHP6 with rHP6 DNA complement with no saliva conditions.

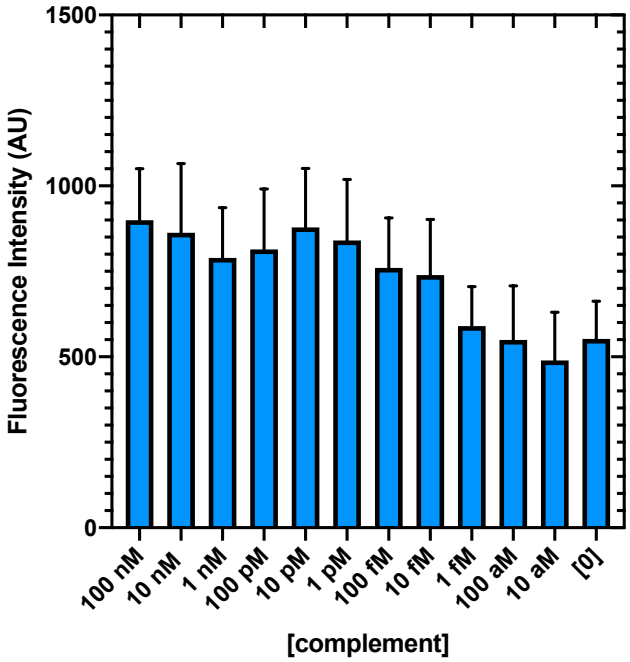

Table 5.2 Fluorescence values for rHP6 with rHP6 RNA complement with no saliva conditions (*Figure 5.4a*).

[Complement] nM	Mean	Std. Dev.
100	1228	159
10	1225	212
1	1126	148

10^{-1}	1166	182
10^{-2}	1203	173
10^{-3}	1166	187
10^{-4}	1106	174
10^{-5}	1068	182
10^{-6}	886	113
10^{-7}	856	163
10^{-8}	832	133
[0]	812	95

Table 5.3 Fluorescence values for rHP6 with rHP6 RNA complement with no saliva conditions (*Figure 5.4b*).

[Complement] nM	Mean	Std. Dev.
100	3628	460
10	3423	450
1	3270	330

10^{-1}	3047	286
10^{-2}	3133	252
10^{-3}	3028	253
10^{-4}	2870	300
10^{-5}	2834	311
10^{-6}	2493	259
10^{-7}	2401	285
10^{-8}	2287	329
[0]	2151	205

Figure 5.11 Comparison of mean intensities of rHP6 with DNA complement in no saliva conditions using one-way ANOVA and Tukey-Kramer HSD test at $p < 0.0001$ evaluated with no complementary RNA (no analyte control).

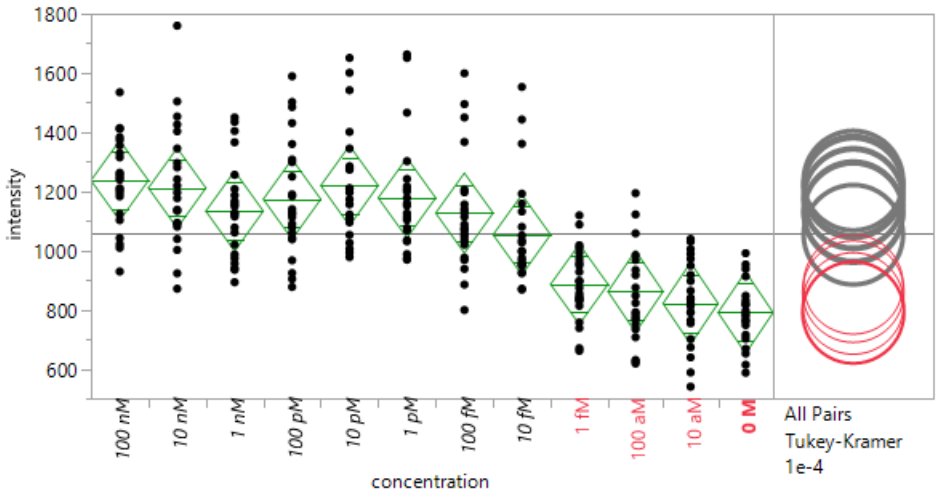

Table 5.4 Raw fluorescence values for rHP6 with rHP6 DNA complement with no saliva conditions.

nM			pM			fM			aM		
100	10	1	100	10	1	100	10	1	100	10	[0]
1373	1345	1078	1129	1273	1104	976	955	928	618	790	715
1415	1241	940	1090	1211	988	1047	950	874	785	754	761
1183	1281	1167	1308	1345	1114	1075	1001	845	985	764	668
1315	1136	1124	1360	1109	1068	1114	1034	839	970	918	991
1021	1134	1127	1140	1122	1152	799	966	895	792	673	796
1211	1002	1150	1299	978	1037	1129	923	738	934	864	778
1263	1426	1256	1431	1278	1208	1156	1132	1088	1058	1005	953
1240	1094	1124	924	1208	1159	1034	952	972	768	793	764
1042	923	1061	1124	1110	969	1070	996	833	630	540	765
929	871	1158	1059	1173	974	1022	923	1010	823	813	816
1125	1403	1435	1502	1285	1035	1495	1443	1119	1195	972	913
1247	1178	935	1079	1053	1152	938	999	874	774	822	847
1205	1219	987	1078	1111	1200	1057	926	661	625	701	652
1009	1177	957	1042	1026	1242	1088	1051	757	707	840	786
1355	1760	1404	1485	1651	1651	1450	1361	992	1122	1039	938
1383	1081	1020	877	1095	1077	1020	975	830	734	833	796
1195	1196	1080	1113	993	1217	1206	1080	813	848	639	702
1103	1504	1366	1184	1542	1663	1197	1553	855	917	949	831
1414	1083	974	904	1156	1126	1367	1192	844	875	897	939

Figure 5.12 Fluorescence values for rHP6 with rHP6 DNA complement with synthetic saliva conditions.

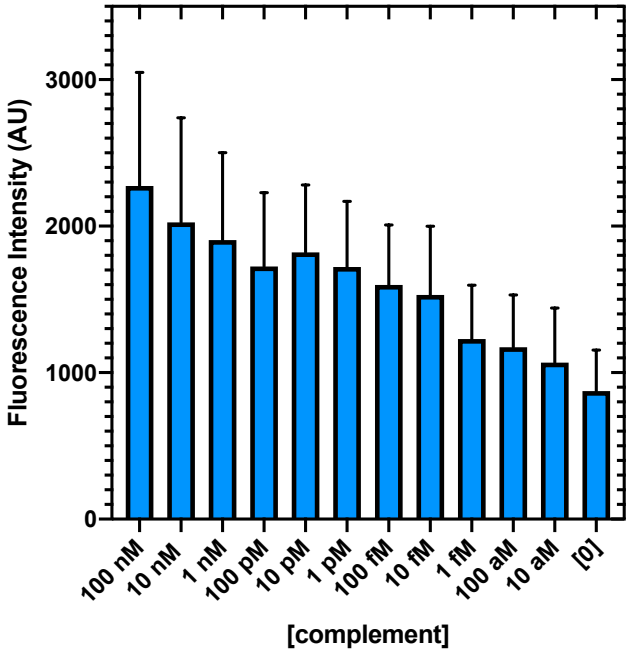

Figure 5.13 Comparison of mean intensities of rHP6 with DNA complement in synthetic saliva conditions using one-way ANOVA and Tukey-Kramer HSD test at $p < 0.0001$ evaluated at no complement condition (0 M of analyte).

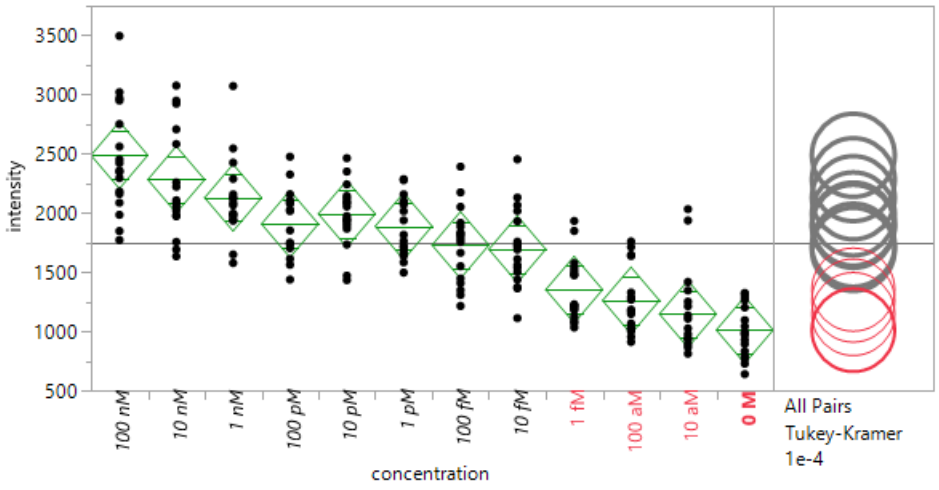

Table 5.5 Raw fluorescence values for rHP6 with rHP6 DNA complement with synthetic saliva conditions.

nM			pM			fM			aM		
100	10	1	100	10	1	100	10	1	100	10	[0]
3496	2923	2126	2329	2122	1721	1823	1111	1484	1169	1417	1041
2358	2258	2128	2475	2241	2071	1834	1500	1576	1328	1251	1264
2346	1976	2157	2325	1866	1938	1663	1930	1179	1146	976	1094
2970	2949	2545	1755	1893	2286	1916	1691	1087	1288	931	991
2970	2949	2545	1755	1893	2286	1916	1691	1087	1288	931	991
2561	2109	2121	2026	1946	2277	2174	2453	1848	1646	1936	1315
2421	2021	1577	1437	1470	1679	1214	1559	1508	953	944	893
2973	2221	3072	2077	1733	2090	1754	1373	1032	1174	1025	638
2950	2707	2425	2091	2084	1713	1307	1610	1932	1636	2032	1324
2452	1755	2065	2158	2463	2157	2391	2065	1481	1266	1345	1288
2751	1980	2288	2107	2350	2099	2051	2130	1218	1759	1107	1202
2161	2582	1974	1612	2144	1762	1550	1733	1538	1712	1134	970
2161	2582	1974	1612	2144	1762	1550	1733	1538	1712	1134	970
3020	1634	1942	1753	1432	2015	1347	2017	1068	912	811	726
1984	3076	1935	2016	1939	1638	1757	1363	1228	1066	1212	927
2086	2056	1649	1562	2054	1815	1884	1536	1210	1028	891	791
1771	1691	2084	1702	2093	1708	1781	1757	1124	910	864	832
2182	2084	1988	1736	2088	1496	1407	1442	1473	1183	942	1201
1847	1972	1996	1852	1974	1583	1446	1437	1233	999	1106	982
2295	2107	1988	1749	1917	1652	1807	1719	1191	1020	932	767

Figure 5.14 Fluorescence values for Hs_RPP30 with Hs_RPP30 DNA complement with no saliva conditions.

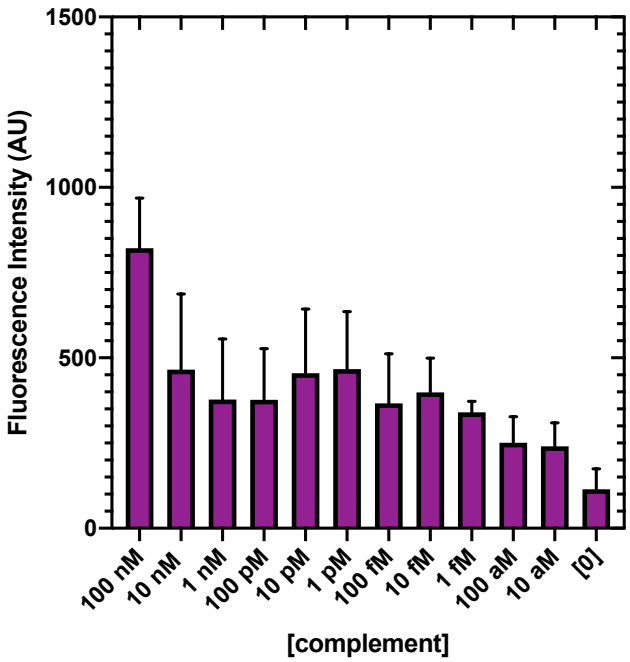

Figure 5.15 Fluorescence values rHP6 and MERS complement sequence.

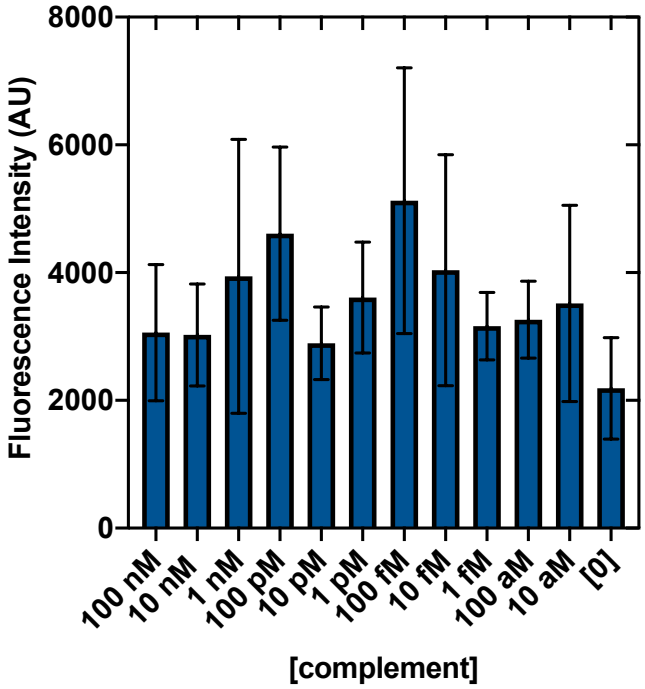

Figure 5.16 Optimization of probe **5.1** concentration from 50 mM to 500 mM with dHP1-Au(I) complex and dHP1 complement with synthetic saliva conditions.

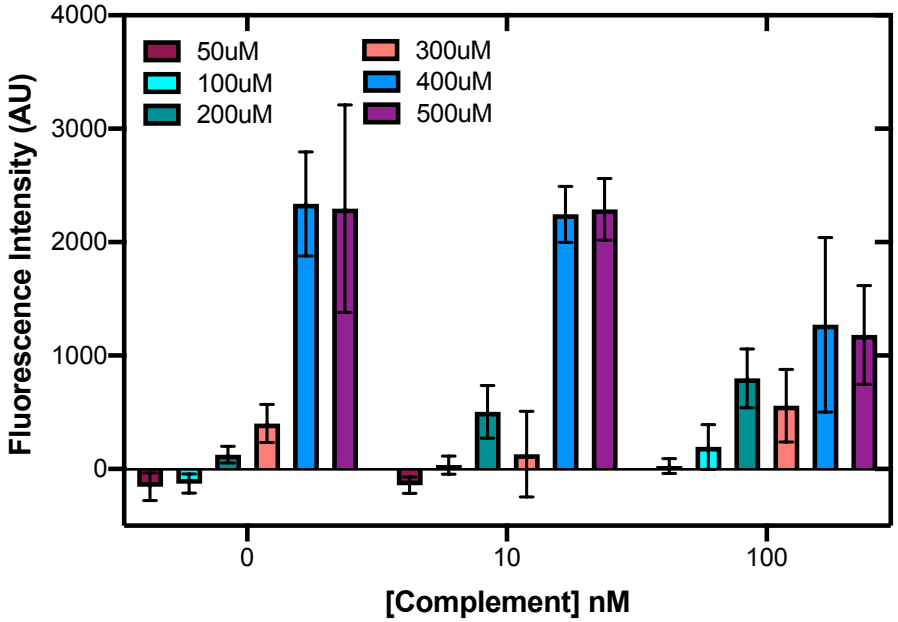

Table 5.6 Fluorescence values for dHP1 with complement with no saliva conditions at various probe (**5.1**) concentrations (*Figure 5.16*).

[Complement] nM	[**5.1**] μM	Mean	Std. Dev.
0	50	-156	122
1	50	-142	72
100	50	26	64
0	100	-128	85
1	100	35	80
100	100	194	197
0	200	126	74
1	200	505	233
100	200	799	260
0	300	401	168
1	300	130	377
100	300	558	319
0	400	2337	459

1	400	2245	247
100	400	1272	770
0	500	2296	914
1	500	2289	272
100	500	1183	435

Figure 5.17 Optimization of salt buffer with dHP1-Au(I) complex and dHP1 complement with synthetic saliva conditions.

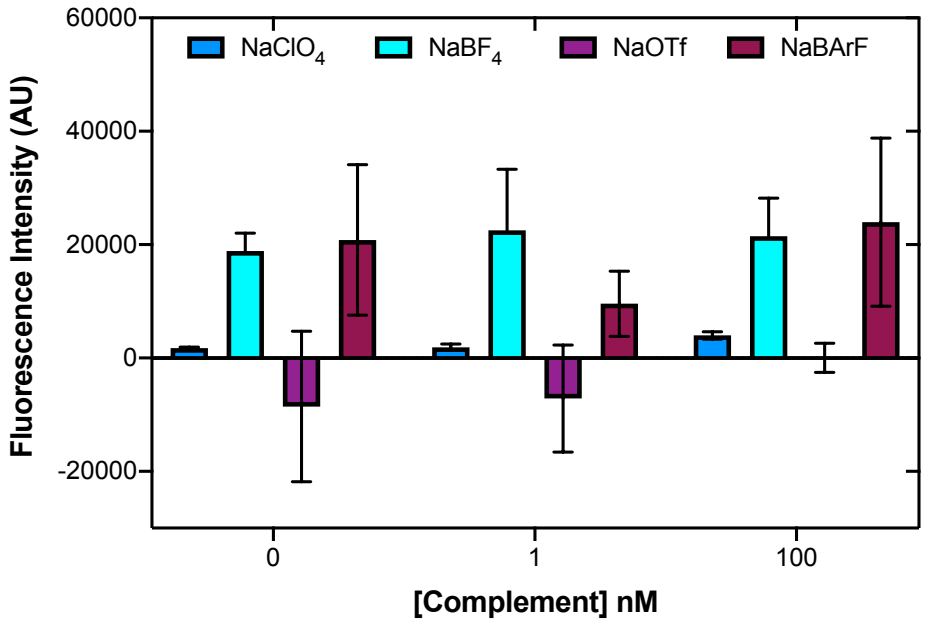

Table 5.7 Fluorescence values for dHP1 with complement with no saliva conditions and other salts (*Figure 5.17*).

[Complement] nM	Salt	Mean	Std. Dev.
100	$NaClO_4$	3992	657
1	$NaClO_4$	1902	544
0	$NaClO_4$	1763	179
100	$NaBF_4$	21471	6742
1	$NaBF_4$	22516	10772
0	$NaBF_4$	18895	3145
100	NaOTf	46	2565
1	NaOTf	-7150	9462
0	NaOTf	-8557	13284
100	NaBArF	23966	14845
1	NaBArF	9582	5756
0	NaBArF	20821	13272

Figure 5.18 dHP1-Au(I) complex and dHP1 complement with synthetic saliva conditions at different temperatures.

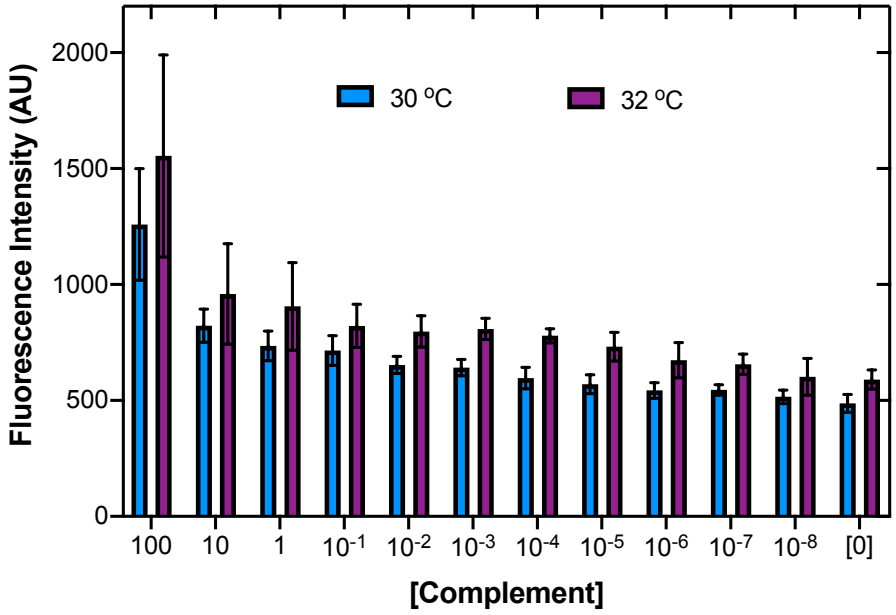

Table 5.8 Fluorescence values for dHP1 with complement with no saliva conditions at 30 °C (*Figure 5.18*).

[Complement] nM	Mean	Std. Dev.
100	1259	241
10	823	72
1	735	64
10^{-1}	653	64
10^{-2}	642	37

10^{-3}	597	35
10^{-4}	570	46
10^{-5}	643	41
10^{-6}	543	34
10^{-7}	546	22
10^{-8}	516	29
[0]	487	38

Table 5.9 Fluorescence values for dHP1 with complement with no saliva conditions at 32 °C (*Figure 5.18*).

[Complement] nM	Mean	Std. Dev.
100	1555	436
10	959	216
1	906	189
10^{-1}	822	93
10^{-2}	797	68

10^{-3}	809	46
10^{-4}	779	30
10^{-5}	731	62
10^{-6}	673	76
10^{-7}	657	44
10^{-8}	603	79
[0]	590	41

Table 5.10 p-values and 95% confidence intervals for experiment with a) rHP6 (*Figure 5.4b*), b) dHP1 (*Figure 5.3b*), and c) Hs_RPP30 (*Figure 5.5a*) based on t-test and f-test. Analysis was done using GraphPad Prism 7.0c with all 20 replicates shown in tables of figures from text.

a) rHP6 with RNA complement

[Complement]	p-value (t-test)	p-value (f-test)	95% CI
100 nM	< 0.0001 (****)	< 0.0001 (****)	2029–2302
10 nM	< 0.0001 (****)	< 0.0001 (****)	1880–2220
1 nM	< 0.0001 (****)	< 0.0001 (****)	1973–2305

100 pM	< 0.0001 (****)	< 0.0001 (****)	1829–2206
10 pM	< 0.0001 (****)	< 0.0001 (****)	1803–2124
1 pM	< 0.0001 (****)	< 0.0001 (****)	1740–2055
100 fM	< 0.0001 (****)	< 0.0001 (****)	1725–2030
10 fM	< 0.0001 (****)	< 0.0001 (****)	1664–1917
1 fM	< 0.0001 (****)	< 0.0001 (****)	1622–1857
100 aM	< 0.0001 (****)	< 0.0001 (****)	1525–1758
10 aM	< 0.0001 (****)	0.1962	1447–1539
[0]	–	–	1313–1380

b) dHP1 with DNA complement

[Complement]	p-value (t-test)	p-value (f-test)	95% CI
100 nM	< 0.0001 (****)	< 0.0001 (****)	1060–1173
10 nM	< 0.0001 (****)	0.0092 (**)	821–899
1 nM	< 0.0001 (****)	0.0044 (**)	733–856
100 pM	< 0.0001 (****)	0.0187 (*)	784–857

10 pM	< 0.0001 (****)	0.0918	759–821
1 pM	< 0.0001 (****)	0.0679	756–820
100 fM	< 0.0001 (****)	0.2131	725–780
10 fM	< 0.0001 (****)	0.5237	705–753
1 fM	< 0.0001 (****)	0.7533	653–698
100 aM	< 0.0001 (****)	0.7606	634–679
10 aM	< 0.0001 (****)	0.7677	601–646
[0]	–	–	534–575

c) Hs_RPP30 with RNA complement

[Complement]	p-value (t-test)	p-value (f-test)	95% CI
100 nM	< 0.0001 (****)	< 0.0001 (****)	1906–2247
10 nM	< 0.0001 (****)	< 0.0001 (****)	1865–2179
1 nM	< 0.0001 (****)	< 0.0001 (****)	1877–2265
100 pM	< 0.0001 (****)	< 0.0001 (****)	1816–2223
10 pM	< 0.0001 (****)	< 0.0001 (****)	1792–2120
1 pM	< 0.0001 (****)	< 0.0001 (****)	1824–2151

100 fM	< 0.0001 (****)	< 0.0001 (****)	1682–1984
10 fM	< 0.0001 (****)	< 0.0001 (****)	1699–1976
1 fM	< 0.0001 (****)	< 0.0001 (****)	1560–1825
100 aM	< 0.0001 (****)	0.0095 (**)	1507–1622
10 aM	< 0.0001 (****)	0.0040 (***)	1396–1544
[0]	–	–	1274–1335

Table 5.11 dHP1 initial values in 125 mM sodium perchlorate conditions (*Figure 5.2b*).

[Complement] nM	Mean	Std. Dev.
100	29507	1585
10	7123	745
1	5386	766
10^{-1}	4374	573
10^{-2}	3519	649
0	2878	242

Table 5.12 dHP2 initial values in 125 mM sodium perchlorate conditions (*Figure 5.2b*).

[Complement] nM	Mean	Std. Dev.
100	37280	1686
10	25677	6460
1	16026	1390
10^{-1}	14120	2474
10^{-2}	14580	1527
0	15289	1150

Table 5.13 dHP3 initial values in 125 mM sodium perchlorate conditions (*Figure 5.2b*).

[Complement] nM	Mean	Std. Dev.
100	47640	7855
10	13078	391
1	7598	804
10^{-1}	5789	521
10^{-2}	5725	605

0	5106	365

5.10.4 Heat-Inactivated Virus Concentration

qPCR with the SARS-CoV-2 kit N1 gene was used to quantify the effective concentration of genome equivalents in heat-inactivated virus VR-1986HK (purchased through ATCC). A standard curve of log[copies/ul] vs. Ct (threshold cycle) was created using the positive control N gene plasmid as well as the SARS-CoV-2 kit was purchased through IDT (10006625 and 10006713). Copies/ul concentrations of the positive control (800 copies/ul, 400 copies/ul, 50 copies/ul, and 5 copies/ul) were in triplicate made from a dilution of the positive control into RNAse free water. The unknown heat-inactivated virus concentration was made through a 1:10 dilution directly from the sample into water with 0.5% tween. Virus concentration was calculated as an average of the three copies/ul of genomic copies using the generated standard curve. qPCR was performed using the GoTaq Probe 1-Step qPCR kit using the conditions listed in the kit instructions: each reaction contains 3.1 ul water, 1.5 ul primer/probe mix, 10 ul GoTaq Probe qPCR master mix, 0.4 Go Script RT Mix and 5 ul target nucleic acid (positive control or virus dilution).

Figure 5.19 Threshold cycle vs log[copies/µl].

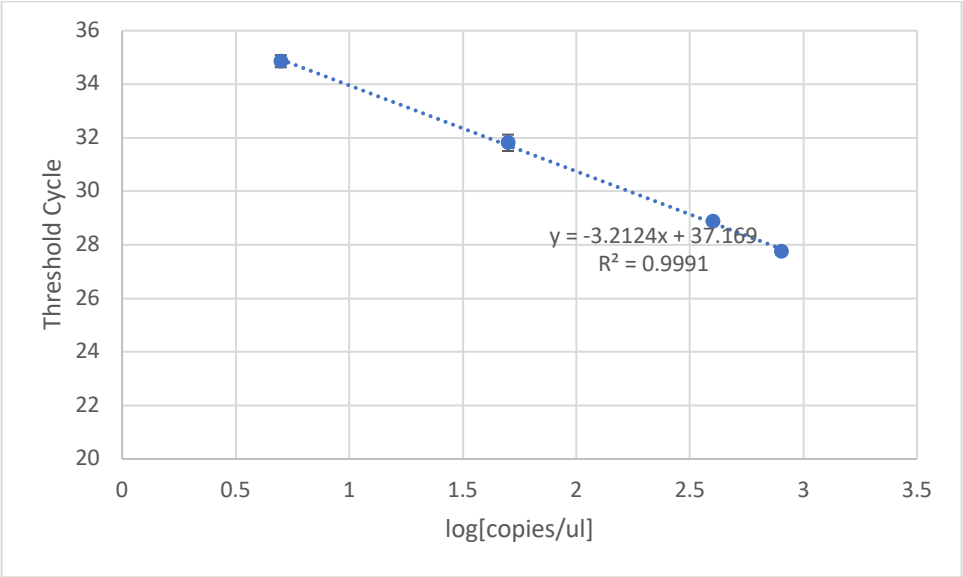

Table 5.14 Ct values for the heat-inactivated RNA based on curve.

	Ct (Threshold Cycle)	**copies/ul**
Trial 1	24.64	317877.083
Trial 2	24.83	277404.441
Trial 3	24.29	408518.781
average		334600.102
standard deviation		67137.8213

Table 5.15 Fluorescence values for reaction containing rHP6 with different concentrations of heat-inactivated virus (*Figure 5.7b*).

[copies/µl]	Mean	Std. Dev.	p-value (t-test)
3500	1365	105	**** (<0.0001)
1750	1338	147	**** (<0.0001)
875	1270	112	**** (<0.0001)
438	1201	141	*** (0.0003)
219	1267	84	**** (<0.0001)
109	1234	52	**** (<0.0001)
55	1148	37	**** (<0.0001)
27	969	110	** (0.0012)
14	885	97	** (0.0067)
7	782	116	0.2470
[0]	712	42	__

5.10.5 Polymerase Chain Reaction and Recombinase Polymerase Reactions

Table 5.16 Primers used in PCR and RPA reactions.

Sequence	DNA (5'-3')
dHP1 forward	GGCATCATATGGGTTGCAAC
dHP1 reverse	GTTAGCAGGATTGCGGGT

Polymerase Chain Reaction General Method

Stock concentration of control plasmid was made at various concentrations such that 5 ul of plasmid was added to each reaction. Three stocks were made (200 copy/µl, 20 copy/µl, and 2 copy/µl), from the 200,000 copies/ml solution purchased from IDT. GoTaq RT-PCR kit was purchased from NE biolabs and the PCR reaction was run according to the standard protocol: n = N+1, where N = number of reactions (with same primers) and reagents were added according to *Table 5.13*. After all reagents from kits were added, 5 ml of template was added and PCR was run according to *Table 5.14*. Following PCR reaction, 30 µl of rHP1-Au(I) complex was added in sodium perchlorate buffer (125 mM) and 50 µl of probe **5.1** in 80% ethanol were added such that the final concentration of dHP1-Au(I) and probe **5.1** were 250 nM and 200 µM, respectively.

Table 5.17 RPA amplification with dHP1.

Reagent	Volume of reagent added per n
Nuclease-free water	3.1
Primer/Probe mix	1.5
GoTaq Probe qPCR master mix	10
Go Script RT mix	0.4

Table 5.18 PCR thermocycling method

Reaction	Temperature (°C)	# Steps	Time
RT	45	1	15 min
RT-stop	95	1	2 min
Anneal	95	40	3 sec
Extension	55	40	30 sec
Hold	10	1	—

Recombinase Polymerase Reaction General Method

Stock concentration of control plasmid was made at various concentrations such that 0.5 ul of plasmid was added to each reaction. Three stocks were made (200 copy/µl, 20 copy/µl, and 2 copy/µl), from the 200,000 copies/ml solution purchased from IDT. TWistAmp Liquid Basic kit was purchased from TwistDx and the RPA reaction was run according to the standard protocol: n = N+1, where N = number of reactions (with same primers) and reagents were added according to *Table 5.13*. After all reagents from kits were added, 0.5 ml of template was added and RPA was run for 30 minutes at 42 °C. Following RPA reaction, 25 µl of rHP1-Au(I) complex was added in sodium perchlorate buffer (125 mM) and 50 µl of probe **5.1** in 80% ethanol were added such that the final concentration of dHP1-Au(I) and probe **5.1** were 250 nM and 200 µM, respectively.

Table 5.19 RPA amplification with dHP1.

Reagent	Volume of reagent added per n
2x reaction buffer	12.5
dNTPs (1.8 mM)	4.6
10x Basic E-mix	2.5
Primer Mix (10 µM mix)	2.4
20x Core Reaction Mix	1.25

5.10.5.1 Data

Table 5.20 PCR amplification with rHP6.

[copies/µl]	Mean	Std. Dev.
10	2216	541
1	1663	979
0.1	698	38
0	599	32

Table 5.21 RPA amplification with rHP6.

[copies/µl]	Mean	Std. Dev.
1	15486	1334
0.1	13537	7678
0.01	8677	1162
0	7368	861

Figure 5.20 PCR with different templates and dHP1-Au(I) with dHP1 primers added.

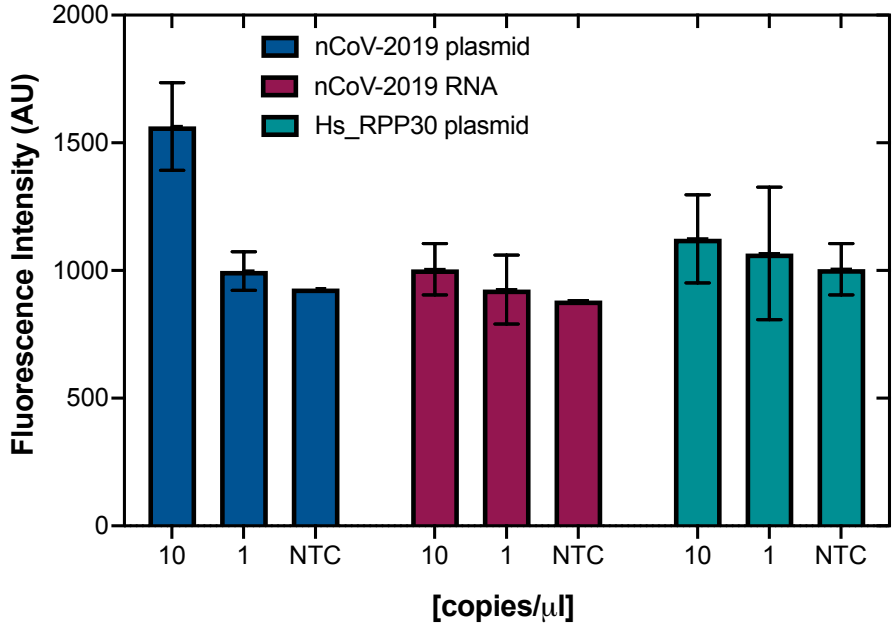

\

Table 5.22 PCR with different templates and dHP1-Au(I) with dHP1 primers added after 1 hour.

[copies/μl]	Template	Mean	Std. Dev.
10	nCoV-2019 plasmid	1564	1712
1	nCoV-2019 plasmid	998	76
0 (NTC)	nCoV-2019 plasmid	929	__
10	nCoV-2019 RNA	1005	101
1	nCoV-2019 RNA	925	135
0 (NTC)	nCoV-2019 RNA	882	__
10	Hs_RPP30 plasmid	1124	172

1	Hs_RPP30 plasmid	1067	259
0	Hs_RPP30 plasmid	1005	100

5.11 Notes and References

(1) CDC. 2019 Novel Coronavirus, Wuhan, Chicna. CDC. Available at https://www.cdc.gove/coronavirus/2019-ncov/about/index.html. January 26, 2020; Accessed: February 12, 2020.

(2) CDC. CDC's Diagnostic Test for COVID-19 Only and Supplies. Available at: https://www.cdc.gov/coronavirus/2019-ncov/lab/virus-requests.html. July 15 2020. Accessed: May 31, 2020.

(3) T. R. Merver, M. Salit, Testing at scale during the COVID-19 pandemic. *Nat Rev Genet* **2021**, https://doi.org/10.1038/s41576-021-00360-w.

(4) C. R. Wells, J. P. Townsend, A. Pandey, S. M. Moghadas, G. Krieger, B. Singer, R. H. McDonald, M. C. Fitzpatrick, A. P. Galvani, Optimal COVID-19 quarantine and testing strategies. *Nat. Commun* **2021**, *12*, 356.

(5) M. J. Mina, R. Parker, D. B. Larremore, Rethinking Covid-19 Test Sensitivity – A Strategy for Containment. *N Engl J Med* **2020**, *383*, e120.

(6) O. Vandeneberg, D. Martiny, O. Rochas, A. van Belkum, Z. Kozlakidis. Considerations for diagnostic COVID-19 tests. *Nat Rev Microbiol* **2021**, *19*, 171–183.

(7) Real-time RT-PCR panel for detection 2019-novel coronavirus. (2020) US Centers for Disease Control and Prevention. https://www.fda.gov/media/134922/download [Accessed 5 July 2020].

(8) S. Maddocks, R. Jenkins, "Understanding PCR-Quantitative PCR: Things to Consider" in Understanding PCR: A practical benchtop guide, (Elsevier, 2017), pp 45–52.

(9) Y.-W. Tang, J.E. Schmitz, D.H. Persing, C.W. Stratton, Laboratory diagnosis of COVID-19: current issues and challenges. *J. Clin. Microbiol.* **2020**, *58*, e00512-2.

(10) R. Chattopadhyaya, K. Grzeskowiak, R. E. Dickerson. Structure of a T4 hairpin loop on a Z-DNA stem and comparison with A-RNA and B-DNA loops. *J Mol Biol.* **1990**, *211*, 189–210.

(11) A. Ono, H. Torigoe, Y. Tanaka, I. Okamoto Binding of metal ions by pyrimidine base pairs in DNA duplexes. *Chem. Soc. Rev.* **2011**, *40*, 5855–5866.

(12) G. Yao, W. Tan Molecular-beacon-based array for sensitive DNA analysis. *Anal. Biochem* **2004**, *331*, 216–223.

(13) W. Geng, A. M. Newbigging, C. Le, B. Pang, H. Peng, Y. Cao, J. Wu, G. Abbas, J. Song, D.-B. Wang, M. Cui, J. Tao, D. L. Tyrrell, X.-E. Zhang, X. C. Le Molecular Diagnosis of COVID-19: Challenges and Research Needs. *Anal. Chem.* **2020**, *91*, 10196–10209.

(14) M. Baer, T. W. Nilsen, C. Costigan, C. Altman, Structure and transcription of a human gene for H1 RNA, the RNA component of human RNase P. *Nucleic Acids Res.* **18**, 97–103 (1990).

(15) Diagnostic test for COVID-19 only & supplies. (2020) Centers for Disease Control and Prevention. https://www.cdc.gov/coronavirus/2019-ncov/lab/virus-requests.html [Accessed 6 July 2020].

(16) M. L. Bastos, S. Perlman-Arrow D. Menzies, J. R. Campbell The Sensitivity and Costs of Testing for SARS-CoV-2 Infection with Saliva Versus Nasopharyngeal Swabs. *Ann. Intern. Med.* **2021**, *174*, 501–511.

(17) A. C. Nelson, B. Auch, M. Schomaker, D. M. Gohl, P. Grady, D. Johnson, R. Kincaid, K. E. Karnuth, J. Daniel, J. K. Fiege, E. J. Fay, T. Bold, R. A. Langlois, K. B. Beckman, S. Yohe. Analytical Validation of a COVID-19 qRT-PCR Detection Assay Using a 384-well Format and

Three Exraction Methods. *BioRxiv. Preprint.* **2020** Doi:

https://doi.org/10.1101/2020.04.02.022186.